Fabrication of polymer composites as potential bone replacement materials

Stephanie Kelly MSci (Hons)

UNIVERSITY
of
GLASGOW

Submitted in fulfilment of the requirements for the Degree of Doctor of Philosophy

School of Chemistry
College of Physical Science
University of Glasgow

September 2012

Abstract

In the field of bone replacement therapy, biomaterials capable of acting in a scaffolding capacity are under constant review and improvement. To operate as a scaffold material, several requirements must be met. Initially, materials must exhibit mechanical properties similar to natural bone. Degradability is another key requirement; the material must degrade at a rate compatible with ongoing bone regeneration at the site of implantation. Finally, the implanted product must induce a biological response to promote bone formation. In this regard, calcium phosphate ceramics are commonly used in clinical applications to promote bone regeneration, whilst composite materials containing several different components satisfying the above criteria have also been developed.

The aim of the research described herein was to investigate the potential of combining polylactic acid (PLA) and calcium phosphate (CaP) compounds together to develop composite materials with good mechanical properties, degradability adjustability, and an increased potential for promoting bone regeneration. CaP materials focused on β-tricalcium phosphate (β-TCP) and magnesium substituted β-tricalcium phosphate (Mg-TCP), whilst an industrial collaboration provided a protein (casein) alternative to investigate. β-TCP samples were synthesised using a surfactant templated process, which allowed for control over the size, morphology and surface area of samples. Cationic substitutions of magnesium for calcium, at a range of levels, were carried out to study the mechanism of substitution into the crystal structure of β-TCP. All films were synthesised *via* the solvent casting method, and the composition and surface morphology was characterised. The degradation of non-filled PLA and composite films was analysed in deionised water, and the bioactive potential of the films was determined in simulated body fluid (SBF). Tensile strength measurements of the films were noted at several time points throughout the degradative process to evaluate maintenance of mechanical stability.*In vitro* assessment of the films was investigated with immunofluorescence and real time polymerase chain reaction (q-PCR) evaluations.

This project addresses the various steps necessary to successfully synthesise a scaffold biomaterial for acceptable bone replacement, from the initial synthesis of the filler materials, through to the various mechanical and biological assessments which must be conducted to the suitability of said materials for use in clinical applications.

Declaration

The content of this thesis is original work, except where reference is made to other authors. This work has not been submitted previously for any other degree or qualification in this or any other university.

Stephanie Elizabeth Kelly

Contents

List of Figures

Page

List of Tables

Acknowledgements

I would firstly like to thank my three supervisors for all their help over the past four years; Professor Duncan Gregory, Professor Liz Tanner, and Dr Matt Dalby. Duncan, thank you for your support and assistance and for keeping me moving in the right direction. Matt, your unending patience and kindness with me when I was struggling with cellular engineering will never be forgotten. And finally Liz, you have been not only a supervisor to me, but also a mentor and a friend, so thank you.

I couldn't have finished this PhD without the help of others, in particular Jamie Gallagher for SEM imaging, Ross Colquhoan for mechanical testing, Carol Anne Smith for cellular engineering, Robert Hughes for rietveld refinements, and Hazel Reardon and Nuria Tapia for Raman.

To all the members of the Gregory group past and present, thank you for injecting laughter into every day. Jen, our insulting greetings each morning made refinements that bit more bearable, and Miss Sorbie, we kept each other from becoming Bunsen and Beaker with random holiday bookings and haircare products. Special thanks also go out to Claire McCormack and Lynsey Pugh, whose random lab visits were a welcome distraction.

To my husband Paul, you have been a pillar of strength from day one of this experience: your support and guidance has helped me immensely, and you have always believed in me, even when I didn't, so thank you always.

Finally, to my family. Megan, you've been my best friend as well as my sister, and life just wouldn't be as fun without you. Dad, you've helped me get to this point over the last ten years, I'll never forget our wee 'joot aboots'. You have always been there for me, and made it possible for me to spend all these years studying, and I appreciate that more than you will ever know. Finally, to my mum. Her strength and love for her family have inspired me daily, and I strive to become a tenth of the woman she was.

1. General Introduction

1.1 Introduction to Bone

"Bone is a remarkable living material which is continually removed and replaced throughout life." [1]

Inorganic salts and an organic matrix constitute the phases which combine to produce the extracellular matrix in bone. Mechanically, bone confers superior strength and rigidity properties, as well as ductility. Such ductility is attributed to the presence of the organic component, which consists primarily of type I collagen, whilst strength and toughness is gained from the biological apatite [$Ca_{10}(PO_4)_6(OH)_2$].[2] A low level of water represents the third component of bone.

Bone forms the skeleton of the body and has three main functions; the most common of which is recognised as a supportive framework for the body, providing protection for the brain and other internal organs. In addition, bone also sustains loads from external actions and allows for movement.[3] Moreover, the 206 bones in the human body store nutrients and minerals, and produce blood cells. Bones, therefore, help protect the body from both internal and external forces which could cause irreparable damage. Bone maintenance is performed by osteoclasts and osteoblasts, which remove and replace bone, respectively. A third class of cells, osteocytes, are responsible for detecting potential damage at the bone surface.

The essential role bone plays within the body, combined with an increase in the average lifespan of the population, has led to major research drives within bone tissue engineering.[4] Stem cell research and the investigation of osteoprogenitor differentiation studies have provided cellular engineers with the tools to study likely biological responses to a range of biomaterials. In the area of bone replacement therapy, calcium phosphate ceramics, coupled with polymer matrices to produce composite materials, display the most promise for continued clinical success.

This research aims to produce composite materials in which the calcium phosphate filler material possesses a pre-determined and controlled morphology and chemical composition. Porosity and levels of ionic substitution are to be investigated as a possible means to

influence osteoconductivity and mechanical strength. Polylactide (PLA), a biodegradable polymer, functions as the polymer of choice to create the matrix of the composite, whilst beta tricalcium phosphate (β-TCP) is the calcium phosphate filler. The primary aim of this PhD is to create composites which stimulate and enhance bone regeneration for eventual use in clinical applications, whilst still maintaining mechanical properties similar to those of natural bone.

To achieve success in synthesising a material for use within bone tissue engineering, a basic knowledge about the composition, structure, and nature of bone growth and regeneration must be developed.

1.2 Bone composition

1.2.1 Inorganic salts

Around 66% of the total mass of bone consists of inorganic salts.[5] From this, 80 % of these salts are present in the form of hydroxyapatite (HA), a calcium phosphate crystal with the molecular formula $Ca_{10}(PO_4)_6(OH)_2$. Biological apatite contains small levels of substitution by ions such as sodium (Na^+), protonated and deprotonated phosphates ($H_2PO_4^-$ HPO_4^{2-}, PO_4^{3-}) and carbonates (CO_3^{2-}), which contribute to its high levels of bioactivity. The remaining 20% consists mainly of calcium carbonate ($CaCO_3$) and magnesium phosphate ($Mg(PO_4)_2$).[6] Bone hardness and rigidity is attributed to the presence of such salts.

1.2.2 Organic matrix

The remaining 34% of bone mass is attributed to an organic matrix consisting of collagen, cells and various proteins. Around 9% of the proteins found in said matrix are accounted for by type I collagen.[7] Collagen is a fibrous protein easily recognised by its shape: a three-stranded polypeptide helical molecule, wrapped into a fibril. A right handed helix coil is formed when the fibrils twist together, and is stabilised by hydrogen bonding.[8] This process of formation and structure contributes to the flexibility of bone.

In addition to collagen, there is a mixture of proteins and polysaccharides present within the organic matrix of bone, known as ground substance. Of these proteins, chondroitin

sulphate, a large protein consisting of over 100 different sugars, provides much of bones resistance to compressive forces.[9] Overall, ground substance contributes to the toughness of bone.

1.3 Bone structure

Bone structure can be categorised into two types: cortical and cancellous (also known as compact and spongy bone, respectively). Cancellous bone is found to be younger, on average, than cortical bone: the metabolic activity of cancellous bone is much higher than cortical bone and it is remodelled more often.[10] Cortical bone is found in the outer layers of bone, whilst cancellous bone fills the interior.[11]

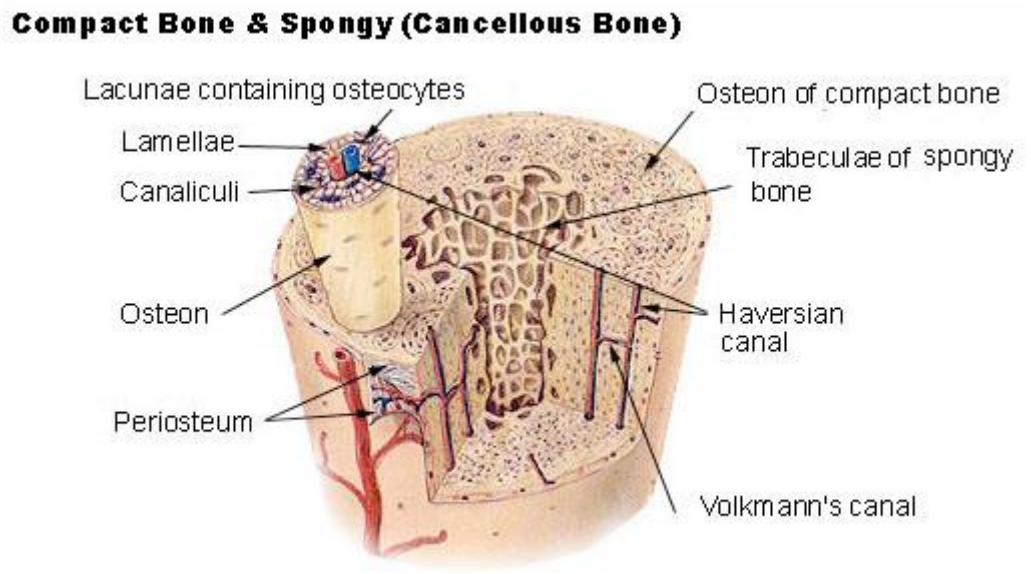

Figure 1.1 Infrastructure of compact and spongy bone.Trabeculae of cancellous bone is observed alongside the Haversian systems of cortical bone.[12]

Bone can also be classified as either lamellar or non-lamellar. Non-lamellar bone only occurs in the foetus, young children or healing fractures, whilst all mature bone is lamellar.

1.3.1 Cortical bone

As the name suggests, compact bone contains very little gaps or spaces; its porosity ranges from 2-15%, ensuring a very hard and dense material.[4] This is essential in the function of bone as a protectant of the organs of the body. Compact bone consists of osteons, or Haversian systems, closely packed together. An osteon is the basic unit of compact bone: it is a cylindrical structure, 20 to 100μm in diameter, and contains many layered rings (lamellae)which surround and protect a central Haversian canal.[13] These canals allow blood vessels to penetrate through cortical bone, providing the nutrients required to regenerate and eliminate waste material.

Osteocyte cells are found in spaces in between the rings (lacunae). Small channels (canaliculi) exist between lacunae to the Haversian canal to provide passageways through the dense material. Nutrients and oxygen reach the osteocytes through the canaliculi, and allow waste products of metabolism to diffuse away.[14] The solid appearance of cortical bone is achieved through the close packing of multiple Haversian systems.

The Young's modulus of any material measures its stiffness, and is a ratio of linear stress to linear strain. It is an important parameter in biomedical engineering as materials must have mechanical properties which can withstand similar levels of stress to bone. Dependant on age, orientation, disease processes and other factors, the Young's modulus for human wet cortical bone is within the range of 7 - 25GPa. [15] The typical mineralisation level for cortical bone is 40-45 vol%. The level of mineralisation within a specific bone sample can affect the Young's modulus significantly.[16]

1.3.2 Cancellous bone

In contrast to cortical bone, the basic structural unit in cancellous bone is called the trabecula. This is an interconnected lattice of bone threads. The width of each thread is thin, contributing to the reduction in mechanical strength observed in comparison to cortical bone. Cancellous bone is less dense than cortical bone, with porosity between 30-90%. Each trabecula is composed of layers of lamellar bone. The alignment of the trabeculae is dependent on the direction of applied stress, so variation can be seen between samples.[17] When stress is applied to cancellous bone, the strongest and thickest trabeculae will orient themselves to counteract and resist the mechanical forces.

Osteocytes are also present within the trabeculae of cancellous bone, found within lacunae. Red bone marrow cells are found in the structure within small cavities, and canaliculi receive their blood supply from adjacent cavities and the blood circulating through such cavities. This differs grossly from compact bone, wherein canaliculi receive supplies from the central Haversian canals.

Whilst the Young's modulus for cortical bone is high, the corresponding value for wet cancellous bone is reported as varying between 0.6 to 2 GPa.[18, 19, 20] This decrease can be directly attributed to the high porosity of cancellous bone.

1.4 Bone cells

In order to produce, maintain and modify bone, a continuous layer of cells are found covering all the extracellular matrix surfaces. Three main types of bone cells are commonly recognised:

- Osteoblasts(bone formation)
- Osteocytes(bone maintenance)
- Osteoclasts(bone resorption)

Osteoblasts and osteoclasts are found covering the surface of bone, whilst osteocytes reside inside the extracellular matrix.

1.4.1 Osteoblasts

Derived from mesenchymal stem cells, osteoblasts are responsible for the formation of new bone through the production of osteiod. Osteoid is composed of collagen and other proteins, and forms part of bone ground substance. Osteoblasts are found in abundance in all areas of active bone growth and repair. They have previously been described as a "cuboidal, polar, basophilic cell", as seen in Figure 1.2.[21] Once the osteiod has been produced, the osteoblasts have fulfilled their function and afterwards become flat and line the surface of the newly laid bone.[22] For this reason, mature osteoblasts are often referred to as lining cells. The passage of calcium into and out of bone is regulated by lining cells, which cover up to 95% of bone surface area.

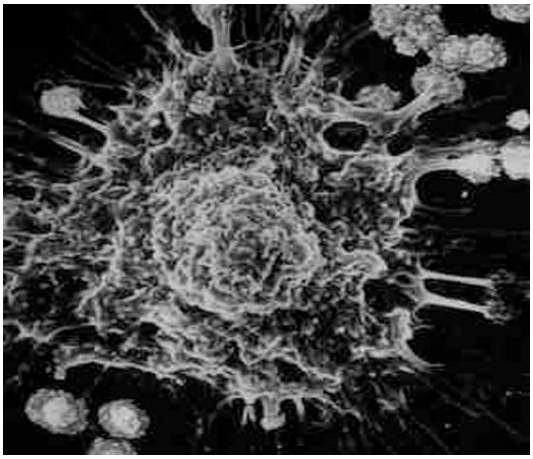

Figure 1.2 Osteoblast cell (in 2D culture)[23]

1.4.2 Osteocytes

At over 90% occupancy, osteocytes constitute the highest number of bone cells within the body. An osteocyte is essentially an inactive osteoblast which is incorporated into mineralised bone within lacunae. Osteocytes are thin cells with long, spidery-like extensions used to communicate with other osteocytes and lining cells (Figure 1.3). This high degree of interconnectivity allows any cracks, pressures or potential injuries to be immediately detected.[24] Bone resorption, or formation thereafter, occurs as a result of biochemical signals transmitted by osteocytes.[25]

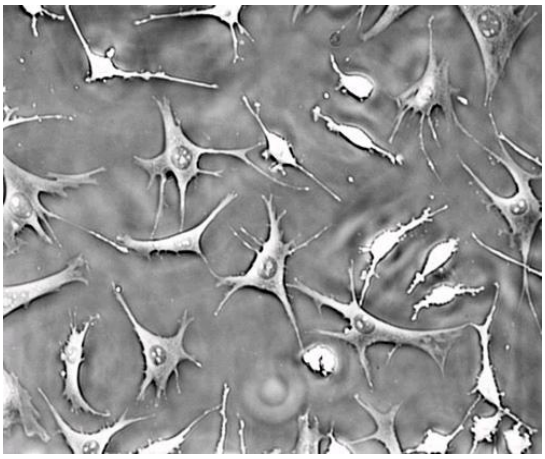

Figure 1.3 Osteocyte cell[26]

1.4.3 Osteoclasts

Osteoclasts are large, multinucleated (5-50 nuclei) cells derived from bone marrow. Found at the surface of bone sites where resorption is actively occurring, they are involved in the dissolution of bone through secretion of acids and proteolytic enzymes. An image of a typical osteoclast cell is given in Figure 1.4. Osteoclasts reside in shallow depressions known as Howship's lacunae, in areas of active resorption.[27]They are required at sites of bone remodelling, repair, and also in cases wherein excess bone has been deposited by osteoblasts.

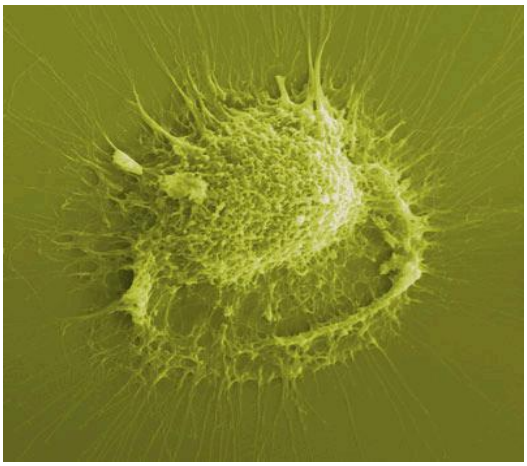

Figure 1.4 Osteoclast cell[28]

1.5 Bone remodelling

Bone is a constantly changing tissue: it undergoes numerous chemical and metabolic reactions, collectively known as bone remodelling, from birth through to death. Bone remodelling is essential in order to adapt to changes in the mechanical stresses and forces of natural movement, and for potential recovery from damage. The two stages which work together in the remodelling process are bone removal (resorption), and bone replacement.[10] The cells required to complete both stages are grouped together in small packets called 'basic multicellular units' (BMUs).The rate of remodelling is governed by the specific region of the body. It must be noted that remodelling rates are significantly different depending on the region. Areas of the femoral shaft will go unreplaced throughout a lifetime, whilst, in contrast, the distal femur of the lower thigh undergoes complete regeneration every four months.[29] Remodelling not only permits damaged bone to be

replaced, but it also allows reservoirs of calcium to be freed for use in other sites of the body.

In certain instances, bone remodelling can be initiated as a result of mechanical stimuli. Precisely how the translation of mechanical loading is conferred to the cells responsible for initiating a range of biochemical reactions, which counteract this loading, is still unknown. The study of this relationship between mechanical stimuli and biological responses is known as mechanobiology, and early research in the field dates back to 1888.[30]

The removal of a specific area of osteoid lining by osteoclasts marks the first phase of bone removal (Figure 1.5). Upon adherence to the surface, a variety of proteolytic enzymes are secreted to begin bone resorption.[31]Osteoprogenitor cells then migrate into the lacunae and stop the former osteoclatic activity. The osteoprogenitor cells thereafter mature into osteoblasts to produce bone matrix to fill the lacunae.[32]Mineralisation of bone occurs as the bone matrix is laid: calcium (Ca^{2+}) and phosphate (PO_4^{3-}) ions are incorporated to form the mineral content of bone (1.5e).Once the gap has been filled, osteoblasts can mature into undifferentiated osteoclasts, and become lining cells (1.5f).

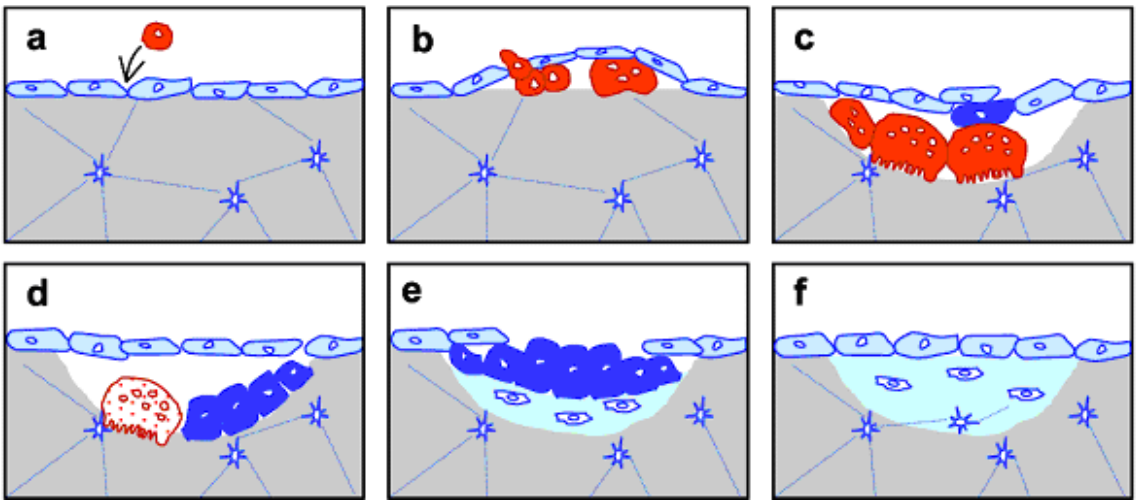

Figure 1.5Schematic of stages of bone remodelling. [33]Osteoblast (light and dark blue) and osteoclast (red) cells are shown.

a) Osteoclast cells recruited at site of resorption.

b) Increase in cell number of osteoclasts through differentiation.

c) Bone resorption by osteoclasts induces osteoblast differentiation (dark blue).

d) Cell death of osteoclasts upon complete resorption.

e) Bone formation by osteoblasts.

f) Transformation of osteoblasts to lining cells.

1.6 Stem cells and osteoblast differentiation

1.6.1 Stem cells

Stem cells are cells which can divide and develop into a range of specialised cells within the body, including blood cells, brain cells and bone cells. When a stem cell divides through mitosis, the "daughter" cell has the potential to either differentiate into a specialised cell, or remain a stem cell. Differentiation refers to the process by which this less specialised cell develops and attains structural or functional features specific to a certain class of highly specialised cells. The ability of stem cells to renew and differentiate into multiple cell types (pluripotency) ensures they are at the forefront of tissue engineering. This potentially allows a range of tissues to be generated from a single cell.[34]

Various signals, both internal and external to cells, trigger each stage of the differentiation process. Internally, the cell undergoes changes in its gene expression as it changes from one cell type to another, becoming more specialised as the development progresses. These changes are monitored by cell signalling, and the influence of growth factors and hormones are well documented. However, the influence of external forces, in particular the influence of mechanical forces on cellular differentiation, is only recently being studied.[34] To fully appreciate the influence each signal has on differentiation requires further research.

Mesenchymal stem cells have multipotency capacity, meaning that they are capable of forming any cell type within the same cell line. They were first discovered in bone marrow by Friedenstein.[35] These cells had the ability to form bone *in vivo*, and demonstrated significant proliferative capacity. From this, further research showed that other cell types could be formed, including fibrous and cartilage cells. These initial *in vivo* findings were further investigated with experiments *in vitro*, the results of which showed the formation of a range of differentiated cell phenotypes.

1.6.2 Osteoprogenitor differentiation

One cell phenotype derived from mesenchymal stem cell differentiation is that of the osteoprogenitor. Found within bone marrow, osteoprogenitor cells are those progenitor cells which are restricted to bone formation, through osteoblast development.

The process by which an osteoprogenitor progresses from a generic stem cell to a fully functionalised osteoblast has been divided into three stages. Firstly, cell proliferation increases cell population. Next, the development and maturation of the type I collagen-rich extracellular matrix occurs. Finally, the organic matrix becomes entwined with inorganic components to become mineralised.[36] These stages have been identified through various *in vivo* and *in vitro* observations.

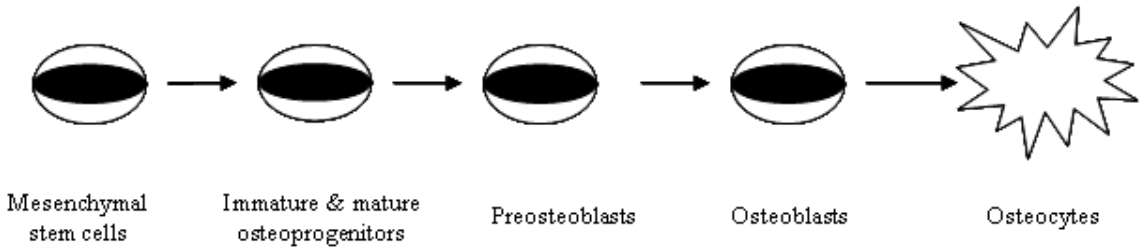

Figure 1.6 Sequence of proliferation and differentiation steps in formation of osteoblast cells from mesenchymal stem cells.

Osteoblast differentiation and development is a highly controlled and complex process, involving many stages. At each stage, differentiation is guided by signalling proteins and transcription factors (TF's) specific to osteoblasts. These are, in turn, activated by various growth factors, hormones and signalling pathway genes.[37] Extensive researches on the influence of TF's have been performed to understand the differentiation process. The most studied form of TF's is the core binding factor alpha 1 (Cbfa1), also known as runt-related gene 2(Runx2). The role of the Cbfa1 TF is to activate osteocalcin, the most osteoblast specific gene, and regulate gene expression.[38] Presently, the roles of certain factors in the differentiation process still have to be determined in order to appreciate the true complexity of the process.

1.7 Bone breakages and methods of repair

Bone breakages (fractures) can occur at all ages, but become more common in the elderly, as overall bone mass decreases and diseases such as osteoporosis become prevalent. Various methods have previously been used to repair damaged bones, including autografts, allografts and artificial materials. However, each substitute poses specific problems and limitations. Autografts, where healthy parts of bones are grafted into a new position of the body of the same individual, have been widely used due to their high performance and low risk of foreign body reaction. However, autografts can be of limited use if large amounts of

tissue are required. Allografts, wherein organs and tissues are transferred to the patient from another individual, have always been prone to immune system reactions and limited availability, and include the risk of disease transmission. Artificial materials, which are deemed safe and freely available, often appear the obvious choice for treatment, and have lead to a surge in biomaterial research and development.

1.8 Biomaterials

1.8.1. Introduction

The concept of using a biomaterial, a material used within the human body to illicit or fulfil a biological purpose, has been occupied since prehistoric times, when the Mayan people integrated dental implants into bone using nacre (mother of pearl).[39] Biomedical materials have since been at the forefront of the healthcare sector, with treatments on skeletal defects in patients in the United Kingdom costing approximately £900 million yearly.[40] This figure is only set to rise with the increasing age of the population. Extensive research into many different options has been carried out in the hope to find a suitable replacement for bone; these include the use of metals, ceramics and polymers as potential candidates. An area of active research is aimed at developing ceramic materials further, which focuses attention on calcium phosphate compounds HA and β-TCP.

Although this area has progressed significantly, there are still many synthetic barriers to overcome in regards to making a material which mimics the natural components of bone. Bone is a vascularised dynamic living tissue which is able to remodel and heal, whilst withstanding high loads within the body. The ability of bone to fulfil such a wide range of requirements is owed to the fact that bone itself is a composite material.[41] Its matrix consists of both a mineral and organic phase, each of which fulfils bone's demands of mechanical strength and flexibility, respectively. Katz *et al* developed this further, presenting the idea that bone itself is "a composite of a composite of a composite".[42] From this, the concept of manufacturing an analogue, a composite of bone itself was developed. Currently the use of composites as a material for biomedical applications is at the forefront of biomaterial research, and forms the basis of research in this PhD.

1.8.2 History and classification of biomaterials

1.8.2.1 Metals

As previously stated, materials have been used in a biomedical capacity for millennia. Damaged patellas were repaired in the USA by using steel fracture plates coated in silver in the 19th Century.[43] The use of metals and their alloys is still commonly employed, and include stainless steel, titanium and cobalt-chromium alloys. Metals used in this capacity are termed 'first generation' materials, indicating that they aim to fulfil the mechanical requirements of a bone graft, but have minimal or no interaction with the surrounding tissue. This class of material was initially used because there would be no response which could detrimentally affect the host. This unfortunately meant that the lack of osteoconductivity caused the host's immune response to reject the implant. When this occurs it leads to pain and further surgeries for the patient. In addition to this, large variances in mechanical properties exist between metals and bone. Attributing to its stiffness, bone has a Young's modulus of 7-25GPa, whilst the Young's modulus of stainless steel is 210GPa. This leads to stress shielding.[44] Stress shielding is where bone loss can occur as a result of such large differences in material moduli. Over time, loosening of the implant has also been reported in patients.

1.8.2.2 Ceramics

To improve on the poor biological properties of metal implants, ceramics were developed which were more favourably bioactive. In the late 19th century Plaster of Paris, a hemihydrate of calcium sulphate ($CaSO_4$) bioresorbable ceramic was the first ceramic used as a bone substitute by Dreesmann. [45] It did not inhibit osteogenesis, but also did not provide any internal strength or support, so was only used to fill small bone defects. Currently, ceramic research revolves around calcium phosphate compounds, which are termed 'second generation' biomaterials. Bioactive second generation materials are those which the body can interact with. They induce a biological response from surrounding tissue. Such biological responses include the ability to promote bone apposition and osseointegration. Common to many bioceramics is the formation of an apatite layer on the surface of the material, which is similar to the natural inorganic component of bone.[46] This is deemed crucial to the heightened bioactivity of ceramics.

First generation biomaterials, i.e. metals, have the ability to partly mimic the mechanical properties of bone. However, the second generation ceramics cannot. The use of calcium phosphate biomaterials for applications that require significant torsion, bending or sheer strength is simply impractical. Similarly to Plaster of Paris in the 19th Century, they too possess low tensile strength and are very brittle, leading to limited application within the body.[44]

1.8.2.3 Polymers

Polymers such as polymethylacrylate (PMMA) have been utilized for decades as a bone substitute. However, it is not reabsorbed, which prohibits new bone formation at the site of the defect. In its place, biodegradable polymers such as PLA and poly(glycolic acid) (PGA) are now used. These biodegradable polymers are considered ideal materials because their rate of degradation can be tuned so that the polymer degrades at the same rate as new bone is being formed, allowing for full regeneration of the defect site.[47] However, low levels of bioactivity and Young's modulus are drawbacks of such polymers. As a consequence of poor mechanical properties, their application in load bearing implants has been severely hindered, in a similar manner to ceramics.

1.8.2.4 Composites

Metals, ceramics and polymers, as biomaterials, have all experienced limited success in their use as bone replacements. Each still lacks at least one specification to make it a truly successful agent in bone replacement therapy. With regards to metals, although they exhibit the most promising mechanical results, they are bioinert. Ceramics, oppositely, have high bioactivity but poor mechanical properties. Although polymers possess the favourable property of biodegradability, they too lack the ability to withstand mechanical demands.[44]

Researchers thereafter decided to mimic the composition of bone itself, and synthesise a material which contains two distinct phases, each of which would fulfil a specific function. At Queen Mary College, University of London, Bonfield and co-workers synthesised the first composite in 1980, containing polyethelyene (PE) reinforced with hydroxyapatite.[48] Using HA as the composite filler fulfils the bioactivity requirement of biomaterials, whilst a matrix of a biopolymer counteracts previous problems of modulus mismatch between the

implant material and bone. The composite with 40vol% HA was given the trade name HAPEX^{TM}, and has been used as a shaft in middle ear implants successfully.[49] HAPEX^{TM} and similar composites which show both resorbable and bioactive properties are termed as 'third generation' biomaterials. This means that this class of materials help the body to heal itself through their presence and subsequent degradation within the body. Composites will be covered in more detail in section1.14.

1.9 Calcium phosphate materials

Various materials have been investigated for their use as potential bone repair agents, including metals, polymers and ceramics. In addition to high bioactivity levels, ceramics have been widely investigated because two thirds of bone consists of an inorganic component. As the mineral in bone is composed of the calcium phosphate material HA, various calcium phosphate compounds have been researched, several of which are listed in Table 1.1:

Table 1.1 Main Calcium Phosphate compounds

Ca/P molar Ratio	Compound	Formula	Symbol
2.0	Tetracalcium phosphate	$Ca_4(PO_4)_2O$	TTCP
1.67	Hydroxyapatite	$Ca_{10}(PO_4)_6(OH)_2$	HA
1.5	β-Tricalcium phosphate	β-$Ca_3(PO_4)_2$	β-TCP
1.5	α-Tricalcium phosphate	α-$Ca_3(PO_4)_2$	α-TCP
1.33	Octacalcium phosphate	$Ca_8(HPO_4)_2(PO_4)_4.5H_2O$	OCP
1.0	Dicalcium phosphate anhydrous	$CaHPO_4$	DCPA
1.0	Dicalcium phosphate dihydrate	$CaHPO_4.2H_2O$	DCPD
0.5	Monocalcium phosphate anhydrous	$Ca(H_2PO_4)_2$	MCPA
0.5	Monocalcium phosphate monohydrate	$Ca(H_2PO_4).2H_2O$	MCPM

Of these, the compounds HA and β-TCP have yielded the most successful results. Both similar to the inorganic component of bone in composition, they vary in osteoconductivity and degradability.

1.9.1 HA

HA is the most studied calcium phosphate phase in biomedical applications due to its similarity in composition and structure to the inorganic component of bone. Exhibiting

lattice parameters of a = 9.4215Å, b =2a, c = 6.8815Å, HA is monoclinic with space group $P2_1/b$, and has the chemical formula $Ca_{10}(PO_4)_6(OH)_2$, as seen in Figure 1.7.[50] Its calcium to phosphorus ratio is universally defined as 1.67; however this can vary dependant on the synthetic method employed. Although HA is chemically similar to bone, acute differences remain. Natural bone is substituted with a range of different cations, including magnesium (Mg^{2+}), sodium (Na^{+}), chlorine (Cl^{-}), fluorine (F^{-}) and carbonate (CO_3^{2-}).[51] To enhance the biological activity of apatites further, different substituted variants have been tested *in vivo* and *in vitro*.

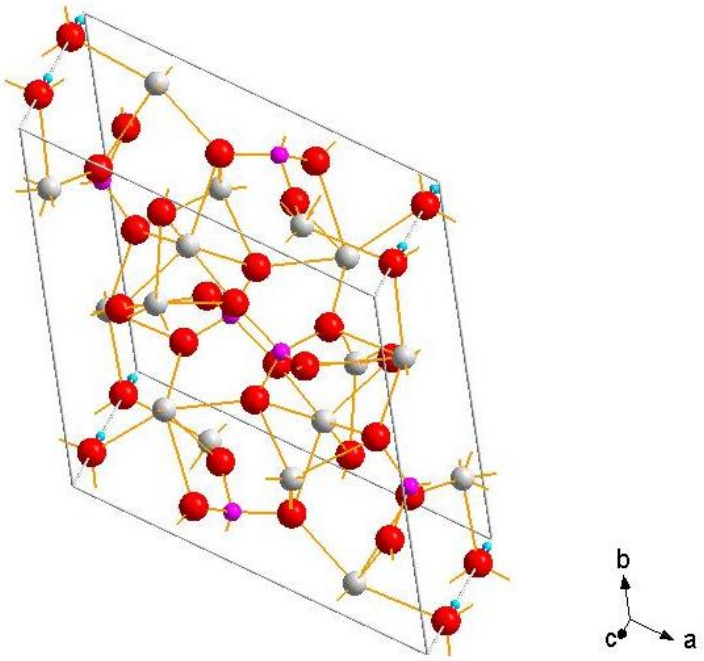

Figure 1.7 Crystal structure of hydroxyapatite (HA)

HA, used within the composite HAPEX™, has found much clinical success and has since been used in various applications. Solid state methods can yield HA through high temperature sintering reactions and the material can also be produced through employment of aqueous methods such as precipitation and sol-gel reactions. Although HA ceramics demonstrate osteoconductivity, their bioresorbability is low, meaning that HA remains in the body for a lengthy period of time after implantation. This property is undesirable from a bone scaffolding perspective, as it ultimately inhibits the formation of new bone ingrowth into the site of defect. However, its low resorption rate optimises the use of HA in areas wherein the rate of bone regeneration is low. Used clinically for the filling of periodontal defects, HA has also found use in the filling of defects remaining after tumour excision in orthopaedics.[52]

1.9.2 β-TCP

In recent years, there has been an exponential growth in research on β-TCP and its use in biomedical applications. Distinct from HA in its calcium to phosphorus ratio (1.5), it has the chemical formula $Ca_3(PO_4)_2$. β-TCP is hexagonal in structure, with space group R*3*c, and exhibits lattice parameters of a =10.4352 Å and c = 37.4029 Å (Figure 8).[53] TCP exists in two principle allotropic forms: α and β, separated by the temperature at which they form. β-TCP can be observed from a minimum temperature of 700°C, whilst α-TCP remains undetected until temperatures of ~1100°C are reached.[54]

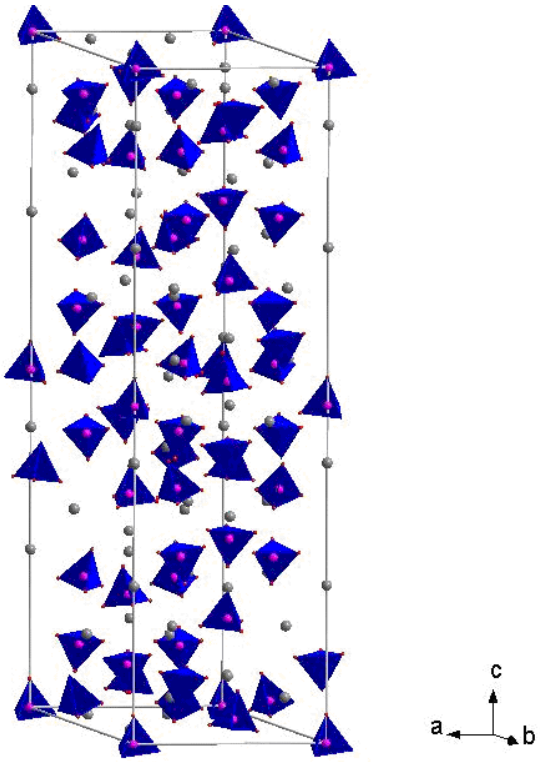

Figure 1.8 Crystal structure of β-Tricalcium phosphate (β-TCP)

β-TCP cannot be directly obtained through aqueous methods such as precipitation due to its instability in water. All synthetic procedures used to obtain the material must, therefore, contain a heat treatment above 700°C to obtain β-TCP. The intermediate formed prior to heat treatment is termed calcium deficient hydroxyapatite, with a calcium: phosphorus ratio of 1.5. Techniques to synthesise this calcium deficient apatite are similar to those for HA, and include wet chemical methods, microwave processing and solid state methods.[55] In contrast to HA, β-TCP shows much improved solubility and degradation properties, leading to its current focus of development for use as a scaffold material in bone regeneration. This resorbability ultimately allows it to be completely substituted for bone

tissue. Its rate of degradability can be tailored such that it matches the rate of formation of bone at the site of injury. Defects associated with periodontal loss have been clinically treated with β-TCP, and it is the material of choice when a resorbable material is required, for example, in an area of bone with high turnover.

1.10 Porosity

Research on calcium phosphate scaffold materials has progressed from the application of dense bulk materials, towards those with porous architecture. A scaffold should, by definition, "serve as a template for the cellular interactions which prelude bone formation, and remain whilst the formation of bone extracellular matrix occurs".[56] Previous densely packed ceramics could not offer the accommodation for these processes to occur, thereby limiting levels of bioactivity.

In order to optimise integration into surrounding tissue, scaffold materials should have a structure similar to bone. As both classes of bone contain a degree of porosity (trabecular: 30-90%, cortical: 2-15% as seen in Figure 1.1), it is essential that research into porous materials is progressed. Porosity accounts for the percentage of material consisting of void space, and a porous structure promotes cell attachment and bone formation through heightened levels of proliferation and differentiation. In addition, porosity allows body fluids to penetrate the scaffold material and provide osteoblasts with nutrients required for bone regeneration. Tissue regeneration is thereby favoured by the presence of a highly porous, interconnected structure.[57] Mechanical stability can also be improved through the introduction of a porous structure. It has been reported to improve mechanical interlocking between the implant material and bone.[58] One common method to change porosity inside the materials is through sintering, as temperature affects the porosity and pore size within the materials. Another method involves leaching out salt crystals, after which the ceramic remains.[59]

An extensive study by Hulbert *et al* produced detailed results on the determining effect pore size played on the bioactivity of a material. [60] It was deduced that mineralised bone could be regenerated, so long as the minimum pore size was ~100μm.This was established from an investigation using implanted calcium aluminate materials in dog femorals. Three pore size ranges were investigated: small (10-44 and 44-75μm), medium (75-100μm) and large (100-150 and 150-200μm). Only fibrous tissue was found inside the smallest pores,

whilst unmineralised osteoid was identified within medium pores. Large pores, however, showed substantial bone ingrowth, as seen in Figure 1.9:

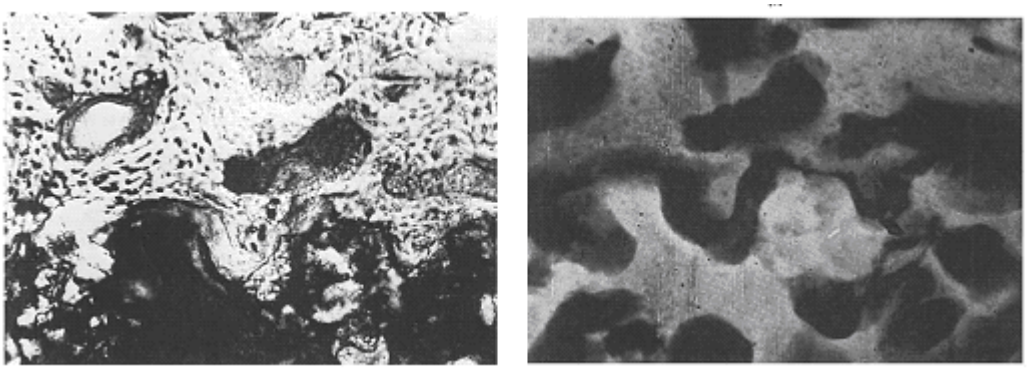

Figure 1.9 (a-b) Photomicrograph and (b) corresponding microradiograph showing initiation of bone ingrowth into 75-100 μm specimens after 4 weeks implantation (x185 magnification)

This research provided evidence on the different biological effects obtained through altering pore size, and suggested that pore sizes in the region of ~100μm constituted the best background for bone regeneration.

Despite the presence of pores increasing bone regeneration, and a small number of reports suggesting otherwise, a weakening in the materials mechanical properties is usually observed. As the level of porosity increases, the mechanical strength proportionally decreases. This poses a major challenge in developing scaffolds for use in load bearing applications. The ideal criteria for a scaffold material should include biocompatibility, biodegradability and mechanical properties similar to bone. Even in their dense form, HA and β-TCP are naturally brittle and the introduction of porosity only heightens the issue. There must, therefore, always be a balance between using a level of porosity which induces bone formation, but which still maintains adequate strength levels. For this reason, the clinical application of such materials has been limited to application in non-load bearing sites.[61]

Porous materials of HA, β-TCP and biphasic calcium phosphate(BCP) have all shown promising results for future development, both in terms of bioactivity, and mechanical properties. T.Uemura *et al* investigated the osteogenic activity of porousHA.[62] Samples of HA, with an average porosity of 77% and an average pore diameter of ~500μm, were implanted into subcutaneous sites of syngeneic rats. Results confirmed bone formation after 2 weeks in the pore areas of the HA, with levels increasing significantly until the end

of the 8 week experiment. Images showed high density levels of active osteoblasts in many of the pore areas, indicating that bone formation was progressive. Compressive (17MPa) and bending strengths (7 MPa) were high for a sample with such high porosity levels. This is attributed to a distinct lack of cracks throughout the material. The high porosity of the HA samples (77%) and interconnectivity of the pores is believed, by the author, to play an integral role in its osteogenic ability *in vivo*.

A porous scaffold of HA and β-TCP nanofibres was developed by Zhang *et al*, to study the capabilities of the biphasic composite in load bearing applications.[63] To investigate the repair of segmental bone defects, cylinders of 1.5cm length were implanted in the femora of 30 dogs. Results indicated that the mechanical properties of the scaffold were enhanced, with bending strengths increasing over time as the implant became integrated with regenerating bone tissue. Evidence for this is attained from the increased amounts of organic material within the pores. The combination of HA and β-TCP proved successful in this trial because the low solubility of HA allows the implant to retain a certain level of mechanical stability, whilst the high resorption of β-TCP allowed space for bone regeneration. Due to this dual regeneration/mechanical stability, the biomechanical strength of the regenerated site was similar to that of surrounding bone.

Bone formation has been observed in porous β-TCP ceramics by Yuan *et al*.[64] Ceramic rods were implanted into the dorsal muscles of dogs and studied over a 150 day time period. Within 30 days, populations of cells were observed within the pores of the ceramic, with the population increasing up to 45 days. By the end of the trial on day 150, bone tissue was observed within the pore structures, and the cells had largely become inactive and converted to lining cells. It is conclusive that bone formation is induced, within porous β-TCP ceramics, under physiological conditions.

1.11 Bone Bonding Mechanism

The bone bonding mechanism of bioactive ceramics (namely HA) and bioresorbable ceramics (β-TCP) are considered distinct from each other. Multiple literature accounts state that HA bonds to bone through the formation of a Ca deficient, carbonate-containing apatite layer on the surface of the ceramic.[65] This is believed to be essential to the osseointegration process, and has allowed for the assessment of bioactivity across many

potential biomaterials. In biomaterial research, the formation of an apatite layer *in vitro* suggests that the material will encourage bonding to bone *in vivo*.

Various reports exist on the mechanism of bonding between β-TCP and living bone, yet debate still resides on the subject of whether the formation of an apatite layer is confirmed. The interface of implanted β-TCP and rabbit tibia was studied by Kotani *et al*.[66] Using various characterisation techniques, it was confirmed that no apatite layer formed on the surface of the ceramic, despite fusion of bone to the material being observed. The driving force behind the direct contact is thought to be due to microanchoring between β-TCP and bone. Later studies confirmed the direct bonding of bone to β-TCP. A distinct lack of surface layer is again confirmed, with a possible mechanism of interlocking explaining the mode of bonding observed. [67]

1.12 Degradation

Degradation is defined as "the deleterious change in the chemical structure, physical properties, or appearance of a material".[68] Composite materials synthesised in this research must fulfil the prerequisite of degradability. Scaffold materials are used in bone regeneration applications, wherein the intention is that new bone will regrow into the site of defect and render the material useless. Therefore, it is essential that these composites are able to degrade under physiological conditions, without producing harmful metabolites which are absorbed by the body.

Both the matrix (PLA) and filler (β-TCP) comprising the composites have proven degradability, with no known harmful by-products.[69]

1.12.1 Polymer (PLA) degradation

PLA is well known within the medical field as a degradable polymer. Hydrolysis of the main ester bonds in the chains leads to its degradation and conversion to lactic acid.[70] These by-products are easily metabolised by the body, and are incorporated within the Krebs cycle, where they are eventually dispelled in the form of carbon dioxide and water. Autocatalysis occurs as a result of cleavage of the ester bonds, when carboxyl end groups are formed.[71] The rate of degradation is, therefore, increased.

Li *et al* compared the degradation rates of the internal and external matrix.[72] Carboxyl end groups produced inside the matrix by hydrolysis of the ester bonds remain there and increase acidity, which subsequently speeds up degradation. However, similar carboxyl groups produced at the matrix surface are able to escape. The environment of the outer surface is not as conducive to degradation, and differences in degradation rates are thus observed.

Numerous factors influence the degradation of PLA and biodegradable polymers in general, some of which are summarized in Table 1.2.[73]

Table 1.2 Factors affecting the degradation of biodegradable polymers

- Composition of polymer
- Structure of polymer
- Molecular weight and its distribution
- Morphology (amorphous versus semicrystalline)
- Configurational structure
- Implantation site
- Storage history
- Hydrolysis mechanism (enzymatic or hydrolytic)
- Ratio of D/L enantiomers

The influence the above factors have on the degradation of PLA will be discussed further in Chapter 5.

1.12.2 Calcium phosphate (β-TCP) degradation

β-TCP has been researched for use in clinical applications distinct from HA because of its heightened level of resorbability. Similarly to PLA, the products of degradation are harmless and can be easily metabolised by the body.

Studies on the degradation of calcium phosphate ceramics have yielded three methods *via* which degradation occurs: (i) cell-mediated mechanisms, (ii) physiochemical dissolution and (iii) loss of mechanical integrity.[52] Biodegradability of calcium phosphate ceramics through cell mediated degradation is performed by osteoclasts (bone-resorbing cells). *In vitro* and *in vivo* experiments have demonstrated that osteoclasts degrade these ceramics in a similar way to natural bone. Briefly, the process involves the osteoclasts adhering to the substrate sealing zone, and the secretion of H^+ ions to decrease the pH from the physiological value of 7.4, down to pH 4 or 5, before the resorption begins. Several factors affect the rate of cellular degradation. Research has shown that the concentration of Ca^{2+} ions released from the biomaterial affects osteoclast activity, and can inhibit resorption when too high.[74] In addition, the surface energy and roughness can affect resorption. Polar components can regulate osteoclastic adhesion, whilst roughened surfaces encourage osteoclast attachment.[75,76]

Physiochemical degradation of ceramics is a coupled process of dissolution and reprecipitation, which occurs at the solid-liquid interface.[52] Hydration of ions within the biomaterial leads to its eventual breakdown and degradation. Again, specific parameters can influence the rate at which degradation *via* this mechanism occurs. A 'perfect' crystalline substance (i.e. no defects) dissolves at a slower rate than one with defects; defects thereby increase dissolution rate.[77] Thermodynamic solubility is also important. HA is known to stay in the body long after it is implanted, whilst β-TCP shows heightened solubility properties. The extent of dissolution decreases in the order of β-TCP>BCP>HA.[78]

Mechanical degradation results as a combination of cellular and physiochemical degradation. As the biomaterial is resorbed, and ions hydrated, its mechanical integrity is compromised. Because of a mismatch between the Young's modulus of bone and that of the ceramic, pressure is heightened on the material, leading to a loss of tensile strength by slow or subcritical crack growth. There is a direct correlation between the parameters which influence the physiochemical dissolution, and those which influence mechanical strength degradation.

1.13 Substituted calcium phosphates

An important aim for biomaterial researchers is to synthesise a material which matches the bioactivity of natural bone. Biological apatites do not consist solely of Ca^{2+} and PO_4^{2-} ions. They are in fact substituted with various amounts of anionic (i.e. F^-, Cl^-, SiO_4^{4-} and CO_3^{2-}) and/or cationic substituents (i.e. Na^+, Mg^{2+}, K^+, Zn^{2+} and Al^{3+}).[52] A natural progression in research therefore lies in synthesising calcium phosphate materials with various ionic substitutions, in order to improve biological performance, and investigate subsequent effects on mechanical properties of the materials. The performance, both biological and mechanical, of HA and β-TCP materials has been researched through alteration of ionic composition in the crystal structures. Of the numerous ions present in bone, research has focused particularly on silicon (Si^{4+}), zinc (Zn^{2+}), potassium (K^+) and magnesium (Mg^{2+}), the reasons for which will be discussed.

1.13.1 Silicon

The physiological role of Si^{4+} in bone was first investigated by Carlisle in the early 1970's.[79] The relevance of the ion appeared to focus on the early stages of bone formation and calcification, thereby deeming it an essential trace element in skeletal development. Further studies by Schwarz *et al*, on the effect of Si^{4+}on mammalian tissues, found that skull deformations were present in rats with a deficiency of Si^{4+}.[80] The loss of biologically available Si^{4+} was also linked to cases of osteopenia and osteoporosis.[81]

Building on early indications of the significance of Si^{4+} to bone development, researchers moved towards increasing the bioactivity of HA by substituting Si^{4+} into the structure. Gibson *et al* compared Si-substituted HA (Si-HA) to unsubstituted HA by implanting granules into the femoral condyle of rabbits. Comparing bone mineral apposition, coverage and ingrowth of the two samples, absolute percentages were significantly greater for Si-HA than HA.[82] An up-regulation in osteoblast cell metabolism was the proposed reason for the observed differences.

Si-substituted β-TCP research by Bandyopadhyay *et al* indicated a strong influence on the materials mechanical properties. Reports showed that compressive strength had increased by over 100% for a doped Si-TCP sample synthesised using 5 wt% SiO_2, whilst a continuous increase in compressive strength for 12 weeks in SBF was noted for a 1 wt% SiO_2 doped sample.[83]

1.13.2 Zinc

Zn^{2+} is an essential trace element that carries out multiple critical functions in the human body. Exceptionally high levels of Zn^{2+} are found within bone, with an average concentration of 125-250 ppm (against 28-33 ppm for the entire body). Such heightened levels are attributed to stimulating bone formation *in vivo* and *in vitro*.[84] It increases proliferation of osteoblast cells, whilst inhibiting osteoclastic bone resorption.[85, 86] Clinical studies have also concluded that a deficiency of Zn^{2+} in elderly subjects can lead to osteoporosis, dispelling previous opinion that the bone disease was caused largely by a deficiency of Ca^{2+}.

The effects of producing Zn-doped β-TCP samples were studied by Xue *et al*.[87] An increase in compressive strength was observed, from 24.0 MPa to 37.8 MPa, upon conversion of undoped β-TCP to 0.3 wt% Zn-TCP. In addition to the improvement in mechanical properties, positive bioactivity results were attained. Higher cell densities were observed on Zn-TCP samples, in addition to excellent cell attachment through filopodia extensions. Cell differentiation is also enhanced, indicated through high alkaline phosphatase (ALP) expression.

Jallot *et al* studied the physico-chemical effect of doping HA with Zn^{2+}ions.[88] It was found that HA doped with 5% Zn^{2+}had a higher dissolution rate than pure HA. Moreover, this concentration of Zn^{2+} lead to the formation of a calcium phosphate layer on the sample, which represents the potential bioactivity of the sample and satisfies the prerequisite for HA bonding to bone.

1.13.3 Sodium

Between 90 to 130g of Na^{+} is present within the adult human body, half of which, approximately, is present in bone.[89] McParland *et al* found that bone remodelling varies inversely with sodium intake; moderate changes in dietary salt intake influenced variables of resorption and formation of bone in elderly women.[90]

Research on the effect of Na^{+} substitution on the bioactivity and mechanical properties of calcium phosphate materials has focused almost entirely on β-TCP. Equivalent doping studies on HA focus on the method of substitution and characterisation, with slight emphasis on thermal stability.[91] β-TCP substitution by monovalent cations was first

investigated in 1988 by Oralkov *et al*.[92] A physico-chemical and *in vitro* study of the properties of Na-doped β-TCP , by Bouler *et al*, demonstrated that compressive strength increases in correlation with Na^+ content, without modifying its *in vitro* behaviour.[93] Similar reports highlight an improvement in the bending strength of β-TCP when low levels of Na^+ are incorporated into the structure.[94]

1.13.4 Magnesium

Mg^{2+} has been shown to increase the thermal stability of β-TCP, favouring its thermal formation over HA.[95] It has been proven to stimulate osteoblast differentiation, and a lack of Mg^{2+} can lead to osteoporosis and other bone diseases.[96] Mg-substitution and its benefits will be discussed in further detail in Chapter 4.

1.14 Composites

1.14.1 Definition

The definition of a composite is "a substance or material created from the combination of two or more phases, which can be differentiated at the microscopic or sub-microscopic scale".[97] Within the two phases there consists a continuous phase, called the matrix, and a second phase, called the filler. The filler is distributed throughout the matrix. The purpose of combining a filler and matrix is to optimise the advantageous properties of each individual phase, and overcome any deficiencies through one's combination with the other.

Composites were first employed in biomaterial research because no singular material could satisfy both the biological and mechanical requirements designated to make a successful bone replacement material. Ceramics were too brittle, despite their obvious bioactivity, and polymers were bioinert, although they possessed mechanical properties favourable to materials looking to mimic the mechanical properties of natural bone. Bonfield *et al* synthesised the first composite of this nature, combining the bioactivity of HA with the mechanical properties of polyethylene. The brittleness of HA was counteracted by the ductility and low modulus of polyethylene, whilst the bioinertness of polyethylene was compensated for by the high bioactivity of HA.[98] After process optimisation this composite, thereafter, went on to become the commercial material HAPEX™, a composite

consisting of HA particles (40 vol%) reinforced with high density polyethylene (HDPE).[99] The composite has optimal stiffness, toughness, and bioactivity.

1.14.2 Biodegradable polymers

Biodegradable polymers such as polylactide are used for applications in which the eventual breakdown of the composite, coupled with the regeneration of bone at the site of defect, is required. The rate of degradation can be controlled by the ratio of filler to matrix in the composition. This is, in turn, reliant on the relative rate of bone regeneration at the site. Polymers used in composites must also have the required mechanical properties, for example, ductility, in order to counteract the brittleness of the ceramic fillers. Drawing on the aforementioned differences in properties between HA and β-TCP, different fillers can be employed in composites depending on the application. An area of high bone turnover would benefit from a composite with β-TCP as the filler due to its increased solubility. Filler particles at the nanoscale are desirable because they are easily distributed throughout the polymer matrix and their nanoscale dimensions mimic those seen in natural bone. Bone mineral particle sizes can include and range from 5*5*20 and 5*10*40 nm.[100]Improved distributions also limit the extent of particle to particle contact, which can have detrimental effects on mechanical properties. The effects of varying particle size will be further discussed in section 1.14.4.

1.14.3 Volume fraction of fillers

Bonfield initially reported that changing the volume fraction of fillers within the composite strongly influenced mechanical properties.[101] It was demonstrated that the Young's modulus increased progressively with an increase in the volume fraction of filler. However, a decrease in percentage elongation to fracture was also observed with increasing filler volume. The failure mode changed from ductile to brittle, and the tensile strength began to drop as the volume of filler approached 45 vol%. This was the result of HA to HA particle contact, as the polymer no longer completely surrounded each HA particle. It became evident, thereafter, that both the maximum, and optimum, vol% of filler would be 40 vol%.

1.14.4 Varying particle size and particle surface area

The effects of varying particle size and particle surface area of the filler were studied. Wang *et al* used two different HA samples, with mean particle sizes of 4.14µm and 7.32µm, respectively, and compared their mechanical properties.[102] Higher torsional modulus, tensile modulus and tensile strength results were noted for the composites containing smaller HA particles. Although these composites also produced lower strain to failure results, overall it was conclusive that smaller particles were more effective for use within the composites.

An investigation into the effect which varying particle surface area had on the mechanical properties of composites was studied by Zhang and Tanner, with particular focus on impact properties.[103] Two HA samples were prepared which had significantly different surface areas. A sintered sample possessed a low surface area of $0.965 m^2 g^{-1}$and a smooth surface (HA 1), whilst the second sample (HA 2) was a rough surface spray-dried sample with a higher surface area of $13.536 m^2 g^{-1}$(Figure 1.10 a-b).

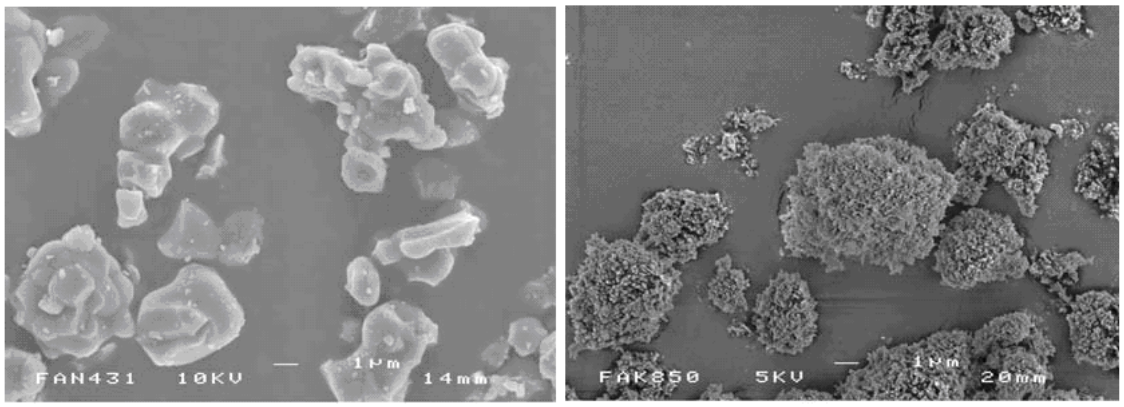

Figure 1.10 (a-b) Particle morphologies of HA 1 (a) and HA 2 (marker bars = 1 µm)

The sintered HA sample, which possessed the smooth surface, showed better impact resistance than the rough surface spray dried HA. Further investigation through SEM showed stronger interface bonding between the sintered HA and HDPE at the impacted fracture surfaces. Improved fracture resistance was the result of more energy being absorbed during impact. It is believed that the discrepancies between the two HA samples results from the variance in surface areas. The larger surface area particles require more matrix material to coat the particles, thereby reducing the amount free to act as matrix between the coated particles.

1.14.5 Mechanical properties

Several different factors can affect the mechanical properties of a composite. These include the filler and matrix, the ratio of filler to matrix, as well as the interface and degree of contact developed between the filler and matrix. The mechanical properties of composites can also be altered by size distribution, shape and size of filler particles.[104]

HAPEX, mechanically, has a modulus value approaching that of cortical bone and a superior toughness. The success of the composite material clinically can be attributed to these properties.

Polypropylene(PP)/$CaCO_3$ and Polypropylene(PP)/$Mg(OH)_2$ composites were used by Jancar to determine whether the Young's and shear moduli were affected by filler particle shapes.[105] Irregular, approximately spherical particles were present in the PP/$CaCO_3$ composites, whilst the PP/$Mg(OH)_2$ composites contained particles either in the form of hexagonal plates or micro-needles. Results showed that rounded filler particles yielded lower tensile strength but higher ductility composites, in comparison to irregular filler particles. The same study demonstrated that particle size becomes a more important factor in determining mechanical properties as the volume of filler increases.

The relative effects of sintered and unsintered HA, and their subsequent differences in surface area on the fracture toughness of HA-PE composites was investigated by Eniwumide *et al*.[106] Both samples had similar average particle sizes. It was found that the composite containing the lower surface area HA (sintered) had higher fracture toughness. The change in fracture toughness of the HA/PE composites can be directly attributed to differences in surface area of the HA filler particles.

1.14.6 Bioactivity of composites

Various methods exist to assess the biological activity of a material. Upon exposure to a model physiological environment, changes in mechanical or physical properties can be studied as a function of the materials degradation. Simulated body fluid (SBF) developed by Kukubo *et al*[107] is frequently employed for the assessment of bioactivity. It mimics the chemical composition of blood plasma, minus cells and other biological entities. After soaking in SBF for a designated time period, the formation of an apatite layer on the surface of the material denotes bioactivity. The thickness of the apatite layer, coupled with

the rate of degradation, is indicative of the level of biological activity within the sample. The most advanced method of *in vitro* testing is cell culture, which assesses the most likely cellular response to the material.

1.14.6.1 In vivo testing of bioactivity

Early *in vivo* studies of the bioactivity of HAPEX™ were initiated in 1986 by Bonfield *et al*.[108] Implants of HAPEX™, with unfilled PE as a control, were implanted into the femoral shaft of rabbits. Whilst the PE did not show any biological incorporation into its surroundings, HAPEX showed direct contact onto bone. Further studies have also demonstrated that bone ingrowth does not occur on the unfilled polymers, but is seen for the composite materials.[109] Further research on the same specimens, through Ultra High Resolution TEM, showed the polymer phase of the composite being replaced by newly formed bone. Crystallites of bone mineral were observed nucleating specifically on the HA present within the composite.[110]

1.14.6.2 In vitro testing of bioactivity

An *in vitro* and mechanical assessment of HAPEX™ was performed by Huang *et al.*[111] Immersion of the composite samples in a physiological solution for 1 and 3 months, at various temperatures, generated no significant change on the mechanical properties tested. Osteoblasts proliferated and matured faster on HAPEX™ than on unfilled PE, shown through increased ALP activity, and early DNA expression. Cell attachment was greater for HAPEX™ than PE; a confluent layer was seen covering the entire surface, with cell filopodia attached to the HA particles. The authors believe that the specific bonding of the cells to HA means that the HA particles may be acting as "microanchors for developing direct bone bonding *in situ.*"

The *in vitro* response of osteoblast cells to variances in both surface topography and HA filler volumes were studied by Dalby and co workers.[112] HA/HDPE composites at 20 vol% and 40 vol% HA were produced with various surface topographies. Samples with both circular and longitudinal machine grooving were studied under SEM. Cells tended to preferentially lay along the groove planes on the surface (Figure 1.11 a-b).

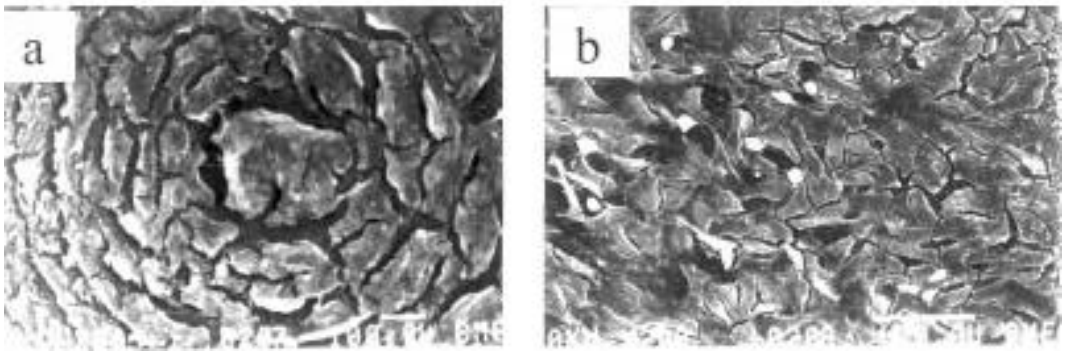

Figure 1.11 (a-b)(a) SEM of HOB cells growing upon highly grooved HA/HDPE surface; (b) SEM of HOB cells growing upon smooth HA/HDPE surface (x86 magnification)

It is clear, as a result, that surface topographies have a significant role to play in promoting and controlling cell attachment. Results also showed a higher level of osteoblast proliferation on the 40 vol% HA/HDPE material compared to the 20 vol% HA/HDPE material. Evidence for a more rapid cell growth and enhanced cellular response is presented. More focal adhesion points were observed on the 40 vol% HA/HDPE material. Previous work has studied the possibility that the molecules involved in focal contact with a material may be able to control cell differentiation and growth. The observation of high numbers of focal points in this work is thereby promising.[113]

1.15 References

[1.] S. Mellon, K.E. Tanner, *Int. Mater. Rev.*, 2012, In press
doi: 10.1179/1743280412Y.0000000008

[2.] J. D. Currey, *Nature*, 1962, **195**, 513

[3.] G. Renaudin, P. Laquerriere, Y. Filinchuk, E. Jallot, *J. Mater. Chem.*, 2008, **18**, 3593

[4.] Bone Quantitative Ultrasound, D. Mitton, C.Roux, P.Laugier, *Springer Science and Business*, 2011, 2

[5.] K. A. Athanasiou, C. F. Zhu, D. R. Lanctot, C. M. Agrawal, X.Wang, *Tissue Eng.*, 2000, **6**, 361

[6.] K.B. Naudi,*PhD Thesis*, University of Glasgow, 2010

[7.] E.F. Eriksen, P.Charles, F. Melsen, L. Mosekilde, L. Risteli, J. Ristelli, *J. Bone Miner. Res.*, 1993, **8**, 127

[8.] Molecular Cell Biology, H. Lodish, A. Berk, S. L. Zipursky, P. Matsudaira, D. Baltimore, J. Darnell,*W.H. Freeman*, 2000,23

[9.] G. E. Maloney, D. S. Bana, S. J. Scrivani, Head, Face and Neck Pain. Science, Evaluation & Management: An Interdisciplinary Approach, *Wiley-Blackwell*, 2009

[10.] A. M. Parfitt, *Bone*, 2002, **30**, 5

[11.] Bone Grafts and Bone Substitutes- Basic Science & Clinical Applications,A. Nather, H. J. C. Ong, Z. Aziz, *World Scientific Publishing Company*, 2005, 3

[12.] F. Kantawong, *PhD Thesis*, GlasgowUniversity, 2009

[13.] Krause's Essential Human Histology for Medical Students,3rd Edition,K. J.William,*Universal Publishers*, 2005, 62

[14.] S. C. Cowin, S. Weinbaum, Y. Zeng, *J. Biomech.*, 1995, **28**, 1281

[15.] W. Bonfield, P. K. Datta, *Biomech.*, 1974, **7**, 147

[16.] J. D. Currey, *Journal of Biomech.*, 1979, **12**, 313

[17.] V. I. Sikavitsas, J. S. Temenoff, A. G. Mikos, *Biomater.*, 2001, **22**, 2581

[18.] R. B. Ashman, R. J. Young, *J. Biomech.*, 1988, **21**, 177

[19.] J. Kabel, A. Odgaard, B. Von Rietbergen, R. Huiskes, *Bone*, 1999, **24**, 115

[20.] R. Hodgskinson, J. D. Currey, *J. Mater. Sci. Mater. Med.*, 1992, **3**, 377

[21.] The Biochemistry and Physiology of Bone, 2nd Edition, J. J. Prichard, *Academic Press*, 1972, 102

[22.] F. Barrere, C. A. Van Blitterswijk, K. de Groot, *Int. J. Nanomedicine*, 2006, **1**, 317

[23.] http://www.mypondsoftware.com/bone.jpg. Accessed 22/02/2012.

[24.] L. E. Lanyon, *Calcified Tissue Int.*, 1993, **S3**, S102

[25.] L. Bonewald, *J. Muscoskelet. Neuronal Interact.*, 2006, **6**, 331

[26.] https://vault.swri.org/cms/upload/cells_500pixels.jpg. Accessed 22/02/2012.

[27.] diFiore's Atlas of Histology with Functional Correlations, 10th Edition, V. P. Eroschenko, *Lippincott Williams & Wilkins*, 2005, 79

[28.] http://www.weizmann.ac.il/sb/faculty_pages/Addadi/osteoclast.html. Accessed 22/02/2012.

[29.] Principles in Anatomy and Physiology, G. J. Tortora, S. R. Grabowski., *Harper Collins*, 1996, 142

[30.] W. Roux, *Arch. Path. Anat. Physiol. Klin. Med.*, 1888, **114**, 246

[31.] M. C. Meikle, S. Bord, R. M. Hembry, J. Compston, P. Croucher, J. J. Reynolds, *J. Cell Sci.*, 1992, **103**, 1093

[32.] P. A. Hill, British *J. Orphod.*, 1998, **25**, 101

[33.] K. Matsuo, N. Irie, *Arch. Biochem. Biophys.*, 2008, **473**, 201

[34.] Mechanical Control of Stem Cell Differentiation, D. M. Cohen, C. S. Chen, Stem Book, The Stem Cell Research Community, doi/10.3824/stembook.1.26.12008. Accessed 25/02/1012.

[35.] Bone & Mineral Research, A. J. Friedenstein, *Elsevier Science Publishers*,1990, 243

[36.] J.E. Aubin, Principles of Bone Biology, 3rd Edition, *Academic Press Inc.*, 2008, 92

[37.] H. Qi, D. J. Aguiar, S. M. Williams, A. L. Pean, W. Pan, C. M. Verfaille, *P. Natl. Acad. Sci.*, 2003, **100**, 3305

[38.] P. Ducy, *Dev. Dynam.*, 2000, **219**, 461

[39.] P. Westbroek, F. Marin, *Nature*, 1998, **392**, 861

[40.] E. Chrischilles, T. Shireman, R.Wallace, *Bone*, 1994, **15**, 377

[41.] K. Piekarski, *Int. J. Eng. Sci.*, 1973, **11**, 557

[42.] J. L. Katz, P. Spencer, Y. Wang, S. Bumrerraj, T. Namura, S. J. Eppell, M. Tabib-Azar, *Mat. Sci. Eng. C: Bio.S*, 2007, **27**, 450

[43.] C.Parkhill, *T. Amer. Surg. Ass.*, 1897, **15**, 251

[44.] E.S. Thian, S.M. Best, *Mater. Sci. Tech.*, 2008, **24**, 1027

[45.] Bone Regeneration and Repair: Biology and Clinical Applications, D. Sutherland, M. Bostrom, *Humana Press Inc*, 2005, 138

[46.] S. R. Radin, P. Ducheyne, *J. Biomed. Mater. Res.*,1993, **27**, 35

[47.] R. Langer, J. P. Vacanti, *Science*, 1993, **260**, 920

[48.] W. Bonfield, J. Bowman, M. D. Grynpas, 1980, UK Patent No GB2005461B

[49.] J. L. Dornhoffer, *Laryngoscope*, 1998, **108**, 531

[50.] P.N. Kumta, C. Sifeur, D. H. Lee, D. O. Iton, D. Choi, *Acta Biomat.*, 2005, **1**, 65

[51.] A. Bianco, I. Cacciotti, M. Lombardi, L. Montanaro, *Mater. Res. Bull.*, 2009, **44**, 345

[52.] Tissue Engineering, 1st Edition, F. Barrere, M. Ni, P. Habibovic, P. Ducheyne, K. de Groot, *Academic Press Elsevier*, 2008, 224

[53.] M. Yashima, A. Sakai, T. Yamiyania, A. Hoshikawa, *J.Solid State Chem.*, 2003, **175**, 272

[54.] B. Jokic, I. Jonkovic-Castvan, DJ. Veljovic, D. Bucevac, K. Obradovic-Djuricic, R. Petrovic, DJ. Janackovic, *J. Optoelectron. Adv. M.*, 2007, **9**, 1904

[55.] L. Sha, Y.Liu, Q. Zhang, M.Hu, Y. Jiang, *Mater. Chem. Phys.*, 2011, **129**, 1138

[56.] V. Karageorgiou, D. Kaplan, *Biomater.*, 2005, **26**, 5474

[57.] H. R. R. Ramay, M. Zhang, *Biomater.*, 2004, **25**, 5171

[58.] B. J. Story, W. R. Wagner, D. M. Gaisser, S. D. Cook, A. M. Rust-Dawicki, *Int. J. Oral Max.Impl.*, 1998, **13**, 749

[59.] M. Mastrogcancoma, S. Scalione, R. Mainetti, L. Dolcini, F. Beltrame, R. Cancedda, R. Quarto, *Biomater.*, 2006, **27**, 3230

[60.] S. F. Hulbert, F. A. Young, R. S. Matheus, J. J. Klawitter, C. D. Talbert, F. H. Stelling, *J. Biomed. Mater. Res.*, 1970, **4**, 433

[61.] M. Jarcho, *Clin. Orthop.*, 1981, **157**, 259

[62.] J. Dong, H. Kojima, T. Uemura, M. Kikuchi, T. Tateishi, J. Tanaka, *J. Biomed. Mater. Res.*, 2001, **57**, 208

[63.]C. Zhang, J. Wong, H. Feng, B. Liu, Z. Song, X. Zhang, *J. Biomed. Mater. Res.*, 2001, **54**, 407

[64.]H. P. Yuan, J. D. de Bruijn, Y. B. Li, J. Q. Feng, Z. J. Yang, K.de Groet, X. D. Zhang, *J. Mater. Sci. Mater. Med.*, 2001, **12**, 7

[65.]K. Ioku, G. Wawachi, K. Nakaharo, E. H. Ishida, H. Munogi, T. Okuda, I. Yonezawa, H. Kurosaura, T. Ikeda, *Key Eng. Mater.*, 2006, **309**, 1059

[66.] S. Kotani, Y. Fujita, T. Kitsugi, T. Nakamura, C. Ohtsuki, T. Kukubo, *J. Biomed. Mater. Res.*, 1990, **24**, 721

[67.]M. Neo, T. Nakamura, C. Ohtsuki, T. Kokubo, T. Yamamura, *J. Biomed. Mater. Res.*, 1993, **27**, 999

[68.]The Williams Dictionary of Biomaterials, D. F. Williams,*LiverpoolUniversity Press*, 1999, 101

[69.]B. Gupta, N. Revagade, J. Hilborn, *Prog. Pol. Sci.*, 2007, **32**, 455

[70.]A. Talal, *PhD Thesis*, University of Glasgow, 2009

[71.]Fabrication of nanocrystalline hydroxyapatite doped degradable composite hollow fibre for guided and biomimetic bone tissue engineering; in: Symposium on Next Generation Biomaterials, N. Zhang, H. L. Nichols, S. Taylor, X. J. Wen,*Elsevier Science*, 2005, 599

[72.]S. Li, *J. Biomed. Mater. Res.*, 1999, **48**, 342

[73.]M. Vert, S. Li, H. Garreau, *Clin. Mater.*, 1992, **10**, 3

[52.] Tissue Engineering, F. Barrere, M. Ni, P. Habibovic, P. Ducheyne, K. de Groot, Academic Press Elsevier, 1st Edition, 2008, 277

[74.]Y. Doi, H.Iwanaga, *J. Biomed. Mater. Res.*, 1999, **47**, 140

[75.]S. A. Redey, S. Razzouk, *J. Biomed. Mater. Res.*, 1999, **45**, 140

[76.] K. Gomi, B. Lowenberg, *Biomater.*, 1993, **14**, 91

[77.] N. L. Porter, R. M. Pilliar, *J. Biomed. Mater. Res.*, 2001, **56**, 504

[78.] P. Ducheyne, S. Radin, *J. Biomed. Mater. Res.*, 1993, **27**, 25

[52.] A. Bianco, I. Cacciotti, M. Lombardi, L. Montanaro, *Mater.Res. Bull.*, 2009, **44**, 345

[79.] E.M. Carlisle, *Science*, 1970, **167**, 179

[80.] K. Schwarz, D.B. Milne, *Nature*, 1972, **239**, 333

[81.] L.L. Hench,*Biol. Implications*, 1999, 116

[82.] N. Patel, S.M. Best, W. Bonfield, I.R. Gibson, K.A. King, E. Damien, P.A. Revell, *J. Mater. Sci. Mater. Med.*, 2002, **13**, 1199

[83.] A. Bandyopadhyay, S. Bernard, W. Xue, S. Bose, *J. Am. Chem. Soc.*, 2006, **89**, 2675

[84.] S. Gomes, J.M. Nedelec, E. Jallot, D. Sheptyakov, G. Renaudin, *Chem. Mater.*, 2011, **23**, 3072

[85.] M. Hashizume, M. Yamaguchi, *Mol. Cell. Biochem.*, 1993, **122**, 59

[86.] S. Kishi, M. Yamaguchi, *Biochem. Pharmacol.*, 1994, **48**, 1225

[87.] W. Xue, K. Dahlquist, A. Banerjee, A. Bandyopadhyay, S. Bose, *J.Mater. Sci. Mater. Med.*, 2008, **19**, 2669

[88.] E. Jallot, J.M. Nedelec, A.S. Grimault, E. Chassot, A. Grandjean-Laquerriere, P. Laqueriere, D. Laurent-Maquin, *Colloids and Surface B*, 2005, **42**, 205

[89.] R.P. Heaney, *J. Am. Coll. Nutr.*, 2006, **25**, 271S

[90.] B.E. McPartland, A. Goulding, A.J. Campbell, *Br. Med. J.*, 1989, **299**, 834

[91.] S. Kannan, J.M.G. Ventura, A.F. Lemos, A. Barba, J.M.F. Ferreira, *Ceram. Int.*, 2008, **34**, 7

[92.] S.Y. Oralkov, B.I. Lazoryak, R.G. Aziev, *Russ. J. Inorg.Chem.*, 1988, **33**, 73

[93.] S. Quillard, M. Paris, P. Deniard, R. Gildenhaar, G. Berger, L. Obadia, J.M. Bouler, *Acta Biomater.*, 2011, **7**, 1844

[94.] K. Yoshida, N. Kondo, H. Kita, *J. Am. Ceram. Soc.*, 2005, **88**, 2315

[95.] A. Bigi, L. Compostella, A.N. Fichera, E. Forest, M.Gazzano, A. Ripamanti, N. Roveri, *J. Inorg. Biochem.*, 1988, **34**, 75

[96.] M. Percival, *Appl. Nutrit. Sci. Rep.*, 1999, **5**, 4

[97.] Encyclopedia of Composites,H.R.C. Screen and K.E. Tanner, *Wiley-Blackwell*, 2012, 2928

[98.] W. Bonfield, M. Grynpas, A.E. Tully, J. Bowman, J. Abram, *Biomater.*, 1981, **2**, 185

[99.] W. Bonfield, *Ann. NY. Acad. Sci.*, 1988, **523**, 173

[100.] J.D. Percival, *P. I. Mech. Eng.H*, 1998, **212**, 399

[101.] W. Bonfield, *J. Biomed.Eng.*, 1988, **10**, 522

[102.] M. Wang, R. Joseph, W. Bonfield, *Biomater.*, 1998, **19**, 2357

[103.] Y. Zhang, K.E. Tanner, *J. Mater. Sci. Mater. Med.*, 2008, **19**, 761

[104.] R. Joseph, K.E. Tanner, *Biomacromolecules*, 205, **6**, 1021

[105.] J. Jancar, *J. Mater. Sci.*, 1989, **24**, 3947

[106.] J. O. Eniwunide, R. Joseph, K. E. Tanner, *J. Mater. Sci.Mater. Med.*, 2004, **15**, 1147

[107.] T. Kukubo, H. Kushitani, S. Sakka, T. Kitsugi, T. Yamamuro, *J.Biomed. Mater. Res.*, **24**, 721

[108.] Biological and Biomechanical Performance of Biomaterials, W. Bonfield, C. Doyle, K. E. Tanner, *Elsevier Science Publishers*, 1986, 153

[109.] C. Doyle, K. E. Tanner, W. Bonfield, *Biomater.*, 1991, **12**, 841

[110.] Z. B. Luklinska, W. Bonfield, *J. Mater. Sci. Mater. Med.*, 1997, **8**, 379

[111.] J. Huang, L. Di Silvio, M. Wang, K. E. Tanner, W. Bonfield, *J. Mater. Sci. Mater. Med.*, 1997, **8**, 775

[112.] M. J. Dalby, L. Di Silvio, G. W. Davies, W. Bonfield, *J. Mater. Sci. Mater. Med.*, 2000, **12**, 805

[113.] A. Curtis, C. D. Wilkinson, *J. Biomater. Sci. Polym. E.*, 1998, **9**, 1313

2. Experimental

Several different synthetic methods were investigated to synthesise β-TCP, including different aqueous precipitation and microwave syntheses.

The main technique used for the characterisation of materials prepared in this work was Powder X-ray Diffraction (PXD). This technique was used to identify products and phases quickly and to estimate purity. Due to the high crystallinity of samples, one hour scans allowed for identification of phases, and elucidation of cell parameters. For samples undergoing further structural investigation using Rietveld refinements, fourteen hour scans were used to obtain higher quality data sets. Refinements also allowed for the extraction of information on multi-phase samples, as well as investigating the substitution of Magnesium into the β-TCP crystal structure.

Raman Spectroscopy acted as a complementary characterisation technique to PXD, whilst sample morphology and particle size were investigated by Scanning Electron Microscopy (SEM). Brunauer, Emmett and Teller (BET) Isotherm studies yielded information on the surface area and average pore diameter of materials.

2.1 Synthetic techniques

2.1.1 Aqueous Precipitation Reactions

Aqueous precipitation reactions refer to those solution-based reactions which take place in water, wherein combining two or more solutions together results in the production of a precipitate. This is due to strong attractive forces between specific anions and cations. Sample analysis in this research revealed that the intermediate product required for β-TCP synthesis was attained from two different aqueous precipitation reactions. A precipitation step was, in this case of one reaction scheme, the first in a multi-step synthesis, which included reflux and rinsing stages.

Aqueous precipitation reactions were the primary method of synthesis in this research because they allowed for a wide range of experimental parameters to be adjusted. These included pH, duration of reflux, calcination temperature, and primary ion

sources. Each of these parameters, as well as others, played a role in the overall formation of the product.

2.1.2 Microwave Reactions

Microwave reactions were investigated briefly as a potential method for synthesising β-TCP. The advantages of using microwaves to synthesise calcium phosphate materials include shorter reaction times and lower temperature reaction conditions, which in turn can yield different sample morphologies. The absence of long periods of high temperature treatments in microwave reactions also illicit the potential to reduce agglomeration.

Microwaves can be found positioned between infrared radiation waves and radio waves in the electromagnetic spectrum (Figure 2.1).[1] This correlates to wavelengths of between 10^{-5} and 10^{3} m, respectively.

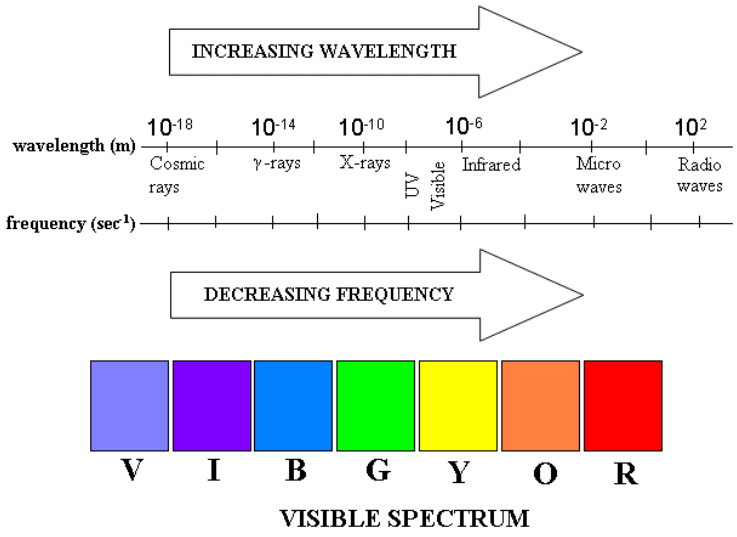

Figure 2.1 Electromagnetic spectrum

Within materials synthesis, a 2.45 GHz frequency is predominantly used to interact with ionic, dielectric semi-conducting and semi-metallic materials, which all have dipolar absorption in the same region of reactor frequency.[2] Materials can interact with microwaves in three ways: reflection, transmission or absorption. In order for a microwave reaction to proceed, at least one of the reactant materials must absorb microwave energy.

Using microwaves as a heating method has many advantages over conventional heating. Energy is transferred, in the form of heat, through the material electromagnetically, which leads to more uniform heating.[3] The time taken for heating is thereby reduced, which concurrently reduces energy costs. Lower reaction temperatures can be applied in microwave heating, which can reduce agglomeration levels in materials and improve product quality.

Conduction and dipolar polarisation are the two major effects responsible for microwave heating. With regards to conduction, this mechanism affects only those materials which are electrical conductors. When an externally applied field is present, free charge carriers are able to move through the material. Heating subsequently occurs due to resistance set up against the electric current. An oscillating field creates said current through agitation of electrons or ions in the material.[4] Dipolar polarisation exists in substances containing a permanent dipole moment. A dipole will always try to align itself with external fields through rotation. However, the dipole cannot reorient itself quickly enough in line with the ever changing field. The constant motion, and collision, of these particles causes heat generation.[5] The effect of an oscillating electromagnetic field on ionic alignment in conduction and dipolar polarisation is given in Figure 2.2:

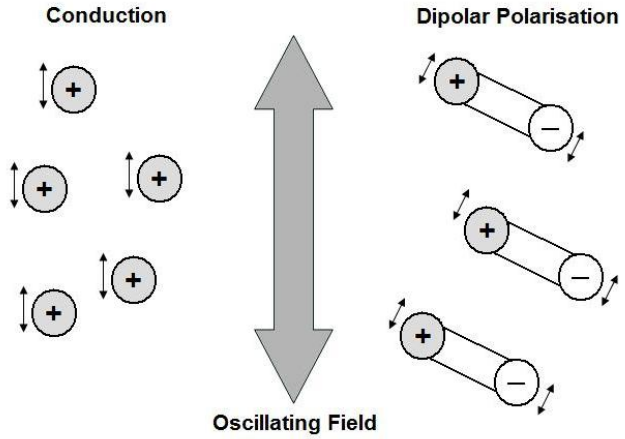

Figure 2.2 Microwave Radiation Heating Methods: conduction and dipolar polarisation

In order for a material to generate heat, microwaves must be able to enter and leave the material, with the transmittance of energy. This, in turn, relates to a material's dielectric properties. When heating occurs in a dielectric material, dielectric heating

occurs and results in the creation of thermal energy.[6] The ability of a material to heat in this manner is measured by its dielectric properties, which consist of two distinct entities, and leads to the complex dielectric permittivity, ε^*:

$$\varepsilon* = \varepsilon' + i\varepsilon'' \quad \textbf{(2.1)}$$

where ε' is the relative permittivity (a measure of the ability of a molecule to be polarised by an electric field) and ε'' is the dielectric loss (which indicates the ability of a material to convert stored energy to heat energy).

A multi-mode domestic microwave oven (DMO) was employed for the microwave reactions performed in this research. DMOs are commonly used in materials research as they are inexpensive, easily attainable, and can be used in a wide range of reactions in different chemical areas. Radiation is dispersed within the reactor to ensure as large a heating area as possible.

2.1.3 Preparation of materials using microwave radiation

Initial microwave reactions were performed by heating reaction solutions in a sealed teflon autoclave for various durations and power settings. However, pressure build up caused the autoclave to burst, so all further microwave reactions were performed using an open glass beaker. This prevented the build up of pressure. The beakers were placed in the DMO with a blast screen placed in front for safety. Each reaction was carefully monitored for the duration of the experiment, due to the sharp increments in temperatures of the solutions.

2.2 Synthesis

2.2.1 Preparation of β-TCP

2.2.1.1 Aqueous precipitation

Two different aqueous precipitation reactions were used to synthesise β-TCP. Firstly, β-TCP was synthesised *via* an aqueous precipitation method developed by Tam *et al.*[7] The method, which was originally directed at hydroxyapatite synthesis, was modified so as to create β-TCP, the details of which will be discussed in Chapter 3. Stoichiometric amounts of potassium phosphate monobasic [$K_2HPO_4.3H_2O$, reagent grade, Sigma-Aldrich] and calcium chloride [$CaCl_2$, ACS reagent, Sigma-Aldrich], were reacted alongside the organic surfactant cetyl trimethylammonium bromide [CTAB, $CH_3(CH_2)_{15}N(Br)(CH_3)_3$, BioXtra ≥ 99%, Sigma Aldrich]. The phosphorus and calcium starting materials were dissolved separately in 25ml of deionised water (CTAB was dissolved alongside the phosphorus starting material), and added together drop wise to yield a milky white precipitate. pH was controlled over a range of values using dilute sodium hydroxide (NaOH). The resultant reaction solution was refluxed at 100ºC for 24 hours (Figure 2.3). The solution was then filtered, the filtrate dried at 100 ºC overnight and calcined at 850 ºC for five hours, followed by a cool down to room temperature overnight. Characterisation was carried out using PXD. Several experimental parameters were altered to optimise the reaction process, which will be discussed in greater detail in Chapter 3.

Figure 2.3 Experimental setup for the aqueous precipitation synthesis of β-TCP

The second aqueous precipitation method used to synthesise β-TCP was adapted from the experimental procedure developed by Zhang *et al*.[8] Calcium nitrate tetrahydrate [$Ca(NO_3)_2.4H_2O$, ≥ 99.0%, Sigma Aldrich] and ammonium phosphate dibasic [$(NH_4)_2HPO_4$, reagent grade, ≥98.0%, Sigma Aldrich] were used in stoichiometric amounts to ensure that the calcium to phosphorus ratio was 1.5. Each starting material was dissolved in 25ml of deionised water, and the phosphorus solution was adjusted to alkaline pH using ammonium hydroxide [$NH_4(OH)$]. The drop wise addition of the calcium solution to the phosphate solution was accompanied by the careful control of the solution pH through the use of ammonium hydroxide (NH_4OH). Resulting precipitates were filtered, washed with deionised water to remove impurities, and dried overnight at 100 °C. Calcinations at temperatures between 700-1100 °C were performed. The roles which pH and calcination temperature played on product formation were investigated, the results of which will be discussed in Chapter 3. Samples were characterised by PXD.

2.2.1.2 Microwave Reactions

It is well documented that β-TCP cannot be obtained directly through precipitation alone. Instead, an intermediate product is formed, called calcium deficient hydroxyapatite [CDHA, $Ca_{10-x}(HPO_4)_x(PO_4)_{6-x}(OH)_{2-x}{\cdot}nH_2O$, $(0 \leq x \leq 1.5)$].[9] From CDHA, the desired final material can be obtained following a high temperature calcination treatment. However, the aqueous techniques employed to synthesise CDHA are often tedious and time consuming. It was the aim of this research to use a microwave synthesis to produce CDHA under quicker and gentler reaction conditions.

A domestic microwave oven (Panasonic 4697 NN-TS53W) was used in this project (Figure 2.4) and the method was based on work by Han *et al*.[10] 1.5g of calcium hydroxide [$Ca(OH)_2$, ACS reagent, ≥ 95.0%, Sigma Aldrich] and 0.924 ml of phosphoric acid [H_3PO_4, 85 wt.% in H_2O, Sigma Aldrich] were mixed in an aqueous solution of 30 ml of deionised water. The pH was adjusted to pH 9 using dilute ammonium hydroxide and the suspension transferred to a 250ml glass beaker. Once inside the microwave, the solution was reacted at various high powers and durations, the results of which will be discussed in Chapter 3. Precipitates were collected and washed through filtration, and dried at 100 °C overnight. Calcination treatments at

various temperatures between 700-1100 °C constituted the last stage of the microwave synthesis. The purity of each sample was determined by PXD.

Figure 2.4 Reaction set-up using a multi-mode microwave reactor

2.3 Product characterisationand structure determination

2.3.1 Diffraction theory

A crystal is defined as a material comprised of planes of atoms, with a regularly repeating structure, which have the ability to scatter X-rays. The theory of how such a crystal diffracts X-rays is explained by Braggs Law, given by the following equation:

$$n\lambda = 2d\sin\theta \qquad \textbf{(2.2)}$$

where n is an integer, λ describes the wavelength of incident X-rays, d is the perpendicular distance between the adjacent planes and θ is the angle of incidence.

Braggs Law was derived by the English physicist Sir W. H. Bragg and his son Sir W. L. Bragg in 1913 after they determined the crystal structure of NaCl. [11, 12] It provided an explanation as to why peaks of scattered intensity are observed from X-rays scattered from points on a set of lattice planes. The points on a set of lattice planes of a crystal can be represented as in Figure 2.5:

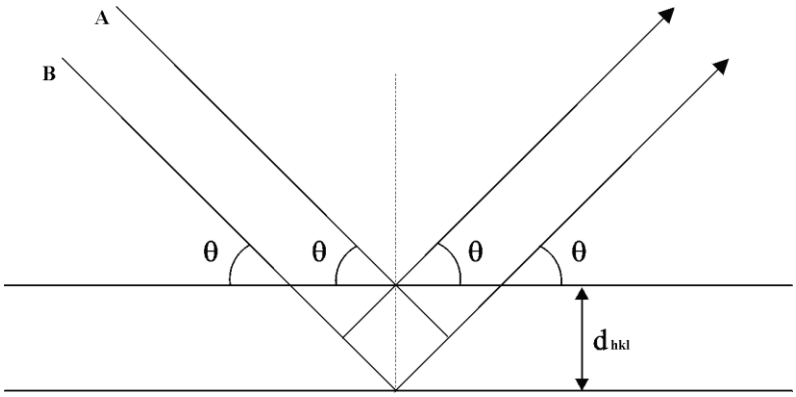

Figure 2.5 Diffraction from parallel planes of point scatterers

For scattering to occur according to Bragg's Law, certain criteria must be met: two parallel X-ray beams with an angle of incidence θ and wavelength λ must be diffracted by adjacent planes on the crystal of separation d. Relationships between the angle of incidence and distance, combined, gives:

$$XYZ = 2d\sin\theta \qquad \textbf{(2.3)}$$

The scattering of the X-ray beam from the two points in neighbouring planes will produce **in phase** diffracted X-ray beams, (constructive interference) if the distance travelled by the X-ray photon scattered from d is an integral number of wavelengths:

$$XYZ = n\lambda \qquad \textbf{(2.4)}$$

This therefore produces the Bragg equation, as seen as Equation 2.2. The angle of incidence, θ, is known as the Bragg angle. At angles of incidence other than the Bragg angle, diffracted beams are out of phase and thus destructive interference occurs.[13]

Crystalline solids have a lattice structure, with the atoms undertaking a regularly repeating pattern. Lattices therefore have long range order and symmetry, and are composed of unit cells. Unit cells constitute the simplest repeating unit in a crystal lattice related by translation, and contain information on the symmetry of the lattice. The lengths of the unit cell (a, b and c) and angles (α, β and γ) are defined as the lattice parameters (Figure 2.6).

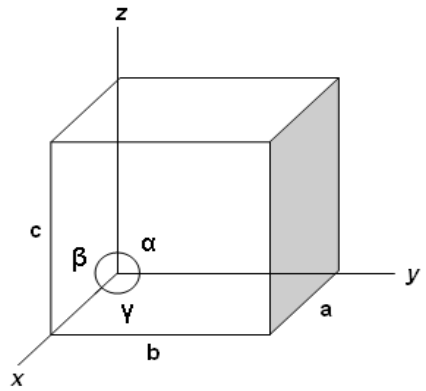

Figure 2.6 Definition of axis, unit cell dimensions and angles for a general unit cell

The seven crystal systems denote all the possible shapes a unit cell can adopt (Table 2.1).

Table 2.1 The seven crystal systems

System	**Unit Cell**
Triclinic	$\alpha \neq \beta \neq \gamma \neq 90^{o}$ $a \neq b \neq c$
Monoclinic	$\alpha = \gamma = 90^{o}$ $\beta \neq 90^{o}$ $a \neq b \neq c$
Orthorhombic	$\alpha = \beta = \gamma = 90^{o}$ $a \neq b \neq c$
Trigonal	$\alpha = \beta = \gamma \neq 90^{o}$ $a = b = c$
Hexagonal	$\alpha = \beta = 90^{o}$ $\gamma = 120^{o}$ $a = b = c$
Tetragonal	$\alpha = \beta = \gamma = 90^{o}$ $a = b \neq c$
Cubic	$\alpha = \beta = \gamma = 90^{o}$ $a = b = c$

Identification of the lattice planes allows the crystal system to be derived (Table 2.2). The planes are defined by their Miller Indices, the system in crystallography used for notating the planes and directions in crystal lattices.[14] A family of lattice planes is defined by the indices h k l, the reciprocal position where the planes cut the *a*, *b* and *c* axes respectively.

Table 2.2 Equations for d-spacings in the different crystal systems

Crystal system	*Expression for d_{hkl}*
Cubic	$\frac{1}{d_{hkl}^2} = \frac{h^2 + k^2 + l^2}{a^2}$
Tetragonal	$\frac{1}{d_{hkl}^2} = \frac{h^2 + k^2}{a^2} + \frac{l^2}{c^2}$
Orthorhombic	$\frac{1}{d_{hkl}^2} = \frac{h^2}{a^2} + \frac{k^2}{b^2} + \frac{l^2}{c^2}$
Hexagonal	$\frac{1}{d_{hkl}^2} = \frac{4}{3}\left(\frac{h^2 + hk + k^2}{a^2}\right) + \frac{l^2}{c^2}$
Monoclinic	$\frac{1}{d_{hkl}^2} = \frac{1}{\sin^2\beta}\left(\frac{h^2}{a^2} + \frac{k^2 \sin^2\beta}{b^2} + \frac{l^2}{c^2} - \frac{2hl\cos\beta}{ac}\right)$
Triclinic	$\frac{1}{d_{hkl}^2} = \frac{1}{V^2}[h^2b^2c^2\sin^2\alpha + k^2a^2c^2\sin^2\beta + l^2a^2b^2\sin^2\gamma + 2hkabc^2(\cos\alpha\cos\beta - \cos\gamma) + 2kla^2bc(\cos\beta\cos\gamma - \cos\alpha) + 2hlab^2c(\cos\alpha\cos\gamma - \cos\beta)]$ where $V = abc(1 - \cos^2\alpha - \cos^2\beta - \cos^2\gamma + 2\cos\alpha\cos\beta\cos\gamma)^{1/2}$

In any powder X-ray diffraction experiment, the sample is irradiated with an X-ray source which moves through a pre-determined range of angles. The intensity of the diffracted X-rays is measured by a moving source, and the measurement of the diffracted maxima gives d spacings which allow Miller Indices to be assigned. Once assigned, the cell size can be calculated.

The intensities of the observed maxima differ between elements. Lighter elements are composed of very few electrons, and as such are unable to scatter X-rays efficiently. Heavier elements, with more electrons, result in the intensity of the observed peaks being increased.

2.3.2 Powder X-ray Diffraction (PXD)

Diffraction has become one of the most widely used characterisation techniques in materials chemistry, ever since Bragg discovered the relationship held between diffraction and the interatomic separation in crystals. Single crystal research initially benefitted most from the introduction of diffraction, as a pattern was attained with clearly defined points of intensity from each crystal plane, yielding plentiful information on crystal structure. However, in the case of powder diffraction, where the sample has an infinite number of randomly orientated crystallites, the diffraction is obtained as rings of intensity, rather than distinct points.[15] The resultant pattern obtained is a 1-d slice through the rings, and this, combined with overlap of diffraction maxima, made extracting information other than the basic cell type and size difficult. To counteract this problem of overlapping, H. M Rietveld created a method which compares an experimental model to a structural model, and the introduction of the program vastly improved the situation.[16] It allowed for further detailed information to be extracted from powder samples. An increase in the capabilities of computers, combined with the Rietveld method, allowed for a range of structural information to be extracted from powder patterns of materials that perhaps could not be crystallised.

2.3.2.1 Powder X-ray diffraction instrumentation

To generate X-rays, electrons must firstly be produced in a cathode tube by heating a filament. The electrons produced are then accelerated towards a metal target. When these accelerated electrons strike said target (usually Cu or Mo), X-rays are produced. Upon impact, a core electron from one of the metal target atoms will be ejected from its atomic orbital. This ejection leaves a ‘hole’, which is filled *via* electron decay from a higher energy orbital. Filling this gap occurs with the emission of radiation, leading to the generation of X-rays.

Copper is one of the most commonly used metals to create X-rays because it generates a number of intense maxima which are easily identified. Bombarding a copper target provides a typical X-ray spectrum such as that seen in Figure 2.7:

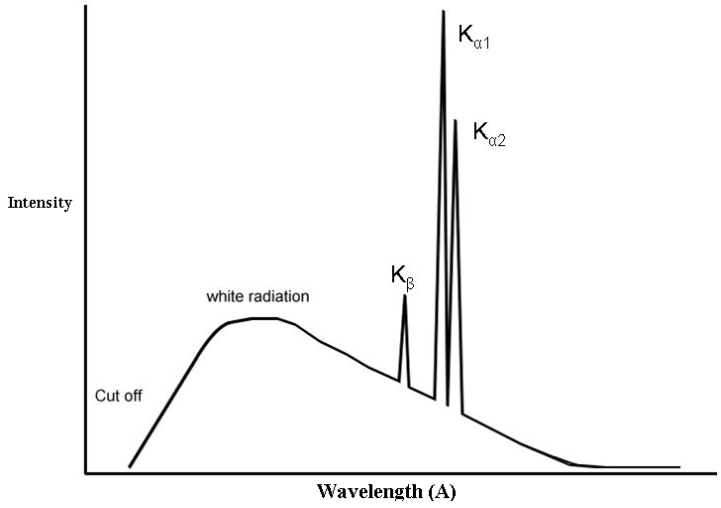

Figure 2.7 Intensities of copper emission

Kα1, Kα2 and Kβ in Figure 2.7 correspond to the electron shells which are involved in producing the X-ray. When a vacant 1s orbital is filled (principal quantum number 1), it is given the symbol K. Referencing copper again, this may be achieved by electron decay from the 2p or 3p levels and the X-ray produced by the 2p-1s and 3p-1s transitions are termed Kα2 and Kβ respectively. Kα1 refers to transitions between the 2s and 1s atomic orbitals.[17] Although distinct in reference to electronic transitions, Kα1 and Kα2 are sufficiently close in terms of wavelength that an average of the two is often used, with CuKα radiation = 1.5418 Å.

As previously discussed, X-rays are generated by heating a filament to produce electrons, which are then bombarded at a metal target to produce X-rays. Diffraction experiments use only a single X-ray wavelength, for this a crystal monochromator is employed. A single X-ray wavelength is obtained by impinging the X-ray beam on a single crystal at a chosen and fixed orientation. When only a specific angle is used, and Bragg's law is employed, only one wavelength can be diffracted from the crystal; thus providing the single wavelength required. Using this method, specific wavelengths can be chosen for use in diffraction experiments through adjustment of the angle θ. Generally CuKα is the preferred wavelength of use due to its relatively high intensity.

The sample is scanned through a range of angles to ensure that all possible diffraction directions of the lattice are attained. When Braggs equation is satisfied through the interaction of an X-ray with the sample, constructive interference occurs and a peak of

intensity is recorded. Figure 2.8 represents the basic schematic for an X-ray diffractometer:

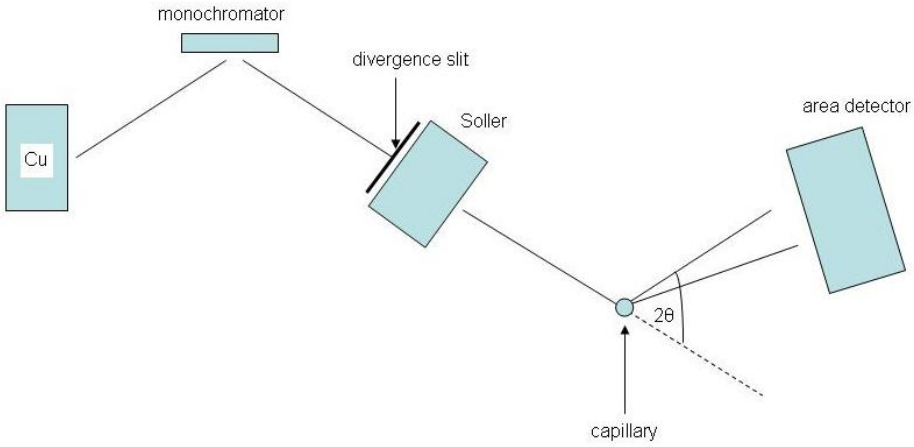

Figure 2.8 Schematic of powder X-ray diffractometer (in transmission geometry)

The majority of data collection was carried out using a PANalytical X'Pert PRO MPD powder diffractometer, using Cu $K_{\alpha 1}$ radiation, and collected over a 2θ range of 5-85^{o} for 1 hour (phase analysis) or 14 hours (structural refinement). This corresponded to a time per step of either 649.6 s or 9125.6 s, respectively.

2.3.2.2 Powder X-ray diffraction sample preparation

Every sample tested using PXD was ground using a mortar and pestle, to break down agglomerates and ensure a powder with random orientation. The PANalytical Xpert has various mounts for measuring samples; this research used the bracket facility, which employed Bragg-Brentano geometry. Powder was mounted into a depression in a sample holder. The surface was flattened with a glass slide to ensure accurate data collection.

2.3.3 Indexing

Unit cell parameters from powder patterns were refined using the computer program CELL, which is based on a least squares method.[18] In addition to the unit cell parameters, this also allowed for the indexing of a small number (~15-20) of major peaks in the pattern by their miller indices (h k l). Indexing provided information on

peak shifts to different 2θ ° values, which proved useful for substitution research, wherein peak shift provided an early indicator of cation substitution.

2.3.4 Rietveld refinement

Extraction of structural information from powder diffraction patterns was minimal until the introduction of the Rietveld method in 1967.[19] Severe overlapping of peaks made it difficult to model them singly, which is ideally required to extract full structural information. To essentially 'break-through' the concealment of a cluster of reflections, Rietveld concluded that individual reflections could be fitted using peak shape parameters. This would in turn determine total intensity and peak shape from the cluster. The Rietveld method uses a least squares, best fit approach, in which a full experimental profile is compared to that calculated from a model structure.[20] Each peak of intensity measured from the experimental data is compared to the corresponding point from the theoretical model structure. Refinements are performed until the best structural fit between the two data sets is achieved.

Initially a starting model is required for a structural refinement, obtained from a similar structure. Scale factors and background parameters are introduced, which can either be manually set or calculated using a polynomial expression. To determine the position of the Bragg reflectionsaccurately, variations of sample displacement, lattice parameters and point corrections are completed. Thereafter, the issue of overcoming severe peak overlap is targeted by refinement of peak shape parameters. Atomic positions are then adjusted to correspond to peak intensities, followed by varying of temperature factors. Finally, refinement of peak shape can be revisited, together with further background co-efficients, to account for asymmetry or sample broadening effects.

The least squares refinement concentrates on minimising the function *M*:

$$M = \sum_i w_i (y_i^{obs} - y_i^{calc})^2 \qquad \textbf{(2.5)}$$

where y_i^{obs} and y_i^{calc} are the intensity observed and calculated, respectively, at the *i*th data step, and w_i represents the weighting factor

In PXD, y_i^{calc} values are calculated from the $|F_k|^2$ values calculated from the structural model. These, in turn, result from summation of the contributions from neighbouring Bragg reflections (k) and the background (b_i) as

$$y_i^{calc} = s\sum_k L_k |F_k|^2 \phi(2\theta_i - 2\theta_k) P_k A + y_{bi} \quad \textbf{(2.6)}$$

where s is the scale factor, L_k contains the Lorentz and polarisation factors for the kth Bragg reflection, F_k is the structure factor, ϕ is a reflection profile function, P_k is the preferred orientation function, θ_k is the Bragg angle for the kth reflection, A is an absorption factor and y_{bi} is the background intensity at the specific ith step.

The structure factor, F, quantifies the intensity of each diffraction maximum scattered by a crystal:

$$F = \sum_{j=1}^{N} f_j \exp[i\delta] \quad \textbf{(2.7)}$$

where f is the sum contributions of the scattering amplitudes and δ refers to the phases of each atom.

Powder crystallite samples have a tendency to align in a certain way, generally along the axis of the sample holder, and are accounted for by:

$$P_k = \left[G_2 + (1 - G_2)\exp(-G_1\alpha_k^2)\right] \quad \textbf{(2.8)}$$

where G_1 and G_2 are refinable parameters and $\alpha_k$is the angle between the presumed symmetry axis and the preferred orientation axis.

Peak shape is dictated by the instrument used in collection: in this case the pseudo-voigt function best described the resultant peak shape. The pseudo-voigt function results from a combination of two broadening mechanisms, known as Gaussian and Lorentzian contributions, and can be modelled by the function pV:

$$\text{pV} = \eta L + (1 - \eta)G \quad \textbf{(2.9)}$$

where L and G are the Lorentzian and Gaussian contributions to peak shape and n is the mixing parameter which can be refined as a linear function of 2θ:

$$\eta = N_A + N_B(2\theta) \quad \textbf{(2.10)}$$

where N_A and N_B are refinable parameters.

The Gaussian (G) and Lorentzian (L) broadening mechanism contributions to the peak shape are represented by the equations:

$$G = \frac{(4\ln 2)^{1/2}}{H_k\sqrt{\pi}} \exp\left(-4\ln 2\left(2\theta_i - 2\theta_k\right)^2 / H_k^2\right) \quad \textbf{(2.11)}$$

and

$$L = \frac{2}{\pi H_k} 1 \Big/ \left[1 + 4\frac{(2\theta_i - 2\theta_k)^2}{H_k^2}\right] \quad \textbf{(2.12)}$$

where $2\theta_k$ is the calculated position for the kth Bragg peak corrected for the counter zero-point and H_k is the full-width-at-half-maximum (FWHM) of the kth Bragg reflection.

The formula given by Caglioti, Paoletti & Ricci (1958) to express the dependence of the full width at half maximum (FWHM), H_k, on the scattering angle $2\theta_k$ can be simplified to [21]

$$H_k^2 = U\tan^2\theta + V\tan\theta + W \quad \textbf{(2.13)}$$

where U, V and W are the refinable half width parameters. This formula takes account of peak broadening effects due to particle size, as the refinable parameters are both instrument and sample dependent.

Refinable parameters fall into two distinct groups in Rietveld refinements. Firstly, there are structural parameters which describe the contents of the unit cell and temperature factors, atom co-ordinates and occupancies of each atom are considered. Secondly, profile parameters are refined that describe the position, shape and FWHM of each

peak. These consist of the profile scale factor, unit cell parameters, *U*,*V* and *W*, zero-point, asymmetry and preferred orientation correction. From these comparisons between the observed and calculated profiles, three reliability factors are calculated;$R_{profile}$, $R_{expected}$and $R_{weighted\ profile}$:

$$R_{profile} = R_p = 100\left[\frac{\sum_i \left|y_i^{obs} - y_i^{calc}\right|}{\sum_i y_i^{obs}}\right] \quad \textbf{(2.14)}$$

$$R_{\exp ected} = R_{\exp} = 100\left[\frac{(N - P + C)}{\sum_i \omega_i (y_i^{obs})^2}\right]^{1/2} \quad \textbf{(2.15)}$$

and

$$R_{wp} = 100\left[\frac{\sum_i \omega_i \left[y_i^{obs} - y_i^{calc}\right]^2}{\sum_i \omega_i \left[y_i^{obs}\right]^2}\right]^{1/2} \quad \textbf{(2.16)}$$

where R_{exp} arises from the statistics of the refinement, *N* is the number of observations, *P* is the number of refinable parameters and *C* is the number of constraints.

From these, $R_{weighted\ profile}$ (R_{wp}) should be considered the most meaningful, at least for following the progress of a refinement, because its numerator is the quantity being minimised, (M, equation 3).

The quality of the whole fit, minimised throughout the refinement, is finally defined as the chi-squared parameter, also known as the goodness of fit:

$$\chi^2 = \left[\frac{R_{weightedprofile}}{R_{\exp}}\right]^2 \quad \textbf{(2.17)}$$

For a strong fit of data between the experimental and calculated model, the R_{wp} should approach the statistically expected R_{exp} factor. Visually, the goodness of fit can be examined through a plot of the profile fit: a good fit should have the difference line between the calculated and observed patterns as flat as possible. All Rietveld

refinements presented in this thesis were performed using the Generalised Structure Analysis System, GSAS, of Von Dreele and Larson, and EXPGUI packages.[22, 23]

2.3.5 Scanning electron microscopy

In order to obtain information on the size and morphology of the materials, scanning electron microscopy (SEM) was employed. A scanning electron microscope is a type of electron microscope which uses a high energy beam of electrons to image a sample. SEM techniques are employed in various areas of science, including Materials Science, Chemistry, Geology and Biological Studies. Sir Charles Oatley produced the first SEM for general use in 1952.[24]

The high energy beam of electrons required to operate a SEM are generated through a process called thermoionisation, wherein a filament is heated to high temperatures to cause some of the material to ionise.

Accelerating a high energy electron beam at a sample produces a range of inelastic and elastic scattering effects between atoms and electrons. Elastic scattering occurs when the scattered electron maintains the same energy as the incident electrons, whereas inelastic scattering happens when the energy of the scattered electron is changed.[25] Different types of scattered electrons and radiation can be emitted when incident beam electrons strike the sample, as illustrated in Figure 2.9:

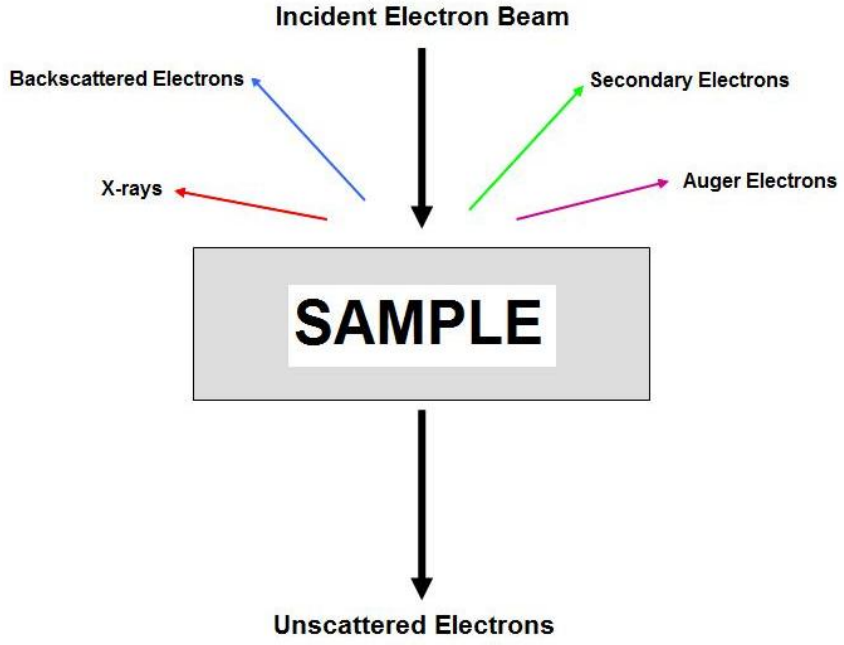

Figure 2.9 Schematic of possible electron scattering within SEM experiment

Elastic scattering accounts for one of four forms of electrons shown in diagram 2.10: *backscattered electrons*. These are high energy electrons which result from the elastic collision of an incident electron with a sample atoms nucleus. Due to this interaction with nuclei, backscattered electrons intensity varies with atomic number. Those atoms with a greater atomic number (Z) have a greater cross-sectional area, increasing the probability of an incident electron striking the sample, and therefore such atoms appear 'brighter' in images. Backscattered electrons therefore provide information on the distribution of elements in a sample, and are used for imaging and diffraction.

Secondary electrons are low energy electrons formed from the inelastic scattering of the incoming electron with the sample.[26] They are predominantly produced by the interactions of beam electrons with weakly bonded or valence electrons. As a substantial amount of energy is lost from the incident electron to the sample, secondary electrons typically only have energies of less than 50eV, and are used in imaging to give information on the topography of a sample, for example.

Inelastic scattering also produces *Auger electrons*. Initially the Auger process begins when a sample is exposed to the high energy beam of electrons. Upon exposure, a core hole is created. In order to fill this vacancy, a higher energy level electron falls into the vacancy, resulting in a release of energy.[27] This energy can be emitted in two forms: as

a photon, or through energy transfer to another electron which is thereafter ejected. Ejected electrons formed under these circumstances are termed Auger electrons. Energies for this form of radiation are in the range of 100eV to a few KeV, and are therefore strongly absorbed by the specimen. This strong absorption limits Auger spectroscopy to being a surface analysis technique only.

Inelastic scattering of *X-rays* in SEM provides information in a similar way to Auger spectroscopy. X-ray emission is also initiated through the creation and subsequent filling of a core hole. Instead of an emitted photon or electron, the difference in energy released when a high energy level electron fills the hole is released in the form of an X-ray. The composition of a sample can be studied through X-ray emission (Energy dispersive X-ray spectroscopy (EDX)) as the energy levels of the atomic structures correspond to the energy of specific X-rays.

2.3.5.1 SEM Instrumentation

Information about a material can be obtained, through SEM, by directing a high energy beam of electrons at the sample. The various forms of electrons and X-rays can then be gathered and analysed. In order to control the electron beam and gather as much information as possible, the SEM is composed of various parts, as shown in the schematic below in Figure 2.10:

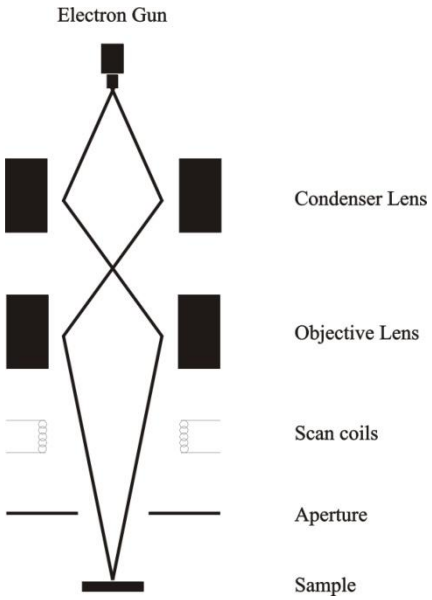

Figure 2.10 Scanning electron microscope schematic

Firstly, the electron gun, located at the top of the column, is where free electrons are generated by thermoionic emission from a tungsten filament. This is conducted at extremely high temperatures, and the electrons are accelerated towards an anode. The condenser and objective lenses thereafter focus the beam and determine its intensity when it strikes the specimen. Scan coils ensure the entire sample surface is scanned, whilst a detector counts the output of low energy secondary electrons emitted from the sample in the specimen chamber. Information obtained is then transferred to a computer, where the images can be viewed.[28]

The SEM is under vacuum during imaging of a sample. This is for several reasons: to prevent the high temperature tungsten filament burning out in air and to allow the SEM to operate in a dust-free environment, thus ensuring that no dust or air particles block the electron beam from reaching the sample.

Sample morphology was studied through SEM using either a Philips XL30 ESEM, or on a Hitachi S-4700 SEM. The former was run with an applied accelerating voltage of 20kV, a working distance of 10 mm for imaging and in high vacuum mode. Characterisation using the Hitachi S-4700 SEM equipment was carried out by J. Gallagher, with an applied accelerating voltage of 5kV and a working distance of 12.5mm.

2.3.5.2 Preparation of sample for SEM

Samples were prepared for SEM by passing them through a 4 μm sieve and depositing a small amount of powder onto adhesive carbon tabs. These were then secured onto aluminium stubs. Prepared samples were kept inside glass vials to prevent surface contamination.

2.3.6 Raman Spectroscopy

Raman spectroscopy is a spectroscopic technique, first observed by the Indian physicist C.V Raman, which is based on the inelastic scattering of monochromatic light by certain ‘Raman active’ molecules.[29] Photons sourced from a laser light are absorbed and then reemitted. The frequency of the reemitted photons (whether they are shifted up or down in comparison to the original monochromatic frequency) provides

information about vibrational and rotational transitions in molecules. These vibrational transitions occur between $10^2 – 10^4 \nu$ cm^{-1} in the electromagnetic spectrum.

As a form of vibrational spectroscopy,[30] Raman spectroscopy acts as a complementary technique to PXD for material characterisation.

2.3.6.1 Theory of Raman scattering

A molecule is termed Raman active if molecular bond vibrations attained through photon absorption result in a change in molecular polarisability. Molecular polarisability defines the electric dipole moment induced in a molecule by an electric external field, in this case through the absorption of incoming photons. When a molecule undergoes a change or distortion in the electron cloud which surrounds the molecule, molecular polarisation occurs.

Two forms of photon scattering thus exist: Rayleigh and Raman scattering. Rayleigh scattering is observed more frequently than Raman scattering; this elastic effect is seen when incoming photons, directed at a molecule, scatter with no change in their energy. The vast majority of photons will be scattered in this manner. This indicates that the electron distortion has not resulted in the movement of the nucleus. Therefore the photon remains unchanged, and retains its original energy and wavelength.

Raman scattering, or inelastic scattering, is seen when the electron cloud is distorted to such an extent that nuclear motion occurs. Through this motion, energy is transferred between the incoming photon and molecule. The outgoing photon will therefore scatter with a shifted energy;[31] whether this energy is increased or decreased will be determined by whether the photon has undergone Stokes or Anti-Stokes scattering.

Two types of Raman scattering exist: Stokes and Anti-Stokes. Stokes scattering occurs when the molecule absorbs energy and increases its vibrational energy from its lowest vibrational level to a virtual state. The virtual state is highly unstable and only exists for a brief period of time ($\sim 10^{-14}$ seconds). Upon scattering of the photon, the molecule returns to the first vibrational level of the electronic ground state. This process occurs because the incident photon is able to polarise the electron cloud, and as a result

effectively ‘donates’ some of its energy to the molecule. The resulting photon therefore generates a Stokes line on the incident spectrum, indicating its lower energy and longer wavelength. If the molecule is already in the first vibrational level of the electronic ground state at the time when the incident photon interacts with the electron cloud, Anti-Stokes scattering occurs. In this case, the molecule loses energy, returning to a lower vibrational energy than it originally occupied. Incident photons in Anti-Stokes scattering generate Anti-Stokes lines of higher energy and shorter wavelength in the Raman spectrum. The Stokes and anti-Stokes lines frequency of scattering is given by:[32]

$$\text{Frequency } (f): V_o - V_m \text{ - Stokes scattering} \quad \textbf{(2.18)}$$

$$\text{Frequency } (f): V_o + V_m \text{- anti-Stokes scattering} \quad \textbf{(2.19)}$$

Where V_o = incident beam frequency and V_m = vibrational frequency of the molecule.

Figure 2.11 depicts the vibrational level changes observed in Stokes, Anti-Stokes, and Rayleigh scattering. Stokes scattering is more common than Anti-Stokes scattering, because very few molecules are likely to be in the first vibrational level at room temperature.

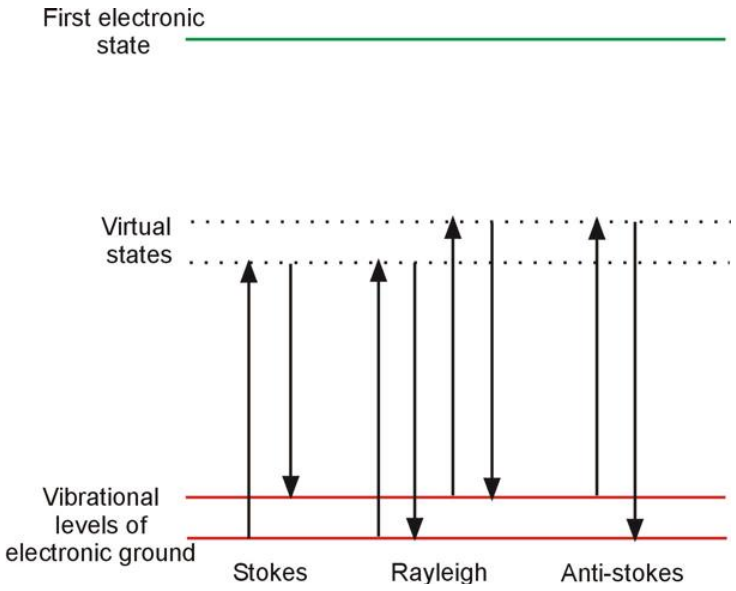

Figure 2.11 Illustration and comparison of the Raman and Rayleigh effect

No overall differences between vibrational levels, before and after absorption, exist in Rayleigh scattering. Whether a molecule undergoes Stokes or Anti-Stokes scattering is dependent on its initial energy state.

The energy of a molecule can be divided into a number of different degrees of freedom. This term describes the movement of the molecule in space. For any given compound, there will be three degrees of freedom which describe the translation of the molecule in space.[33]An additional three degrees of freedom describe the molecules rotational movement about its x, y and z axis. An exception to this rule is linear molecules, where only two types of rotation are possible. Therefore, non-linear molecules will express 3N-6 vibrational degrees of freedom, and linear molecules will express 3N-5, where N is the number of atoms.[34]There is a close correlation between Raman and Infrared (I.R) spectroscopy, as both gather information on molecules based on molecular vibrations. I.R absorption occurs when a vibration causes a change in the electric dipole of a molecule, whereas a molecule is Raman active when its level of polarisability is increased through bond vibrations. It is possible that a molecule can be either I.R or Raman active, satisfy both conditions, or fail to produce either a change in electric dipole or polarisability, thereby being both Raman and I.R inactive.

2.3.6.2 Raman Instrumentation

The instrumental setup for a Raman system begins with a laser acting as an excitation source, directed at the sample. A lens collects light scattered from the illuminated sample, where it is thereafter passed through a monochromator. In comparison to Rayleigh scattering, Raman scattering is weak, so notch or edge filters are used for laser rejection. Charge-coupled device cameras are generally used to detect the Raman scattered light.

2.3.6.3 Preparation of sample for Raman

Preparations of materials for Raman measurements began by grinding the sample with a mortar and pestle to reduce agglomeration and create finer powder samples. The materials were then compacted into a small O-ring (0.5cm in diameter) and pressed down with a glass slide to ensure an even surface for measurement. Placement of the sample directly under the microscope lens in the Raman spectrometer followed

thereafter. All measurements were carried out at room temperature. A number of different measurements were taken at different positions of each sample, to ensure accuracy.

A Horibo Raman LabRAM HR machine was used to analyse all samples. A Horibo-Jobin-Yvon HR confocal microscope was coupled with a Quantum Venus 532 laser. The laser was set at 150mW excited with 532nm light. A 600 gr/mm grating, hole aperture of 50µm, and a Synapse CCD detector were used to collect spectra. Data collection and analysis was through Horiba LabsSpec software, with spectra thereafter manipulated using Origin.

2.3.7 BET Isotherms

Surface area measurements, to assess total surface area and average pore diameters, were performed on all samples. The surface area for biomaterials is important, as high surface areas allow for increased cell populations to adhere to the material surface, and different surface areas can influence cellular response. High porosities allow for increased osteoconductivity of materials.

Brunauer, Emmett and Teller described the method of calculating surface area in 1938.[35] The theory explains how gas molecules are physically adsorbed onto the surface of a solid, and is an expansion of the Langmuir theory. In 1916 Irving Langmuir developed the theory of monolayer adsorption by describing the dependence of the surface coverage of an adsorbed gas on the pressure of the gas above the surface.[36] This is carried out at a fixed temperature. The BET theory expands this to account for multilayer adsorption.

For this expansion to be successfully applied to multilayer adsorption, several assumptions must be made, including;

- The number of gas molecule layers adsorbed on the surface of the solid increases infinitely at saturation pressure

- The first and second layers have different energy of adsorption, and thereafter all layers have the same adsorption energy as the second[27]

- Each layer can be characterised through application of the Langmuir theory

A consideration of these assumptions generates the BET equation:

$$\frac{p}{v_0\left[p_0 - p\right]} = \frac{1}{v_m c} + \frac{c-1}{v_m c}\left(\frac{p}{p_0}\right) \qquad \textbf{(2.20)}$$

where v_o is the volume of adsorbed gas, p_o and p are the saturation and equilibrium pressure of adsorbate gas at the experimental adsorption temperature, v_m is the volume of gas adsorbed in the monolayer, and c is the BET constant.

The BET constant, c, is related to heats of adorption and liquefaction of the gaseous layers:

$$c = \exp\left(\frac{E_1 - E_L}{RT}\right) \qquad \textbf{(2.21)}$$

where T is the absolute temperature, R is the molar gas constant, $E_1$is the first layer heat of adsorption and E_L applies to the second and subsequent layers, and is equal to the heat of liquefaction.

The BET method is applied in various areas, including the pharmaceutical, catalytic and cements industries. To determine the specific surface area (S) and total surface area (S_{total}) of materials, the following equations are employed:

$$S_{total} = \frac{\left(v_m N s\right)}{V}$$
$$S = \frac{S_{total}}{a} \qquad \textbf{(2.22, 2.23)}$$

where a is the sample weight, V is the adsorbent gas molar volume, N is Avogadros number and s is the adsorption cross section.

Surface area analysis (total surface area and average pore diameter) was determined using a Micromeretics Gemini III 2375 surface area analyser, and was conducted by

Andrew Monaghan. To remove moisture, each sample was degassed overnight at 110 ^{o}C.

2.4 References

[1.] http://www.colourwave.co.uk/cpfaq/q1-1.html. Accessed 30/01/2012

[2.] *Developments in Microwave Chemistry*, RSC Special Report, Chemistry World, 2005, **2**

[3.] I. Manjubala, M. Sivakumar, *Mater. Chem. Phys.*, 2001, **71**, 272

[4.] Experiments in Green and Sustainable Chemistry, H. W. Roesky, D. K. Kennepohl, *Wiley VCH*, 2009

[5.] Simon Richard Vallance, *PhD thesis*, University of Nottingham, 2008

[6.] C. Gabriel, S. Gabriel, E. H. Grant, B. S. J. Halstead and D. M. P Mingos, *Chem. Soc. Rev.*, 1998, **27**, 213

[7.] K. C. Tam, J. Yao, W. Tjandra, Y. Z. Chen, J. Ma, B. Soh, *J. Mater. Chem.*, 2003, **13**, 3053

[8.] X. Zhang, F. Jiang, T. Groth, K. S. Vecchio, *J.Mater. Sci. Mater. Med.*, 2008, **19**, 3063

[9.] S. C. Liou, S. Y. Chen, *Biomater*., 2002, **23**, 4541

[10.] J. K Han, H. Y. Song, F. Saito, B. T. Lee,*Mater. Chem. Phys.*,2006**, 99**, 235

[11.] W. L. Bragg, *Proc.Cambridge Philos. Soc.*, 1913, **17**, 4

[12.] Solid State Chemistry: An Introduction, 1st Edition, L. Smart, E. Moore, *Chapman and Hall*, 1992

[13.] Crystal Structure Determination, W. Clegg, *Oxford University Press*, 1998, 17

[14.] Lucia Carrassiti, *PhD Thesis*, University of Glasgow, 2011

[15.] Inorganic Materials Chemistry, M. T. Weller, *Oxford University Press*, 1994

[16.] The Rietveld Method, R. A. Young, *Oxford University Press*, 1993

[17.] X-ray Diffraction: a Practical Approach, C. Suryanarayaria, M. Grant Norton, *Plenum Press*, 1998

[18.] J. Laugier, B. Bochu, "CELREF Unit-Cell Refinement Software on a Multiphase System", Laboratoire des Materiaux et du Genie Physique Ecole Nationale Suprieure de Pysique de Grenable (WG).

[19.] H. M. Rietveld, *Acta Crystallogr. B*, 1967, **22**, 151

[20.] H. M. Rietveld, *J. Appl. Cryst.*, 1969, **2**, 65

[21.]G. Gaglioti, A. Paoletti, F. P. Ricci, *Nucl. Instrum. Methods*, 1958, **3**, 223

[22.] A. C. Larson, R. B. von Dreele, General Structure Analysis System (GSAS), Los Alamos National Laboratories Report LAUR 086-748, Los Alamos, 2004

[23.] B. H. Toby, *J. Appl. Crystallogr.*, 2001, **34**, 210

[24.] C. W. Oatley, *J. Appl. Phys.*, 1982, **53**, R1

[25.]Scanning Microscopy for Nanotechnology Techniques and Applications, W. Zhou, Z. L. Wong, *Springer Link*, 2007

[26.] Saleem Denholme, *PhD Thesis*, University of Glasgow, 2011

[27.]Surfaces, G. Attard, C. Barnes, *OxfordUniversity Press*, 1998

[28.]Scanning Electron Microscopy and X-ray Microanalysis, 3rd Edition, J. Goldstein, D. E. Newbury, D. C. Joy, C. E. Lyman, P. Echlin, E. Lifshin, L.Sawyer and J.R. Michael, *Springer*; 2003

[29.]Introductory Raman Spectroscopy, 2nd Edition, J. R. Ferraro, K. Nakamoto, C. W. Brown, *Elsevier Inc.*, 2003,

[30.] R. S. Krishnan, R. K. Shankar, *J. Raman Spectrosc.*, 1981, **10**, 1

[31.]Modern Raman Spectroscopy: A Practical Approach, E. Smith, G. Dent, *John Wiley & Sons Ltd.*, 2005

[32.]Analytical Applications of Raman Spectroscopy, M. J. Pelletier, *Blackwell Science*, 1999

[33.]Infrared and Raman Spectroscopy: Methods and Applications, B. Schrader, *VCH Publishers Inc.*, 1995, 9

[34.]IR and Raman Spectroscopy: Principles and Spectral Interpretation, P. Larkin, *Elsevier*, 2011, 8

[35.] S. Brunauer, P. H. Emmett, E. Teller, *J. Am. Chem. Soc.*, 1938, **60**, 309

[36.]I. Langmuir, *J. Am. Chem. Soc.*, 1918, **40**, 1361

3. Synthesis and PXD characterisation of β-Tricalcium Phosphate

3.1 Introduction

In recent years, research into the use of calcium phosphate compounds as biomaterials has increased exponentially [1] and at the forefront of such interest is tricalcium phosphate, TCP. Four polymorphs of TCP exist: γ, β, α and α*, each of which exist under different physical parameters. [2] Under high pressure, γ-TCP is formed, whilst β-TCP forms at temperatures between 700-800 °C. Transitions from β to α-TCP occur at around 1180 °C, whereupon the α stage remains stable until 1430 °C. [3] At temperatures above 1430 °C, the α*-TCP phase is observed. Due to a combination of its proven bioactivity and rate of resorbability, β-TCP is the most studied of the four TCP polymorphs, and is the primary focus of this research. [4]

3.1.1 β-TCP structure

β-TCP crystallises in the R*3c* space group, with lattice parameters of a = 10.4352 Å and c = 37.4029 Å. [5] The structure of β-TCP was first determined by Schroeder *et al* in 1974. [6] The β-$Ca_3(PO_4)_2$ structural model consists of an arrangement of Ca atoms surrounded by PO_4 polyhedra. Ca atoms are located at five crystallographic sites, from Ca (1) to Ca (5), as shown in Figure 3.1. The coordination number (CN) for the Ca (1) site is 8, and the Ca (2) site has a CN of either 6 or 8; 6 oxygen atoms bond strongly to this cation site, whilst 2 oxygen atoms exhibit longer bonds. Ca (3) has a CN of 8 and Ca (4) and Ca (5) display lower CNs of 6. Stoichiometry, symmetry and site multiplicity dictate that some cation vacancies must exist in the structure, and refinements of site occupancies by Schroeder *et al* confirm that such vacancies only occur on the Ca (4) site.[6] Phosphorus atoms are located at three crystallographic sites, P (1)- P (3). Each P atom in the structure has four-fold coordination with oxygen atoms. The crystal structure of β-TCP can be separated into two types of columns, A and B, running along the *c*-axis (Figure 3.1).[5] Only two of the five cation sites, Ca (4) and Ca (5), reside within the A column, surrounded by PO_4 polyhedra. The three remaining Calcium sites, Ca (1-3), reside in column B, again surrounded by PO_4 polyhedra.

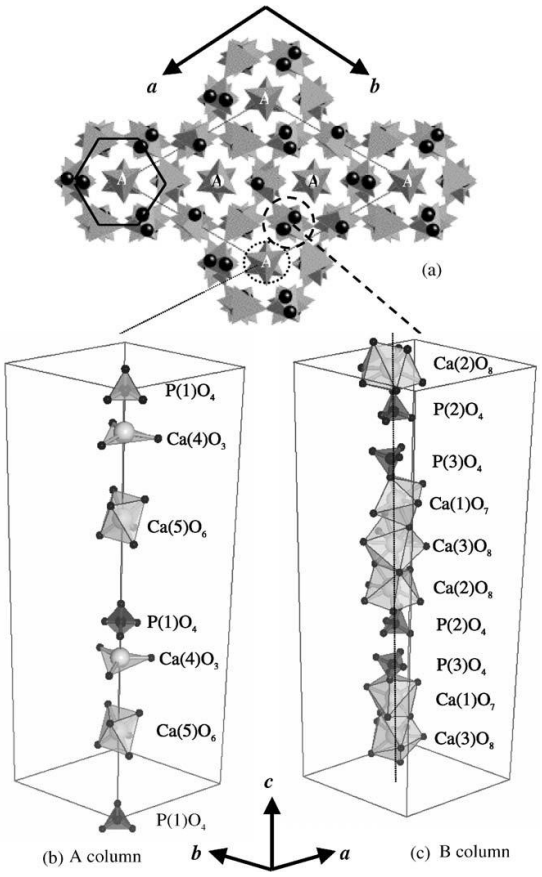

Figure 3.1 Projection of the crystal structure of β-TCP. Adapted from Yashima *et al*.[5]

3.1.2 β-TCP synthesis

β-TCP has been synthesised using a range of synthetic methods, which can be loosely divided into three categories; wet-chemical methods, hydrothermal methods and solid-state reactions.[7, 8] Regardless of the method used, starting materials must be added in quantities which satisfy the Ca: P ratio of 3:2. Solid state reactions allow for greater control over stoichiometric ratios, as starting materials are added in a pre-determined ratio and subsequently offer excellent composition control.[9] In wet chemical methods, the Ca: P ratio can be affected by the slightest change in parameters, for example pH, reaction temperature or reaction time, which can thereafter lead to a wide range of by-products.[10] Solid state reactions, however, offer little or no control over the materials particle size or morphology, as a result of the reactants being maintained at high temperatures for long periods of time. Hydrothermal reactions have been successfully employed to synthesise β-TCP, which possesses a highly porous micro structure.[11]

β-TCP cannot be obtained directly from solution *via* wet-chemical methods, for example in sol-gel reactions. Instead, an intermediate product, Ca-deficient hydroxyapatite [$Ca_9(HPO_4)(PO_4)_5(OH)$, CDHA] is formed. To transform CDHA into β-TCP, a heat treatment of between 700-800 ºC must be applied, shown in Equation 1:[12]

$$Ca_9(HPO_4)(PO_4)_5(OH) \longrightarrow 3Ca_3(PO_4)_2 + H_2O \quad \textbf{(3.1)}$$

Liou and Chen studied the transformation of CDHA into β-TCP using an aqueous precipitation method.[13] Calcium and phosphorus starting materials were used to yield a stoichiometric Ca: P ratio of 3:2 and the pH of the solution was kept alkaline throughout the precipitation stage. Powders were then placed within Al_2O_3 crucibles and calcined at temperatures between 700-900 ºC to form the final β-TCP product. Adopting the solid state method, Bigi *et al*[14] prepared β-TCP by reacting $CaCO_3$ and $CaHPO_4.2H_2O$ at 1000 ºC for 15 hours, in the correct molar ratio.

3.1.3 Morphological control

In addition to the synthesis of phase-pure β-TCP, control over particle size and morphology of the calcium phosphate material is desirable. Various reports have shown that changes in particle size, shape and surface area can influence both the mechanical properties and biological activity of biomaterials (as discussed in Chapter 1). [15, 16] Moreover, the introduction of porosity into the overall morphology of ceramics has proven to have significant effects on the bioactivity *in vivo*. [17] Pore size and distribution in a ceramic dictate the form of linkages made with surrounding tissue and play a critical role in bone formation. Porous ceramics with controlled morphology can be prepared by various techniques such as gel casting, combustion synthesis, freeze casting and surfactant directed synthesis. [18]

Surfactants can control the growth and porosity of a material by acting at the early stages of crystal growth as structure-directing agents, wherein surfactant micelles determine structure and act in a templating capacity. The first research which used surfactants to create porous materials with a controlled morphology was published in 1992, where it was successfully demonstrated that a surfactant templating technique could be used to prepare silicon based mesoporous materials.[19] Since this initial publication, relatively few reports on mesoporous calcium phosphate materials have been published (in comparison to other

materials such as bioglasses). Most of these have relatively low BET surface areas.[20] The significant difference in calcium phosphate syntheses, compared to those of other classes of biomaterials, is the necessity for high temperature calcination steps. The high temperatures required to facilitate phase transformations of the required products and removal of the surfactant molecules consequently induce sintering of the materials, which thereafter reduces surface area.

Organic surfactants are commonly used in a templating capacity in calcium phosphate material synthesis because they can be easily removed at the calcination stage, leaving behind a material with controlled morphology and porosity. The nucleation and regulation of crystal growth can be controlled by organic surfactants as a result of geometric, electrostatic and chemicalcomplementarities between surfactant and substrate. Zhang *et al* synthesised HA nanoparticles, with controlled morphology and size, through the use of the organic cationic surfactant cetyl trimethly ammonium bromide ($C_{19}H_{42}NBr$, CTAB) as the template for the reaction.[21]

3.1.4 Clinical applications

The biocompatibility, cell-mediated resorbability and osteoconductivity of β-TCP has been studied extensively *in vivo* with positive results.[22] This has prompted further research into the use of β-TCP in clinical applications, including regenerative dentistry, drug and growth factor delivery systems and fillers for bone defects.

Reichert *et al* investigated the effect β-TCP had on dental follicle cells (DFC's) attachment, cell vitality/proliferation and differentiation.[23] Compared to a standard protocol control, improved cell attachment, survival and proliferation was observed for the β-TCP samples, with the cells forming close contacts to the scaffold material. Osteogenic differentiation of DFC's was stimulated in the β-TCP surfaces, with upregulated gene expression of several osteogenic markers, including osteopontin, RUNX 2 and fibronectin. The authors conclude that β-TCP could be used successfully as a scaffold in this area of tissue engineering.

Drug therapy carriers are required to deliver drugs or therapeutic agents to a site of defect within the body, at which stage they then release said agents over a sufficient length of time as the carrier degrades, whilst exposing the rest of the body to a minimal dosage.[24]

β-TCP can function well in this capacity when fabricated as a porous material, because agents can be stored inside the pores, which thereafter are released when β-TCP is resorbed within the body. Chung *et al* synthesised β-TCP composites with chitosan and growth factors with the overall aim of enhancing periodontal regeneration in calvarial defects in rats.[25] Results indicated that an effective therapeutic concentration of growth factor was released throughout the experiment, and that the composite material promoted osseous healing of defects in comparison to the controls. This supports the use of β-TCP in carrier systems.

The potential application of bioceramics as scaffold materials to induce bone formation was studied by Zaffe *et al*.[26] Holes were drilled into sheeps mandibular bones and filled separately with β-TCP and HA. Bone deposition was viewed only in the β-TCP filled holes at 4 months, with the new bone directly deposited on its surface. At 12 months holes filled with β-TCP were completely closed as a result of new bone formation, and no presence of the calcium phosphate granules remained, having been completely resorbed. HA filled holes, in comparison, showed little bone ingrowth into the holes and consequently were unable to induce bone growth.

Research in this chapter focused on the use of several aqueous precipitation methods to synthesise β-TCP, and the various experimental parameters which influenced product formation. Morphological control over the surface area and pore size of samples was investigated through the use of a surfactant templated method using organic cationic surfactants. A microwave processing method was used to assess the possibility of synthesising β-TCP without the use of a high temperature calcination stage.

3.2 Experimental

3.2.1 Synthesis of β-TCP

Three experimental methods were used to synthesise β-TCP in this research: two aqueous precipitation reactions and a microwave method. For each, a range of experimental parameters were adjusted to optimise reaction conditions and product formation.

3.2.1.1 Aqueous precipitation from $CaCl_2$ and $K_2HPO_4.3H_2O$

The chemical procedure employed by Tam *et al*[27] to synthesise HA nanostructures was modified for this research. Calcium chloride [$CaCl_2$, ACS reagent, Sigma-Aldrich] and potassium phosphate monobasic [$K_2HPO_4.3H_2O$, reagent grade, Sigma-Aldrich] were used as starting reagents for calcium and phosphorus, respectively. To control morphology, the organic surfactant Cetyl trimethylammonium bromide [$CH_3(CH_2)_{15}N(Br)(CH_3)_3$, BioXtra ≥ 99%, Sigma Aldrich] was included. Reaction parameters including pH, reflux conditions and calcination temperatures were adjusted accordingly to investigate their effect on the formation of β-TCP.

Calcium chloride and potassium phosphate monobasic were used in a 3:2 ratio, in order to fulfil the Ca: P ratio of 1.5 required for β-TCP formation.

Calcium chloride (0.009 moles) was weighed, crushed using a mortar and pestle and dissolved in 20 ml of deionised water. Potassium phosphate monobasic (0.006 moles) and cetyl trimethlyammonium bromide (0.006 moles) were dissolved in 30 ml of deionised water. Throughout the precipitation process pH was maintained at ~8 through the addition of dilute NaOH solution. β-TCP powders were synthesised by adding the calcium solution to the phosphate solution drop wise. Upon addition a white precipitate was immediately yielded. The precipitate in solution was refluxed at 100 ºC for 12 hours, after which it was washed thrice with deionised water to remove impurities and counter ions and dried at 100 ºC for 24 hours. Conversion from the calcium deficient apatite to the β-TCP structure was achieved through calcination of the samples at 800 ºC for 5 hours. The overall reaction equation is shown in equation 3.2:

$$3CaCl_2 + 2K_2HPO_4 + 2NaOH \longrightarrow Ca_3(PO_4)_2 + 4KCl + 2H_2O + 2NaCl \qquad \textbf{(3.2)}$$

The material was then ground using a mortar and pestle for PXD measurements. Tables 3.1 and 3.2 summarises the various experimental parameters altered to optimise the synthetic procedure.

Table 3.1 Summary of samples prepared by aqueous precipitation of $CaCl_2$ and K_2HPO_4

Sample	pH	Reflux conditions	Calcination Temp/ °C	CTAB Conc/ mol
1	7	12 hours/100°C	800	0.006
2	8	12 hours/100°C	800	0.006
3	10	12 hours/100°C	800	0.006
4	8	12 hours/100°C	800	0
5	8	2 hours/100°C	800	0.006
6	8	6 hours/100°C	800	0.006
7	8	12 hours/100°C	800	0.006
8	8	12 hours/100°C	650	0.006
9	8	12 hours/100°C	700	0.006
10	8	12 hours/100°C	750	0.006
11	8	12 hours/100°C	800	0.003
12	8	12 hours/100°C	800	0.006
13	8	12 hours/100°C	800	0.009

Table 3.2 Summary of samples prepared by aqueous precipitation of $CaCl_2$ and K_2HPO_4, usingdifferent cationic surfactants (pH 8, reflux 12 hrs at 100 °C, 800 °C calcination)

Sample	pH	Surfactant	Concentration/ mol
14	8	Hexadecyltrimethylammoniumbromide	0.006
15	8	Hexadecylpyridinium bromide	0.006
16	8	Tetradecyltrimethylammonium bromide	0.006

3.2.1.2 Aqueous precipitation from $Ca(NO_3)_2$ and $(NH_4)_2HPO_4$

The preparation of β-TCP using calcium nitrate tetrahydrate and ammonium phosphate dibasic is well documented and was modified for this procedure.[28] Calcium nitrate tetrahydrate [$Ca(NO_3)_2.4H_2O$, ACS reagent, Sigma-Aldrich] and ammonium phosphate

dibasic [$(NH_4)_2HPO_4$, reagent grade, Sigma-Aldrich] were used as starting materials for calcium and phosphorus, respectively.

Calcium nitrate tetrahydrate (0.900 moles) was dissolved in 40ml of deionised water and titrated against an ammonium phosphate dibasic solution (0.600 moles in 40 ml of deionised water) under continuous stirring. The pH of the ammonium phosphate dibasic solution was adjusted to ~10 before the titration and maintained at pH 9 during the titration. Resultant precipitates were rinsed with deionised water to remove NH_4^+ and NO_3^- counter ions, filtered, and dried at 100 °C overnight. Calcination steps were thereafter carried out at 800 ºC for 3 hours to produce β-TCP. Equation 3.3 shows the reaction of the calcium and phosphate starting materials to form the intermediate product required pre-calcination.

$$9Ca(NO_3)_2 + 6(NH_4)_2HPO_4 + 6NH_4OH \longrightarrow Ca_9(HPO_4)(PO_4)_5(OH) + 5H_2O + 18NH_4NO_3 \quad \textbf{(3.3)}$$

Table 3.3 details the experiments conducted in this research and the experimental parameters altered to optimise the experimental procedure

Table 3.3 Summary of samples prepared by aqueous precipitation of $Ca(NO_3)_2$ and $(NH_4)_2HPO_4$

Sample	pH of solution	Calcin. Temp/ °C	CTAB conc/ mol
3.1	9	800	0
3.2	9	800	1
3.3	n/a	800	0
3.4	9	650	0
3.5	9	700	0
3.6	9	750	0

3.2.1.3 Microwave Procedure

Synthesis of β-TCP using a microwave method was investigated alongside a BSc project student, David Connell. Work carried out by Lee *et al*, [29] who synthesised biphasic calcium

phosphates (BCP) by a microwave assisted process, was used as a reference for this research, with calcium and phosphorus ratios adjusted accordingly.

Calcium hydroxide [$Ca(OH)_2$, ACS reagent, Sigma Aldrich] and phosphoric acid [H_3PO_4, 85%, Sigma-Aldrich] were used as the primary starting materials for calcium and phosphorus, respectively. Both calcium hydroxide (0.900 moles) and phosphoric acid (0.600 moles) were dissolved in 30 ml of deionised water. The pH of the solution was adjusted to ~8 using concentrated ammonium hydroxide solution (1 mol l^{-1}). The suspension was then transferred to a domestic microwave oven and heated for various durations and powers (Table 3.4).

Table 3.4 Summary of samples prepared by microwave irradiation of $Ca(OH)_2$ and H_3PO_4

Sample	Power (Watts)	Time (Minutes)	CTAB conc/ moles	PO_4 Source
8-1	600	25	0	H_3PO_4
8-2	900	25	0	H_3PO_4
8-4	900	50	0	H_3PO_4
8-6	900	25	0	$(NH_4)_2HPO_4$

Reactants were left to cool overnight, before being separated *via* filtration techniques, dried at 100 °C for 12 hours, and ground using a mortar and pestle for PXD analysis. Equations 3.4 and 3.5 highlight the reactions of calcium hydroxide with phosphoric acid and ammonium phosphate monobasic, respectively, to produce calcium-deficient hydroxyapatite.

$$2H_3PO_4 + 3Ca(OH)_2 \longrightarrow Ca_3(PO_4)_2 + 6H_2O \quad \textbf{(3.4)}$$

$$Ca(OH)_2 + 6(NH_4)2HPO_4 \longrightarrow Ca_9(PO_4)_5(HPO_4)(OH)_2 + 12NH_4OH + 5H_2O \quad \textbf{(3.5)}$$

3.2.2 Powder X-ray Diffraction (PXD) Experiments

All compounds synthesised were characterised by PXD, as described in section 2.3.2.2. The materials were packed into flat-plate sample holders for each PXD experiment. Data

collection ranged from 5-85 ° 2θ for 1 h or 14 h by using a time per step of either 649.6 s or 9125.6 s, respectively. Shorter scans of 1 h allowed for quick phase determination, whilst PXD experiments conducted over 14 h produced high quality data for Rietveld refinements and cell indexing.

3.2.3 Rietveld refinement against PXD data

The General Structure Analysis System (GSAS) [30] was employed, using the EXPGUI[31] interface, to carry out Rietveld refinements on the substituted samples and the equivalent unsubstituted sample. The data were fit against appropriate starting models of unsubstituted TCP from ICSD.[32] Cell parameters were obtained through indexing using CELREF V3, a graphical unit cell refinement software program which compares an experimental model to a proposed model.

In the Rietveld refinement of β-TCP materials, the background was manually fitted using 14 coefficients. Subsequently the scale factor, cell parameters and zero point were refined. Further cycles added refinement of the atomic positions, profile coefficients and peak widths. Peak profiles were modelled using function 2 within GSAS, a multi-term Simpsons rule integration of the Pseudo-Voigt function. The refinement was improved at this stage by the addition of a β-$Ca_2(P_2O_7)$ impurity phase. With a reasonable fit achieved, the atomic parameters could be cycled again and varied. To simplify the structure, initially the isotropic temperature factors of each atom type were set at equal values and constrained together.

3.2.4 Scanning electron microscopy (SEM)

To prepare a required sample for SEM analysis, the material was sieved at 70 μm to avoid large agglomerates and a small amount deposited onto an adhesive carbon tab, which was then fixed onto an aluminium stub. Preparation of samples was carried out in a fume hood due to the fine powdery materials produced, and each tab was placed in a closed glass vial to minimise surface contamination.

The samples were transferred to the vacuum column of the SEM (further details in section 2.3.5) and sealed inside using an air tight door. The column was then evacuated. The

samples often charged under the electron beam, which made obtaining images of clarity difficult, as will be discussed later in this chapter. On occasion, the samples were gold-coated to minimise the level of charging. However, this improved the situation only marginally.

3.2.5 Surface area measurements

BET isotherm measurements were taken to investigate the average pore size and surface area. Measurements were carried out by Andrew Monaghan, using a Micromeritics Flow Prep 060 and Gemini BET machine. Five point BET analysis was performed on each sample. Samples were degassed at 110 °C overnight to remove any adsorbed moisture prior to the analysis.

3.3 Results

3.3.1 Aqueous precipitation from $CaCl_2$ and $K_2HPO_4.3H_2O$

Numerous experimental parameters can affect and influence the formation of calcium phosphate materials in aqueous precipitation reactions. With regards to β-TCP particularly, the calcium phosphate materials synthesis can be affected by changes in variables such as pH, reaction solution temperature, and calcination temperature, to name but a few. [10] Research conducted within this particular aqueous system aimed to determine which parameters influence β-TCP formation and demonstrate how adjusting them, even slightly, can lead to large fluctuations in phase purity.

The initial parameter studied in the optimisation process was pH. To investigate at which pH ranges β-TCP could be formed, three syntheses were carried out, the only difference between each being the pH of the starting solution. Figure 3.2 shows the PXD patterns attained at the end of each reaction after calcination, with reactions carried out at pH 7 (blue, sample 1), 8 (red, sample 2) and 10 (green, sample 3).

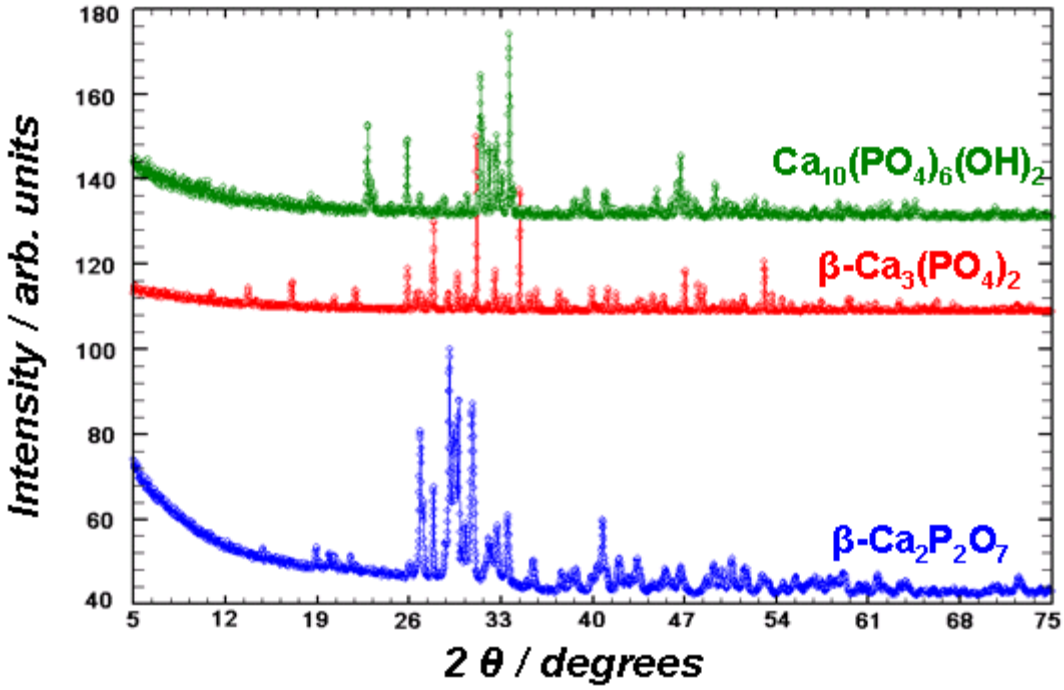

Figure 3.2 PXD patterns of samples synthesised at pH 7 (blue, sample 1), 8 (red, sample 2) and 10 (green, sample 3)

Analysis using HighScore PLUS software confirmed that β-$Ca_2P_2O_7$, not β-TCP, was formed at pH 7 (blue powder pattern in Figure 3.2, sample 1). To synthesise β-TCP, the calcium and phosphorus sources were added in a 1.5 ratio.[33] However, the result obtained indicates that adjusting the solution pH to 7 has reduced the Ca: P ratio, because β-$Ca_2P_2O_7$ only forms at Ca: P ratios lower than 1.5.[34] This result will be discussed in section 3.4. When the pH was increased to 8 (red powder pattern in Figure 3.2, sample 2), the formation of β-TCP was confirmed, alongside a low level impurity of β-$Ca_2P_2O_7$. β-$Ca_2P_2O_7$ can be difficult to assign in the PXD pattern as many of its peaks overlap with those of β-TCP, although the presence of the (204) and (212) reflections are indicative of the phase. The continued presence of this unwanted side product is commonly observed in the synthesis of β-TCP. Indeed β-$Ca_2P_2O_7$ is present within the commercial product Bioresorb®. [35] Increasing the pH to 10 (green powder pattern in Figure 3.2) provides a pattern with peaks attributable to both HA and $Ca_8H_2(PO_4)_6(H_2O)$. HA has a Ca: P ratio higher than 1.5,[36] allowing for a trend to be observed: as the pH of the reaction solution increases, the Ca: P ratio in the product increases.

SEM analysis of the β-TCP sample formed at pH 8 highlighted a material with a highly porous architecture, consisting of fused, agglomerated spheres. Figure 3.3 (a) illustrates the grouping of the calcium phosphate particles into segregated clumps of materials. In stark

contrast, an equivalent sample synthesised without CTAB shows large blocks of material, with no porosity, and average particle sizes greater by orders of magnitude than those with CTAB present within the reaction (Figure 3.3(b)). Changes in pH did not affect the morphology of the samples.

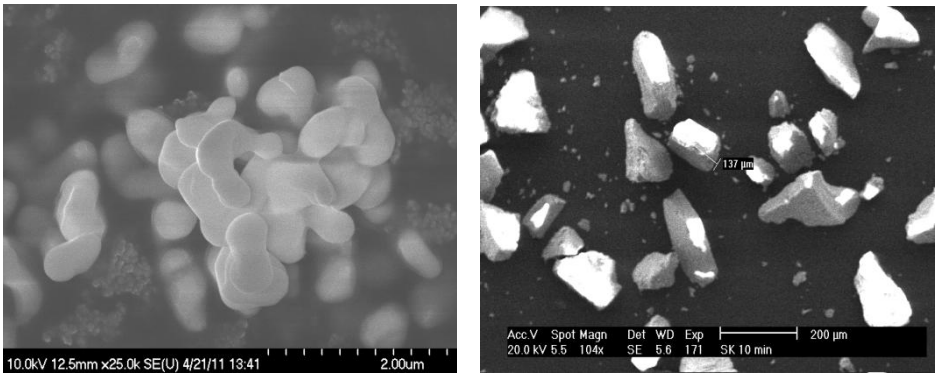

Figure 3.3 (a-b) SEM image of β-TCP material (a) with CTAB and (b) without CTAB

Within this synthesis is a reflux step, wherein the precipitate and its solution are refluxed overnight at ~ 100 °C. Reactions performed without this stage, or at reflux temperatures lower than 100 °C, did not produce β-TCP after calcination. To streamline the process, thereby reducing time and energy costs, the duration of the reflux period was studied. Figure 3.4 shows the effects of refluxing the solution for 2 (red, sample 5), 6 (green, sample 6) and 12 (blue, sample 7) hours at 100 °C. The shortest reflux duration of 2 hours is not long enough to obtain the required result, as mixtures of both starting materials and several intermediate products are obtained as the final products, and the mixture is composed of so many different compounds that it is difficult to accurately assign individual reflections to specific compounds. As reflux duration is increased to 6 hours, characteristic peaks of β-TCP are observed at 25, 28, 31 and 34 ° 2θ. However, peaks attributable to unwanted side products are still clearly visible, including those observed between 30.5-31.5 ° 2θ. Only when the reflux duration is increased to 12 hours is a material containing β-TCP as the main phase obtained (low levels of β-$Ca_2P_2O_7$ are still present).

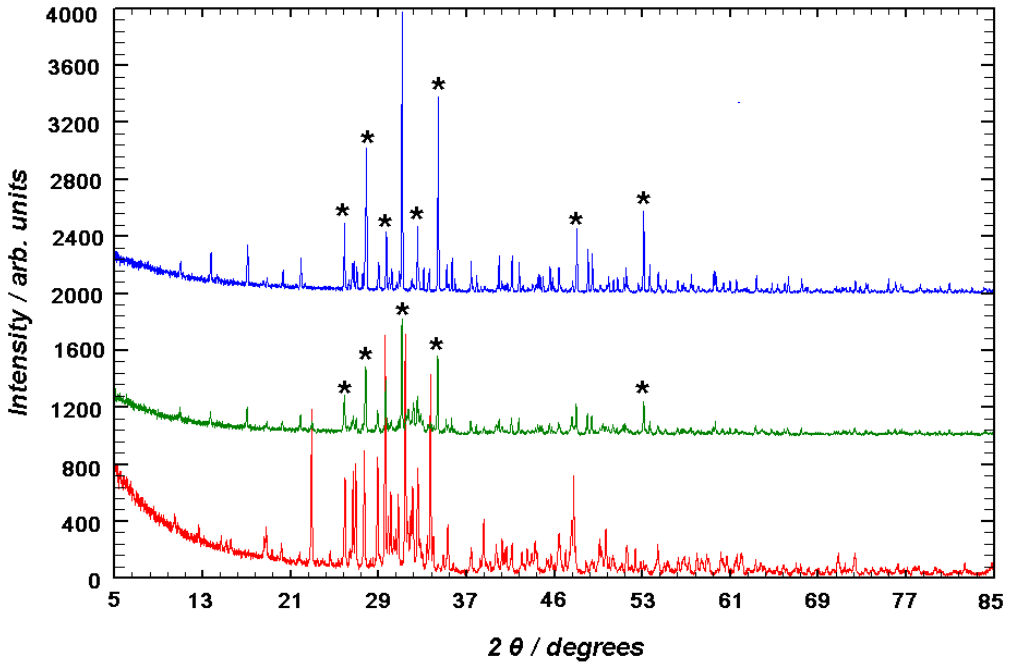

Figure 3.4 PXD patterns of samples refluxed at 100 °C for 2 (red, sample 5), 6 (green, sample 6) and 12 (blue, sample 7) hours. Major reflections attributable to β-TCP are marked by *.

It is clear that, within this aqueous precipitation system, the reflux step is not only essential, but must also be maintained for long time periods. This is in order to allow the starting materials to react fully and form the required intermediate product calcium-deficient hydroxyapatite, which can then be sintered to form β-TCP.

At high temperatures, amorphous intermediate products such as CDHA are transformed into highly crystalline calcium phosphate materials such as HA, β-TCP and α-TCP, depending on the temperature used in the calcination step.[37] To assess the relationship between calcination temperature and β-TCP formation, intermediate samples were washed and dried after precipitation, and calcined at 650, 700 and 750 °C. The resultant PXD patterns are compared in Figure 3.5:

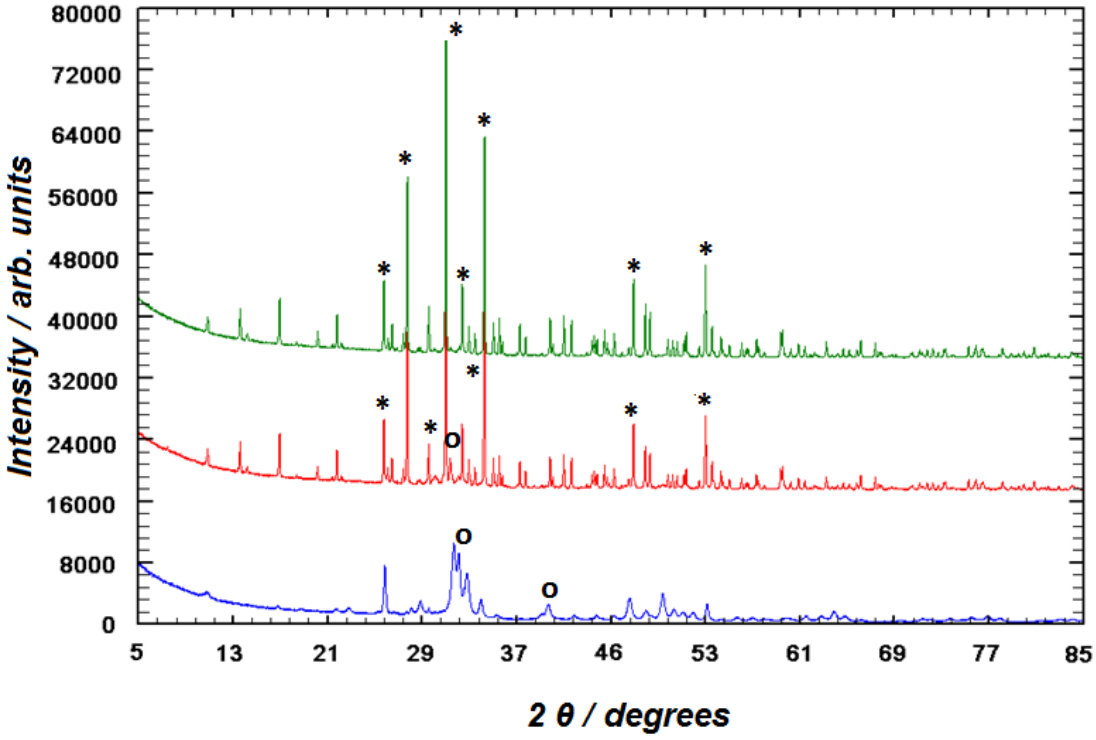

Figure 3.5 PXD patterns of samples calcined at 650 (blue, sample 8), 700 (red, sample 9) and 750 °C (green, sample 10). Main phase reflections attributable to CDHA are highlighted as o, whilst the main reflections of β-TCP are given as *.

Reactions at 650 °C show the presence of CDHA, which can generally always be attained with less energy than that required for transformation into β-TCP.[27] As the temperature increases from 650 to 700 °C, the formation of β-TCP occurs, with the characteristic peaks of the material noted at 25.8, 27.6, 30.9 and 34.2 ° *2θ*. This result is maintained at higher calcination temperatures (750 ºC), with cell parameters of *a* = 10.4323 (5) Å, *c* = 37.3945 (7) Å, and a cell volume of 3541.65 (4) Å^3, which correlate well with literature values.[6] β-TCP samples are highly crystalline, with each pattern showing sharp, narrow peaks. The optimum temperature for calcination in this reaction is 750 °C.This represents the lowest temperature of formation of β-TCP without an impurity phase.

With the experimental parameters of pH, reflux and calcination temperature optimised, attention was turned to controlling the morphology of the samples. Until this point, the concentration of CTAB was kept constant in each experiment. To ascertain whether increasing or decreasing surfactant concentration influences the morphology and surface area of the samples, three different molar ratios were used: 0.003 moles, 0.006 moles, and 0.009 moles. XRD was used to characterise the products and assess the effects of altering surfactant concentration. Figure 3.6 illustrates that, regardless of surfactant concentration,

the production of β-TCP remains unaffected, suggesting that CTAB only acts in a templating capacity and does not interfere with the aqueous precipitation reaction.

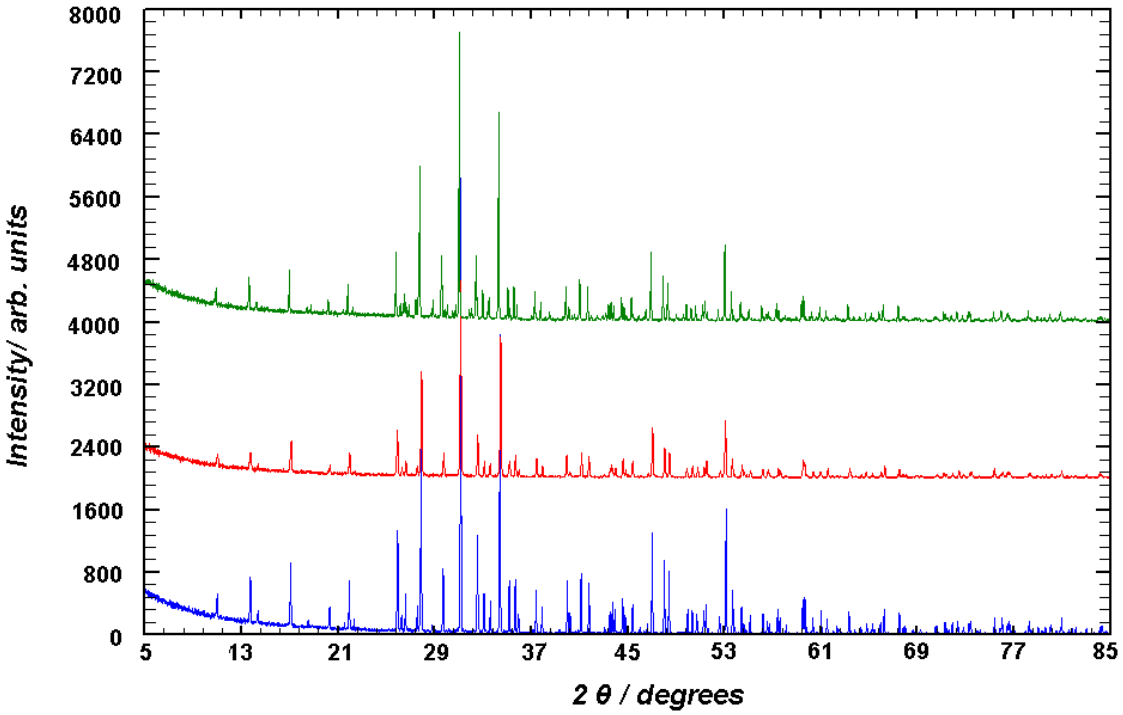

Figure 3.6 PXD patterns of samples containing 0.003 moles (green, sample 11), 0.006 moles (blue, sample 12) and 0.009 moles (red, sample 13) of CTAB

It is difficult to ascertain, from SEM imaging alone, what impact increasing or decreasing CTAB concentration has on the morphology and surface structure of the samples. Figure 3.7 and Table 3.5 show the morphology, specific surface area and average pore diameter of samples of each CTAB concentration. The highest surface area of 5.080 m^2g^{-1} is attained with a CTAB concentration of 0.006 moles. Concentrations below (0.003 moles) and above (0.009 moles) produced reduced surface areas of 2.566 and 1.565 m^2g^{-1}, respectively. The overall surface areas are very low, possibly as a consequence of the high temperature sintering step in the reaction. SEM images appear to correlate with surface area results, as samples synthesised with the highest concentration of CTAB show large agglomerated clusters of materials, some of which have diameters greater than 40 µm. Lower surfactant concentrations show images in which finer particles of materials are dispersed throughout the surface, as opposed to showing such high levels of agglomeration. The largest pore diameters are also noted for those materials synthesised with 0.006 moles of CTAB, at 78.38 Å. Smaller pore sizes of 45.4 Å and 52.5 Å are noted for 0.003 and 0.009 moles of CTAB, respectively.

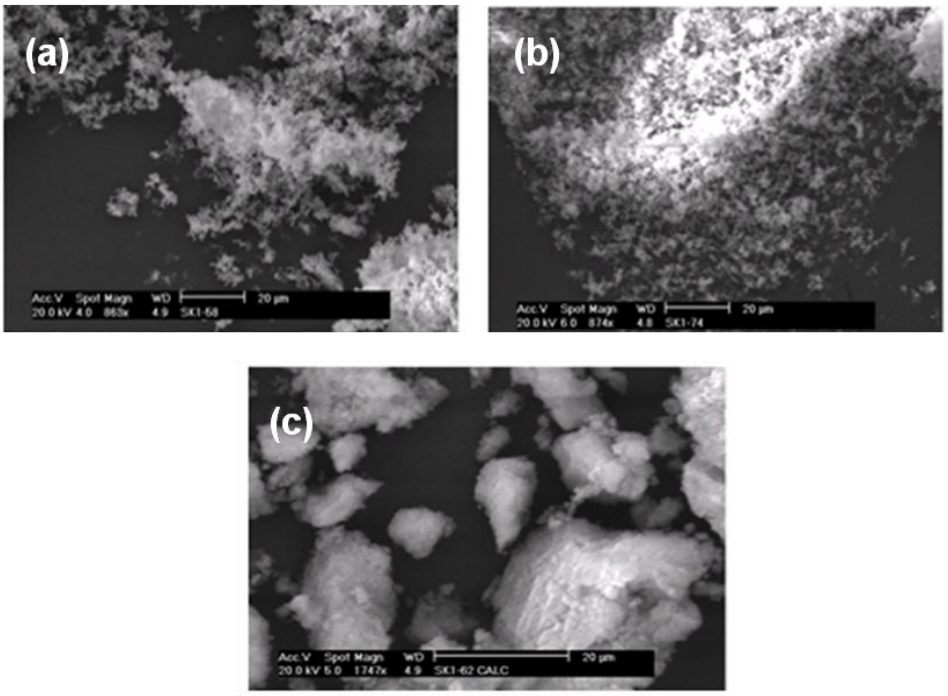

Figure 3.7 SEM images of surface morphology on materials synthesised with (a) 0.003 mol, (b) 0.006 mol and (c) 0.009 mol of CTAB surfactant

Table 3.5 Sample morphology, surface area and average pore diameter for materials with differing CTAB concentration

Sample	BET S.A. (m^2g-1)	Average pore diameter/ Å	Surfactant conc./mol
11	2.566	45.4	0.003
12	5.080	78.38	0.006
13	1.565	52.5	0.009

In addition to adjusting the concentration of CTAB within the reaction system, different cationic organic surfactants were introduced, to investigate whether varying carbon chain lengths and end groups influenced particle size, shape, surface area and average pore diameter. Among the surfactants investigated were hexadecyltrimethylammonium bromide ($C_{19}H_{42}BrN$), hexadecylpyridinium bromide ($C_{21}H_{38}BrN$) and tetradecyltrimethylammonium bromide ($C_{17}H_{38}BrN$). Figure 3.8 shows that, in similarity to experiments in which CTAB concentration was varied, the use of different cationic surfactants does not influence the formation of β-TCP. Each PXD pattern in Figure 3.7 shows that β-TCP has been produced.

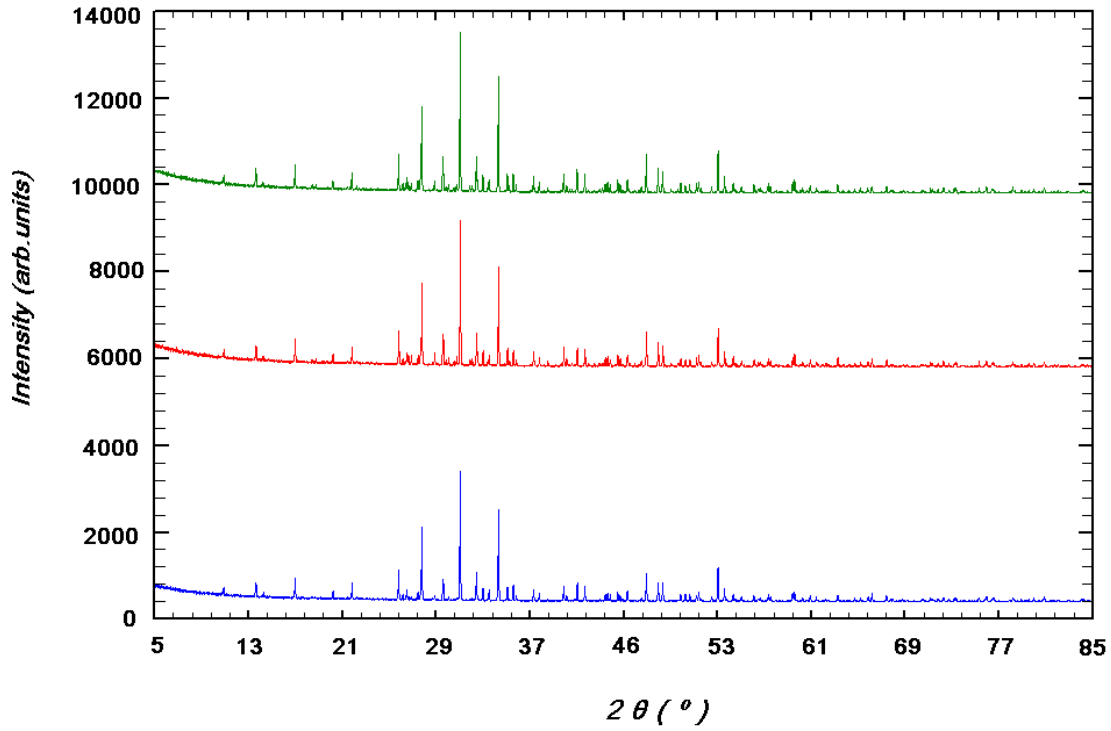

Figure 3.8 PXD patterns of reaction systems using hexadecyltrimethylammonium bromide (blue, sample 14), hexadecylpyridinium bromide (red, sample 15) and tetradecyltrimethylammonium bromide (green, sample 16)

Figure 3.9 and Table 3.6 show SEM images of each final β-TCP product, its surface area, average pore diameter, and the corresponding surfactant used to attain said sample morphology. The largest pore diameters are seen with the employment of 1-hexadecylpyridinium bromide, which was the only surfactant used which possessed aromaticity. Using an aromatic surfactant did not, however, increase the surface area of the material, with a reduction to 2.17 m^2g^{-1} in comparison to CTAB. Pore diameters were averaged to be 93.4 Å, in comparison to the CTAB equivalent of 78.38 Å. Using a cationic surfactant with a smaller carbon chain length (tetradecyltrimethylammonium bromide) reduces the average pore diameter to 22.81 Å. Smaller surface areas and a less porous, dense morphology is noted for the tetradecyltrimethylammonium bromide templated materials.

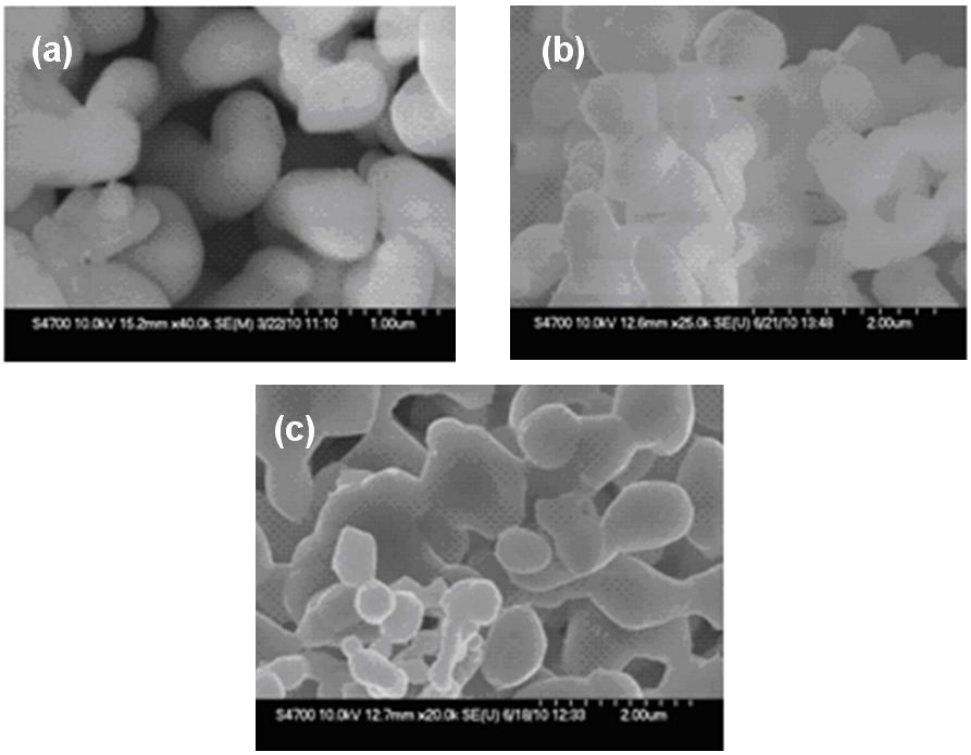

Figure 3.9 Surface morphology of samples synthesised with a templating surfactant of (a) hexadecyltrimethyl-ammonium bromide, (b) tetradecyltrimethyl ammonium bromide and (c) 1-hexadecylpyridinium bromide. All surfactants were added at a molar ratio of 0.006.

Table 3.6 Surface area and average pore diameter of samples produced using different cationic organic surfactants in a templating capacity

Sample No.	BET S.A.m^2g^{-1}	Average pore Diameter/ Å	Surfactant conc./mol
14	5.08	78.38	**Hexadecyltrimethyl-ammonium bromide, 0.006**
15	1.60	22.81	**Tetradecyltrimethyl ammonium bromide, 0.006**
16	2.17	93.4	**1-Hexadecylpyridinium bromide, 0.006**

3.3.2 Aqueous precipitation of $Ca(NO_3)_2$ and $(NH_4)_2HPO_4$

In this reaction system a sample was firstly synthesised (sample 3.1) without any surfactant present. Initially, all reactions were conducted under slightly alkaline conditions (pH 9) to facilitate deprotonation of hydrogen phosphate. The material produced was a fine, white powder, and cell parameters after indexing were a = 10.4475 (13) Å, c = 37.4204 (5) Å,

with a cell volume of 3537.29 (8) $Å^3$, which correlate well to literature values.[5] A visual comparison of the powder pattern of the sample to the experimental model showed strong correlations between peaks (Figure 3.10).

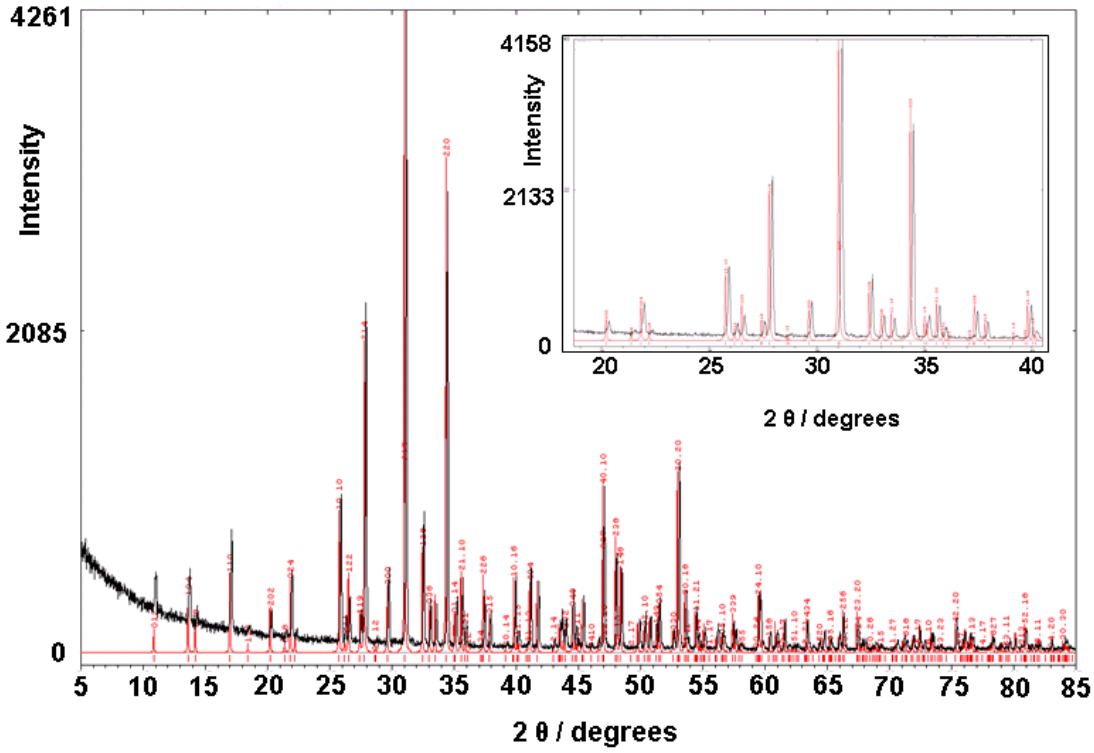

Figure 3.10 Experimental (black) and calculated (red) PXD patterns for sample 3.1. Inset is a zoomed area between 20 ≤ 2θ º≤ 40.

Closer inspection of the PXD pattern, however, indicated a low level impurity in the form ofcalcium hydrogen phosphate hydrate, Ca_8H_2 $(PO_4)_6$ $(H_2O)_5$. Intensities are too low to illustrate in Figure 3.10, but peaks attributable to the impurity phase appear at 27.2, 29.2, 30.5, 32.1 and 38.8 º 2θ.

SEM images reveal very different sample morphology from experiments wherein CTAB is used in the reaction system; instead of agglomerated spheres, larger particles can be seen with smaller crystallites growing on their surfaces. The BET surface area of this sample was 41.9 m^2g^{-1}, which is a vast improvement on that observed for previous agglomerated samples. However, it does not appear to possess the porous architecture present in most bioactive ceramics. Images with a higher resolution, however, may indicate porosity on a smaller scale.

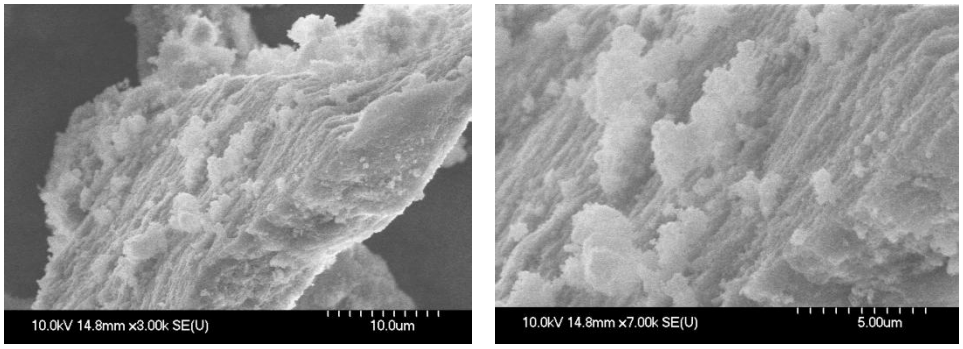

Figure 3.11 (a)-(b) SEM micrographs of sample 3.1 at (a) x3k and (b) x7k magnification

Synthesising β-TCP in the presence of CTAB produced a fine, bright white powder. Figure 3.12 presents the PXD pattern for the material (sample 3.2), which shows that a single phase sample of β-TCP can be synthesised. The experimental pattern for the sample, shown in black, fits well with the calculated pattern shown in red. Indexing produced cell parameters in good agreement with literature reports[5] (a = 10.4317 (11) Å and c = 37.3506 (6) Å, with a cell volume of 3520.01 (8) Å^3). The online Inorganic Crystal Structure Database (ICSD) was used to obtain a model for indexing[6] and Powdercell 2.4 provided a visual comparison between the experimental and theoretical models.

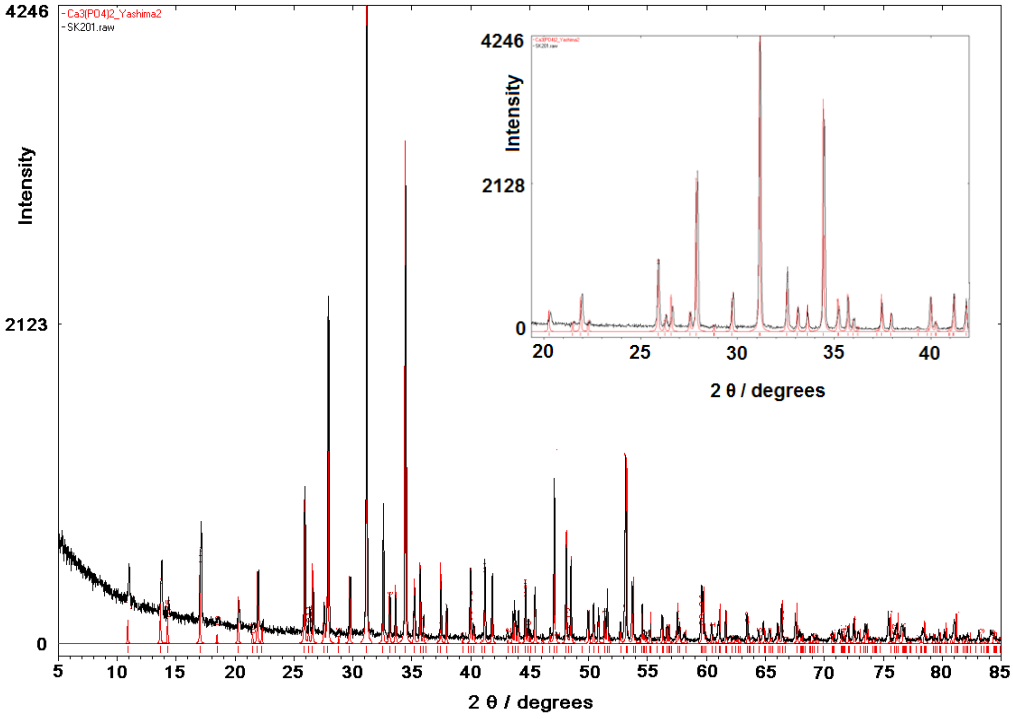

Figure 3.12 Experimental (black) and calculated (red) PXD patterns for sample 3.2. Inset is a zoomed area between 20 ≤ 2θ º≤ 40.

Selected Rietveld refinement data for sample 3.2 are presented in Table 3.7 and the observed, calculated and difference plot is displayed in Figure 3.14. Atomic positions and temperature factors for the atoms in this sample are shown in Table 3.8. Specific bond lengths between atoms are presented in Table 3.9.

Table 3.7 Selected Rietveld refinement data from the X-ray refinement of β-TCP (sample 3.2) at 298 K

Empirical Formula	β-$Ca_3(PO_4)_2$
Collection temperature/ K	298
Crystal system	Hexagonal
Space Group	*R 3c*
Lattice parameters/ Å	*a* = 10.4469 (2)
	c = 37.4047 (7)
V / Å ^{3}	3535.34 (2)
Z	18
Unit cell formula weight, M_w	6513.8
Density/ g cm^{-3}	3.060
No. of varied parameters	66
No. of observations	4786
R_{wp}	0.1269
R_p	0.0871
χ^2	1.292

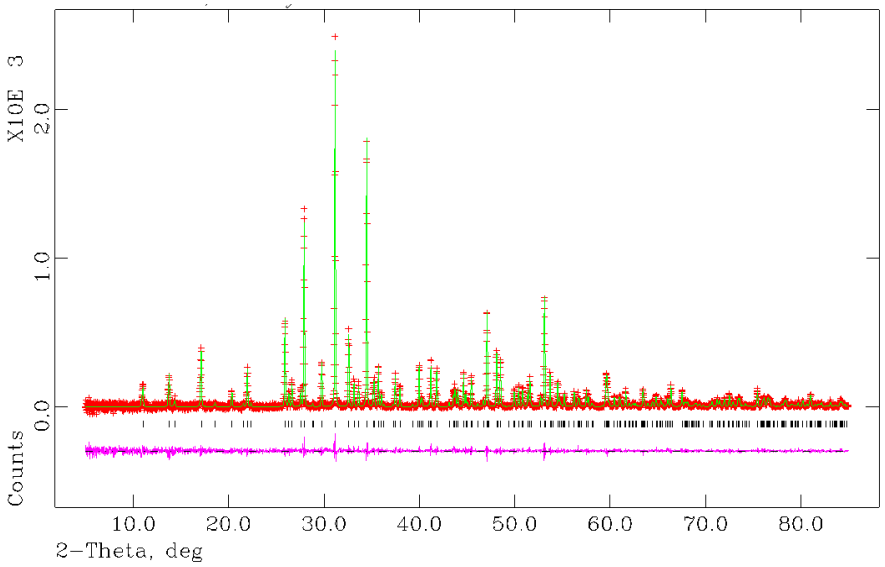

Figure 3.14 Observed (red), calculated (green) and difference (pink) OCD plot from structural refinement of sample 3.2 against data collected from 14 h X-ray diffraction scan at 298 K. Black tickmarks indicate reflections from β-$Ca_3(PO_4)_2$.

Table 3.8 Atom positions generated by PXD Rietveld refinement for β-$Ca_3(PO_4)_2$ phase in sample 3.2 at 298 K

Atom	Wyckoff Symbol	x	y	z	Occ.	Uiso/ *100 Å^2
Ca1	18b	0.7239(7)	0.8549(9)	0.166(2)	1	1.47(2)
Ca2	18b	0.6190(7)	0.819(1)	-0.032(9)	1	2.06(2)
Ca3	18b	0.7251(6)	0.8486(8)	0.061(2)	1	2.88(2)
Ca4	6a	0.0000	0.0000	-0.083(5)	0.50	3.77(7)
Ca5	6a	0.0000	0.0000	0.734(3)	1	1.75(2)
P1	6a	0.0000	0.0000	-0.000(3)	1	2.68(4)
P2	18b	0.6680(8)	0.859(3)	0.868(2)	1	2.75(3)
P3	18b	0.652(2)	0.846(2)	0.767(2)	1	2.01(3)
O1	18b	0.734(8)	-0.086(7)	-0.092(5)	1	1.58(5)
O2	6a	0.772(2)	0.783(3)	0.857(5)	1	2.14(5)
O3	18b	0.729(2)	0.006(4)	0.848(5)	1	2.46(5)
O4	18b	0.524(1)	0.761(7)	0.861(5)	1	1.92(5)
O5	18b	0.602(2)	-0.045(3)	0.781(6)	1	2.29(5)
O6	18b	0.570(2)	0.687(3)	0.784(5)	1	1.44(5)
O7	18b	0.079(3)	0.898(2)	0.777(5)	1	0.79(5)
O8	18b	0.630(1)	0.827(2)	0.727(4)	1	1.23(5)
O9	18b	0.009(2)	0.864(7)	-0.014(7)	1	3.78(5)
O10	18b	0.0000	0.0000	0.039(8)	1	2.29(5)

Table 3.9 Bond lengths generated by PXD Rietveld refinement for β-$Ca_3(PO_4)_2$ phase in sample 3.2 at 298 K

Bond	Length(Å)	Bond	Length(Å)	Bond	Length(Å)
P1-O9	1.56 (2)	Ca1-O2	2.99 (2)	Ca3-O1	2.61 (6)
P1-O9	1.56 (2)	Ca1-O3	2.56 (2)	Ca3-O2	2.54 (2)
P1-O9	1.56 (2)	Ca1-O4	2.50 (6)	Ca3-O3	2.38 (1)
P1-O10	1.49 (3)	Ca1-O4	2.40 (7)	Ca3-O5	2.46 (4)
		Ca1-O5	2.39 (4)	Ca3-O6	2.48 (3)
		Ca1-O6	2.28 (1)	Ca3-O8	2.62 (8)
P2-O1	1.57 (3)	Ca1-O8	2.43 (5)	Ca3-O8	2.57 (2)
P2-O2	1.51 (2)	Ca1-O9	2.48 (8)	Ca3-O10	2.63 (1)
P2-O3	1.56 (1)				
P2-O4	1.51 (7)	Ca2-O1	2.49 (2)	Ca4-O1(*3)	2.47 (7)
		Ca2-O2	2.48 (1)	Ca4-O3(*3)	2.98 (9)
P3-O5	1.55 (5)	Ca2-O3	2.32 (1)		
P3-O6	1.58 (1)	Ca2-O5	2.60 (4)	Ca5-O6(*3)	2.28 (8)
P3-O7	1.57 (6)	Ca2-O6	2.83 (4)	Ca5-O9(*3)	2.29 (2)
P3-O8	1.51 (8)	Ca2-O7	2.38 (4)		
		Ca2-O7	2.47 (3)		
		Ca2-O9	2.31 (9)		

Refinement data from Table 3.7 and Figure 3.14 confirm a single phase β-TCP sample. Table 3.9 lists the cation-anion distances for the five Ca sites and PO_4 polyhedra in the crystal structure. All three PO_4 polyhedra display slight distortion, in comparison to reported values.[38] Calcium-oxygen bond lengths compare well with those reported by Schroeder *et al.* [39]

Figure 3.15 shows the morphology of sample 3.2. As previously seen in section 3.3.1 (Figure 3.3 a), the morphology consists of highly agglomerated, fused spheres, which give rise to a porous architecture.

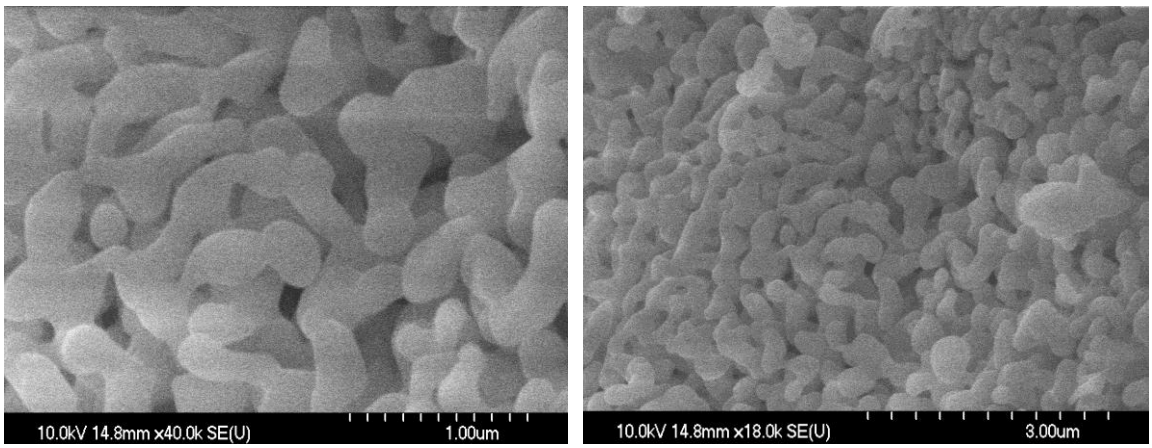

Figure 3.15 (a)-(b) SEM micrographs showing the presence of highly porous agglomerated substituted β-TCP samples at (a) x40 k and (b) x18 k magnification

At this point the intermediate product in the synthesis, i.e. that which is obtained after precipitation, but before the high temperature calcination stage, was analysed for reactions 3.1 and 3.2. Both reactions produced the same compound: calcium deficient hydroxyapatite (CDHA), $Ca_9(HPO_4)(PO_4)_5(OH)$.

ICSD was used to obtain an appropriate structural model for indexing.[40] Figure 3.16 presents the powder pattern for this intermediate product, which shows that the experimental data (black) fit well to the theoretical data (red). Experimental cell parameter values obtained were a = 9.3717 (5) Å, c = 6.8416 (9) Å and the cell volume was 520.39 (8) Å^3. These values correspond to literature values for CDHA.[40] The formation of CDHA at this point of the reaction is well documented, with the next stage of the reaction (calcination) converting the apatite to the desired final product ofβ-TCP.[41]

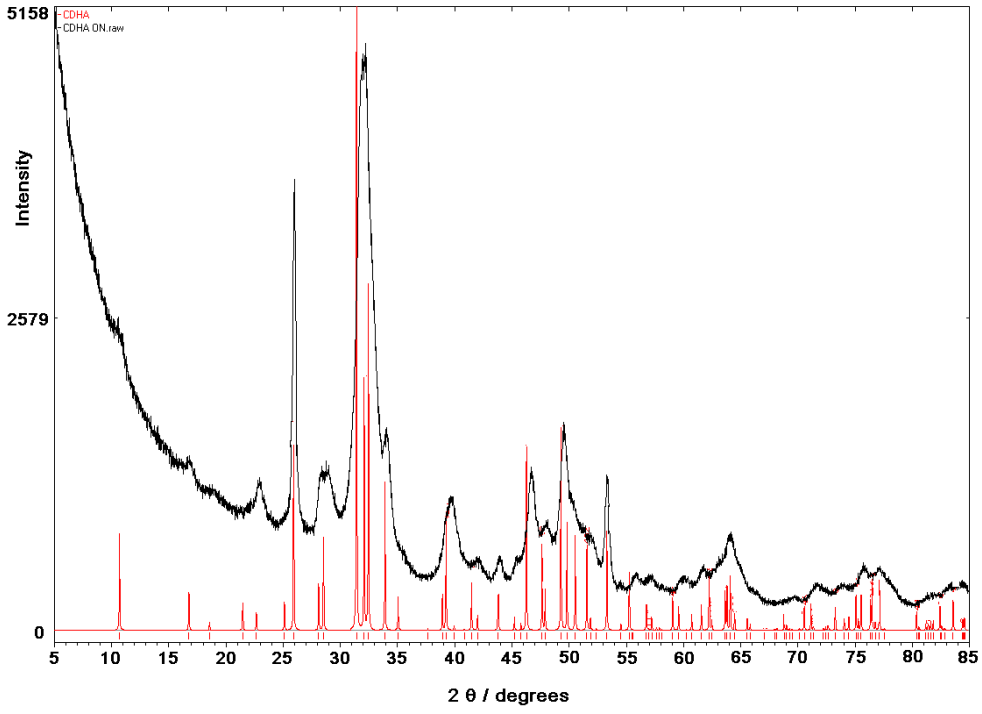

Figure 3.16 PXD analysis showing the experimental (black) and calculated (red) patterns for CDHA

In the synthesis of any calcium phosphate material, pH plays a pivotal role in product formation.[27] Whilst samples 3.1 and 3.2 both demonstrated a successful synthesis of β-TCP at alkaline pH, sample 3.3 was synthesised without any addition of ammonium hydroxide

to elevate pH. As a result, the pH of the solution throughout the precipitation fluctuated between 6 and 7.5. It was immediately evident from the PXD pattern that β-TCP had not been formed from this reaction, so the pattern was run through HighScore PLUS software in order to identify the material. Results indicated that β-$Ca_2P_2O_7$ had been formed as a single phase from this reaction, as shown in Figure 3.17. As the reaction had not yielded the desired product, the sample was not analysed further.

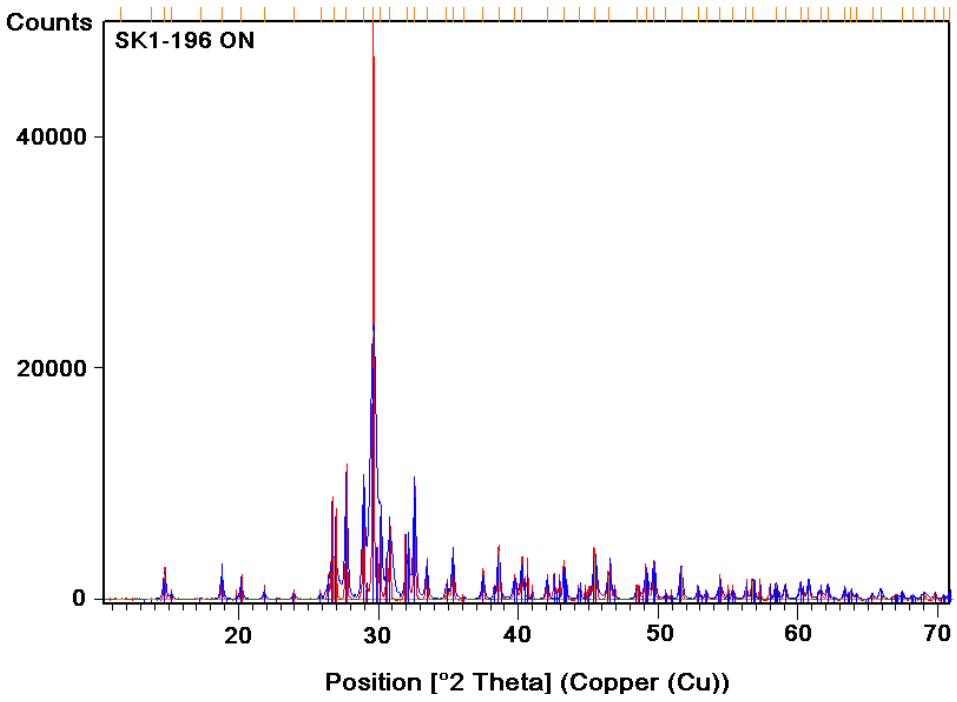

Figure 3.17 Analysis of the pattern of sample 3.3 with HighScore PLUS, indicating the formation of β-$Ca_2P_2O_7$ (blue calculated profile) as the final and sole product

As well as pH, the formation of calcium phosphate compounds is reliant on the temperature of the calcination stage of the reaction.Figure 3.18 shows the results obtained when a sample of CDHA was calcined at temperatures between 650 and 750 °C. At 650 °C (sample 3.4), only CDHA is present, which is in keeping with literature reports that HA is formed in the temperature range of 500-650 °C.[27] Calcination at 700 °C (sample 3.5) yields a biphasic mixture, with peaks attributable to both HA and β-TCP visible. Increasing the calcination temperature by a further 50 °C to 750 °C, however, yields a single phase sample of β-TCP (sample 3.6).

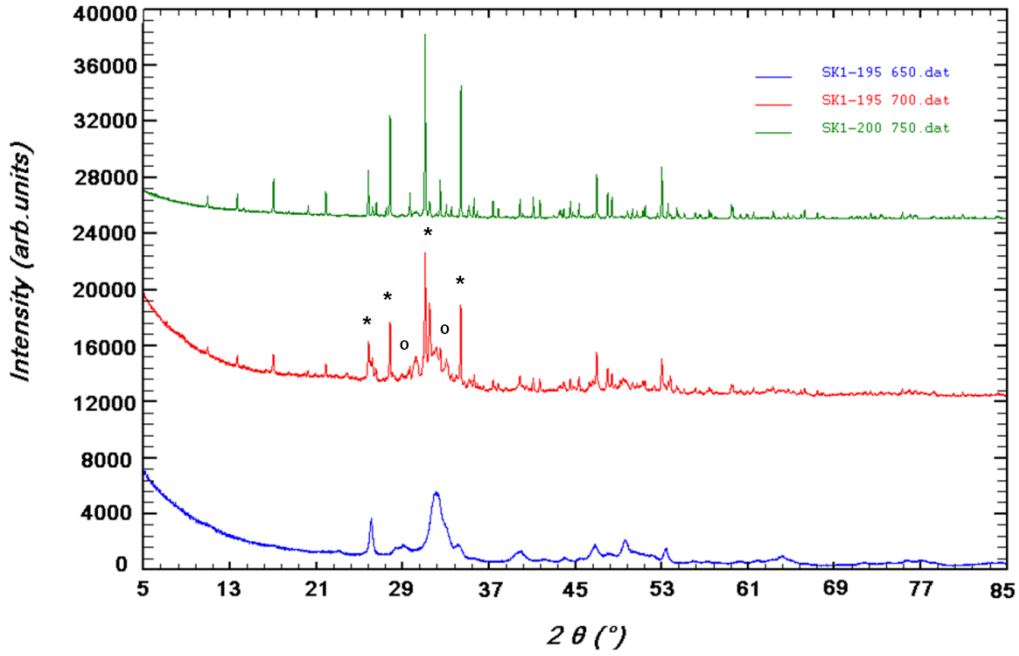

Figure 3.18 PXD analysis showing the patterns obtained after calcination of CDHA at 650 °C (blue), 700 °C (red) and 750 °C (green). The blue pattern shows the formation of CDHA at 650 °C, whilst calcination at 750 °C produces β-TCP (green pattern). Calcination at 700 °C yields a biphasic mixture of CDHA and β-TCP (red pattern). Black circles on this pattern indicate prominent reflections from CDHA and black stars indicate prominent reflections from β-TCP.

3.3.3. Microwave Procedure

Reacting H_3PO_4 and $Ca(OH)_2$ *via* a microwave synthesis produced a fine white powder. Figure 3.19 presents the PXD pattern for sample 8-1, irradiated at 600 Watts for 25 minutes, which does not display the characteristic pattern associated with β-TCP. Upon further analysis using HighScore software, the sample was identified as a mixture of β-$Ca_2P_2O_7$ and $CaHPO_4$.

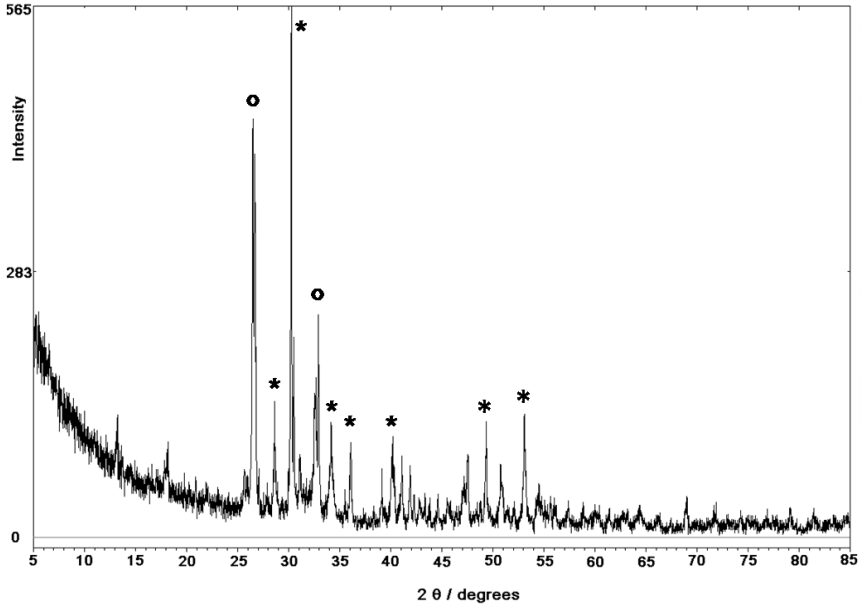

Figure 3.19 PXD pattern for sample 8-1, whereblack circles indicate main reflections from β-$Ca_2P_2O_7$, and black stars indicate reflections from $CaHPO_4$ up to 55 2 *θ* / °

To investigate the effect that microwave power has on product formation, sample 8-2 was synthesised at 900 W, as opposed to the initial 600 W used for sample 8-1. Despite physical appearances mimicking that of β-TCP, the PXD pattern was not that of the desired product, and again showed the formation of β-$Ca_2P_2O_7$ and $CaHPO_4$ (Figure 3.20).

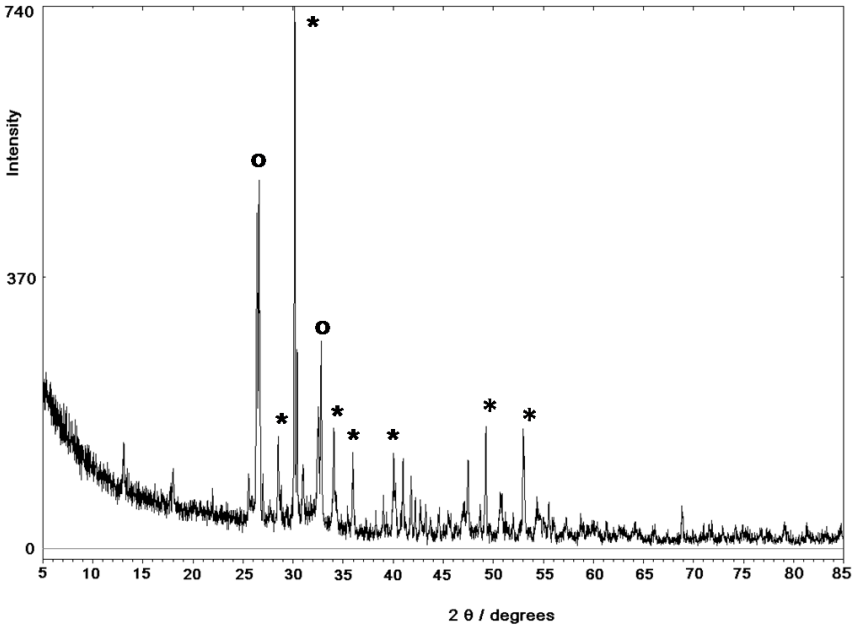

Figure 3.20 PXD pattern for sample 8-2, whereblack circles indicate main reflections from β-$Ca_2P_2O_7$, and black stars indicate reflections from $CaHPO_4$ up to 55 2 *θ* / °

It was recognised, at this stage, that increasing power had not influenced the overall product formation, as a comparison of the two PXD patterns shows that the same products were produced (Figure 3.21):

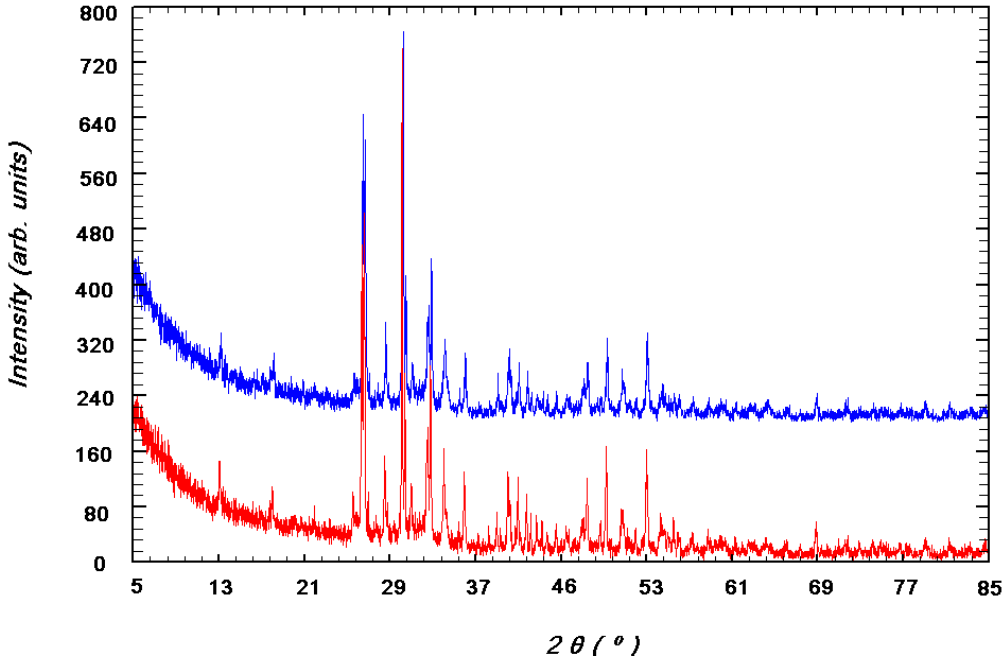

Figure 3.21 Comparison of samples 8-1 and 8-2, which show similar PXD patterns, irrespective of different microwave powers used in synthesis

The duration of irradiation was doubled from 25 minutes to 50 minutes at 900 W for sample 8-4, the PXD pattern of which can be seen in Figure 3.22. Similarly to results seen with altering irradiation power, changing the duration of irradiation did not influence overall product formation. A mixture of β-$Ca_2P_2O_7$ and $CaHPO_4$ was again yielded in the reaction.

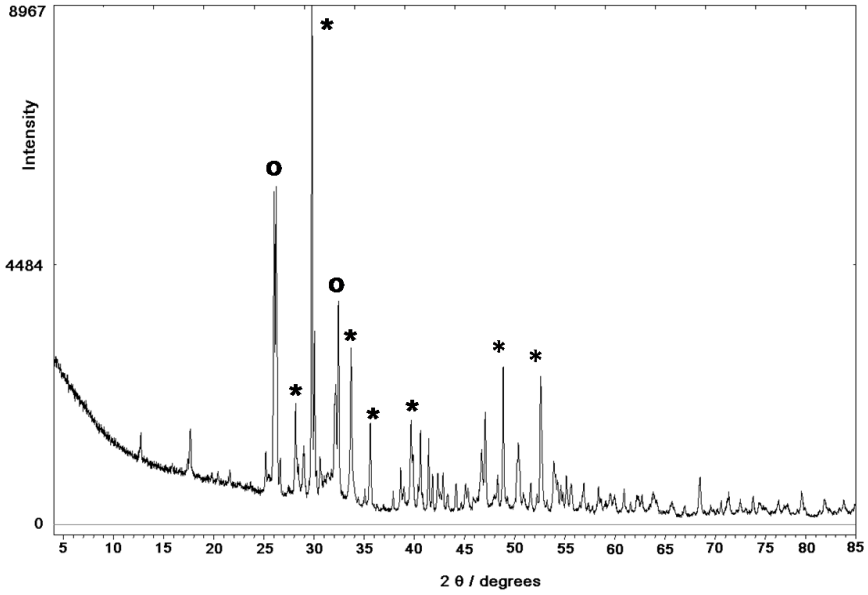

Figure 3.22 PXD pattern for sample 8-4, whereblack circles indicate main reflections from β-$Ca_2P_2O_7$, and black stars indicate reflections from $CaHPO_4$ up to 55 2 *θ* / °

With both microwave irradiation power and duration having no effect on overall product formation, the influence of starting materials on the reaction was investigated by changing the phosphate source used, from H_3PO_4 to $(NH_4)_2HPO_4$. The resulting PXD pattern of sample 8-6 indicates a mixture of CDHA and $Ca_3H_2P_4O_{14}$ as a by-product of unreacted starting materials.

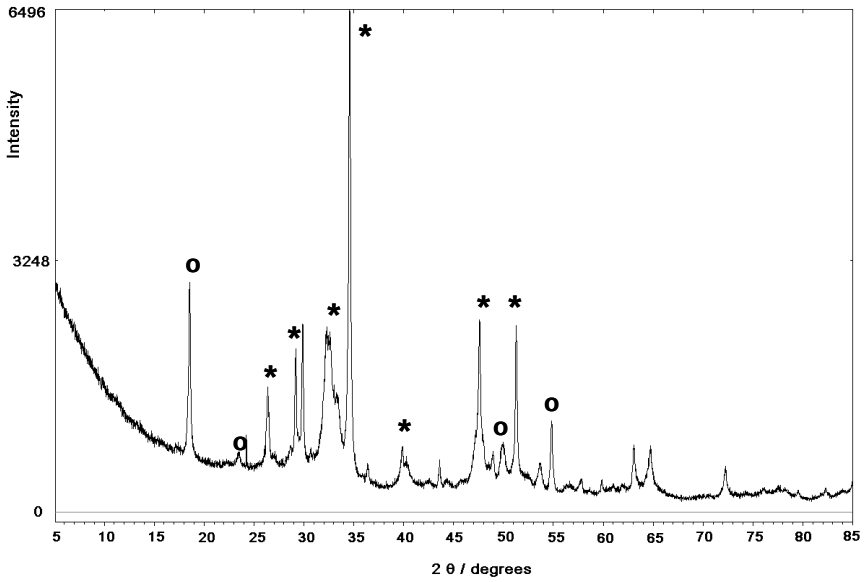

Figure 3.23 PXD pattern for sample 8-6, whereblack circles indicate main reflections from $Ca_3H_2P_4O_{14}$ and black stars indicate reflections from CDHA up to 55 2 *θ* / °

It became evident at this stage that the synthesis of β-TCP without the application of a high temperature calcination stage in the reaction was not possible. Literature also states that pure phase β-TCP cannot be synthesised directly from a microwave treatment only.[42] The products of the microwave reactions were therefore calcined at temperatures ranging between 700-1100 °C, and the transformation process was monitored. Samples 8-1, 8-2, and 8-4, which were synthesised using H_3PO_4 as the phosphate source, all yielded near identical PXD patterns throughout each temperature specific calcination stage. Figure 3.24 highlights the different compounds attained from different calcination treatments of sample 8-1.

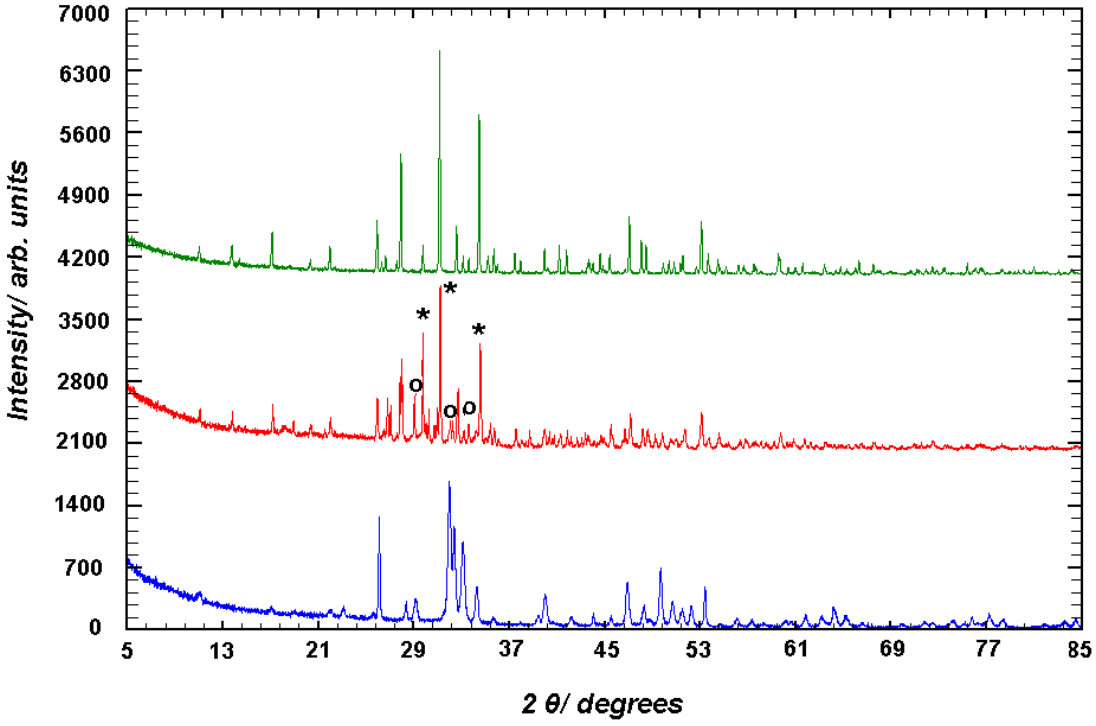

Figure 3.24 PXD patterns of samples calcined at 600 (blue), 700 (red) and 800 (green). * represent primary reflections from β-TCP and o represent CDHA reflections

At temperatures of 600 °C, peaks attributable to CDHA are observed. This is in keeping with various literature reports that HA is obtained at lower temperatures than β-TCP.[43] The PXD pattern taken for the sample calcined at 700 °C, shows that a biphasic mixture of HA/β-TCP is produced, with peaks attributable to each of the two calcium phosphate materials. Literature also documents that a biphasic product exists in this temperature range. Only at a temperature of 800 °C is the PXD pattern of β-TCP displayed, which again is widely documented to be at the lower end of possible temperatures required for the

attainment of β-TCP.[44] Experimental cell parameter values obtained for sample 8-1, calcined at 800 °C, were *a* = 10.4296 (7) Å and *c* = 37.3501 (3) Å and the cell volume was 3483.43 (5) Å^3. These values correspond to literature values for β-TCP.[5]

Interestingly, the sample synthesised using $(NH_4)_2HPO_4$ as the phosphate source did not follow the same calcination profile as the other samples. Figure 3.25 compares the products of an 800 °C calcination of a sample made with $(NH_4)_2HPO_4$ (8-6) to a sample made with H_3PO_4 (8-4). Whilst sample 8-4 shows the PXD pattern of crystalline β-TCP, peaks attributable to HA are seen in the corresponding PXD pattern of sample 8-6. There is a distinct reduction in phase transformation present due to the phosphate source used in the synthesis, and it is clear that the presence of $(NH_4)_2HPO_4$ has suppressed the conversion of HA into β-TCP, showing preference for material formed at lower, less harsh conditions.

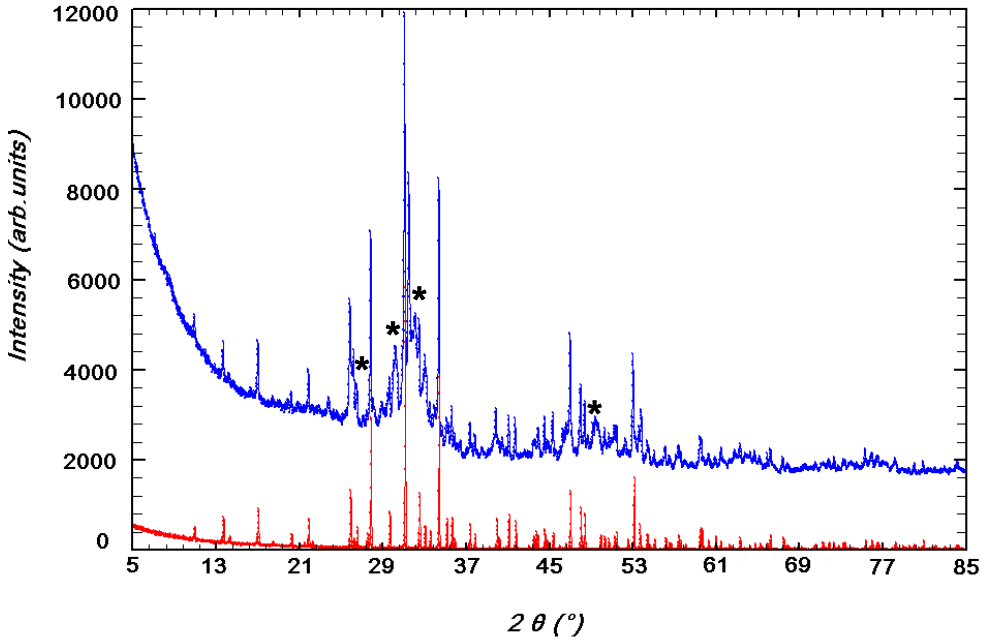

Figure 3.25 Comparison of PXD patterns formed after calcination at 800 °C from samples 8.4 (red) and 8.6 (blue). Black stars indicate prominent reflections attributable to HA.

The surface morphology of sample 8-1 was characterised by SEM, pre- and post calcination (Figure 3.26 (a-b)). Pre-calcination, the material, synthesised by microwave irradiation, is composed of flat platelets stacked together and on top of each other in a disorientated manner. Most of the platelets are fused together, although a degree of porosity is observed.

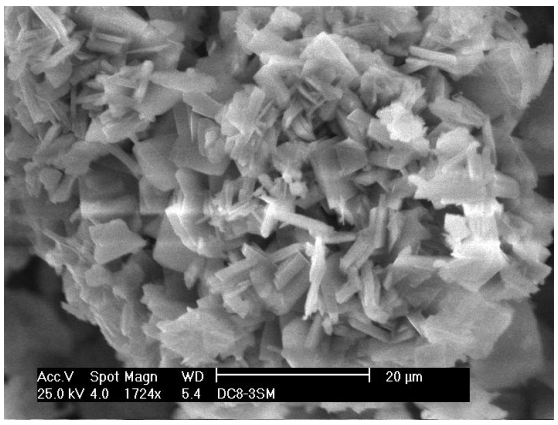

Figure 3.26 (a) SEM image of sample 8-1 pre-calcination, x1724k magnification.

Post calcination, it can be observed from Figure 3.26 (b) that the sample morphology is not as uniform as before the high temperature treatment: a 'collapse' of the structure is noted, with higher levels of agglomeration and reduced porosity. The same result of higher agglomeration and reduced porosity was observed when each of the intermediate phases was calcined. BET measurements give a surface area of 6.21 m^2g^{-1} for sample 8-1 calcined at 850 ºC.

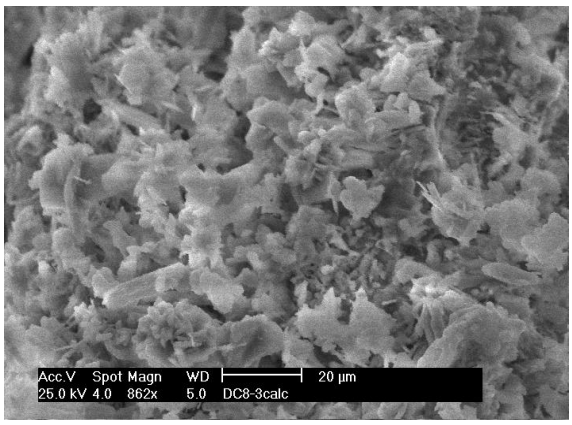

Figure 3.26 (b) SEM image of sample 8-1 post-calcination at 850 °C, x862 k magnification.

As calcination temperature increases, the degree of agglomeration increases, as shown in Figure 3.27. The complete fusion of particles is evident on close examination of the SEM image, with the previously seen flat and distinct edges of the uncalcined sample completely unrecognisable. Surface areas of the sample decrease with increasing calcination temperature: sample 8-1 calcined at 1100 °C has a surface area of only 0.278 m^2g^{-1}.

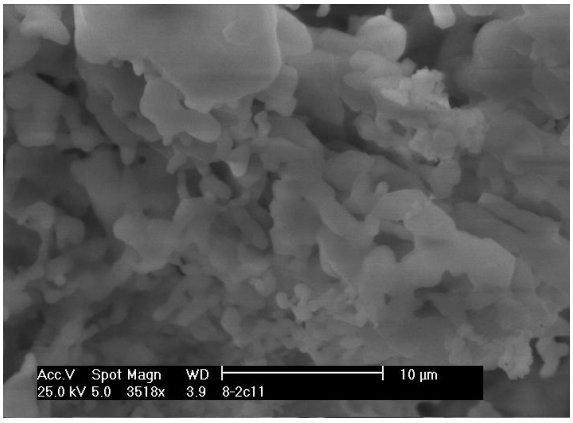

Figure 3.27 SEM image of sample 8-1 post-calcination at 1100 °C, x3518k magnification.

3.4 Discussion

For each of the three synthetic techniques, careful control of solution pH was critical to obtain single phase materials, as slight changes in pH can greatly affect Ca: P ratios. Slight changes in pH produced a range of unwanted by-products. This is because pH dictates the state in which the PO_4^{3-} precursor will exist, and has a decisive effect on the dissociation of reagents. [45] Thissubsequently can alter the characteristics of precipitates and final products. In addition to pH, there is a wide range of experimental parameters such as calcination temperature, maturation time, and precursor solubility which can all actively adjust the Ca: P ratio, contributing to the well documented conclusion that calcium phosphate synthesis is difficult to control.[10]

It was not possible to synthesise β-TCP without a high temperature calcination step in each synthetic method. Careful control of Ca: P ratios are required so that the intermediate products formed pre-calcination possess the same ratio as β-TCP (1.5). Such an intermediate usually takes the form of CDHA, which has the same Ca:P molar ratio as β-TCP and can be transformed upon the application of high temperatures:

$$Ca_9(HPO_4)(PO_4)_5(OH) \longrightarrow 3Ca_3(PO_4)_2 + H_2O \quad \textbf{(3.1)}$$

Although CDHA has the same molar ratio as β-TCP, it is structurally and chemically similar to HA, which allows for transformations between the two hydroxyapatite forms at lower temperatures than those needed for β-TCP formation.

The steps involved in the conversion of CDHA to β-TCP were studied by Mortier *et al*,[46] who concluded that the overall change occurring during calcination happens in two steps, over two distinct temperature ranges. Firstly, at temperatures between 300-680º, water is evolved as a result of two hydrogenphosphate groups reacting to give one pyrophosphate group and water, as illustrated in equation 3.6:

$$2HPO_4^{2-} \longrightarrow P_2O_7^{4-} + H_2O \qquad \textbf{(3.6)}$$

Following this, the produced pyrophosphate reacts with two hydroxyl groups to synthesise two phosphate groups and water, given in equation 3.7:

$$P_2O_7^{4-} + 2OH^- \longrightarrow 2PO_4^{3-} + H_2O \qquad \textbf{(3.7)}$$

3.4.1 Aqueous precipitation of $CaCl_2$ and K_2HPO_4

Synthesising β-TCP using $CaCl_2$ and K_2HPO_4 precursors occurs via equation 3.2:

$$3CaCl_2 + 2K_2HPO_4 + 2NaOH \longrightarrow Ca_3(PO_4)_2 + 4KCl + 2H_2O + 2NaCl \qquad \textbf{(3.2)}$$

Figure 3.2 illustrates that changes in pH greatly influence final product formation. Various products were formed as a result of different pH values of the reaction environment. At pH 7, β-$Ca_2P_2O_7$ is formed, which could initially, it is hypothesised, be the result of two deprotonated phosphate groups joining together to form a $[P_2O_8]^{6-}$ anion. Schematic 3.1 shows how this compound thereafter transforms into $[P_2O_7]^{4-}$ in the presence of H^+ ions.

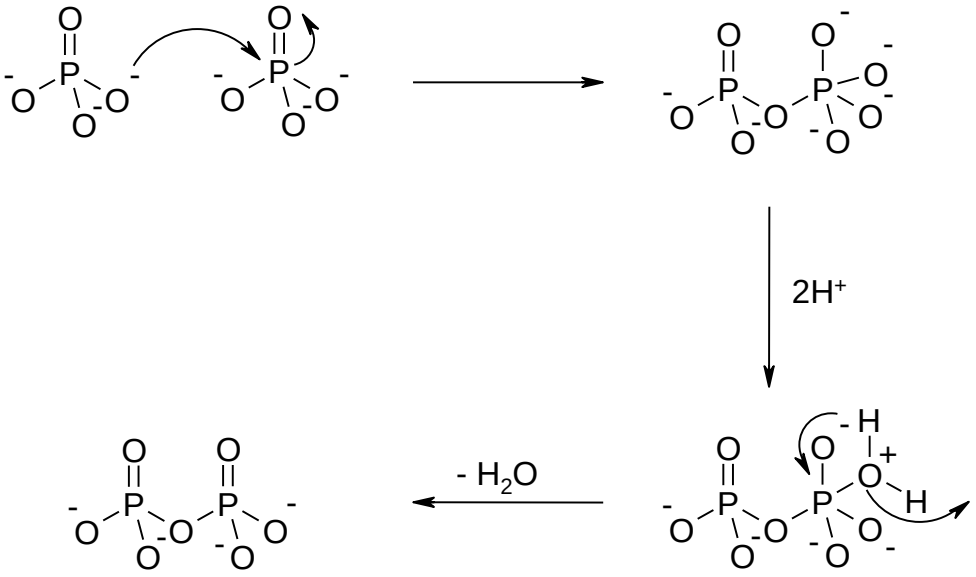

Schematic 3.1: Nucleophilic addition of two PO_4^{3-} groups, followed by protonation and ejection of a water molecule, to form $[P_2O_7]^{4-}$.

Only one oxygen atom can be protonated and lost as water per $Ca_2P_2O_7$ molecule as two Ca^{2+} ions are sequestered per molecule. β-$Ca_2P_2O_7$ is formed when the Ca: P ratio is <1.5, indicating that both the pH of the reaction solution and the Ca: P ratio has been decreased. At pH 8, β-TCP is the final product, indicating that CDHA was formed at the precipitation stage of the reaction. Few works deal with the mechanisms in which non-stoichiometric apatites are produced in precipitation reactions.[34] It was proposed by Heughebaert that an amorphous compound with a stoichiometry close to that of β-TCP is formed: [47]

$$9Ca^{2+} + 6PO_4^{3-} \longrightarrow Ca_9(PO_4)_6 \qquad \textbf{(3.8)}$$

This is then followed by the hydrolysis of the phosphate ions into hydrogenphosphate and hydroxide ions:

$$PO_4^{3-} + H_2O \longrightarrow HPO_4^{2-} + OH^- \qquad \textbf{(3.9)}$$

The products attained thus far in the reactions lead to the non-stoichiometric CDHA compound.

At a slightly alkaline pH there is a greater chance of deprotonating the K_2HPO_4 precursor to the PO_4^{3-} ion, as opposed to at a neutral pH. Increasing the alkalinity again, this time to pH 10, favours the formation of HA ($Ca_{10}(PO_4)_6(OH)_2$) due to the abundance of OH^- ions which can be incorporated into the crystal structure. Compared to CDHA

($Ca_9(HPO_4)(PO_4)_5(OH)$) formed at pH 8, it is logical that the K_2HPO_4 reagent would be fully dissociated at pH 11, therefore only PO_4^{3-} ions would be available for incorporation into the structure.

The results of calcining intermediate products at different temperatures (Figure 3.5) highlight that HA is formed at lower temperatures than those required to produce β-TCP. HA and CDHA both have a similar apatite structure, shown by XRD peak positions of CDHA matching closely to those of HA.[48] Such similar structures explain the lower temperatures required to bring upon this transformation, which involves the process of HPO_4 ions being substituted by PO_4 ions, as shown in equation3.10:

$$Ca_{(10-x)}(HPO_4)_x(PO_4)_{6-x}(OH)_{2-x} \longrightarrow (1-x)Ca_{10}(PO_4)_6(OH)_2 + 3xCa_3(PO_4)_2 + xH_2O \quad \textbf{(3.10)}$$

The structural, physical and chemical properties of nanoparticles are determined by the size and shape of the materials. It is therefore important to be able to yield control over such properties in the synthesis of β-TCP. CTAB has been used to control sample morphology in a range of experimental systems, from copper oxide to silica systems. [49,50] Table 3.5 highlights that, as CTAB concentration increased from 0.006 moles to 0.009 moles, so too did the average size of the particles, alongside a reduction in surface area. This trend has also been observed in other reaction systems. One example of this involved research conducted by Zhang *et al* to synthesise nano-sized Cu_2O particles using a CTAB template, wherein it was found that grain size increased in relation to increasing CTAB concentration. [51]

In low concentrations of aqueous solution the CTAB molecules primarily form a monolayer structure at the water-surface interface and then the monolayer structure changes progressively into micelles as the concentration is increased. (Figure 3.28)

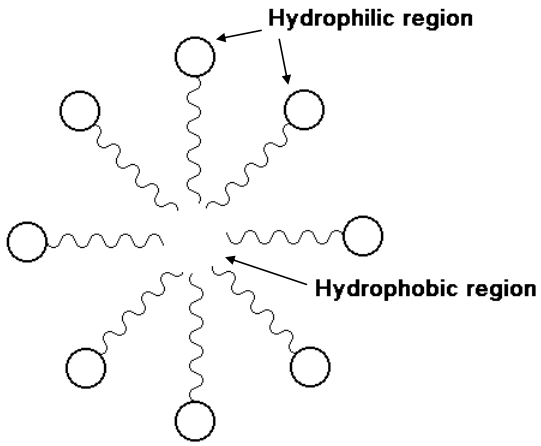

Figure 3.28 Micelle structure of surfactant molecules in solution

Micelles form aggregates in solution, with the hydrophilic entities on the outside circumference and in contact with the surrounding solvent, subsequently sequestering the hydrophobic entities in the middle of the micelle. In the specific case of CTAB, this means that the long chain, hydrophobic carbon tails congregate in the centre of the micelle, leaving the cationic nitrogen end group to interact with the reagents dissolved in solution. In water or other aqueous solutions, CTAB would ionise completely to form a bromide anion and a tetrahedral cation. This cation has a tetrahedral structure which means that it, hypothetically, can be incorporated with the anionic phosphate species in solution through charge and structure complementarities, as seen in Figure 3.29. [21]

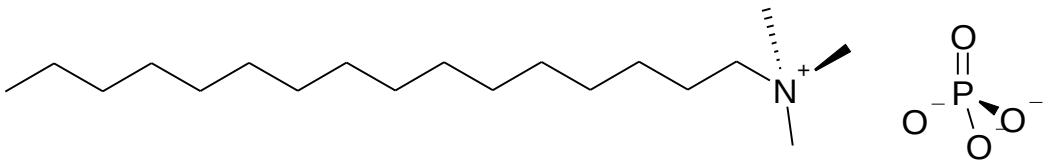

Figure 3.29 Molecular recognition between the cationic CTAB surfactant and anionic phosphate

Whilst no definitive mechanism for the action of CTAB in solution has been proven, probable mechanisms for its actions exist. One such mechanism suggests that the CTAB-PO_4^{3-} mixtures alluded to in Figure 3.29 form micelles which contain many PO_4^{3-} ions on the hydrophilic surface of said micelle. When Ca^{2+} ions are added in the precipitation step, $Ca_9(PO_4)_6$ clusters are formed on the micellar surface. The micelles are therefore acting as nucleating points for the growth of the material. [21] Whilst this mechanism is commonly

stated as a prelude to HA formation, it has also been found to form amorphous calcium phosphate as the precipitate. As the intermediate stage of the reaction system should theoretically produce CDHA, which is in fact very similar in composition and structure to HA, it is conceivable that this mechanism, or one very similar, takes place in the systems studied here.[52] As mentioned previously, Heughebaert suggests that a very similar mechanism of formation exists for TCP formation. [47] Certain points must be clarified in this argument, however, including the real concentrations and chemical compositions of the clusters in solution, and whether the cluster formation is definitely involved in the nucleation process.

It should be noted that the hydrophobic region remains devoid of any calcium or phosphate ions, thus explaining a contributing factor towards the materials porosity: when the surfactant is removed during the calcination stage of the reaction, pronounced spaces are left behind in the place of the hydrophobic entity. Literature reports also agree that the absence of material within these micelle regions results in 'holes' observed throughout the samples. Li *et al* stated that rod-like, porous HA nanoparticles were formed from the precipitation of calcium phosphate on the surface of the micelles and then porosity was introduced through the removal of the surfactant molecules by calcination.[53]

The concentration of CTAB within the reaction system is influential in determining the surface area of the materials; at too low a concentration, it may be impossible for the surfactant molecules to disperse throughout the reaction system fully. Conversely, too high a concentration may lead to the formation of too many micelles which may group together in the reaction solution, which again would inhibit optimum distribution of the calcium phosphate materials. Sun *et al* confirmed that increasing CTAB concentration in a [Cu(btc)2] reaction system from 0.01 M to 0.5 increased crystal size from 300 nm to 1 μm. They found that CTAB slowed the nucleation rate of crystal growth, causing increased crystal size and decreased surface area. [54] The size of carbon chain, and end group of different surfactants can also change both the surface area, and pore size of β-TCP. Reducing the length of the carbon chain yielded a reduction in both surface area and average pore diameter; tetradecyltrimethyl ammonium bromide-templated materials displayed a more 'collapsed' architecture, which could be attributable to smaller hydrophobic regions, thereby creating smaller pores and gaps in the sample. Using a surfactant which possessed an aromatic end group (1-hexadecylpyridinium bromide) generated a sample with the largest average pore diameter of 93.4 Å. This could be the

result of the aromaticity function possessing a greater volume in space than the other end groups.

3.4.2 Aqueous precipitation of $Ca(NO_3)_2$ and $(NH_4)_2HPO_4$

A major difference in the way in which β-TCP was synthesised *via* this aqueous precipitation method, compared to previous syntheses, was the heightened care taken to maintain the pH at exactly the same value throughout the addition process, thereby reducing the variability of the Ca: P ratio observed previously. The reaction proceeds according to equations (3.3) and (3.1), shown below:

$$9Ca(NO_3)_2 + 6(NH_4)_2HPO_4 + 6NH_4OH \longrightarrow Ca_9(HPO_4)(PO_4)_5(OH) + 5H_2O + 18NH_4NO_3 \quad \textbf{(3.3)}$$

$$Ca_9(HPO_4)(PO_4)_5(OH) \longrightarrow Ca_3(PO_4)_2 + H_2O \quad \textbf{(3.1)}$$

As observed in previous results, if the pH of the reaction solution is allowed to decrease, the Ca: P ratio also decreases, which is in keeping with other literature results. [55] A decrease in reaction solution pH leads to the protonation of $[P_2O_7]^{4-}$ anions to form β-$Ca_2P_2O_7$, as discussed in Schematic 3.1. Without the addition of a base like NH_4OH solution, pH can decrease to as low as 3.5-4.The successful synthesis of single phase β-TCP produced for sample 3.2 highlights the importance of pH maintenance in calcium phosphate synthesis. Without the addition of any base (sample 3.3) a reduction in the Ca: P ratio occurs to form β-$Ca_2P_2O_7$.

$$2Ca^{2+} + 2HPO_4^{2-} \longrightarrow Ca_2P_2O_7 + H_2O \quad \textbf{(3.11)}$$

SEM results highlight that the influence of CTAB templating in reaction systems is consistent throughout different aqueous precipitation reactions. When present, it continues to produce materials with spherical particles fused together to create a highly agglomerated product. As discussed, micelle formation within the reaction solution contributes to the spherical appearance. Materials prepared without CTAB showed a completely different morphology; large platelets were noted, with smaller crystallites growing on the surface. The large platelets formed could be the result of severe agglomeration of particles during the calcination process. The smaller crystallites provide evidence that nanoparticles can be

formed from this reaction, however a method of separating and breaking down the large platelets must be developed to obtain a material with a lower average particle size and higher surface area.

As shown in Figure 3.18, CDHA is completely converted into β-TCP by 750 ºC, which is slightly lower than results stated in other literature reports.[56] At temperatures below 750 °C, peaks attributable to HA are visible. This result corresponds to results attained in 3.3.1, which also suggest a minimum calcination temperature of 750 °C.

3.4.3 Microwave Processing

Synthesising calcium phosphate ceramics *via* microwave processing, instead of traditional wet chemical methods, is advantageous because there is an efficient transformation of energy and heating throughout the volume of the sample in a very short period of time.[57] Reduced reaction time also minimises thermal gradients and particle diffusion and agglomeration; [42] two synthetic challenges which are commonly associated with β-TCP synthesis. However, disadvantages of using microwave processing in reactions also exist. It can be difficult to accurately predict the exact nature of electromagnetic field interactions with materials, as changes in a materials shape, volume, chemical structure or moisture content can all affect material interactions with incident irradiation. Obtaining temperature uniformity is also a challenge, as material characteristics or boundary conditions influence heating.[58] A combination of the synthetic challenges of microwave processing and the many experimental parameters which can influence calcium phosphate synthesis suggests that a more thorough investigation into this method is required than that presented in this thesis.

For this microwave synthesis, $Ca(OH)_2$ was used instead of $Ca(NO_3)_2$ because it reduces the number of by-products produced, such as nitrate, which would need to be removed through a filtration step. It has been reported by Tas *et al.* that rinsing precipitates repeatedly removes HPO_4^{2-} ions, which are the main source of phosphate for β-TCP during the calcination stage.[59]

Neither changes in incident power of irradiation or duration affected the products formed after irradiation from $Ca(OH)_2$ and H_3PO_4: both yielded β-$Ca_2P_2O_7$ and $CaHPO_4$. Literature states that both compounds are formed when the Ca: P ratio drops below the 1.5

ratio, which is below that required for the formation of CDHA, the intermediate product of β-TCP formation.[60]

It is obvious from results that microwave processing of $Ca(OH)_2$ and H_3PO_4 consistently yielded products formed from Ca: P ratios of below 1.5. Since the starting reagents were added in the correct stoichiometric amounts, it is conclusive that either pH or the microwave irradiation is altering the composition of the precipitate material. It is plausible that, as the reaction progressed during the irradiation period within the domestic microwave oven, without any maintenance of pH being possible, the pH of the solution could decrease. Measurements taken after irradiation showed the solutions to have pH values in the range of 6-6.9. This decrease in solution pH may result from the incomplete dissociation of the acid into H_2PO^{4-} and HPO_4^{2-} to produce $CaHPO_4$ and β-$Ca_2P_2O_7$, as shown in equations 3.12 and 3.13 respectively:

$$Ca^{2+} + \quad H_2PO_4^- \longrightarrow CaHPO_4 + H^+ \qquad \textbf{(3.12)}$$

$$2Ca^{2+} + 2HPO_4^{2-} \longrightarrow Ca_2P_2O_7 + H_2O \qquad \textbf{(3.13)}$$

As stated previously for other synthetic routes to β-TCP, pH is one of the most important experimental parameters when it comes to determining which calcium phosphate compounds will be synthesised. The pH of the precipitate solution has likely changed as the two starting materials reacted together, which has decreased the Ca: P ratio to below 1.5. It has also been reported that the expected intermediate, CDHA, absorbs much energy during microwave processing through its compositional structure and vacancies within the crystal unit, so it is formed quickly, but with poor stability. It has been proven to convert to β-$Ca_2P_2O_7$ under non-equilibrium, low temperature conditions.[42] This may explain the prevalence of β-$Ca_2P_2O_7$ as the main intermediate product formed from microwave processing.

Changing the phosphate source from H_3PO_4 to $(NH_4)_2HPO_4$ resulted in the formation of CDHA as the intermediate product after irradiation, as opposed to the before seen β-$Ca_2P_2O_7$ and $CaHPO_4$. The final products after calcination at the same temperature of 800 °C are also different (Figure 3.25). Such differences in results could be attributable to differences in the dissociation, dielectric properties, or activation energies of the reagents. $(NH_4)_2HPO_4$ has the capacity to act as a buffer in the region of 7.7-8.1, which may assist in

the maintenance of an alkaline pH, allowing for incorporation of OH ligands into the crystal structure to form CDHA. Whilst no thermodynamic studies were conducted as part of this research, it would be useful in further research to study the activation energies of the transformations of the starting materials to CDHA, HA and β-TCP. Chen *et al.* studied the effects of different precursors on the activation energies of calcium phosphate ceramics.[13] Firstly, it was observed that the activation energy required to convert amorphous calcium phosphate intermediate products into HA was lower than the equivalent transformation energy of amorphous product into β-TCP (189 kJ/mol compared to 492 kJ/mol, respectively). It is conceivable, therefore, that if either HA or β-TCP were to be formed directly from a microwave syntheses, then HA would be the most likely candidate, as less overall energy is required for the transformation.

SEM results of materials pre-calcination indicate the formation of nano platelets fused together, creating an agglomerated structure with a degree of porosity. As temperature increases, the platelets fuse together, reducing the appearance of the platelets. This concurrently leads to further agglomeration and a reduction in porosity.

The reproducibilityof β-TCP *via* microwave processing is still debatable, as results indicate too much variability in the Ca: P ratio. An additional step in the synthesis which would add stability to the composition solutions pH, perhaps through ripening, should be imposed.

3.5 Conclusions

β-TCP was successfully synthesised by microwave processing and two aqueous precipitation reactions. PXD experiments highlighted the composition of resultant materials, and confirmed that altering a range of experimental parameters could influence final product formation dramatically. Information on particle size, morphology and surface area were attained from SEM and BET analysis.

An aqueous precipitation method for producing β-TCP, using $CaCl_2$ and K_2HPO_4 starting materials, was initially studied. PXD results indicated that changes in pH, reflux conditions, and calcination temperature all influenced β-TCP formation. The Ca: P ratio is strongly influenced by pH: as the pH of the reaction solution increases, the Ca: P ratio increases. Sustained reflux conditions (12 hours, 100 °C) were required to form the desired productsuccessfully, in addition to a minimum calcination temperature of 700 °C. Lower

calcination temperatures (650 °C) yielded HA as the final product, which is consistent with literature reports. [27] Sample morphology was altered through adjustments in CTAB concentration and the introduction of other similar cationic surfactants into the reaction system. Increasing or decreasing CTAB concentration, beyond a fixed range, caused increased agglomeration of materials, whether it be the result of too few surfactant molecules dispersing throughout the system, or too high a concentration causing micelle formation within the solution. Introducing surfactant molecules with an aromatic head group increased pore diameter, arguably due to the higher volume of space previously occupied by the surfactant molecule before removal by calcination.

Synthesising β-TCP via a second aqueous precipitation reaction, using $Ca(NO_3)_2$ and $(NH_4)_2HPO_4$ as starting materials, enabled further investigation into the complexity of synthesising calcium phosphate materials. Fewer side products were attained in this synthesis, compared to the previous aqueous precipitation method, due to heightened monitoring of pH throughout the precipitation stage of the reaction. This ensured greater control over the Ca: P ratio, and as a result single phase β-TCP was produced at pH 8, with cell parameters calculated as a = 10.4317 (11) Å and c = 37.3506 (6) Å, and a cell volume of 3520.01 (8) $Å^3$. Minimum calcination temperatures of 750 °C were required to convert the intermediate phase CDHA into β-TCP. Temperatures below750 °C yielded mixtures of β-TCP and CDHA (700 °C) or CDHA only (650 °C), confirming that each aqueous precipitation reaction requires a high temperature calcination step to attain β-TCP. Removing CTAB from the reaction system generated samples composed of large platelets with small crystallites growing on the surface. No porosity is observed, further proving that the presence, and subsequent removal of CTAB from the reaction system, is responsible for the previous morphological features observed.

Although microwave processing allows reactions to be carried out in shorter periods of time, adjustments in starting materials, and irradiation power and duration did not yield β-TCP. As in the previous two synthetic methods, a high temperature calcination stage had to be applied after the microwave reaction to synthesise the final desired product. This is in keeping with literature results. [42]

Despite using three different synthetic techniques, several observations were common throughout the reactions. Firstly, to synthesise β-TCP as a single phase material requires careful control over a range of experimental parameters, particularly the pH of the solution.

Secondly, it has proven impossible in this research to synthesise β-TCP without the addition of a high temperature calcination step, at a minimum of 700 °C. The morphology of materials can be controlled by the incorporation of surfactant into the reaction system, with further alterations resulting from changes in concentration and surfactant structure.

The next stage in this project builds upon the successful synthetic techniques developed in this chapter to synthesise β-TCP. It is widely reported that calcium phosphate materials which are substituted with a range of different ions can illicit increased biological responses, both *in vitro* and *in vivo*. As a result, we aim to substitute magnesium for calcium in the crystal structure β-TCP, to synthesise a range of substituted Mg-TCP materials. Biological and mechanical comparisons can latterly be carried out between the substituted and unsubstituted samples, with the aim of optimising the composite materials.

3.6 References

[1.] S. M. Best, A. E. Porter, E. S. Thian, J. Huang, *J. Eur. Ceram. Soc.*, 2008, **28**, 1319

[2.] Biomaterials Science: An Introduction to Materials in Medicine, 2nd Edition, B. D. Ratner, *Elsevier Inc*, 2004, 166

[3.] Functional Nanostructures: Processing, Characterisation and Application, Sudipta Seal, *Springer*, 2008, 18

[4.] Biomaterials for Tissue Engineering Applications: A Review of the Past and Future Trends, J. A. Burdick, R. L. Mauck, Y. Yang, Y. Kang, M. Sen, S. Park, *Springer Wein*, 2011, 188

[5.] M. Yashima, A. Sakai, T. Kamiyamana, A. Hoshikawa, *J. Solid State Chem.*, 2003, **175**, 272

[6.] B. Dickens, L. W. Schroeder, W. E. Brown, *J. Solid State Chem.*, 1974, **10**, 232

[7.] S.Kannan, J.M. Ventura, J. M.F. Ferreira, *Ceram. Int.*, 2007, **33**, 637

[8.] N. Matsumoto, K. Yoshida, K. Hashimoto, Y. Toda, *Mater. Res. Bull.*, 2009, **44**, 1889

[9.] N. Matsumoto, K. Yoshida, K. Hashimoto, Y. Toda, *J. Am. Chem. Soc.*, 2010, **93**, 3663

[10.] M. Tonković, M. Sikivić, V. Babić-Ivančić, *Colloids and Surfaces A: Physicochem. Eng. Aspects*, 2000, **170**, 107

[11.] T. Okuda, I. Yonezawa, K. Ioku, H. Minagi, H. Kurosawa, T. Keda, *Key Eng. Mater.*, 2006, **309-311**, 1063

[12.] J. S. Bow, S. C. Liou, S. Y. Chen, *Biomater.*, 2004, **25**, 3155

[13.] S. C. Liou, S. Y. Chen, *Biomater.*, 2002, **23**, 4541

[14.] A. Bigi, E. Foresti, M. Gandolfi, M. Gazzano, N. Roveri, *J. Inorg. Biochem.*, 1997, **66**, 259

[15.] M. Wang, R. Joseph, W. Bonfield, *Biomater.*, 1998, **19**, 2357

[16.] Y. Zhang, K.E. Tanner, *J. Mater. Sci: Mater. Med.*, 2008, **19**, 761

[17.] S. F. Hulbert, F. A. Young, R. S. Matheus, J. J. Klawitter, C. D. Talbert, F. H. Stelling, *J. Biomed. Mater. Res. Part A*, 1970, **4**, 433

[18.] Y. Zhang, D. Kong, X. Feng, *Ceram. Int.*, 2012, **38**, 2991

[19.] C. T. Kresge, M. E. Leonowicz,W. J. Roth, J. C. Vartuli, J. S. Beck, *Nature*, 1992, **359**, 710

[20.] S. Ng, J. Guo, J. Ma, S. C. J. Loo, *Acta Biomater.*, 2010, **6**, 3772

[21.] Y. Wang, S. Zhang, K. Wei, N. Zhao, J. Chen, X. Wang, *Mater. Lett.*, 2006, **60**, 1484

[22.] S. Ghanaati, M. Barbeck, C. Orth, I. Willershausen, B. W. Thimm, C. Hoffman, A. Rasic, A. Sader, R. E. Unger, F. Peters, C. J. Kirkpatrick, *Acta Biomater.*, 2010, **6**, 4476

[23.] S. Viale-Bouroncle, B. Bey, T. E. Reichert, G. Schmalz, C. Morczeck, *J. Mater. Sci: Mater. Med.*, 2011, **22**, 1719

[24.] Y. Liu, H. Miyoshi, M. Nakamura, *Int. J. Cancer*, 2007, **120**, 2527

[25.] Y. M. Lee, Y. J. Park, S. J. Lee, Y. Ku, S. B. Han, P. R. Klokkeuol, C. P. Chung, *J. Periodontol.*, 2000, **71**, 418

[26.] A. M. Gatti, D. Zaffe, G. P. Poli, *Biomater.*, 1990, **11**, 513

[27.] J. Yao, W. Tjandra, Y. Z. Chen, K. C. Tam, J. Ma, B.Soh, *J. Mater. Chem.*, 2003, **13**, 3053

[28.] X. Xhang, F. Jiang, T. Groth, K. S. Vecchio, *J. Mater. Sci: Mater. Med.*, 2008, **19**, 3063

[29.] B-T. lee, M-H. Youn, R. K. Paul, K-H. Lee, H-Y. Song, *Mater. Chem. Phys.*, 2007, **104**, 249

[30.] A.C. Larson and R.B. Von Dreele, *Generalized Structure Analysis System*, 1990, MS-H805, Los Alamos, NM87545

[31.] B. H. Toby, *J. App. Crystallog.*, 2001, **34**, 210

[32.] B. Dickens, L.W. Schroeder, W.E. Brown, *J. Solid State Chem.*, 1974, **10**, 232

[33.]M. S. Sader, R. Z. LeGeros, G.A. Soares, *J. Mater. Sci: Mater. Med*, 2009, **20**, 521

[34.] A. Destainville, E. Champion, D. Bernache-Assollant, E. Laborde, *Mater. Chem. Phys*., 2003, **80**, 269

[35.] D. Tardic, M. Epple, *Biomater*., 2004, **25**, 987

[36.] S. Loher, W. J. Stark, M. Maciejewski, A. Baiker, S. E. Pratsinis, D. Reicherdt, F. Maspro, F. Krumeich, D. Gunther, *Chem. Mater.*, 2005, **17**, 36

[37.] Functional Nanostructures: Processing, Characterisation and Application, Sudipta Seal,*Springer*, 2008, 20

[38.] H. Assaaoundi, Z. Fang, D. H. Ryan, I. S. Butler, J. A. Kazinski, *Can. J Chem*., 2006, **84**, 124

[39.] L. W. Schroeder, B. Dickens, W. E. Browns, *J. Solid State Chem*., 1977, **22**, 253

[40.] R. M. Wilson, J. C. Eliott, S. E. P. Dowker, *J. Solid State Chem*., 2003, 174, 132

[41.]I. R. Gibson, I. Rehman, S. M. Best, W. Bonfield, *J Mater. Sci-Mater Med.*, 2000, **12**, 799

[42.] L. Sha, Y. Liu, Q. Zhang, M. Hu, Y. Jiang, *Mater. Chem. Phys*., 2011, **129**, 1138 42

[43.] Y. X. Pang, X. Ba, *J. Eur. Cer. Soc.*, 2003, **23**, 1697

[44.] A. S. F. Alqap, I. Sopyan,*Indian J. Chem., Sect. A: Inorg., Bio-inorg., Phys., Theor. Anal. Chem.*, 2009, **48A**, 1492

[45.] A. Slosarczyk, E. Stobierska, Z. Paszkiewicz, M. Gawlicki, *J. Am. Ceram. Soc.*, 1996, **79**, 2539

[46.] A. Mortier, J. Lemaitre, P. G. Rouxhet, *Thermochim. Acta*, 1989, **143**, 265-282

[47.] J.C. Heughebaert, Thesis, Institut National Polytechnique, Toulouse, 1977.

[48.] S. V. Dorozhkin, *Mater.*, 2009, **2**, 1975

[49.] Y. Zou, Y. Li, N. Zhang, X. Liu, *Bull. Mater. Sci.*, 2011, **34**, 967

[50.] F. Cagnol, D. Grosso, G. J. de, A. A. Soler-Illia, E. L. Crepaldi, F. Babonneau, H. Amenitsch, C. Sanchez, *J. Mater. Chem.*, 2003, **13**, 61

[51.] H. Zhang, C. Shen, S. Chen, Z. Xu, F. Liu, J.Li, H. Gao, *Nanotech.*, 2005, **16**, 267

[52.] K. Onuma and A. Ito, *Chem. Mater.*, 1998, **10**, 3346

[53.] Y. Li, W. Tjandra, K. C. Tam, *Mater. Res. Bull.*, 2008, **43**, 2318

[54.] Q. Liu, L.N. Jin, W.Y. Sun,*Chem Commun.*, 2012, **48**, 8814

[55.] S-H. Kwon, Y-K. Jun, S-H. Hong, H-E. Kim, *J. Eur. Ceram. Soc.*, 2003, **23**, 1039

[56.] C. M. Lopatin, V. B. Pizziconi, T. L. Alford, *J. Mater. Med-Mater. Med.*, 2001, **12**, 767

[57.] P. Parhi, A. Ramanan, A. R. Ray, *Mater. Lett.*, 2004, **58**, 3610

[58.] http://www.amtmicrowave.com/pros_cons.html. Accessed 11/08/12

[59.] A. C. Tas, F. Karkusuz, M. Timicin, N. Akkas, *J. Mater. Sci- Mater. Med.*, 1997, **8**, 91

[60.] J-K. Han, H-Y. Song, F. Saito, B-T. Lee, *Mater. Chem. Phys*., 2006, **99**, 235

4. Investigation of magnesium doped β-Tricalcium Phosphate

4.1 Introduction

There has been a marked increase in research within substituted calcium phosphate chemistry in recent years, as the composition of bone is mimicked in heightened detail and accuracy. The inorganic component of bone does not consist solely of Ca^{2+} and PO_4^{3-} ions: it is substituted with a wide range of different anions and cations, including Zn^{2+}, Na^{+}, Mg^{2+}, F^{-} and K^{+}. Trace quantities of these elements are known to play a profound role in the numerous biological processes in bone. Of these, Mg^{2+} is considered one of the most important and abundant bivalent cations, constituting between 0.44-1.23wt%, making it the fourth most abundant cation in the human body. Enamel, dentin and bone contain, respectively, 0.44, 1.23 and 0.72 wt% of Mg.[1]

Mg offers both structural and biological advantages as an ionic substitute inbone. From a structural perspective, Mg is able to easily replace Ca in a whole range of biological calcium phosphate compounds, including HA and β-TCP. Mg has been found in various studies to favour the thermal formation of β-TCP over HA, by destabilisation of the HA structure.[2] Increased stability of the β-TCP structure is attained through the smaller ionic radii of the Mg^{2+} ions. Shorter (and stronger) bonding exists between Mg-O atoms than Ca-O atoms.[3] This, in turn, causes a decrease in unit cell parameters.

Biologically, Mg has been proven to play pivotal roles in the bioactivity of bone. The hormones which control calcium adsorption and utilisation require Mg to maintain normal levels of activity: a lack of this cation therefore can lead to low levels of Ca being absorbed in the body, which can subsequently cause decreased bone mass and a progression towards osteoporosis and other bone diseases in extreme cases.[4] Mg is also closely associated with the mineralisation of calcified tissues, directly stimulating osteoblast proliferation.[5] Banddyopadhyay *et al* confirmed that there is a higher level of Mg present in the apatitic phase at the beginning of the calcination process, and this level decreases with increasing calcification.[6] In general, a lack of Mg in the body can lead to cessation of bone growth and bone fragility, thereby decreasing the activity of osteoblasts.

Mg-substituted β-TCP, like the parent material, crystallises in the*R3c* space group, with lattice parameters dependant on the extent of substitution. The structure of the doped material was determined by Schroeder *et al* in 1974. [7] Mg-TCP is commonly prepared by aqueous precipitation, [8] or through solid state reactions. [9] Irrespective of route of preparation, the method of incorporation of Mg is always through direct displacement of the Ca^{2+} ion. Various cationic occupancy levels have been achieved, yielding a range of materials from $(Ca_{2.589}Mg_{0.411})(PO_4)_2$[7]to $(Ca_{2.89}Mg_{0.11})(PO_4)_2$. [10]

This chapter describes the synthesis and characterisation of various Mg substituted tricalcium phosphate compounds. An in-depth study of the crystallographic site occupancies of Mg by PXD and subsequent Rietveld refinements is conducted and the results of morphology and surface property studies are also presented.

4.2 Experimental

4.2.1 Synthesis of Mg-TCP

Mg-substituted β-TCP can be synthesised by a range of experimental routes, all similar to those suitable for unsubstituted β-TCP: solid state and precipitation reactions, [11] as well as emulsion and micro-emulsion techniques. [12] The samples for this research were synthesised using the aqueous precipitation method used previously for unsubstituted β-TCP, with Mg added as a separate dopant at the precipitation stage of the reaction. [13]

Synthesis of Mg-TCP was investigated alongside a visiting undergraduate summer student, Romain Campanini. Numerous reactions were performed to investigate various levels of substitution into the β-TCP structure. The level of substitution was varied by varying the levels of Ca and Mg in the starting materials.

Mg-TCP was prepared using an aqueous precipitation method previously described in section 3.2.1.1. For each reaction, all experimental parameters were kept constant and only the cation levels were varied. This was due to the reaction parameters being optimised in previous work (as discussed in section3.3.1).

Calcium chloride [$CaCl_2$, ACS reagent, Sigma-Aldrich], magnesium chloride hexahydrate [$MgNO_3.6H_2O$, ACS reagent, Sigma-Aldrich] and potassium phosphate

monobasic [$K_2HPO_4.3H_2O$, reagent grade, Sigma-Aldrich] were used as starting reagents for calcium, magnesium and phosphorus, respectively. To control morphology, the organic surfactantcetyl trimethylammonium bromide [$CH_3(CH_2)_{15}N(Br)(CH_3)_3$, BioXtra ≥ 99%, Sigma Aldrich] was included.

Calcium chloride and potassium phosphate monobasic were used in a 3:2 ratio, in order to fulfil the Ca: P ratio of 1.5 required for β-TCP formation. Mg-TCP powders of differing composition were synthesised assuming that Mg ions would substitute at the calcium sites in order to obtain a nominal composition in terms of a (Ca+Mg): P ratio of 1.5.

Calcium chloride (0.009 moles) was weighed out, crushed using a mortar and pestle, and dissolved in 20ml of deionised water. Potassium phosphate monobasic (0.006 moles) and cetyl trimethlyammonium bromide (0.006 moles) were dissolved in 30ml of deionised water. Varying masses of magnesium chloride were dissolved in 5ml of deionised water to produce a range of different concentrations. Throughout the precipitation process, pH was maintained at 8 through the addition of dilute NaOH solution. Mg-TCP powders were synthesised by adding the magnesium and calcium solutions to the phosphate solution simultaneously: upon addition a white precipitate was immediately yielded. The precipitate was refluxed at 100ºC for 24 hours, where after it was washed thrice with deionised water and dried at 100ºC for 24 hours. Conversion from the calcium deficient apatite to the β-TCP structure was achieved through calcination of the samples at 850ºC for 5 hours. The material was then ground using a mortar and pestle for PXD measurements.

4.2.2 Powder X-ray Diffraction (PXD) Experiments

All compounds synthesised were characterised by PXD, as described in section 2.3.2.2. The materials were packed into flat-plate sample holders for each PXD experiment.Data collection ranged from 5-85 ° 2θ for 1 h or 14h by using a time per step of either 649.6s or9125.6s, respectively. Shorter scans of 1 h allowed for quick phase determination, whilst PXD experiments conducted over 16 h produced high quality data for Rietveld refinements and cell indexing.

4.2.3 Rietveld refinement against PXD data

The General Structure Analysis System (GSAS) [14] was employed, using the EXPGUI[15] interface, to carry out Rietveld refinements on the substituted samples and the equivalent unsubstituted sample. The data were fit against appropriate starting modelsof Mg-TCP from ICSD.[7] Cell parameters were obtained through indexing using CELREF V3, a graphical unit cell refinement software program which compares an experimental model to a proposed model.

In the Rietveld refinement of β-TCP materials, the background was manually fitted using 14 coefficients. Subsequently the scale factor, cell parameters and zero point were refined. Further cycles added in the atomic positions, profile coefficients and peak widths. Peak profiles were modelled using function 2 within GSAS, a multi-term Simpsons rule integration of the Pseudo-Voigt function. The refinement was improved at this stage by the addition of a β-$Ca_2(P_2O_7)$ impurity phase. With a reasonable fit achieved, the atomic parameters could be cycled again and varied. To simplify the structure, initially the isotropic temperature factors of each atom type were constrained together.

Once everything was stable the Ca/Mg site fractions could be investigated. It proved impossible to freely refine the ratios between Ca and Mg across five separate sites, with site fractions ending up with Ca occupancies ≥ 1. A constrained approach was therefore attempted, with the ratios on each cation site altered and refined. After each cycle the refinement was inspected to see whether the fit had improved, and whether the temperature factors remained physically sensible.

4.2.4 Scanning electron microscopy (SEM)

To prepare a required sample for SEM analysis, the material was sieved at 70 μm to avoid large agglomerates, and a small amount deposited onto an adhesive carbon tab, which was then fixed onto an aluminium stub. Preparation of samples was carried out in a fume hood, and each tab was placed in a closed glass vial to minimise surface contamination. The samples were transferred to the vacuum column of the SEM, and sealed inside using an air tight door. The column was then evacuated.

The samples often charged under the electron beam, which made obtaining images of clarity difficult, as will be discussed further later in this chapter. On occasion, the samples were gold-coated to minimise the level of charging. However, this improved the situation only marginally.

4.2.5 Surface area measurements

BET isotherm measurements were taken to investigate the average pore size and surface area. Measurements were carried out by Andrew Monaghan, using a Micromeritics Flow Prep 060 and Gemini BET machine. Five point BET analysis was performed on each sample. Samples were degassed at 110°C overnight to remove any adsorbed moisture prior to the analysis.

4.2.6 Raman spectroscopy

Samples were prepared for Raman spectroscopy by compacting the ground powders into a small O-ring and pressed down with a glass microscope slide to ensure an even surface for measurement. A Horiba Raman LabRAM HR machine was used to analyse all samples. A Horiba-Jobin-Yvon HR confocal microscope was coupled with a Quantum Venus 532 laser.Measurements were taken at room temperature and in several different positions of each sample.

4.2.7 Summary of reactions

Table 4.1 Summary of β-TCP and Mg-TCP samples prepared *via* aqueous precipitation

Experiment	$CaCl_2$ (g)	$MgCl_2$ (g)	K_2HPO_4 (g)	CTAB (g)	mol% Mg added
1	1.000	0	0.792	1.74	0
3	0.99	0.02	0.792	1.74	0.55
5	0.90	0.18	0.792	1.74	6
6	0.80	0.37	0.792	1.74	13.6
7	0.60	0.73	0.792	1.74	36.3
8	0	1.83	0.792	1.74	100

4.3 Results

4.3.1 Synthesis of β-TCP and Mg-TCP

An unsubstituted β-TCP sample was synthesised in the laboratory for comparison to the substituted samples. Regardless of substitution levels, the product formed was a bright white fine powder. For the purpose of this chapter, four samples will be discussed in detail: those with 0, 0.55, 6 and 13.6 mol% added to the sample during synthesis (1, 3, 5, and 6, respectively).

Initial results from powder X-ray diffraction data highlights that in the case of each sample, a β-TCP type phase is formed. The characteristic pattern of these samples does not, initially, appear to differ markedly from that of an unsubstituted sample. This was expected, because the Mg^{2+} ions are directly replacing Ca^{2+} ions on the same crystallographic sites, and are therefore not changing the overall crystal structure.

However, on closer inspection of PXD data and from Rietveld refinements, variations as a result of cation dopant levels can be seen. PXD analysis of the unsubstituted sample (1) showed a strong correlation between the experimental and theoretical pattern. To establish the cell parameters, indexing of the material was performed by CELREF V3 against a model obtained from the Inorganic Crystal Structure Database (ICSD). [7] This yielded cell parameters of a = 10.453 (9) Å,c= 37.331(4) Å and a cell volume of 3532.97 (6) $Å^3$. Those were similar to values stated in literature of a = 10.435 (2)Å and c = 37.403 (5). [16]

Whilst CELREF provided cell parameters, Powdercell 2.4 was used to obtain a visual comparison between the experimental and theoretical models (Figure 4.1). [16] The characteristic peaks of β-TCP are visible at 25.9, 28.0, 31.3 and 34.3 º 2θ.

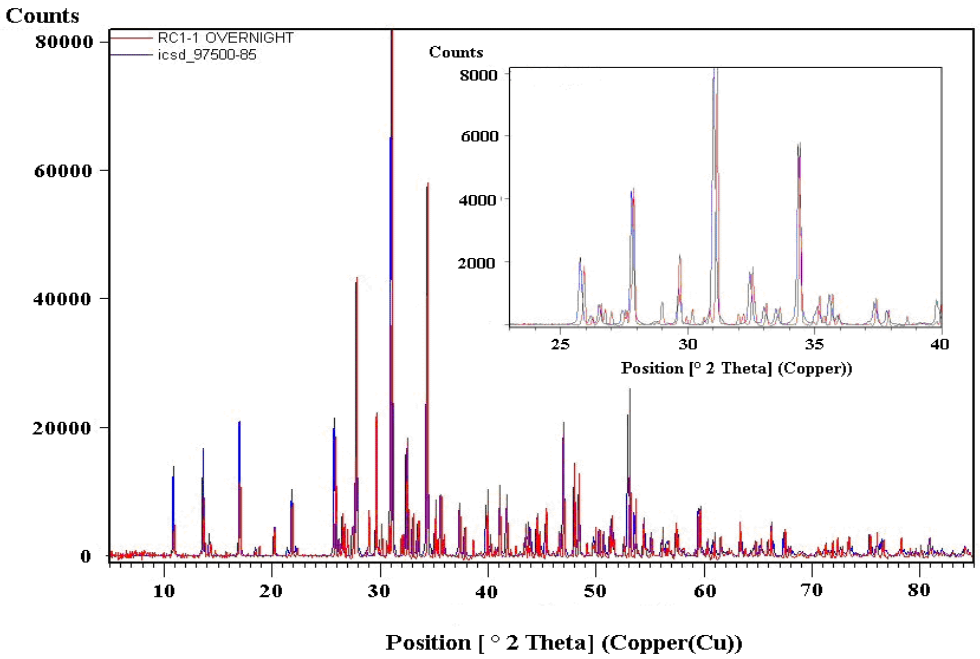

Figure 4.1 PXD analysis showing the experimental (red) and calculated (blue) patterns for laboratory synthesised β-TCP (1). Inset is a zoomed area between 25 ≤ 2θ °≤ 40.

Upon analysis of the patterns, it should be noted that several peaks remained unaccounted for in the experimental pattern: these will be discussed further when considering the Rietveld refinements in section 4.3.2. Both data sets provide similar PXD patterns: the experimental peaks (red) are recorded at the same values as the literature model (blue).

Upon the initial synthesis of doped materials, the levels of Mg substitution were kept low, in keeping with the desired dopant concentrations observed to give optimum bioactivity levels. [1] Sample 3 had a dopant level of 0.55 mol% Mg added during the synthesis. However, it was soon recognised that, at this substitution level, it would be difficult to investigate any distinct changes in the structure of the unit cell, as can be demonstrated from Figure 4.2:

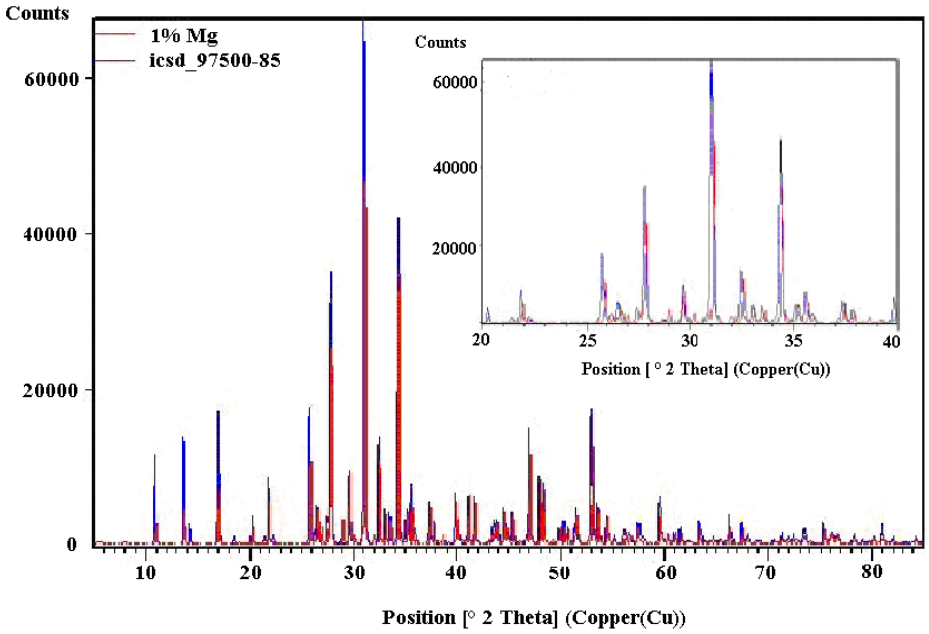

Figure 4.2 PXD analysis showing the experimental (red) and calculated (blue) patterns for laboratory synthesised Mg-TCP (3).Inset is a zoomed area between 25 ≤2θ °≤ 40.

The pattern attained from this sample essentially could be mistaken for that of the unsubstituted β-TCP. The powder pattern has changed only slightly due to the inconsequential level of Mg dopant, with (10 10), (214), (217) and (220) reflections shifted marginally to higher 2θ values. For this sample peaks occur at 25.95, 27.98, 31.16 and 34.42 ° 2θreflections, respectively. Indexing produced cell parameters of a = 10.441 (9) Å, c = 37.328 (4) Å, and a cell volume of 3524.33 (5) Å^3, which proved similar to the unsubstituted sample.

It was thereafter decided that higher levels of dopant would be introduced, in order to investigate the effect this had on the crystal structuremore fully. It is expected that, due to the smaller ionic radii of Mg, increasing levels of cationic substitution should result in a compression of the crystal lattice structure. This would be reflected in smaller cell parameters and cell volume. The level of dopant added to sample 5 was 6 mol% Mg. Cell parameters after indexing in this instance were a = 10.384 (11) Å, c = 37.246 (4) Å, with a cell volume of 3471.54 (6)Å^3. A visual comparison of the powder pattern of the sample to the experimental model showed strong correlations between peaks (Figure 4.3), but in this instance there was a notable shift to higher 2θ, with the four Miller indices of the major reflections noted at 26.02, 28.15, 31.36 and 34.74° 2θ, respectively.

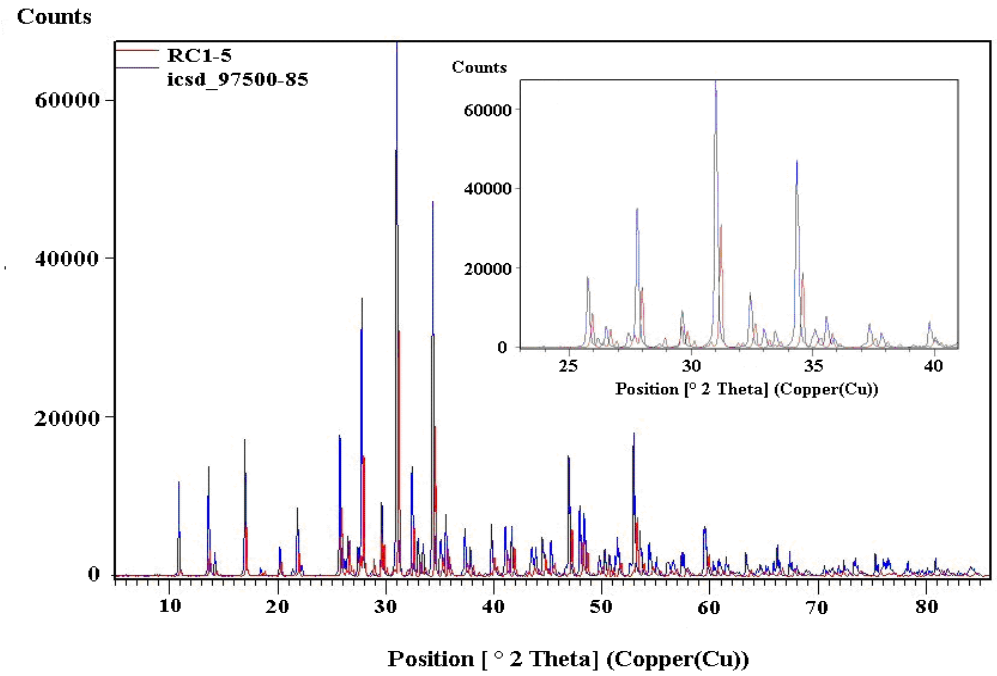

Figure 4.3 PXD analysis showing the experimental (red) and calculated (black) patterns for laboratory synthesised Mg-TCP (5).Inset is a zoomed area between 25 ≤2θ º≤ 40.

The largest peak shift was observed for sample 6, which involved 13.6 mol% substitution of Mg, indicating a clear pattern between the level of dopant used, and the position of peaks. As the % of dopant is increased, the PXD pattern shifts to a higher 2θ range (Figure 4.4).

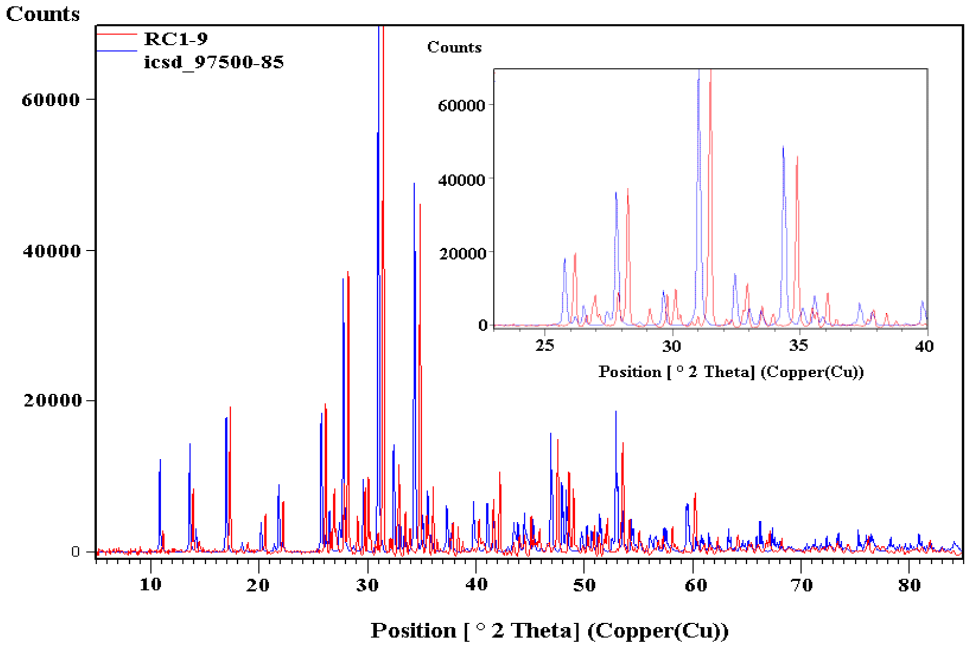

Figure 4.4 PXD analysis showing the experimental (red) and calculated (blue) patterns for laboratory synthesised Mg-TCP (6). Inset is a zoomed area between 25 ≤ 2θ º≤ 40.

The four characteristic β-TCP miller indices (10 10), (214), (217) and (220) shifted marginally to the highest 2θpeaks observed for any sample. For sample 6, with 13.6 mol% Mg added, they are observed at 26.16, 28.30, 21.44 and 34.97 ° 2θ. Figure 4.4 strongly illustrates the relationship between the level of substitution and the decrease in cell parameters, with a = 10.350 (16) Å and c = 37.165 (6) Å for compound 6. The cell volume decreases to 3448.06 (10) Å^3.

To investigate the maximum substitution levels possible in the β-TCP structure, the dopant level was increased significantly, to 36.3 mol% Mg (7). Cell parameters for this structure were a = 10.368 (30) Å and c = 37.238 (12) Å, and the cell volume was 3467.18 (18)Å^3. The cell parameters for sample 7 did not follow the general trend for the lower Mg-substituted samples. On closer inspection of the PXD pattern (Figure 4.5), key differences between the synthesised product and the calculated model for β-TCP were observed, indicating that multiple impurities were present. For this reason, the 36.3 mol% sample was treated with caution and not used in analysing the overall changes in cell parameters of the samples.

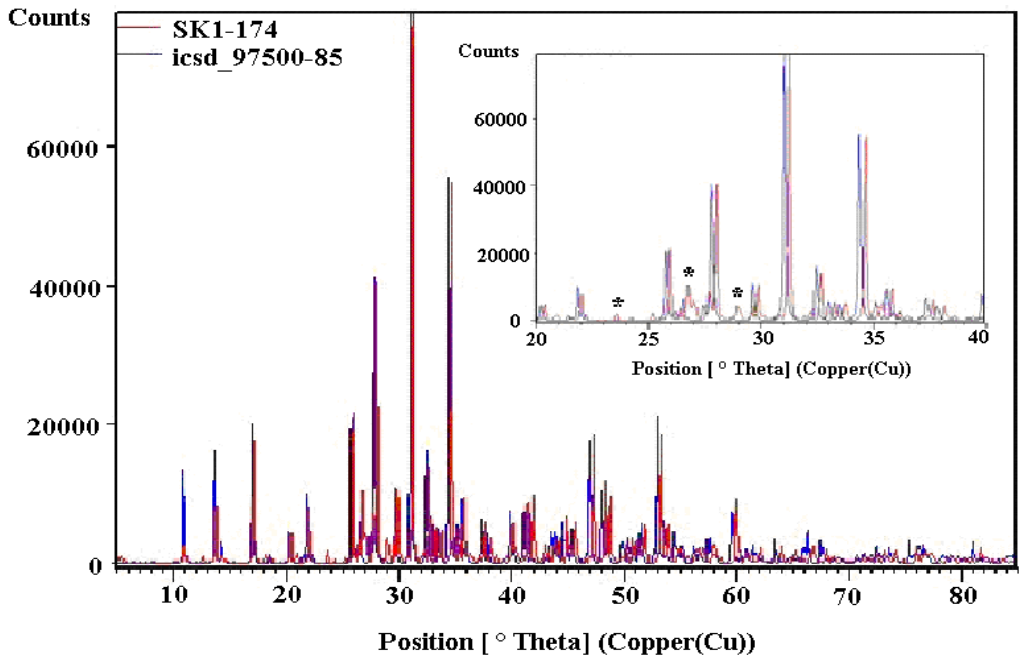

Figure 4.5 PXD analysis showing the experimental (red) and calculated (blue) patterns for laboratory synthesised Mg-TCP (7). Inset is a zoomed area between 25 ≤2θ °≤ 40.Impurity phase peaks are identified by *.

HighscorePLUS software was employed to analyse the samplefurther. The main phase matched a substituted β-TCP structure with the stoichiometry $Ca_{2.589}Mg_{0.411}(PO_4)_2$.

Additional Mg, not substituted into the main crystal structure, distributed itself between the impurity phases of magnesium pyrophosphate ($Mg_2P_2O_7$), calcium magnesium phosphate ($Ca_3Mg_3(P_2O_7)$) and magnesium phosphate ($Mg_3(PO_4)_2$).Specific 2θ peaks are highlighted in Figure 4.5 at 23.5 º, 26.7 º and 29.6 º 2θ. The first two peaks are due to the presence of α-$Ca_2P_2O_7$, with the latter attributed to β-$Ca_2P_2O_7$.In total, fiveimpurity phases were present: $Mg_2P_2O_7$, $Mg_3(PO_4)_2$, $Ca_3Mg_3(P_2O_7)$, α-$Ca_2P_2O_7$andβ-$Ca_2P_2O_7$.

With evidence of an upper limit on the levels of Mg which can substitute into the β-TCP structure, the synthesis of a material containing **only** Mg as the cation was considered; theoretically yielding the compound $Mg_3(PO_4)_2$. PXD results shown of sample 8 in Figure 4.6, and subsequent analysis using HighscorePLUS indicate that three main magnesium phosphate compounds are present within the sample: two different crystal structures of $Mg_3(PO_4)_2$,[17, 18]and $Mg_2P_2O_7$.[19] Figure 4.6 denotes a general match of diffraction data between 20-30 ° 2θ, albeit with variances in relative intensity. Impurity phases are easily seen throughout the rest of the pattern. With the overall aim of this study focused towards the investigation of Mg for Ca substitution in the β-TCP structure, further analysis through Rietveld refinement was not performed for this sample. The possibility of completely different crystal structures and synthetic techniques for the calcium and magnesium phosphate compounds was considered. This will be discussed further in section 4.4.

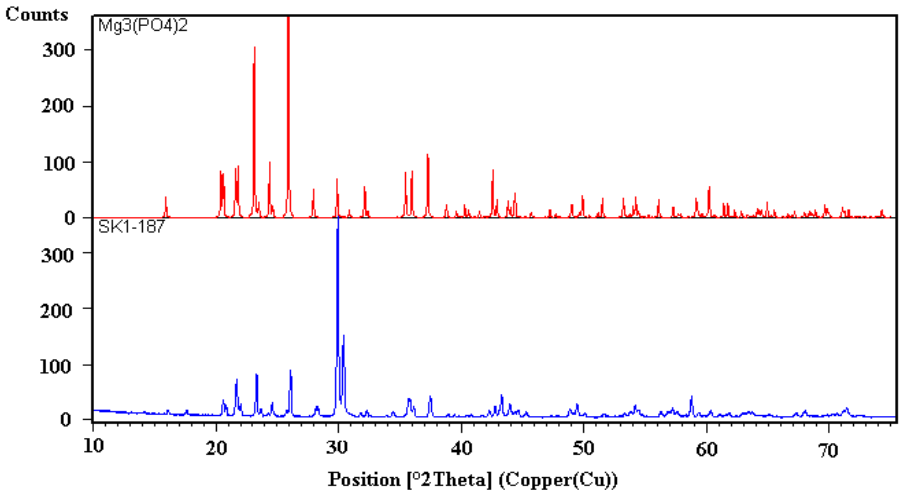

Figure 4.6 PXD analysis showing the experimental (blue) and calculated (red) patterns for laboratory synthesised $Mg_3(PO_4)_2$ (8).

Table 4.2summarises the peak shifts observed for each substituted sample: it can be clearly noted that there is a distinct shift to higher 2θ across each of the main four peaks, ranging from 0.12 up to 0.61º 2θ, as mol% Mg increases. The specific dopant levels were investigated through Rietveld refinements, to confirm that the increasing peak 2θ values

were observed as a result of increasing Mg substitution. Generally, a shift in peaks to higher 2θ values indicates a decrease in lattice parameters, due to Bragg's Law. [20]

Table 4.2Summary of peak shifts in relation to increasing substitution

Sample	mol% added	Peak values of key intensity (hkl/° 2θ)			
		10 10	214	217	220
1	0	25.97	28.03	31.32	34.36
3	0.55	25.95	27.98	31.16	34.42
5	6	26.02	28.15	31.36	34.74
6	13.6	26.16	28.30	31.44	34.97

4.3.2 Rietveld refinement against PXD data

Samples selected for Rietveld refinement analysis were scanned for 16 hours, to improve quality and reduce noise background in the data. Figure 4.7 highlights the difference between a one hour and overnight scan: it is evident that overnight data collection gives an improved signal: noise ratio. For this reason, overnight scans were collected for each sample undergoing Rietveld analysis.

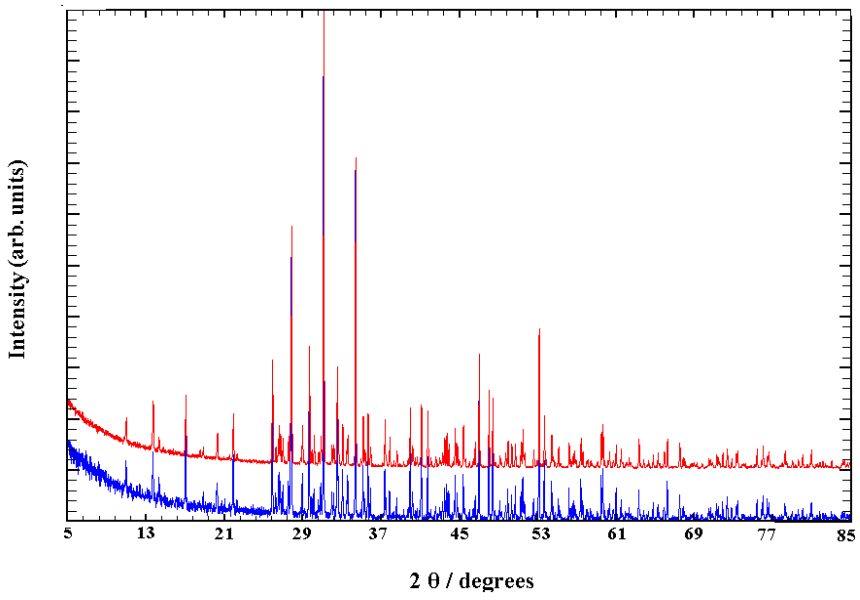

Figure 4.7 Comparison of 1 h PXD data collection vs. 12 h PXD data collection for β-TCP (red-overnight data set, blue-1 hour data set)

Rietveld refinements against PXD data were performed to investigate the % cation substitution of Mg for Ca, and to confirm the presence of a low level impurity within the sample.

β-TCP is a difficult system in which to locate substituted cations. In the crystal structure there are five cation sites, any of which may contain some or no Mg. This is further complicated by the fact that it is unknown exactly how much Mg is in the system in total. Schroeder *et al*[10] reported Mg situated on two of the five sites. This structure was the starting model for the refinement of the substituted samples, with the previously indexed cell parameters (CELREF). Initially Mg was located on one of the same cation sites as in the Schroeder*et al* paper: Ca (5). Substitution occurs preferentially on this site as a result of reduced site coordination, with a lower coordination number of 6 for Ca (5). After the occupancy had been adjusted on this site, Mg was introduced onto the other cation sites to see whether an improved fit could be achieved.

Selected Rietveld refinement data for unsubstituted β-TCP are presented in Table 4.3and the observed, calculated and difference plot is displayed in Figure 4.8. Atomic positions and temperature factors for the atoms in this sample are shown in Table 4.4. Specific bond lengths between atoms are presented in Table 4.5.

Table 4.3 Selected Rietveld refinement data from the X-ray refinement of unsubstituted β-TCP (1) at 298K

Empirical Formula	β-$Ca_3(PO_4)_2$	β-$Ca_2(P_2O_7)$
Collection temperature (K)	298	
Crystal system	Hexagonal	Tetragonal
Space Group	*R3c*	*P41*
Lattice parameters	*a* = 10.4534 (9)	*a* = 6.6945 (26)
	c = 37.3325 (4)	*c* = 24.1815 (11)
V / Å ^{3}	3532.97 (6)	1083.75(8)
Z	18	4
Unit cell formula weight, M	6634.02	2032.80
Density (g/cm^3)	3.118	3.116
Phase fraction/ wt. %	75.891 (2)	24.109 (2)
No. of varied parameters	87	
No. of observations	4786	
R_{wp}	0.0852	
R_p	0.0609	
χ^2	1.876	

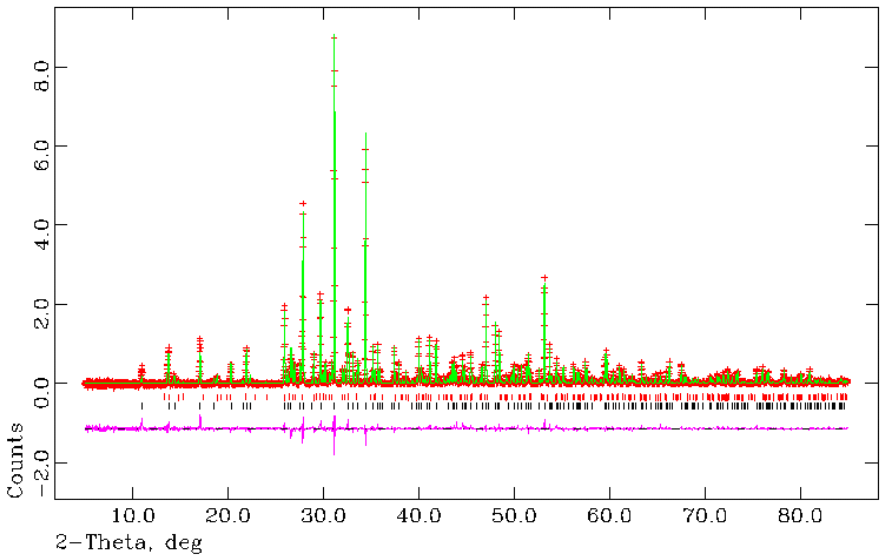

Figure 4.8 Observed (red), calculated (green) and difference (pink) OCD plot from structural refinement of sample 1 againstdata collected from 14 h X-ray diffraction scan at 298K. Black tickmarks indicate reflections from β-$Ca_3(PO_4)_2$ and red tickmarks indicate reflections from the second β-$Ca_2(P_2O_7)$ phase.

Table 4.4 Atom positions generated by PXD Rietveld refinement for the main β-$Ca_3(PO_4)_2$ phase from sample 1 at 298 K

Atom	Wyckoff Symbol	x	y	z	Occ.	U_{iso}/ *100 Å^2
Ca1	18b	0.725(3)	0.8576(7)	0.167(2)	1	64(7)
Ca2	18b	0.617(3)	0.8265(8)	-0.033(1)	1	1.62(7)
Ca3	18b	0.735(3)	0.8558(6)	0.061(2)	1	2.24(7)
Ca4	6a	0.0000	0.0000	-0.835(3)	0.5	1.05(7)
Ca5	6a	0.0000	0.0000	0.735(3)	1	1.68(7)
P1	6a	0.0000	0.0000	0.000(3)	1	2.6(1)
P2	18b	0.6919(6)	0.8690(9)	0.868(3)	1	2.2(1)
P3	18b	0.6539(9)	0.8457(9)	0.765(3)	1	2.2(1)
O1	18b	0.726(2)	-0.088(1)	-0.0890(4)	1	2.3(4)
O2	18b	0.762(2)	0.772(2)	0.8567(5)	1	3.9(6)
O3	18b	0.719(2)	0.011(2)	0.8480(5)	1	0.8(5)
O4	18b	0.508(1)	0.766(2)	0.8627(5)	1	0.5(4)
O5	18b	0.597(2)	-0.045(2)	0.7780(5)	1	1.6(5)
O6	18b	0.574(2)	0.697(2)	0.7836(5)	1	0.9(4)
O7	18b	0.094(2)	0.908(2)	0.7786(5)	1	1.7(4)
O8	18b	0.626(2)	0.826(2)	0.7289(4)	1	1.3(4)
O9	18b	0.002(2)	0.853(1)	-0.0127(6)	1	1.7(4)
O10	6a	0.0000	0.0000	0.0336(7)	1	2.6(8)

Initial refinements of the unsubstituted β-TCP data demonstrate four Ca sites with full occupancy, whilst Ca(4) has a fixed occupancy of 0.5. The presence of an impurity (β-$Ca_2(P_2O_7)$) is confirmed.

Table 4.5 Bond lengths generated by PXD Rietveld refinement for the main β-$Ca_3(PO_4)_2$ phase from sample 1 at 298 K

Bond	Length(Å)	Bond	Length(Å)	Bond	Length(Å)
P1-O9	1.64(1)	Ca1-O2	2.91(1)	Ca3-O1	2.67(3)
P1-O9	1.64(1)	Ca1-O3	2.34(2)	Ca3-O2	2.52(4)
P1-O9	1.64(1)	Ca1-O4	2.48(2)	Ca3-O3	2.33(5)
P1-O10	1.28(5)	Ca1-O4	2.45(2)	Ca3-O5	2.32(2)
		Ca1-O5	2.43(3)	Ca3-O6	2.59(6)
		Ca1-O6	2.34(3)	Ca3-O8	2.52(3)
P2-O1	1.66(2)	Ca1-O8	2.48(2)	Ca3-O8	2.52(4)
P2-O2	1.57(2)	Ca1-O9	2.33(5)	Ca3-O9	2.59(8)
P2-O3	1.60(2)				
P2-O4	1.65(3)	Ca2-O1	2.34(1)	Ca4-O1(*3)	2.55(3)
		Ca2-O2	2.43(5)	Ca4-O9(*3)	2.83(2)
P3-O5	1.60(2)	Ca2-O3	2.41(5)		
P3-O6	1.54(2)	Ca2-O5	2.81(6)		
P3-O7	1.49(1)	Ca2-O6	2.76(4)	Ca5-O4(*3)	2.15(5)
P3-O8	1.39(3)	Ca2-O7	2.39(1)	Ca5-O7(*3)	2.35(5)
		Ca2-O7	2.41(2)		
		Ca2-O9	2.39(2)		

Table 4.5 lists the cation-anion distances for the five Ca sites and PO_4 polyhedra in the crystal structure. All three polyhedra display slight distortion, in comparison to reported values. [21] Calcium-oxygen bond lengths compare well with those reported by Schroeder *et al*[10] Ca (1)-O display an average bond length of 2.47 Å, with one significantly longer distance observed between the cation and O(2) position of 2.91 Å. This is still in agreement with other results. The second Ca site (Ca (2)) has an average bond length of 2.49 Å to its surrounding anions, whilst Ca (3) similarly displays an average bond length of 2.50 Å.

The coordination numbers stated for the fourth and fifth calcium sites (Ca (4) and Ca (5)) can differ dependant on the literature report. Many quote Ca (4) as having a coordination number of 3, as opposed to the 6-fold coordination stated in Table 4.5. This is because the longer than average bonds between the Ca (4) site and O (9) sites are often discounted because they are too weak, and as a result Ca (4) is deemed a deficient site with a reduced occupancy of 0.5, instead of a full occupancy level of 1. In the case of this research, the Ca (4) -O (9) bonds have been included in the interest of full disclosure of the structure. With regards to the Ca (5) site, it should be noted that the average bond lengths to surrounding oxygen are significantly shorter than any noted for the other four cation sites.

Refinements thereafter progressed to the range of substituted materials.Selected Rietveld refinement data for 0.55 mol% Mg substituted β-TCP (sample 3) are presented in Table 4.6and the observed, calculated and difference plot is displayed in Figure 4.9. Atomic positions and temperature factors for the atoms in this sample are shown in Table 4.7. Bond lengths generated through refinement are provided in Table 4.8.

Table 4.6Selected Rietveld refinement data from the X-ray refinement of β-TCP sample 3 at 298 K

Empirical Formula	β-$Ca_3(PO_4)_2$	β-$Ca_2(P_2O_7)$
Collection temperature/ K	298	
Crystal system	Hexagonal	Tetragonal
Space Group	*R 3c*	*P41*
Lattice parameters/ Å	*a* = 10.4410 (9)	*a* = 6.69097 (6)
	c = 37.3298 (4)	*c* = 24.1654 (7)
V / Å ^{3}	3524.33 (5)	1081.86 (5)
Z	18	4
Unit cell formula weight, M_w	6513.7	2032.80
Density / g cm^{-3}	3.069	3.12
Phase Fraction/ wt. %	78.816 (4)	21.184 (4)
No. of varied parameters	71	
No. of observations	4786	
R_{wp}	0.0737	
R_p	0.0491	
χ^2	9.668	

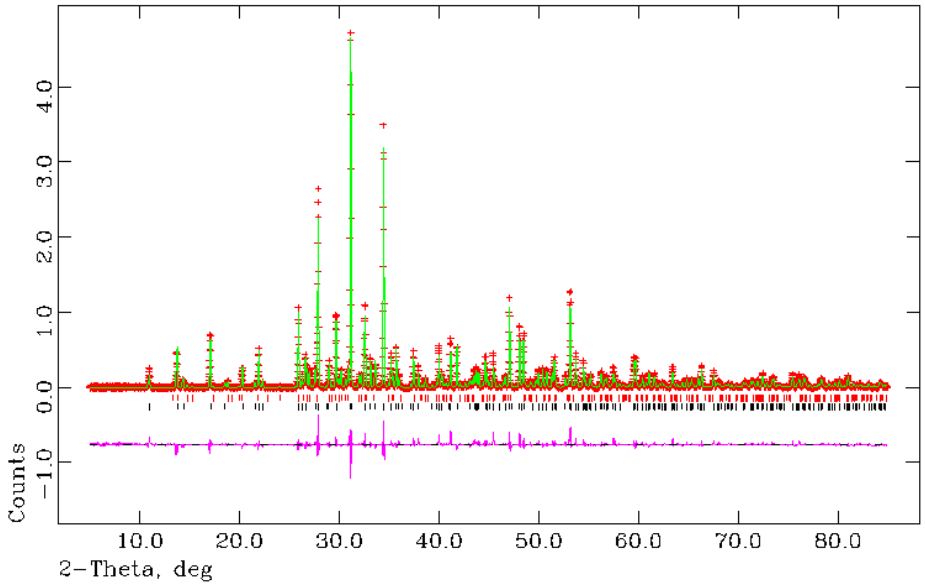

Figure 4.9 Observed (red), calculated (green) and difference (pink) OCD plot from structural refinement of sample 3 against data collected from 14 hour X-ray diffraction scan at 298K. Black tickmarks indicate reflections from β-$Ca_3(PO_4)_2$ and red tickmarks indicate reflections from the second β-$Ca_2(P_2O_7)$ phase.

Table 4.7 Atom positions generated by PXD Rietveld refinement for the main β-$Ca_3(PO_4)_2$ phase from sample 3 at 298 K. † indicates a fixed Uiso value.

Atom	Wyckoff Symbol	x	y	z	Occ.	Uiso/ *100 Å^2
Ca1	18b	0.7253(4)	0.8548(6)	0.1665(3)	1	1.98(15)
Ca2	18b	0.6191(4)	0.8203(7)	-0.0325(2)	1	1.17(15)
Ca3	18b	0.7310(4)	0.8522(5)	0.0611(3)	1	2.26(14)
Ca4	6a	0.0000	0.0000	-0.081(4)	0.5	0.28(32)
Ca5	6a	0.0000	0.0000	0.734(2)	1	1.19(18)
P1	6a	0.0000	0.0000	0.00(2)	1	2.80(10)
P2	18b	0.690(5)	0.8632(9)	0.868(2)	1	2.80(10)
P3	18b	0.654(7)	0.8467(8)	0.767(2)	1	2.61(10)
O1	18b	0.006(1)	0.865(1)	-0.017(5)	1	1.63(11)
O2	6a	0.0000	0.0000	0.043(3)	1	3.01(11)
O3	18b	0.744(2)	-0.081(2)	-0.092(2)	1	1.03(11)
O4	18b	0.776(6)	0.780(5)	0.858(2)	1	0.58(11)
O5	18b	0.734(1)	0.009(6)	0.847(3)	1	2.01(11)
O6	18b	0.526(1)	0.771(2)	0.861(4)	1	2.50†
O7	18b	0.602(6)	-0.040(6)	0.781(2)	1	2.01(11)
O8	18b	0.565(4)	0.691(4)	0.787(3)	1	1.00(11)
O9	18b	0.819(2)	-0.082(1)	0.777(8)	1	0.73(11)
O10	18b	0.631(1)	0.826(2)	0.726(7)	1	2.50†

Table 4.8 Bond lengths generated by PXD Rietveld refinement for the main β-$Ca_3(PO_4)_2$ phase from sample 3 at 298 K

Bond	Length(Å)	Bond	Length(Å)	Bond	Length(Å)
P1-O1	1.61(1)	Ca1-O1	2.51(4)	Ca3-O2	2.54(3)
P1-O1	1.61(1)	Ca1-O4	3.03(5)	Ca3-O3	2.64(4)
P1-O1	1.61(1)	Ca1-O5	2.63(5)	Ca3-O4	2.49(4)
P1-O2	1.54(2)	Ca1-O6	2.44(5)	Ca3-O5	2.39(4)
		Ca1-O6	2.47(4)	Ca3-O7	2.44(4)
		Ca1-O7	2.22(5)	Ca3-O8	2.58(4)
P2-O3	1.52(1)	Ca1-O8	2.40(5)	Ca3-O10	2.61(4)
P2-O4	1.59(1)	Ca1-O10	2.39(4)	Ca3-O10	2.54(4)
P2-O5	1.56(1)				
P2-O6	1.51(1)	Ca2-O1	2.30(4)		
		Ca2-O3	2.54(4)	Ca4-O1(*3)	2.80(8)
P3-O7	1.61(1)	Ca2-O4	2.47(5)	Ca4-O3(*3)	2.44(1)
P3-O8	1.58(1)	Ca2-O5	2.27(5)		
P3-O9	1.55(1)	Ca2-O7	2.59(6)		
P3-O10	1.53(1)	Ca2-O8	2.87(6)	Ca5-O6(*3)	2.28(5)
		Ca2-O9	2.43(5)	Ca5-O9(*3)	2.29(6)
		Ca2-O9	2.43(5)		

Based on literature reports, a small amount of Mg was introduced onto the Ca (4) and Ca (5) sites in the first instance. Goodness of fit values worsened with the inclusion of Mg on either, and both, of these sites. Mg was then introduced randomly across all five Ca sites; however a worse fit was always displayed on substitution of the cation, regardless of site position. It was therefore assumed that the low level of Mg added had been unable to substitute into the crystal structure, or that the levels were too low to be detected based on the PXD data. This is supported by similar cell parameters between this sample and unsubstituted β-TCP: a = 10.441 (9) Å and c = 37.329 (4) Å, compared to a = 10.453 (9) Å and c = 37.332 (6) Å.

Bond lengths given in Table 4.8 also indicate that no Mg has substituted into the crystal structure. It is well known that Mg preferentially substitutes onto the 6a Ca sites (Ca (4) and Ca (5)) and so one would assume shorter bond lengths between Ca^{2+} and O^{2-} ions at these specific sites, if Mg^{2+}, with its smaller ionic radius (0.69 Å vs. 0.96 Å) were substituted into the structure. However, Table 4.8 clearly shows that there is no significant shortening of bonds at either of these two sites. Comparing the bond lengths of the Ca (4) and Ca (5) sites for unsubstituted β-TCP and for sample 3 provides average bond lengths

of 2.69 Å (Ca 4) and 2.25 Å (Ca 5), in contrast to 2.62 Å (Ca 4) and 2.28 Å (Ca 4), respectively.

Subsequent increases in Mg concentration allowed the levels and sites of substitution to be investigated further. Selected data obtained from the Rietveld refinement of 6 mol% Mg substituted β-TCP (sample 5) are presented in Table 4.9 and the observed, calculated and difference plot is illustrated in Figure 4.10. Atomic positions and temperature factors for the atoms in this sample are shown in Table 4.10. Table 4.11 shows the bond lengths between atoms in the crystal structure.

Table 4.9 Selected Rietveld refinement data from the X-ray refinement of substituted β-TCP at 298 K (sample 5)

Empirical Formula	β-$Ca_3(PO_4)_2$	β-$Ca_2(P_2O_7)$
Collection temperature (K)	298	
Crystal system	Hexagonal	Tetragonal
Space Group	*R3c*	*P41*
Lattice parameters	a = 10.3847 (1)	a = 6.6919 (2)
	c = 37.2466 (4)	c = 24.1663 (6)
V / Å ^{3}	3478.61 (6)	1082.21 (4)
Z	18	4
Unit cell formula weight, M	6423.86	2032.80
Density (g/cm^3)	3.066	3.119
Phase fraction/ wt. %	81.119 (3)	18.808 (3)
No. of varied parameters	83	
No. of observations	5684	
R_{wp}	0.0566	
R_p	0.0425	
χ^2	3.905	

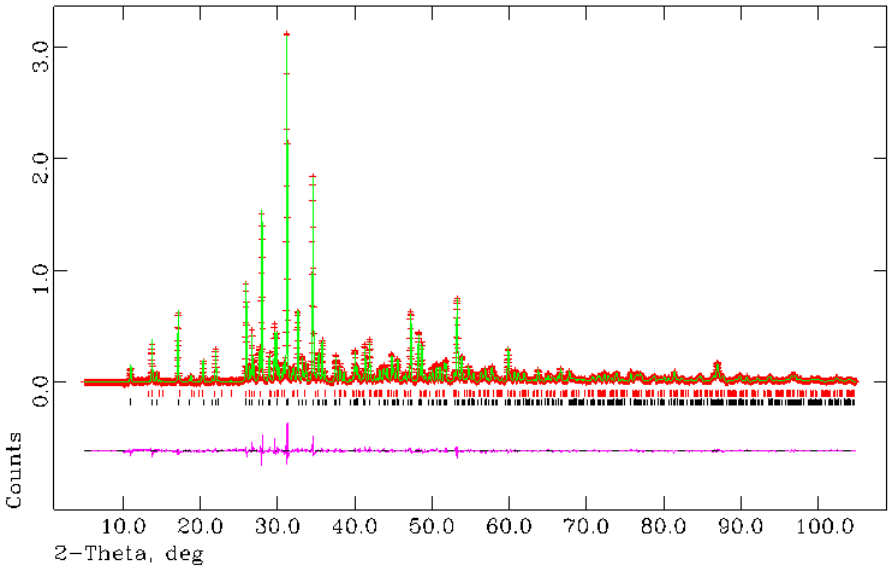

Figure 4.10 Observed (red), calculated (green) and difference (pink) OCD plot from structural refinement of sample 5 against data collected from 14 hour X-ray diffraction scan at 298K. Black tickmarks indicate reflections from β-$Ca_3(PO_4)_2$ and red tickmarks indicate reflections from the second β-$Ca_2(P_2O_7)$ phase

Table 4.10 Atom positions generated by PXD Rietveld refinement for the main β-$Ca_3(PO_4)_2$ phase from sample 5 at 298K.† indicates a fixed UISO value

Atom	Wyckoff Symbol	x	y	z	Occ.	Uiso/ *100 Å^2
Ca1	18b	-0.2748(1)	-0.1462(6)	0.1663(10)	1	1.66(1)
Ca2	18b	-0.3829(2)	-0.1799(6)	-0.3395(6)	1	1.54(1)
Ca3	18b	-0.2744(9)	-0.1496(5)	0.0604(1)	1	2.01(1)
Ca4	6a	0.000000	0.000000	-0.0815(4)	0.50	0.44(3)
Ca5	6a	0.000000	0.000000	-0.2667(7)	0.3989(4)	1.12(7)
Mg2	6a	0.000000	0.000000	-0.2667(1)	0.6011(8)	1.12(7)
P1	6a	0.000000	0.000000	-0.0015(2)	1	3.27(2)
P2	18b	-0.3144(4)	-0.1426(8)	-0.1319(6)	1	2.30(7)
P3	18b	-0.3465(7)	-0.1534(7)	-0.2345(6)	1	1.99(7)
O1	18b	0.0036(2)	-0.1347(9)	-0.0177(8)	1	4.28(3)
O2	6a	0.000000	0.000000	0.0391(4)	1	3.52(6)
O3	18b	-0.2457(9)	-0.0840(9)	-0.0935(6)	1	2.55(3)
O4	18b	-0.2278(4)	-0.2218(2)	-0.1420(1)	1	2.67(4)
O5	18b	-0.2694(4)	0.0018(1)	-0.1526(9)	1	0.15(3)
O6	18b	-0.4806(1)	-0.2342(7)	-0.1345(4)	1	1.30(2)
O7	18b	-0.3972(2)	-0.0411(3)	-0.2197(5)	1	2.5†
O8	18b	-0.4247(2)	-0.3049(2)	-0.2142(4)	1	0.38(3)
O9	18b	-0.1788(1)	-0.0769(5)	-0.2254(8)	1	1.86(3)
O10	18b	-0.3703(8)	-0.1714(2)	-0.2738(3)	1	2.5†

Table 4.11 Bond lengths generated by PXD Rietveld refinement for the main β-$Ca_3(PO_4)_2$ phase from 5 at 298 K

Bond	Length(Å)	Bond	Length(Å)	Bond	Length(Å)
P1-O1	1.54(8)	Ca1-O1	2.49(1)	Ca3-O2	2.59(6)
P1-O1	1.54(8)	Ca1-O4	2.96(2)	Ca3-O3	2.62(9)
P1-O1	1.54(8)	Ca1-O5	2.59(3)	Ca3-O4	2.44(1)
P1-O2	1.51(7)	Ca1-O6	2.49(9)	Ca3-O5	2.40(1)
		Ca1-O6	2.50(9)	Ca3-O7	2.44(2)
		Ca1-O7	2.40(3)	Ca3-O8	2.59(2)
P2-O3	1.56(1)	Ca1-O8	2.26(1)	Ca3-O10	2.57(1)
P2-O4	1.54(1)	Ca1-O10	2.39(8)	Ca3-O10	2.58(1)
P2-O5	1.54(1)				
P2-O6	1.50(9)	Ca2-O1	2.35(1)	Ca4-O1(*3)	2.77(4)
		Ca2-O3	2.25(1)	Ca4-O3(*3)	2.37(9)
P3-O7	1.60(3)	Ca2-O4	2.50(1)		
P3-O8	1.60(1)	Ca2-O5	2.34(2)		
P3-O9	1.55(1)	Ca2-O7	2.58(3)	Ca5-O6(*3)	2.11(1)
P3-O10	1.48(1)	Ca2-O8	2.76(3)	Ca5-O9(*3)	2.23(2)
		Ca2-O9	2.37(4)		
		Ca2-O9	2.47(4)		

Of the five Ca sites, Mg only substituted onto the Ca (5) position: this observation has also been presented in literature.[22] The level of occupancy in this site is 0.6011 (8), yielding an overall cationic substitution of 5.45 mol% in the structure, and a stoichiometry of $Ca_{2.84}Mg_{0.16}(PO_4)_2$. Bond lengths also confirm that Mg has substituted onto the Ca (5) site. Distances for bonds between Ca (5) ions and oxygen ions in sample 5 are shorter than those observed in the unsubstituted sample, with an average bond length of 2.16Å, compared to 2.25 Å, respectively. This strongly indicates that Mg has substituted onto this specific cation site.

Selected Rietveld data obtained from the refinement of 13.6 mol% Mg substituted β-TCP (sample 6) are presented in Table 4.12 and the observed, calculated and difference plot is illustrated in Figure 4.11. Atomic positions and temperature factors for the atoms in this sample are shown in Table 4.13. Bond lengths are detailed in Table 4.14.

Table 4.12 Selected Rietveld refinement data from the X-ray refinement of substituted β-TCP at 298 K (sample 6)

Empirical Formula	β-$Ca_3(PO_4)_2$	β-$Ca_2(P_2O_7)$
Collection temperature (K)	298	
Crystal system	Hexagonal	Tetragonal
Space Group	*R3c*	*P41*
Lattice parameters	*a* = 10.3502 (16)	*a* = 6.6945 (26)
	c = 37.1658 (6)	*c* = 24.1816 (11)
V / Å ^{3}	3448.06 (10)	1083.75 (8)
Z	18	4
Unit cell formula weight, M	6513.78	2032.80
Density (g/cm^3)	3.173	3.115
Phase fraction/ wt. %	84.104 (6)	15.896 (6)
No. of varied parameters	80	
No. of observations	4786	
R_{wp}	0.0659	
R_p	0.0451	
χ^2	4.156	

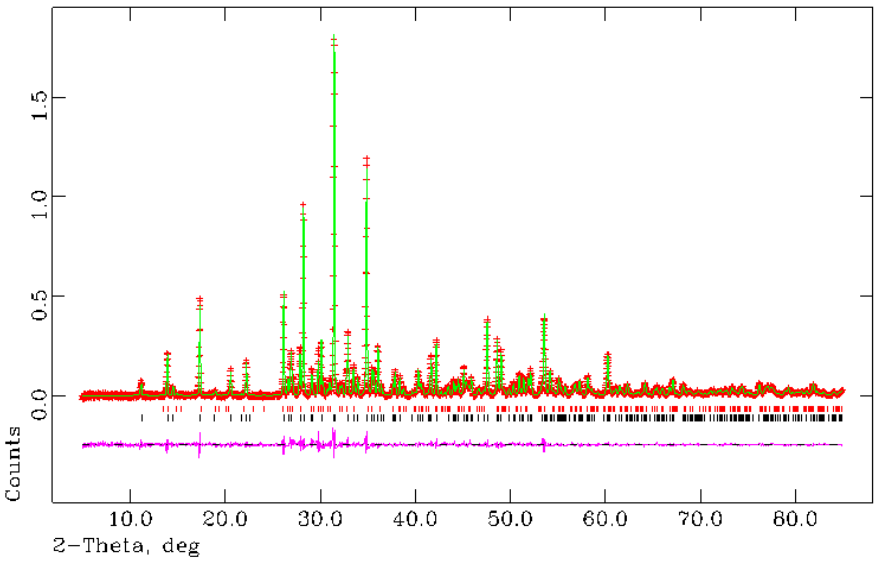

Figure 4.11 Observed (red), calculated (green) and difference (pink) OCD plot from structural refinement of sample 6 against data collected from 14 hour X-ray diffraction scan at 298K. Black tickmarks indicate reflections from β-$Ca_3(PO_4)_2$ and red tickmarks indicate reflections from the second β-$Ca_2(P_2O_7)$ phase

Table 4.13 Atom positions generated by PXD Rietveld refinement for the main β-$Ca_3(PO_4)_2$ phase from sample 6 at 298K. † indicates a fixed Uiso value

Atom	Wyckoff Symbol	x	y	z	Occ.	Uiso/ *100 Å^2
Ca1	18b	0.7273(5)	0.8549(8)	0.1694(3)	1	2.05(7)
Ca2	18b	0.6183(5)	0.8216(8)	-0.0315(3)	1	1.00(5)
Ca3	18b	0.7242(4)	0.8508(6)	0.0634(3)	1	2.28(6)
Ca4	6a	0.000000	0.000000	-0.0740(6)	0.50	3.70(5)
Ca5	6a	0.000000	0.000000	0.7369(5)	0.0749(3)	1.21(3)
Mg2	6a	0.000000	0.000000	0.7369(5)	0.9251(7)	1.21(3)
P1	6a	0.000000	0.000000	0.000000	1	2.30(1)
P2	18b	0.6859(6)	0.8582(1)	0.8727(4)	1	2.23(1)
P3	18b	0.6545(9)	0.8458(1)	0.7682(3)	1	2.50(1)
O1	18b	0.006(2)	0.8632(2)	-0.0159(5)	1	3.8(5)
O2	6a	0.000000	0.000000	0.0446(8)	1	2.4(5)
O3	18b	0.7452(3)	-0.0816(2)	-0.0917(5)	1	2.5†
O4	18b	0.7714(8)	0.7782(5)	0.8592(5)	1	2.5†
O5	18b	0.7323(2)	0.0052(7)	0.8507(4)	1	2.5†
O6	18b	0.5176(1)	0.7636(2)	0.8698(6)	1	2.5†
O7	18b	0.6075(1)	-0.0409(7)	0.7822(5)	1	2.5†
O8	18b	0.5831(1)	0.6970(5)	0.7902(5)	1	2.5†
O9	18b	0.8247(4)	-0.0770(2)	0.7746(4)	1	2.5†
O10	18b	0.6240(2)	0.8240(7)	0.7286(5)	1	2.5†

Table 4.14 Atom bond lengths generated by PXD Rietveld refinement for the main β-$Ca_3(PO_4)_2$ phase from 6 at 298 K

Bond	Length(Å)	Bond	Length(Å)	Bond	Length(Å)
P1-O1	1.56(1)	Ca1-O1	2.50(3)	Ca3-O2	2.57(8)
P1-O1	1.56(1)	Ca1-O4	2.93(2)	Ca3-O3	2.57(2)
P1-O1	1.56(1)	Ca1-O5	2.59(2)	Ca3-O4	2.46(4)
P1-O2	1.66(3)	Ca1-O6	2.51(3)	Ca3-O5	2.36(3)
		Ca1-O6	2.49(2)	Ca3-O7	2.42(1)
		Ca1-O7	2.46(7)	Ca3-O8	2.65(6)
P2-O3	1.46(4)	Ca1-O8	2.23(3)	Ca3-O10	2.54(6)
P2-O4	1.56(4)	Ca1-O10	2.39(1)	Ca3-O10	2.54(6)
P2-O5	1.58(5)				
P2-O6	1.52(3)	Ca2-O1	2.29(3)		
		Ca2-O3	2.53(4)	Ca4-O1(*3)	2.60(3)
P3-O7	1.56(8)	Ca2-O4	2.46(4)	Ca4-O3(*3)	2.43(4)
P3-O8	1.56(4)	Ca2-O5	2.35(7)		
P3-O9	1.55(3)	Ca2-O7	2.55(8)		
P3-O10	1.50(3)	Ca2-O8	2.66(3)	Ca5-O6(*3)	2.08(7)
		Ca2-O9	2.43(2)	Ca5-O9(*3)	2.11(7)
		Ca2-O9	2.48(0)		

Refinement data for 13.6 mol% substitution confirms that Mg has substituted onto one Ca site again, that of Ca (5). There is almost complete incorporation of Mg for this site, with an occupancy level of over 90%, providing an overall substitution level of 8.81% and yielding a compound with the stoichiometry $Ca_{2.7357}Mg_{0.2643}(PO_4)_2$. Bond lengths given in Table 4.14 show the greatest contraction in bonds between oxygen ions and the Ca(5) site, in comparison to all of the previous substituted samples. This is concurrent with this sample having the highest refined substitution levels thus far. In this instance significant reductions are seen between this and the unsubstituted sample: whilst the unsubstituted sample provides an average Ca (5) - O bond length of 2.25 Å, the 13.6 mol% substituted sample shows a corresponding bond length of 2.10 Å. It should be noted that there is also contraction of the average Ca (4) - O bond length (from 2.69 Å to 2.52 Å), which suggests that there could also be a degree of Mg substitution at this site also, despite refinement results reporting otherwise.

Results from refinements performed on the 36.3 mol% sample were not of a high enough quality to include, most likely due to the large number of impurities present in the sample. It appears, from the materials with refinable data that regardless of the amount of Mg present at the aqueous precipitation stage of the reaction, Mg remains selective to specific sites of substitution. Literature reports state that when excess amounts of Mg are added to the crystal system, they will fill the Ca(5) site completely before substituting into the Ca(4) position.[22] Regardless of the dopant levels, Mg does not substitute onto the Ca (1)- (3) sites, a trend in agreement with published reports.[23] The highest level of cationic doping in β-TCP was reported to be 12 mol% by Enderle *et al*, which shows substitution across both the Ca (4) and Ca (5) sites. [24]

Rietveld refinements were performed on the samples to investigate not only the level of substitution, but also to ascertain the subsequent effect this had on both lattice parameters, and cell volumes. In agreement with higher *2θ* peak values previously observed, compression of the lattice structure is again confirmed through a reduction in both the *a*- and *c*- parameters as the % of Mg increases, as shown in Table 4.15, and illustrated in Figure 4.12:

Table 4.15 Summary of *a*- and *c*- parameters in accordance with refined % Mg substitution

Sample	mol% Mg added	Refined mol% Mg substituted	*a*- parameter (Å)	*c*- parameter (Å)
1	0	0	10.453 (9)	37.331 (4)
3	0.55	0	10.441 (9)	37.329 (4)
5	6	5.45	10.384 (11)	37.246 (4)
6	13.6	8.81	10.350 (16)	37.165 (6)

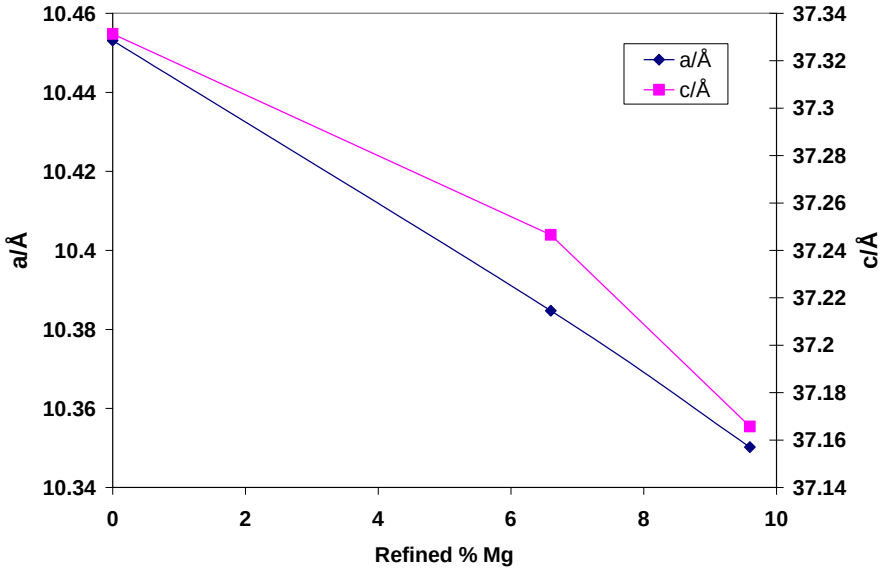

Figure 4.12 Plot of changes in *a*- and *c*- parameters as a function of refined wt% Mg substitution

As the level of dopant is increased, the cell volume decreases, again indicating that the overall crystal structure has been compressed by the introduction of the cation dopant, shown in Figure 4.13. This is similar to results presented by Stoleriu *et al*. [25]

Table 4.16 Summary of cell volume in accordance with refined wt% Mg substitution

Sample	mol% Mg added	Refined mol %Mg subst	Cell Volume(Å^3)
1	0	0	3532.97 (6)
3	1	0	3524.33 (5)
5	10	5.45	3471.54 (6)
6	20	8.81	3448.06 (10)

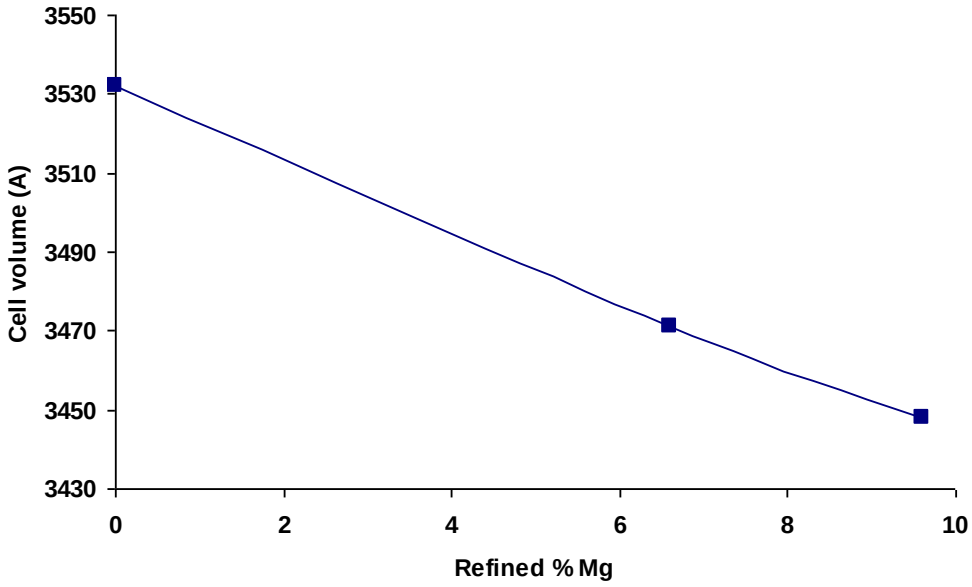

Figure 4.13 Plot of changes in cell volume as a function of refined wt% Mg substitution

4.3.3 Scanning electron microscopy (SEM)

Scanning electron microscopy was employed to investigate the particle size and morphology of the samples, and to determine whether these changed significantly upon increasing levels of Mg substitution.

Figures 4.14 a-h demonstrate that no discernable difference can be observed between the samples. All samples demonstrate the same highly porous, agglomerated morphologies now associated with the CTAB surfactant templated process discussed in section 3.4.1. There are no published reports of a cation dopant affecting the morphology of materials: therefore consistency in these results is expected. It is also worth noting that the role of the surfactant in this reaction does not disrupt the substitution of Ca for Mg; it would appear that its presence does not inhibit substitution. Mg substituted samples synthesised without CTAB showed results consistent with Figure 3.3, indicating a material consisting of large clumps in the range of 5-20 µm, with no porosity.

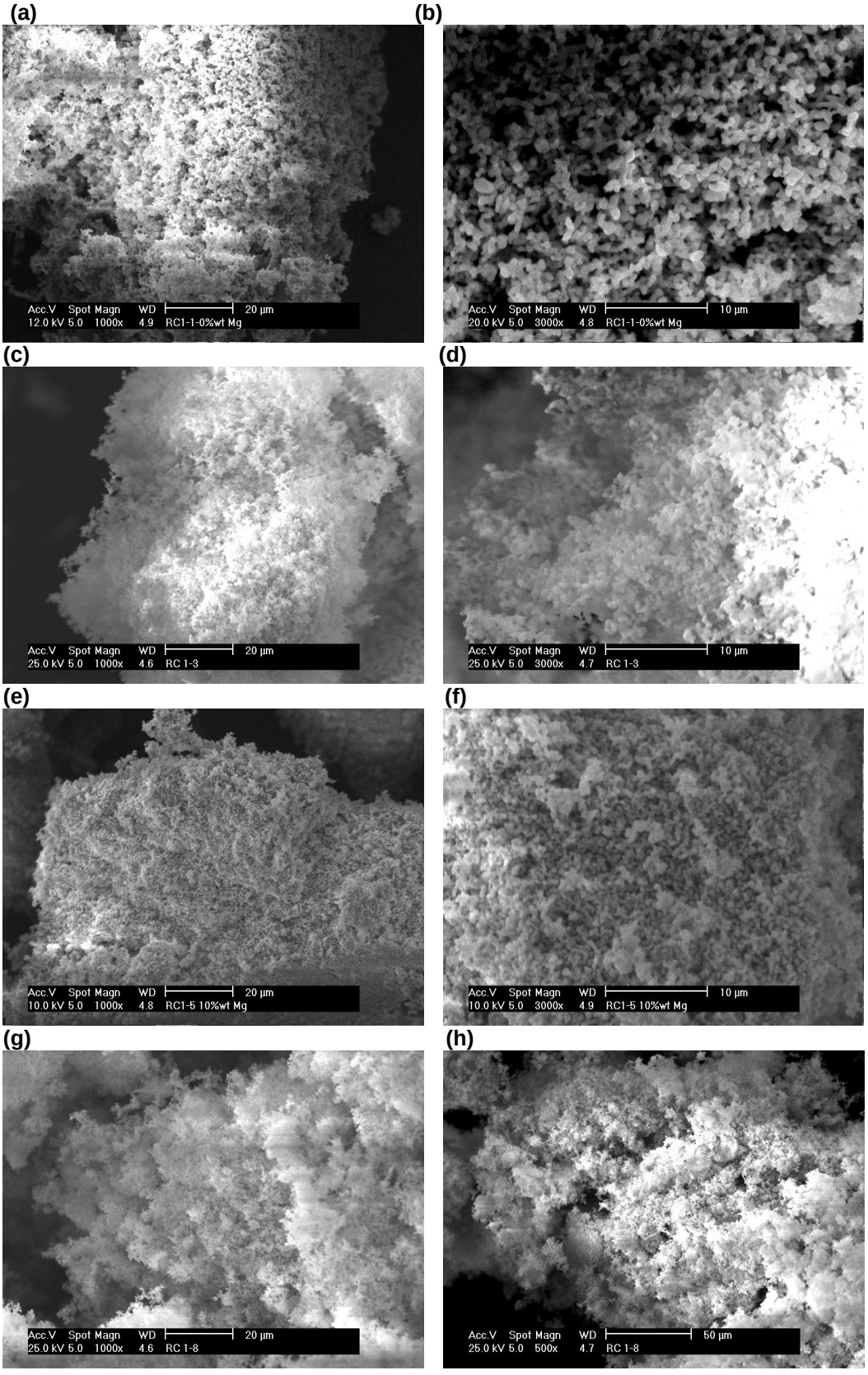

Figure 4.14 (a)-(h) SEM micrographs showing the presence of highly porous agglomerated substituted β-TCP samples at 1000x and 3000x magnification respectively for 1 (a,b), 3 (c,d), and 5 (e,f), and 1000x and 500x for 6 (g,h)

4.3.4 Surface area measurements

BET isotherm measurements investigated the potential effect of Mg-substitution on the surface area and average pore diameter of samples. Although no discernable pattern exists to suggest that Mg plays an inherent role in the pore size of the materials, there is an increase in surface area as the percentage of Mg substituted increases, as can be seen in Table 4.17.

Table 4.17 Summary of surface area and pore size as a function of Mg substitution

Sample	Refined mol% Mg added	BET specific S.A/ m^2g^{-1}	Average Pore Diameter/ Å
1	0	2.8770 (3)	63.06 (9)
3	0	1.5730 (2)	122.03 (6)
5	5.45	6.6522 (2)	31.26 (8)
6	8.81	7.0802 (5)	88.29 (5)

Although there appears to be a correlation between average surface area and Mg content, it must be noted that differing impurity levels are present within each sample, which could also influence surface area measurements. Changes in such measurements were not expected to be significant, because of direct substitution of Mg into pre-existing Ca cation sites, and a minor change overall in the crystal structure.

4.3.5 Raman Spectroscopy

Raman spectroscopy analysis was performed on samples to investigate whether the overall contraction of the unit cell would be manifestedthrough shifts of bands in the spectra, and whether bands specific to Mg-O bonding would be observed. It was also used to further verify thepresence of the β-$Ca_2(P_2O_7)$ impurity, through spectra specific to this calcium phosphate phase.

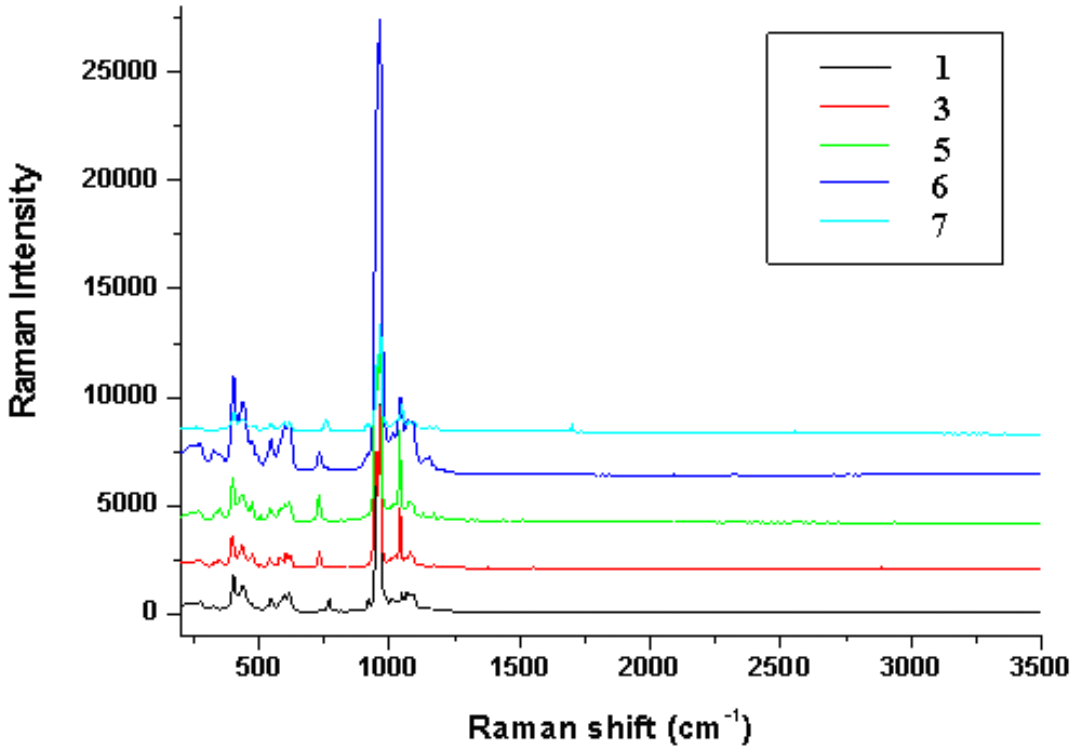

Figure 4.15 Raman spectra of β-TCP samples from 250-3500cm^{-1}, where black = 1 (unsubstituted β-TCP) red = 3 (0.55 mol% added, no Mg substitution), green = 5 (5.45% refined Mg substitution), blue = 6 (8.81% refined Mg substitution) and turquoise = 7 (36.3 mol% added, sample not refined)

High intensity peaks for β-TCP are regularly observed at 944 cm^{-1} and 967 cm^{-1} [26] as two distinct sharp peaks. These correspond to free and internal mode frequencies of the PO_4^{-3} ion, respectively. As a result of low resolution parameters used to obtain spectra, only one broad, high intensity peak is observed at 946 cm^{-1}(Figure 4.15). However, higher resolution imaging of the peak revealed two separate peaks, as originally expected for these materials.

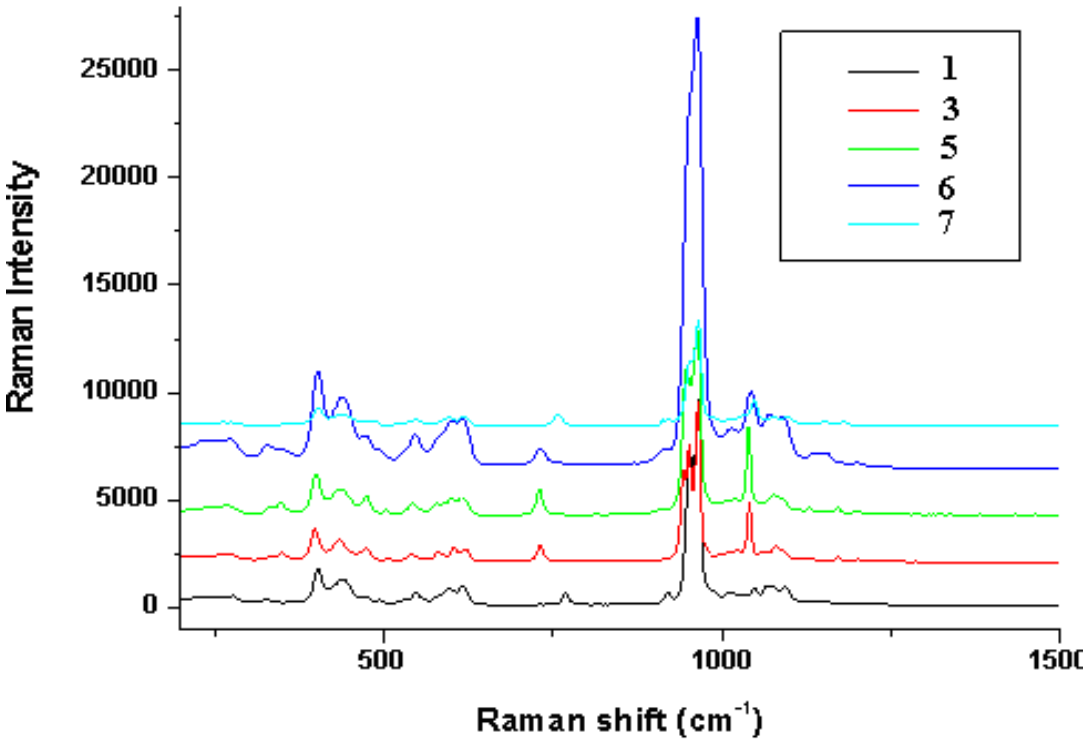

Figure 4.16 Raman spectra of β-TCP samples from 250-1500cm^{-1}, where black = 1 (unsubstituted β-TCP) red = 3 (0.55 mol% added, no Mg substitution), green = 5 (5.45 mol% refined Mg substitution), blue = 6 (8.81% refined Mg substitution) and turquoise = 7 (36.3 mol% added, sample not refined)

Within the 250-1500 cm^{-1} range, three distinct bands can be observed between 402-503 cm^{-1}, 540-614 cm^{-1}, and 1010-1100 cm^{-1}(Figure 4.16). By analogy with other calcium phosphates, the latter three bands and intense integrated peak at 964 cm^{-1} can be associated with internal vibrations of the PO_4^{3-} ions in the β-TCP system. Specifically, these can be assigned to the different free PO_4^{3-} mode frequencies *v*1 = 964 cm^{-1}, *v*2 = 450 cm^{-1}, *v*3 = 1020 cm^{-1} and *v*4 = 570 cm^{-1}. [27] Figure 4.17 also demonstrates that there is no substantial shift in the peaks for Mg substituted β-TCP, which is in agreement with other literature sources. [28]

The single peak observed in the region of 740 cm^{-1} in each sample is attributed to the β-$Ca_2P_2O_7$ impurity, already confirmed *via* Rietveld refinement. [29] Across all substituted samples, it was anticipated that additional bands might be visible due to Mg-O bonding. A weak band is seen at ~375cm^{-1} in all samples, except the unsubstituted β-TCP. This is attributed to Mg-O stretching modes, with similar bands seen for MgO_6 octahedra.[30]

4.4 Discussion

4.4.1 Structure of β-TCP

In order to discuss Mg substitution into the β-TCP structure, it is useful to revisit the analysis of the unsubstituted β-TCP crystal structure (3.3.1). To recap briefly, five cationic sites (Ca1-5) exist in the structure, in addition to PO_4 polyhedra. Ca sites (1-3) are 8 coordinate, whilst Ca (4-5) are 6 coordinate sites. All five sites have coordination numbers ranging from 6-10. The Ca (4) site is the exception; it has a reduced occupancy of 0.5 due to weak Ca-O bonding. The crystal structure of β-TCP can be considered as two types of columns: A and B. Within the A column resides P (1), Ca (4) and Ca (5), whilst column B contains Ca (1), Ca (2), Ca (3), P (2) and P(3). The B column has a dense structure compared with the A column: in the A column four Ca atoms and two P atoms exist, while the B column has six Ca atoms and four P atoms (Figure 4.17).

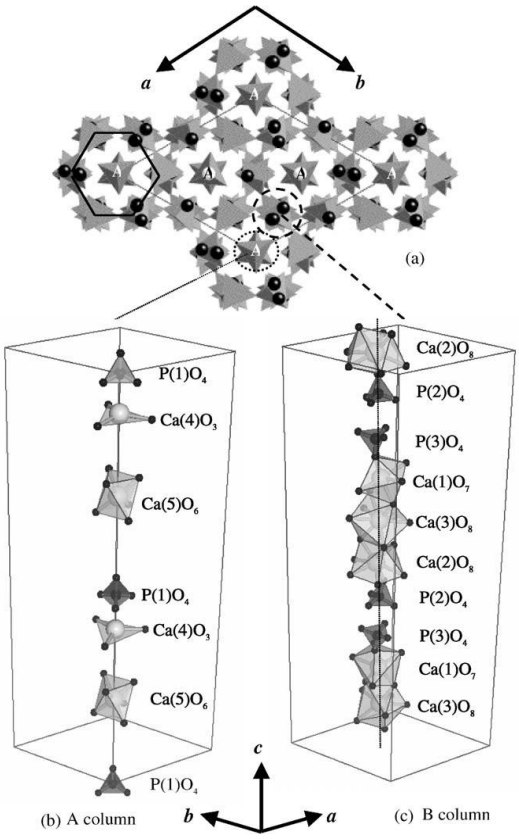

Figure 4.17 Projection of the crystal structure of β-TCP. Adapted from Yashima *et al*. [16]

As discussed in Chapter 3, phosphorus atoms are located at three crystallographic sites of P 1 (6a), P 2 (18b) and P 3 (18b). For the Mg-substituted samples, the first PO_4 groups (P (1)) consistently displayed the least distortion. In samples 1 and 6 (the unsubstituted and

8.81 % substituted samples, respectively) the largest difference between the 109º angles was 0.3º. This denotes the formation of tetrahedra with minimum distortion. In comparison, the second tetrahedron showed the most distortion in each sample: sample 5 (5.45 % substitution) angles ranged from 100.6-117.3º, indicating substantial distortion. To a lesser degree, distortion is also observed for the third PO_4 tetrahedron (P (3)). Distortion of the latter two PO_4 tetrahedra is observed because the arrangement of the four different Ca atoms around the tetrahedral group is less uniform, with the oxygen atoms each residing in different chemical environments. Reports of overall distortion in column B within the crystal structure, in which the P(2) and P(3) tetrahedra reside, also add to greater levels of distortion than for P(1), which resides in column A.[16]

It is significant that the incorporation of Mg into the β-TCP structure has resulted in a distinct contraction of both the *a*- and *c*- axis. This is attributable to the difference in ionic radii between Ca^{2+} (0.96 Å) ions and Mg^{2+} (0.69 Å) ions. [22] Incorporating Mg into the structure allows the substituted atoms to reside closer to the axis of the cluster than Ca atoms, allowing for shorter and stronger Mg-O bonds (Figure 4.18). [31]

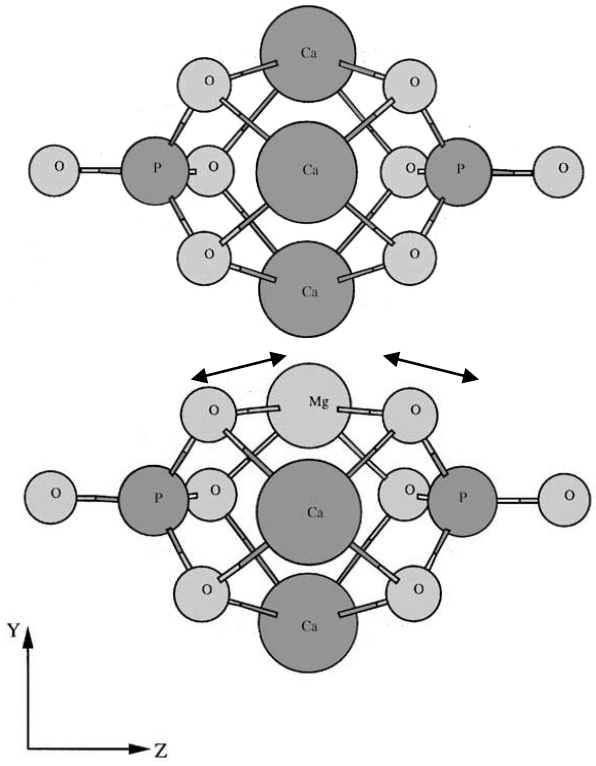

Figure 4.18 Cluster diagram of β-$Ca_3(PO_4)_2$ and β-$Mg_x(Ca_{3-x})(PO_4)_2$.Adapted from Yin *et al*. [32] Arrows highlight shorter bond distances between Mg and O, when compared to Ca-O bonding in the equivalent structure

These results are consistent with previous reports. [31] Mg stabilises the β-TCP structure because of these shorter Mg-O bonds on the Ca (4) and Ca (5) sites, compared to the equivalent Ca-O bonds at the same positions in an unsubstituted sample.

4.4.2 Rietveld refinements

Rietveld refinements performed for the substituted samples found that Mg preferentially substitutes onto one of the five Ca sites: Ca(5). In addition to refinement results, bond lengths also provide evidence for this. Random distribution of Mg over Ca (1) - Ca (3) sites was excluded by refinement results: including even a slight degree of Mg substitution on any of these three sites worsened refinement results greatly, with R factors increasing and cell parameters becoming unrealistic. Literature reports also state that substitution occurs on the Ca (4) site: [24] refinements performed with a degree of substitution on the Ca (4) site did show an improvement on the refinement with smaller R factor values than the unsubstituted model, but were marginally better with only the Ca (5) site substituted. It is therefore conceivable that some Mg could be substituted onto the Ca (4) site in all of the compounds synthesised.

The major effects, however, of the inclusion of Mg into the crystal structure are associated with Ca (5). Data for sample 5, which contained 5.45% of Mg, shows substitution of Mg on the site with occupancy of 0.65 (Table 4.12). When the % of Mg is increased to 8.81% (sample 6), Mg has again exclusively substituted on the Ca (5) site with an occupancy of 0.9251 (Table 4.15). As the shortest average bond length in the structures was observed for the Ca (5)-O bonds in the 13.6 mol% substituted sample 6 (2.08Å) it is evident that the structure can most easily accommodate the Mg^{2+} ions at the six fold Ca (5) coordination site. However, previous research states that substituted Mg^{2+} ions preferentially occupy the Ca (5) site to certain concentration limits (10 mol%) and thereafter begin to occupy the Ca (4) site.[9] It could be argued that results attained from sample 6 (8.81% substitution) could concur with literature observations, as significant contraction of the Ca (4)-O bonds is seen for the material. Further investigation into a fuller range of cationic substitutions would assist in confirming whether this is the case.

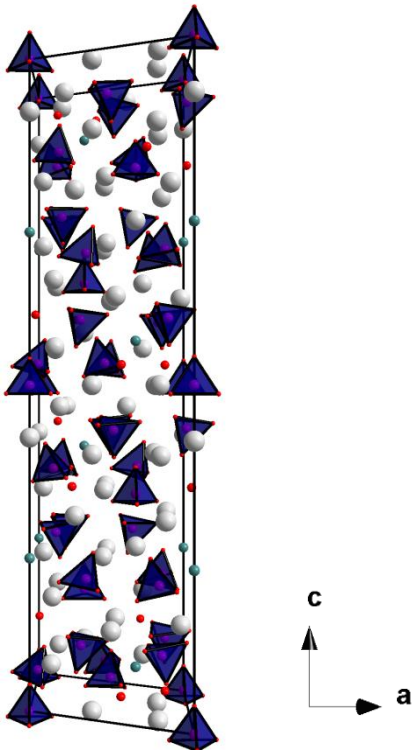

Figure 4.19 Hexagonal structure adopted by Mg-TCP(Blue- PO_4, Red- O, White- Ca, Green - Ca/Mg)

To summarise results attained from refinements, the average bond lengths of the Ca (5) site in each compound are highlighted in Table 4.18. As expected from ionic radius arguments, the unit cell contractions are a result of shorter Mg-O bonds within the structure. Significant reductions in bond length are only observed at the Ca (5) site, in keeping with preferential site substitution. Table 4.18 summarises the reduction in bond lengths at the Ca (5) site, in accordance with increasing Mg substitution:

Table 4.18 Cation site Ca (5)- O average bond lengths in different Mg-substituted samples

Sample	% refined Mg substitution	Average cation site Ca (5) – O bond length (Å)
1	0	2.28
5	5.45	2.16
6	8.81	2.10

For all samples studied, there is incomplete substitution of Mg. To account for this loss, Mg was substituted into each Ca site of the impurity phase (β-$Ca_2P_2O_7$). However, in the case of each Ca site, this resulted in an increase in Chi^2, R_w, and R_{wp} values, thereby discounting the presence of Mg in the impurity phase. This was surprising, as the presence

of $MgCa_2P_2O_7$ was highlighted as an impurity phase in sample 7. It, thereby, must be assumed that the missing Mg remained in the reaction solution, given that the starting material is very hydroscopic.

Failure to substitute all of the Mg into the β-TCP structure prompted further investigation into the $Mg_3(PO_4)_2$ structure. It appears obvious from XRD results of the 36.3 mol% sample (Figure 4.5) that a direct substitution of Ca for Mg is impossible, and the assumption was made that differences in crystal structures could prohibit a large-scale replacement of Mg for Ca. Indeed, $Mg_3(PO_4)_2$ has a completely different structure to that of β-TCP: monoclinic, space group *P*21/*n*. The structure can be described in terms of somewhat distorted MgO_6 polyhedra, and nearly regular PO_4 polyhedra (Figure 4.20). [33]

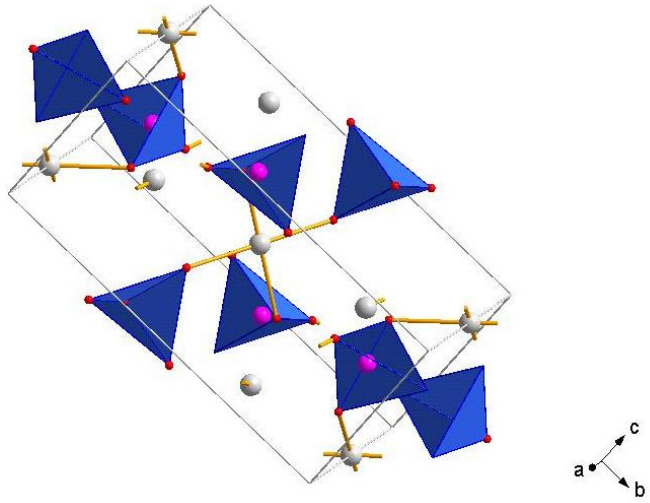

Figure 4.20 Crystal structure of $Mg_3(PO_4)_2$

Due to the large difference in Mg^{2+} and Ca^{2+} ionic radii, one would not expect a continuous transfer between hexagonal β-$Ca_3(PO_4)_2$ and monoclinic $Mg_3(PO_4)_2$ structures under the exact same experimental conditions. Poor results seen for sample 7 could in fact be a combination of the two materials, as well as various other impurities. To verify this, an experiment was conducted to check whether a complete exchange of Mg for Ca, under the specified experimental conditions, would solely produce $Mg_3(PO_4)_2$: as reported in section 4.3.1, the reaction yielded a combination of two different crystal structures of $Mg_3(PO_4)_2$(monoclinic *P*21/*a*, anorthic P-2), as well as a high level impurity phase (α-$Mg_2P_2O_7$). Distinct differences between the respective $Ca_3(PO_4)_2$ and $Mg_3(PO_4)_2$ crystal structures, as well as separate synthetic conditions, place an upper limit on cationic substitution. [24]

4.4.3 SEM, BET and Raman Spectroscopy

Both SEM and BET results show no pronounced difference due to Mg substitution.All SEM micrographs display the same porous structures, with some fusing of spheres as a result of high calcination temperatures. Specific surface area of the samples increases as the At % Mg increases (Table 4.17): unsubstituted β-TCP shows a specific surface area of 2.8770 m^2g^{-1}, whilst the 13.6 mol% compound has an increased surface area of 7.0802m^2g^{-1}. Average pore diameters show no discernable trend amongst samples. This could be attributable to the distinct lack of structural change within the crystal lattice: a more pronounced structural difference would have proven more likely to influence surface properties. In order to confirm that it is the increasing Mg substitution which is influencing the specific surface area, more measurements would need to be taken across a broader range of substituted samples.

Raman spectra of the β-TCP display no distinct changes as a result of increasing substitution levels. Spectra are dominated with the characteristic bands produced by the PO_4 tetrahedra in the β-TCP structure, with an additional peak observed for the impurity phase. A weak band at ~375cm^{-1} is visible in all substituted samples, attributed to Mg-O bonding in β-TCP.

4.5 Conclusions

Successful synthesis of Mg-substituted β-TCP using a surfactant templated precipitation process was carried out. Initial PXD experiments were performed to confirm the synthesis of the substituted calcium phosphate ceramic. Variances in diffraction patterns and cell volumes provided early indications that Mg had successfully integrated into the crystal structure, with a reduction in *a*- and *c*- parameters.

Rietveld refinements against diffraction data confirmed the presence, level and position of Mg in samples with dopant levels of 6 mol% and above. Refined dopant levels ranged from 5.45% to 8.81%. Although dopant levels of 36.3 mol% proved unsuccessful to refine due to the presence of various impurity phases, improved data through the use of synchrotron diffraction could yield more information. The discrepancies between the levels of Mg added experimentally, and the amount substituted can be attributed to the high water solubility of the Mg starting material: it is believed that the unsubstituted mass of Mg

remained present in solution. There remains the possibility that more Mg than recorded resides within the crystal structure and, as a consequence of the complex β-TCP structure, is unable to be refined.

Mg substituted into the β-TCP structure in a manner similar to that reported in literature. Of the five Ca sites, Mg preferentially substituted onto one: Ca (5). This is attributable to the lower coordination number of this cation site (and its shorter Ca-O bond lengths). High levels of substitution were observed on the Ca (5) site, with a maximum occupancy value of 0.9251 (7) recorded. As well as the aforementioned specific coordination environment of the cation site, the fact that it also contains no shared PO_4 edges adds to its success as the primary site of substitution, providing less physical barriers to substitution.Indexing cell parameters provided early indications of unit cell contractions and the significance of the Ca (5) site. Investigation of bond lengths in each sample followed thereafter, which showed shortening at the sites of substitution. As a result of the smaller ionic radius of Mg^{2+} compared to Ca^{2+}, substantial differences are seen at the Ca (5) site bond lengths.Lengths are seen to decrease from an average of 2.25Åon the unsubstituted β-TCP material (1), to 2.10 Åfor a material containing 8.81% dopant levels (6).

Raman spectroscopy spectra show no significant changes in spectra of the main β-TCP phase, with an additional band observed due to Mg bonding.Morphology and surface properties remain unaffected by increases in dopant levels, with no significant trends given in relation to porosity. The specific surface area of samples increases in accordance with increasing Mg-substitution; although more data points should be acquired to confirm.

Cell cultures and mechanical testing have also been investigated on Mg-TCP, when incorporated with PLA to form a composite, the results of which will be discussed in the following chapters.

4.6 References

[1.] I. Cacciotti, A. Bianco, M. Lombardi, L. Montanaro, *J. Eur. Ceram. Soc.*, 2009, **29**, 2969

[2.] A. Bigi, L. Compostella, A.N. Fichera, E. Forest, M.Gazzano, A. Ripamanti, N. Roveri, *J. Inorg. Biochem.*, 1988, **34**, 75

[3.]M.S. Sader, R.Z. LeGeros, G.A. Soares, *J. Mater. Sci- Mater. Med.*, 2009, **20**, 521

[4.] M. Percival, *ANSR*, 1999, **5**, 4

[5.]E.Bertoni, A. Bigi, G. Cojazzi, M. Gandolfi, S. Panzavolta, N.Roveri, *J. Inorg. Biochem.*, 1998, **72**, 29

[6.] A.Bandyopadhyay, S.Bernard, W.Xue, S.Bose, *J. Am. Chem. Soc.*, 2006, **89**, 2675

[7.]B. Dickens, L. W. Schroeder, W. E. Brown, *J. Solid State Chem.*, 1974, **10**, 232

[8.] S.Kannan, J.M. Ventura, J. M.F. Ferreira, *Ceram.Int.*, 2007, **33**, 637

[9.]N. Matsumoto, K. Yoshida, K. Hashimoto, Y. Toda, *Mater. Res. Bull.*, 2009, **44**, 1889

[10.]L. W. Schroeder, B. Dickens, W. E. Brown, *J. Solid State Chem.*, 1977, **22**, 253

[11.]A. P. Oliveira, M. Motisuke, C. V. Leal, M. M. Beppu, *Key Eng.Mater.*, 2008, **361**, 355

[12.]M. Bohner, G. H. van Lenthe, S. Grunenfelder, W. Hirsiger, R. Eviso, R. Muller, *Biomater.*, 2005, **26**, 6099

[13.] J. Yau, W. Tjandra, Y. Z. Chen, K. C. Tam, J. Ma, B. Soh, *J. Mater. Chem.*, 2003, **13**, 3053

[14.] A.C. Larson and R.B. Von Dreele, *Generalized Structure Analysis System*, 1990, MS-H805, Los Alamos, NM87545

[15.]B. H. Toby, *J. App. Crystallog.*, 2001, **34**, 210

[16.]M. Yashima, A. Sakai, T. Kamiyama, A. Hoshikawa, *J. Solid State Chem.*, 2003, **175**, 272

[17.] R. Du Fresne, *Geochim. Cosmochim. Acta*, 1964, **24**, 198

[18.] S. Jaulmes, A. Elfakir, M. Quarton, F. Brunet, C. Chopin, *J. Solid State Chem.*, 1997, **129**, 341

[19.]K. Lukaszewicz, *Bull.Pol. Acad.Sci., Chem*, 1967, **15**, 53

[20.]I. Cacciotti, A. Bianco, *Ceram.Int.*, 2011, **37**, 127

[21.]H. Assaaoundi, Z. Fang, D. H. Ryan, I. S. Butler, J. A, Kazinski, *Can. J. Chem.*, 2006, **84**, 124

[22.]S. Kannan, F. Goetz-Neunhoeffer, J. Neubauer, P. M. C. Torres, J. M. C. Ferreira, *Acta Biomater.*, 2010, **6**, 571

[23.]S. Kannan,F. Goetz-Neunhoeffer, J. Neubauer, A. H. S. Rebelo, P. Valario, J. M. F. Ferreira, *J. Biomed. Mater. Res. Part B: App. Biomat.*, 2009, **90B**, 405

[24.]R. Enderle, F. Gőtz-Neunhoeffer, M. Gőbbels, F. A. Muller, P. Greil, *Biomater.*, 2005, **26**, 3379

[25.]C. Tardei, F. Grigore, I. Pasuk, S. Stoleriu, *J. Optoelectron. Adv. Mater.*, 2006, **8**, 568

[26.]I. de Fátima Gimenez, I. O. Mazali, O. L. Alves, *J. Phys. Chem. Solids.*, 2001, **62**, 1251

[27.] P. N. de Aza, C. Santos, A. Pazo, *Chem.Mater.*, 1997, **9**, 912

[28.]A. A. Chaudhry, J. Goodall, M. Vickers, J. K. Cockcroft, I. Rehman, J. Knowles, J. A Darr, *J. Mater. Chem.*, 2008, **18**, 1

[29.] S. Boudin, A. Grandin, M. M Borel, A. Leclaire, B. Raveau, *Acta Crystallogr.*, 1993, **C49**, 2062

[30.] R. L. Frost, J. Cejka, J. Sejkara, D. Ozdin, S. Bahfenne, E. C. Keefe, *J. Raman Spect.*, 2009, **40**, 1907

[31.] S. Quillard, M. Paris, P. Deniard, R. Gildenhaar, G. Berger, L. Obadia, J. M. Bouler, *Acta Biomater.*, 2011, **7**, 1844

[32.] X. Yin, L. Calderin, M. J. Stett, M. Sayer, *Biomater.*, 2002, **23**, 4155

[33.] A.G. Nord, P. Kierkegaard, *Acta Chemica. Scand.*, 1968, **22**, 1466

5. Mechanical Testing of Composites

5.1 Introduction

Materials meant for biomedical applications are selected and tested according to their intended application.To reach this stage, a range of criteria must be met, which can include osteoconductity, mechanical functionality, degradability andbiocompatibility. In composite materials, it is common for the filler to satisfy one or more of the above requirements, whilst the matrix ensures that all other properties are satisfactorily met. Previous chapters have focused solely on the synthesis and characterisation of the filler material, β-TCP and its substituted form, Mg-TCP. In this chapter, the matrix component of the composite material, PLA, will also be considered with regards to the composite films mechanical functionality and degradability. Biocompatibility of the composite films will also be assessed to provide early indications of expected bioactivity results.

5.1.1 Mechanical properties

In order for a material to be used in a particular application, it must firstly possess certain mechanical properties to fulfil specific engineering requirements. Within polymer composite research, tensile properties are one of the key areas of mechanical focus. These refer to how a material will react to forces being applied in tension, and a tensile test measures the applied load and elongation of the specimen, usually up to failure. Upon completion, a tensile test produces a graph showing a curve of the load versus elongation. This is converted to a stress-strain curve, from which information on the tensile strength, modulus of elasticity and ductility of a sample can be obtained.[1]

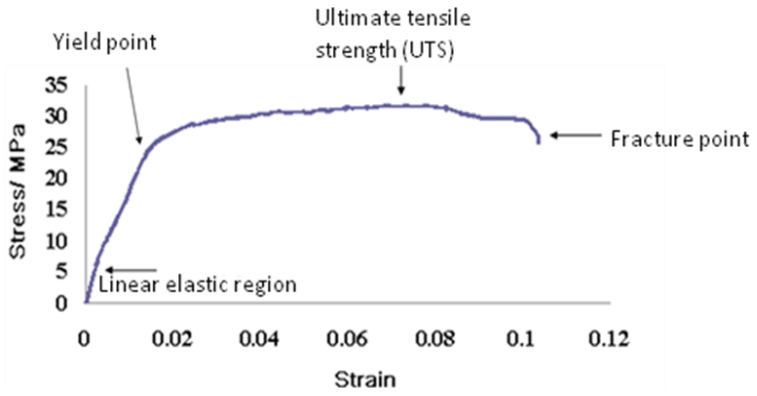

Figure 5.1 Stress-strain curve highlighting linear elastic region, yield stress, ultimate tensile strength and fracture point

5.1.1.1 Tensile strength and yield stress

The tensile strength of a material is the maximum stress it can withstand without breaking; therefore its strength is the stress required to break the material.[2]Tensile strength is often referred to as the Ultimate Tensile Strength (UTS). The other strength commonly calculated is the yield strength which occurs at the end of linear region of the stress/strain curve. The stress at any load (σ) is calculated by noting the force (F) applied, and dividing it by the area (A) of the sample, which gives

$$\sigma = F/A \quad \textbf{(5.1)}$$

This is the maximum amount of stress reached during the test, and is generally identified on a stress strain curve as the highest level where flattening of the line occurs (Figure 5.1). Engineering strain (ε) is calculated as the change in length (Δl) divided by original length (l) so that

$$\varepsilon = \Delta l/l \quad \textbf{(5.2)}$$

5.1.1.2 Hooke's Law and Young's Modulus

For most materials there will be a short region within which stress and strain increase linearly, and no permanent deformation occurs. Within this specific region, Hooke's Law is observed, which observes that when strains are small, the strain is very nearly proportional to the applied stress.[3] This behaviour is called linear elastic behaviour. The tensile strength is proportional to the nominal tensile strain, providing the relationship:

$$\sigma = E_E \quad \textbf{(5.3)}$$

where E is the Young's modulus, σ is the stress and $_E$ is the strain.

The Young's modulus (also referred to as modulus of elasticity) describes the stiffness of a sample, and indicates how much it will deform as a result of applied stress.[1] For many engineering applications, such as construction, the Young's modulus is an extremely important mechanical property. Rearrangement of equation 5.3 shows that the Young's modulus, E, can be attained by dividing the tensile stress (σ) by the tensile strain ($_E$), so long as the values used are within those obeying Hooke's Law, that in the linear region:

$$E = \sigma/_E \quad \textbf{(5.4)}$$

5.1.1.3 Ductility

Ductility considers the behaviour of a material before it reaches fracture. It measures how far a material will deform when tensile force is applied.[2] Ductile materials will deform by a large amount before breaking, whilst brittle materials will not. Ductility properties are generally obtained by measuring the elongation at failure of the samples, which is the amount by which a sample has stretched during the tensile test. A common occurrence in polymer mechanical testing is 'necking' of materials; this occurs when a certain site in the sample deforms proportionately more than the rest, as a result of strain localisation. In metals fracture generally occurs soon after necking is observed, but in some polymers a substantial neck can develop, leading to strain to failure of more than 200%.

5.1.2 Polymers

Polymers are defined as long-chain, high molecular weight compounds, consisting of up to millions of small repeating units called monomers.[4] Existing either naturally or synthetically, polymers have numerous applications in everyday life, including clothing, electrical devices and food packaging. In the last 30 years, polymers have become increasingly important in the biomedical industry, ever since biodegradable polymer sutures were first approved for clinical use in the 1960's.[5]

5.1.2.1 Natural polymers

Natural polymers have been researched extensively, and are of great interest for use in biomedical applications. Because they themselves are naturally derived, it is safe to assume a heightened chance of successful integration into another biological system, in comparison to a synthesised material. Excellent biocompatibility and biological recognition may support cell function and adhesion.[6] Synthetic materials can often provoke inflammatory and immunological responses; these are suppressed with respect to their natural counterparts. Naturally occurring enzymes have the capabilities to degrade certain polymers, which ensure their eventual breakdown by physiological mechanisms.[7] So long as the application requires only a temporary function, many observe this as a useful property. However, natural polymers also have disadvantages. As they are produced

naturally, significant variability can be seen from batch to batch.[8] They are expensive, limited in supply, and possess poor mechanical properties.

5.1.2.2 Synthetic polymers

Contrary to natural polymers, synthetic polymers can be synthesised in large quantities at relatively low cost. Physical and chemical properties can be controlled throughout the synthetic process to ensure that variability between batches is not an issue. Synthetic polymers can be synthesised through either addition or condensation polymerisation. Addition polymerisation involves joining unsaturated monomers together through the breakage of double bonds, whilst condensation polymerisation joins monomers together with the loss of a small molecule such as hydrogen chloride or water. [9] Two main classifications of synthetic polymers exist: nonbiodegradable and biodegradable. Biodegradable polymers are used in many biomedical applications as they can act in a scaffolding capacity, providing support at the site of injury or reconstruction until natural tissue reforms, after which point they should degrade and be excreted from the body. In addition to acting as scaffolds, biodegradable polymers are also used in drug delivery systems and fracture fixation devices.[10] Non degradable polymers such as polyethylene are used for permanent implants such as the articulated surface of joint replacements.

Two of the most commonly used biodegradable synthetic polymers in biomedical applications are polyglycolic acid (PGA) and polylactic acid (PLA). Both belong to the aliphatic polyester family, but differ in their starting materials and physical properties. Whilst the starting material of PGA is glycolic acid and the respective starting material for PLA is lactic acid, the two polymers are both formed by the ring opening polymerisation of the acidic dimers. PGA has a melting point between 224 and 228 °C, whilst PLA melts at a slightly lower temperature of 200 °C.[11]

PLA is emerging as one of the most promising biodegradable polymers, as it is easily processed and modified to fulfil specific biological and physical requirements. Current applications of PLA include fracture fixation devices and drug delivery systems.[12,13] As PLA was the chosen polymer for use in the composite materials, it will be discussed in more detail in the following section.

5.1.3 PLA

PLA is a thermoplastic, high modulus, high strength polymer.[14] It is synthesised through the ring-opening polymerisation of a cyclic dimer of lactic acid.[15] Lactic acid is therefore the staring material for PLA formation, and the simple hydroxyl acid is a chiral molecule with two enantiomeric forms, D- and L-lactic acid (Figure 5.2).

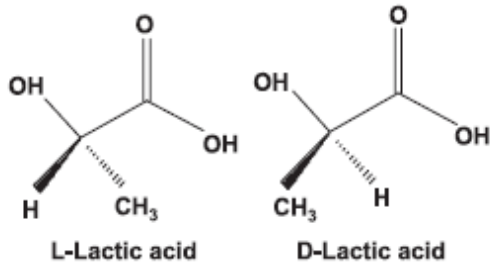

Figure 5.2 D and L lactic acid[16]

Figure 5.3 depicts two synthetic routes employed to synthesise PLA from lactic acid. The first begins when lactic acid undergoes condensation polymerisation, through the loss of water, to form the low molecular weight prepolymer of PLA. Depolymerisation into the cyclic molecule lactide occurs, which is then converted to high molecular weight PLA *via* ring opening polymerisation.The second route is a direct conversion of lactic acid into PLA *via* azeotropic dehydrative condensation, wherein distillation removes water from the system.

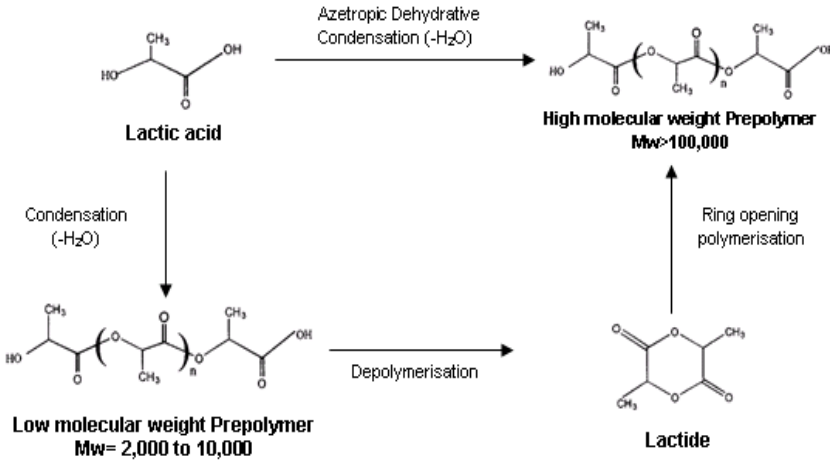

Figure 5.3 Schematic of routes for PLA synthesis[16]

Both routes produce PLA with the general structure shown in Figure 5.4:

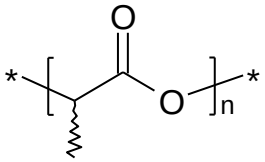

Figure 5.4 Monomer unit of PLA[16]

One of the main advantages of using PLA in any application is that its stereochemistry can be tailored to suit its function, because lactic acid is a chiral molecule. Research has shown that PLA containing only the L-lactic acid monomer gives a highly crystalline polymer, whilst a higher D-lactic acid content favours the production of a more amorphous material.[17, 18] Adjusting the ratios of the enantiomers also allows the physical and mechanical properties to be adjusted, as well as the degradation rates.[19, 20]

The degradation of PLA in the body is discussed in chapter 1 (1.12.1). To reiterate, PLA degrades to lactic acid, within physiological systems, through hydrolytic cleavage of the ester bonds in the polymer. Lactic acid is then converted into carbon dioxide and water, which can be easily eliminated out of the body. The fact that the degradation of PLA produces products which occur naturally in the body is one of the reasons PLA is preferred for use in scaffolding capacities: it is safe to assume that the patient will be able to excrete the breakdown products without any difficulty. The rate of degradation is controlled by the ratio of D- to L- enantiomers: the degradation rate of the polymer is proportional to the D-content.[14] Those polymers with higher crystallinity (more L-lactic acid) possess polymer chains which are more highly ordered and closely packed, and thus degrade slower than polymers with a more random orientation of the polymer chains (more D-lactic acid). In addition to enantiomer ratio, the degradation rate is also influenced by the polymer molecular weight. High molecular weight polymers degrade slower than the corresponding low molecular weight materials.[21]

5.1.3.1 Clinical applications of PLA

The processability of PLA, and the ease with which its stereochemistry and physical properties can be manipulated, has contributed to its success in many chemical applications. Current major applications of the polymer include sutures and internal fixation devices.Its biodegradability removes the need for secondary removal surgery, and due to its lower Young's modulus, stress shielding is avoided.

Sutures are required to hold body tissues in place after an injury or surgery. The suture must degrade once natural healing has occurred. Although PLA has been approved for use as a suture by the Federal Drug Administration (FDA, USA), [22]it exhibits slow degradation, which can limit its use. To counteract this, the polymer is mixed with other biodegradable polymers which degrade faster to create a copolymer with better degradation properties. Marketed as Vicryl by Ethicon, a copolymer unit with a mole ratio of 90:10 of glycolic acid to lactic acid has been commercialised.[16]

PLA can be used in a range of internal fixing devices, as its degradability can be controlled, relative to the rate of regeneration at the site of the body. Clinical rates of degradation can range from 10 months to 4 years.[23] In 1971 Kulkarni *et al* studied the degradation behaviour of PLA pins in the treatment of mandibular fractures in dogs. The fracture site showed no evidence of PLA pins after 8 months, indicating that they had completely degraded. In comparison to the stainless steel controls, the rate of healing at the fracture site using PLA pins was similar.[24]

It should be noted that PLA does have disadvantages which limits is use in clinical applications: it is mechanically weak and bioinert, problems which are counteracted by combining it with a filler material such as a bioceramic, which produces a polymer composite with stronger mechanical properties and bioactivity. As with any synthetic biomaterial, the potential problems of toxicity and infection remain.

5.1.4 Bioactivity of Composites

Once composite materials have been synthesised and their mechanical properties assessed, bioactivity must then be considered. (For a full discussion on composites, please refer to section 1.14.) It is common for several types of ceramics, including HA, β-TCP, and Bioglass, to encourage living bone to bond directly to them.[25] The bone-bonding ability of a sample can be evaluated using Simulated Body Fluid (SBF). SBF contains ion concentrations nearly equal to those of human blood plasma, and so mimics the human physiological environment without any biological activity. The introduction of SBF into biomaterials science reduced the use of animals in research, and offers a straightforward method for initial evaluation of *in vivo* bioactivity levels in materials.

It was proposed by Kokubo *et al* that 'the essential requirement for an artificial material to bond to living bone is the formation of bonelike apatite on its surface when implanted in the living body, and that this *in vivo* apatite formation can be reproduced in SBF'.[26] This means that the bone-bonding ability of a material can be predicted by its reaction in SBF, and that the formation of an apatite layer on the surface of the sample is a strong indication that *in vivo* bone bioactivity is likely.

Strong correlations exist between materials which give positive results under SBF and which subsequently go on to bond directly to living bone in human trials. An apatite layer was observed on the surface of sintered HA in SBF [27] and the same sample later successfully formed bonds from bone to the material through an apatite layer *in vivo*.[28] Similarly, apatite/β-TCP biphasic ceramics also formed an apatite layerand bonds to living bone in vivo; prior to this, successful apatite formation was witnessed in SBF solution.[29]

5.2 Experimental

5.2.1 Materials

5.2.1.1 Polylactic acid (PLA)

Polylactic acid was obtained from PURAC Biochem, The Netherlands. With an L: D ratio of 70/30 and an average molecular weight of between 500,000 and 600,000 g, the polymer was supplied in granular form.

5.2.1.2 β-Tricalcium Phosphate (β-TCP) and magnesium substituted β-Tricalcium Phosphate (MgTCP)

Both calcium phosphate materials were synthesised using an aqueous precipitation method described in sections 2.1.1 and 4.3.1. Samples were used without further purification.

5.2.1.3 Casein nanoclusters

Casein nanoclusters were developed and synthesised by Dr Carl Holt, at the Hannah Research Institute, Ayr, and used in composite films as part of an industrial collaboration.

Confidentiality agreements restrict detailed description of the synthesis method, however it can be confirmed that the protein component of the material is extracted from the caseinoglycomacropeptide product Lacprodan®, available commercially from Arla Foods.

5.2.2 Methods

5.2.2.1 PLA and PLA-Ca P composite production

A solvent casting method was used to produce all films.For the non-filled PLA films, 50mL of acetone was poured into conical flasks and 1g of PLA was added whilst stirring. The solution was then stirred, at room temperature, for 48 hours. After this time the solution was spread in 120mm glass petri dishes which were almost completely covered, to allow slow evaporation of the solvent. After evaporation, the films were removed from the dishes and annealed. Annealing was carried out by pressing the films between the bases of two glass petri dishes and placing the dishes in an oven at 70ºC for 1 hour. The films were then allowed to cool gradually overnight. The heat treatment was done to relax any stresses produced in the films during the casting process and to prevent curling up of the films during later experiments.

For PLA-Ca P film fabrication, as before, 50mL of acetone was poured into conical flasks and 1g of PLA was added whilst stirring. The solution was then stirred, at room temperature, for 5 hours to dissolve the polymer. β-TCP, MgTCP, or casein were added to the dissolved PLA after 5 hours, in the required massesto give 40 or 60 weight% (wt%) after the evaporation of acetone. PLA-CaP solutions were then stirred for a further 48 hours to ensure thorough mixing of the composite materials (Figure 5.5).After this stage, treatment of the composite films was identical to the PLA films; slow evaporation of solvent from 120 mm petri dishes, followed by the annealing process. All samples were then surface treated through plasma etching for five seconds, details of which will be discussed in Chapter 6.

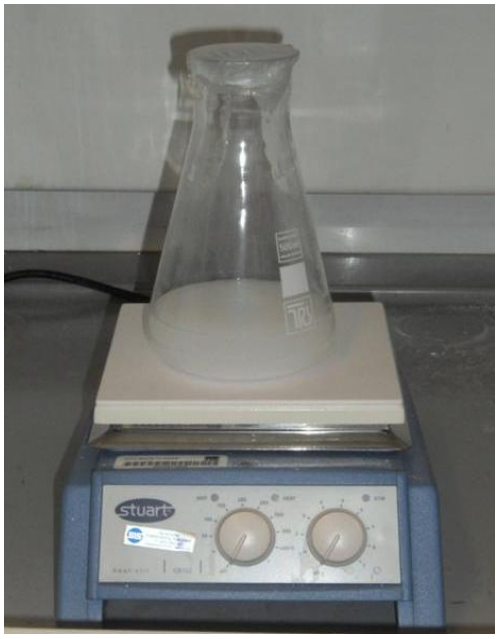

Figure 5.5 PLA/Ca P mixture during composite film fabrication

5.2.2.2 Scanning electron microscopy (SEM)

The dispersion of filler material throughout the polymer matrix was investigated through SEM. Measurements were carried out by Dr Peter Chung within the School of Geology and Earth Sciences using an Inspect F microscope (EFI Company, The Netherlands). Samples were gold coated before analysis to reduce charging, and a 5 keV electrical field was used to analyse the PLA and PLA/Ca P films. This relatively low voltage was to reduce damage to the PLA, which can occur with higher electrical yields.

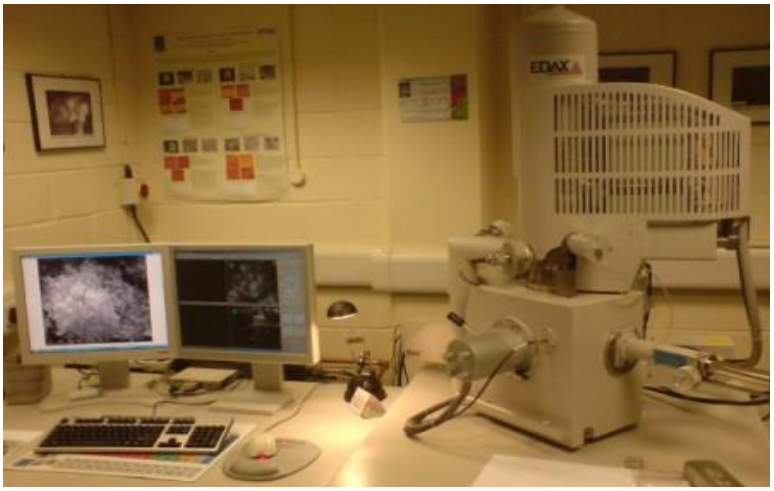

Figure 5.6 Inspect F scanning electron microscope

5.2.2.3 Raman Spectroscopy

Raman spectroscopy was used to characterise the films. A Horibo Raman LabRAM HR machine was used to analyse all samples. A Horibo-Jobin-Yvon HR confocal microscope was coupled with a Quantum Venus 532 laser. The laser was set at 150mW excited with 532nm light. A 600 gr/mm grating, hole aperture of 50µm, and a Synapse CCD detector were used to collect spectra. Data collection and analysis was through Horiba LabsSpec software, with spectra thereafter manipulated using Origin. Spectra were collected between 500-4000 cm^{-1}.

5.2.2.4 Degradation of PLA and PLA-Ca P films

Degradation studies were carried out to assess the average rate of degradation of each film *in vitro* and to assess whether different filler materials and filler volumes affected degradation rates. Analysis was conducted by incubating samples of each composite film in deionised water at 37 ºC, for different time periods. Fresh deionised water was replaced every two weeks.

For each sample and time point, five dumbbell shaped samples were cut out and sterilized in 70% ethanol for 5 minutes. They were then dried at 50 ºC. Samples were weighed before incubation to provide a reference initial mass (W_O), before immersion in 20 ml of deionised water. Time points of 1, 2, 4 and 8 weeks were tested. Each sample was immersed singly, in small glass bottles. Once the time point was finished, each sample was wiped gently with a tissue to remove excess water; this was recorded as the wet weight (W_W). Dry weight (W_D) was obtained after drying samples at 37 ºC for 24 hours. The wet weight gain (WG) could thereafter be calculated as the difference between W_O and W_W, whilst the weight loss (WL) was attained through the difference between W_O and W_D, as shown in equations 4 and 5:

$$WG\ (\%) = (W_W - W_O)\ 100/W_O \quad \textbf{(5.2)}$$

$$WL\ (\%) = (W_O - W_D)\ 100/W_O \quad \textbf{(5.3)}$$

After each time point, mechanical testing was carried out to investigate the effect of degradation on the tensile properties of the composite films.

5.2.2.5 Tensile testing of PLA and PLA Ca P films

The thickness of each sample was measured using a Keyence laser displacement machine, modelLC-2400A. Tensile tests were performed on all films using Zvick/Roell Z2.0 equipment and a 2 kN load cell, with rubber faced film grips used to hold the film samples. Data was recorded using Zwich/Roell Test Xpert II software. Tests were carried out by Mr John Davidson, and the deformation was applied at a rate of 1 $mm.min^{-1}$. Five samples were tested for each sample and time point, and averages were calculated. Figures 5.7 (a) and 5.7 (b) show the experimental setup for tensile testing.

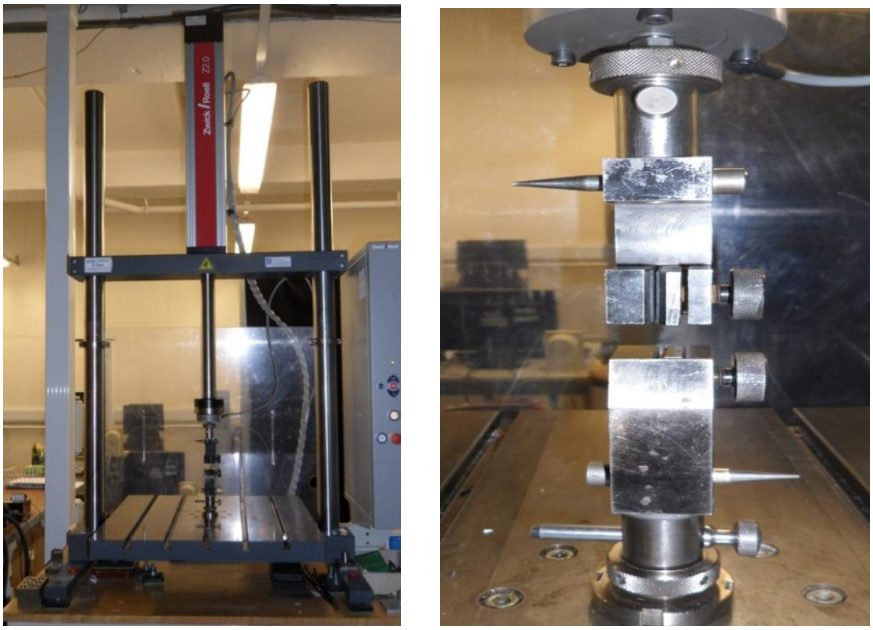

Figure 5.7 Experimental setup for tensile testing showing (a) the mechanical testing machine and (b) a close-up of the sample gripping system.

Each sample produced a curve of standard force versus standard travel. For analysis, this was later converted into stress versus strain curves.

5.2.2.6 Bioactivity of PLA and PLA Ca P films

Simulated body fluid (SBF) was initially prepared and used on test specimens by Kokubo and Takadama;[25] their method for the synthesis of SBF was followed in this work. To prepare 1000 ml of SBF solution, 700 ml of deionised water was poured into a 1000 ml plastic beaker, and stirred using a magnetic stirrer bar. The water was heated to 36.5 ± 1.5

°C. The reagents of 1st to 8th order were dissolved in the deionised water in the specific order detailed in Table 5.1:

Table 5.1 Amounts, purities and order of reagents for preparing 1000ml of SBF

Order	Reagent	Quantity	Purity (%)
1	NaCl	8.035 g	99.5
2	$NaHCO_3$	0.355 g	99.5
3	KCl	0.225 g	99.5
4	$K_2HPO_4.3H_2O$	0.231 g	99.0
5	$MgCl_2.6H_2O$	0.311 g	98.0
6	1.0 M HCl	39 ml	-
7	$CaCl_2$	0.292 g	95.0
8	Na_2SO_4	0.072 g	99.0
9	Tris	6.118 g	99.0
10	1.0 M-HCl	0-5 ml	-

Each reagent was completely dissolved before the next was added. All reagents were purchased from Sigma Aldrich and used without further purification. Once the 8th reagent (Na_2SO_4) was completely dissolved, the volume of the solution was increased to 900 ml. Before the addition of the 9th reagent, Tris buffer, the pH of the solution was checked to ensure it was in the range of 2.0 ± 1.0. Tris was then added, in small amounts, into the reaction solution. The temperature of the solution was kept between 35 and 38 °C. When the pH reached 7.30 ± 0.05, the temperature of the solution was monitored more closely and maintained at a temperature of 36.5 °C for the duration of the experiment. More Tris was added until the pH reached just beneath 7.45. At this stage reagent 10, 1.0 M HCl, was introduced to reduce the pH to 7.42 ± 0.01, whilst ensuring that the pH did not decrease to below 7.40. Once the pH had dropped to 7.42 ± 0.01, Tris was added to increase the pH to ≤ 7.45. The remainder of Tris was then added to the solution, using HCl to maintain the pH within the range of 7.42-7.45. Once all Tris had been added, the solution of the temperature was adjusted to 36.5 ± 0.2 °C. The pH was lastly adjusted to 7.40 using HCl solution. After mixing for 30 minutes, the solution was cooled down to 20 °C and distilled water added to make up to the 1000 ml mark.

For each time point and composite, two 1 cm^2square samples were used. The samples were sterilised by soaking in 70 % ethanol for five minutes, followed by drying at 50 °C. Each sample was immersed in 15 ml of SBF solution and incubated at 37 °C for the required duration. Fresh SBF was used to replace the original solution after 14 days. After 28 days, each sample was removed, washed with deionised water, and dried at 50 °C.

5.3 Results

5.3.1 PLA and PLA-Ca P film fabrication

In the production of the composite films, the mixing of PLA and filler material takes place *via* a general dispersal method; therefore dispersion will differ between different films. In most instances, dispersion occurs similarly to that seen in Figure 5.8, which highlights good dispersal of the filler to all areas of the film.

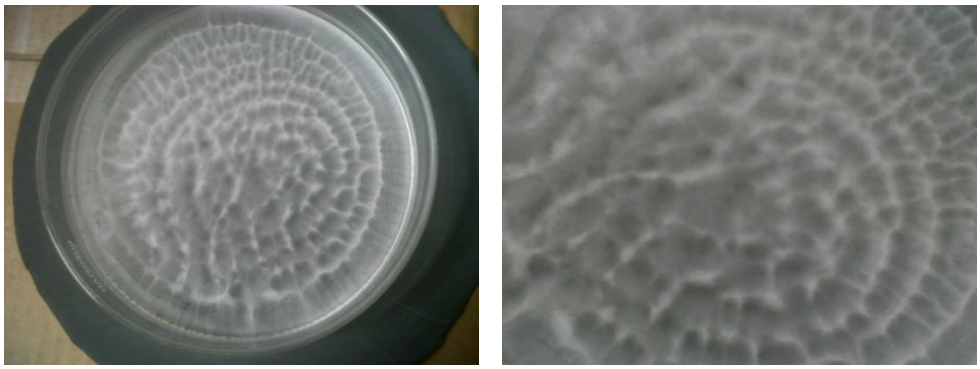

Figure 5.8 (a) Image of composite film in 120 mm diameter Petri dish and (b) higher magnification of dispersal across a 90 mm diameter.

5.3.2 Scanning electron microscopy

PLA film

SEM images of the PLA film show the surface of the film to be smooth, with some surface contaminants (Figure 5.9).

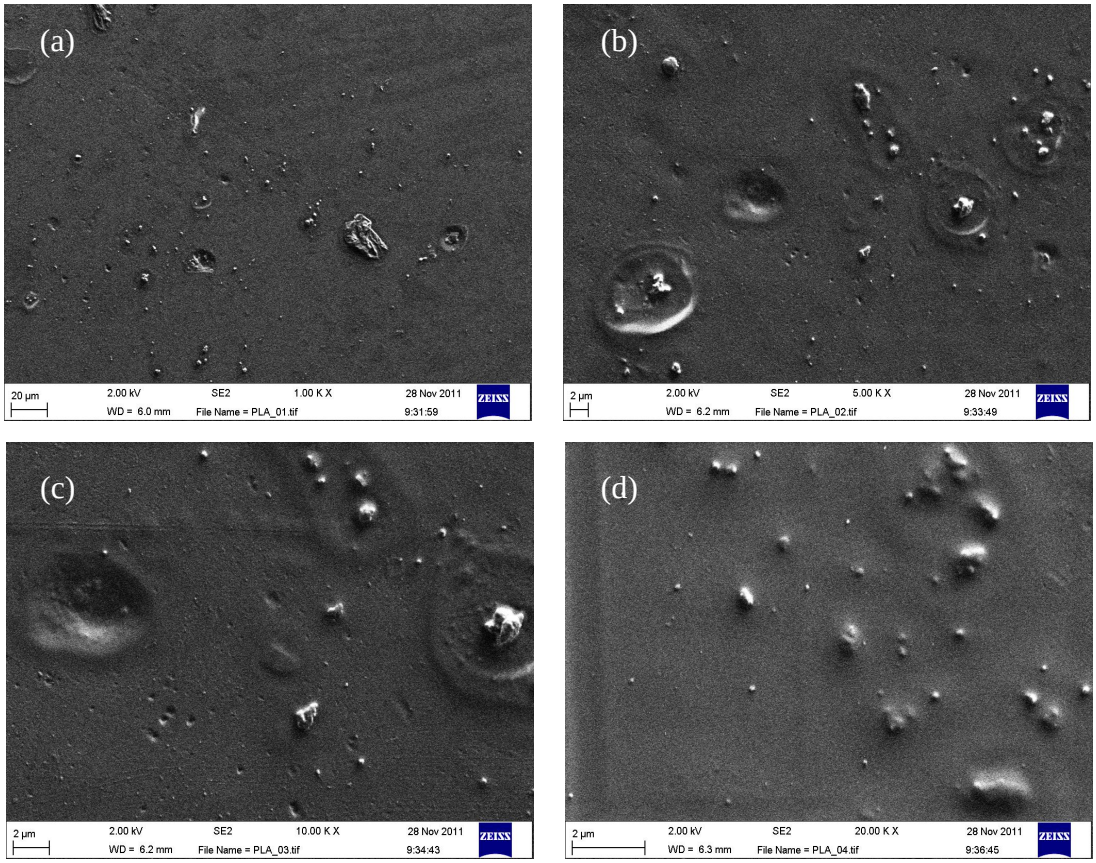

Figure 5.9 SEM images of PLA film at (a) 1 k, (b) 5 k, (c) 10 k and (d) 20 k magnification (scale bars (a) 20 µm and (b-d) 2 µm, respectively)

40 wt% PLA-βTCP composite film

Figure 5.10 shows the SEM images of the surface of the 40 wt% PLA-βTCP composite film.

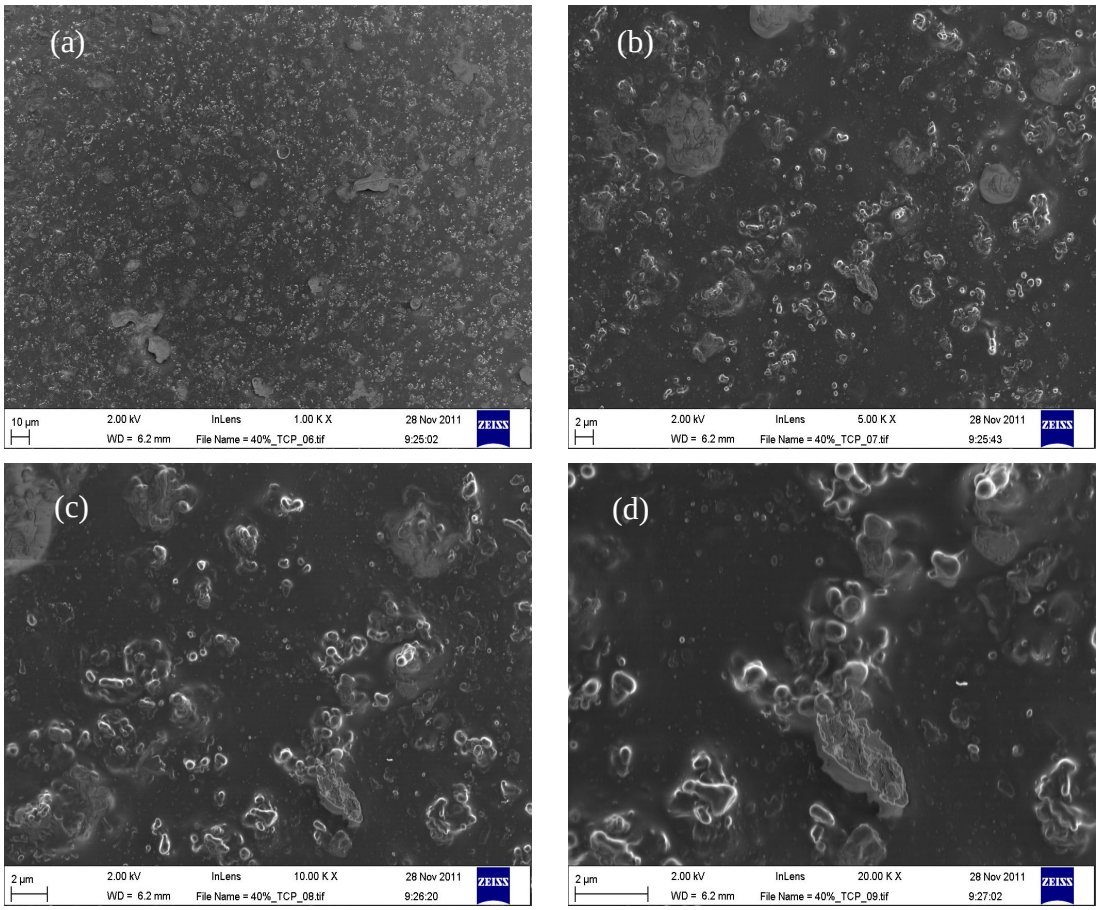

Figure 5.10 SEM images of 40 wt% PLA-βTCP film at (a) 1 k, (b) 5 k, (c) 10 k and (d) 20 k magnification (scale bars (a) 10 µm and (b-d) 2 µm, respectively)

Most of the β-TCP is covered by PLA, as seen in Figure 5.10 (a), with a fairly even distribution of filler throughout the film. However, closer inspection (Figures 5.10 (c) and (d)), shows that some larger β-TCP agglomerates have exposed surfaces. Small singular particles are seen in the films, at an average size of 0.1 µm, with agglomerates ranging from 0.5 to 2 µm.

40 wt% PLA-MgTCP composite film

The surface morphology of the 40 wt% PLA-MgTCP composite film is shown in Figure 5.11. For this composite there are areas in which mainly PLA resides (Figure 5.11 (a)), whilst the filler is grouped together in large clusters (Figure 5.11 (b)). Figures 5.11 (c) and (d) show that MgTCP has grouped together in a tight and seemingly organised manner. Particles appear flattened with regards to the surface, and cubical in shape.

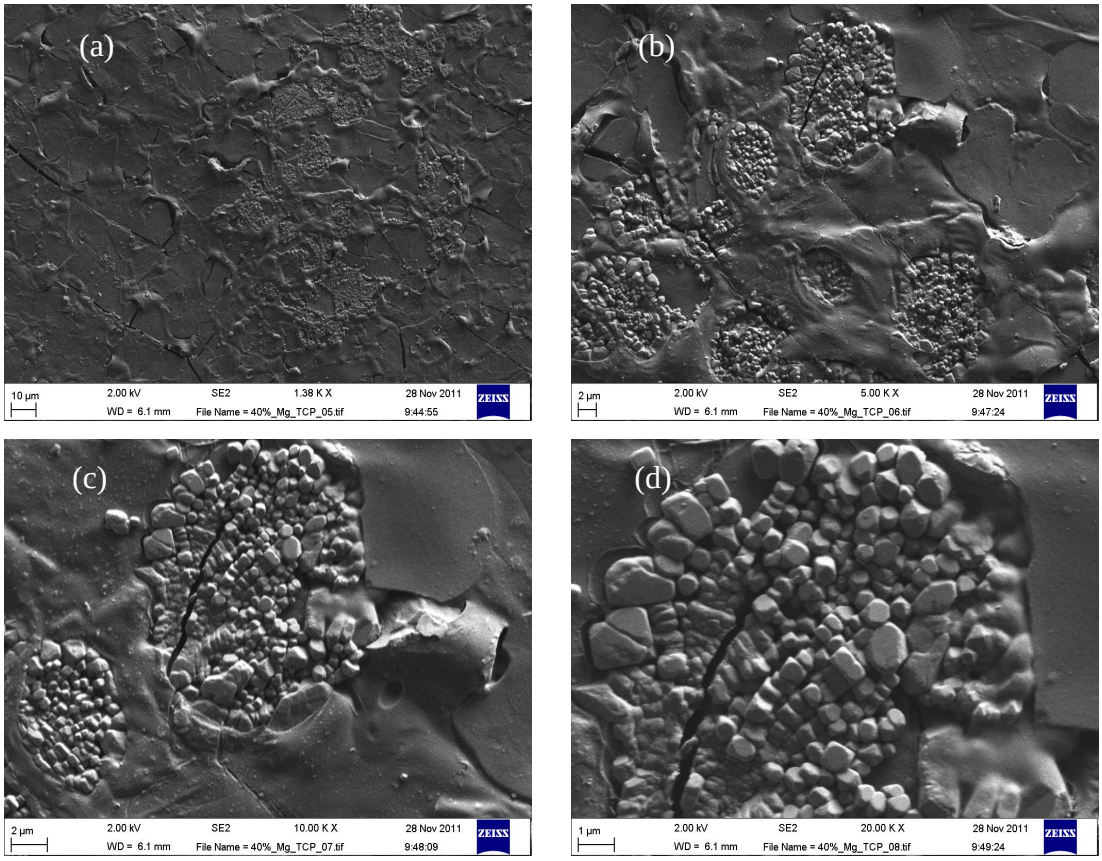

Figure 5.11 SEM images of 40 wt% PLA-MgTCP film at (a) 1 k, (b) 5 k, (c) 10 k and (d) 20 k magnification (scale bars (a) 10 µm, (b-c) 2 µm and (d) 1 µm, respectively)

40 wt% PLA-casein composite film

Similarly to the equivalent weight percentages of β-TCP and MgTCP, Figure 5.12 (a) indicates that the casein nanoclusters have been well distributed throughout the polymer film. As magnification increases, clusters of filler material can be observed, ranging in size from ~ 0.2 µm to 2 µm. Almost all of the casein material is covered by PLA, only a few areas of the clusters appear to be exposed at the surface (Figure 5.12 (b)).

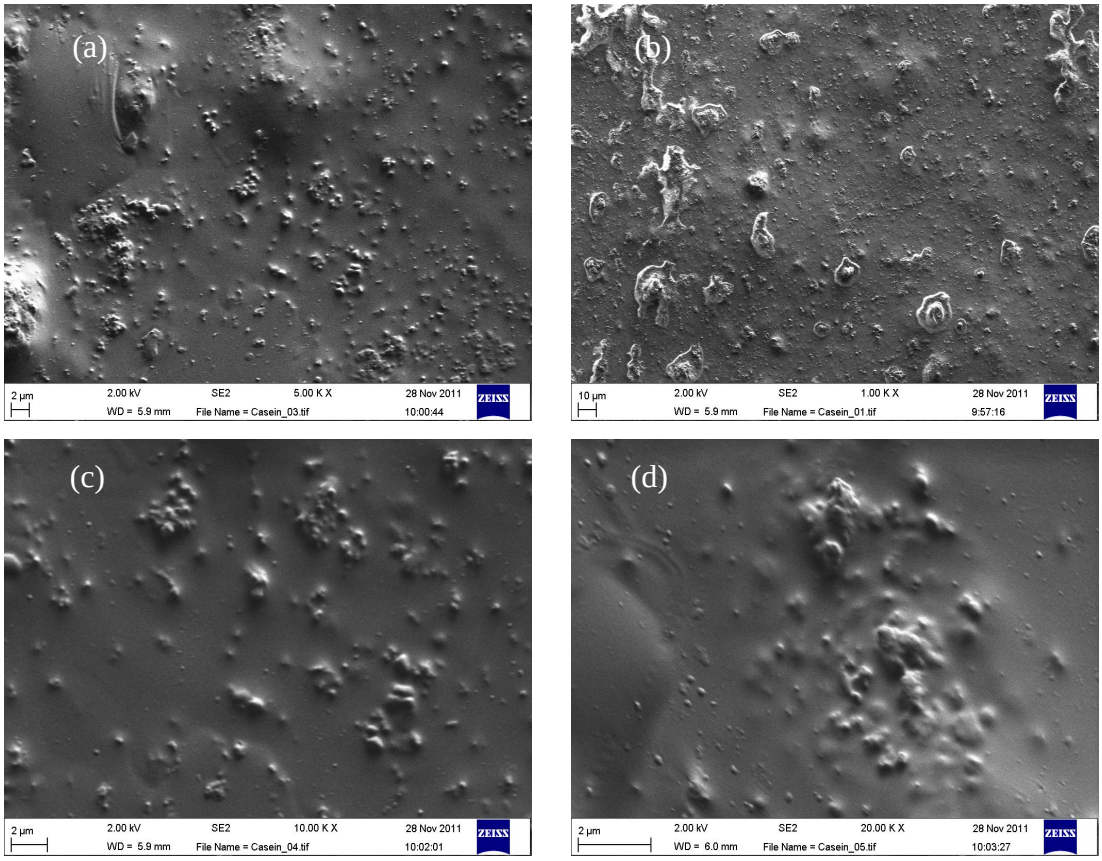

Figure 5.12 SEM images of 40 wt% PLA/Casein film at (a) 1 k, (b) 5 k, (c) 10 k and (d) 20 k magnification (scale bars (a) 10 µm and (b-d) 2 µm)

60 wt% PLA-βTCPcomposite film

In the first of the three higher wt% filler composite films, a difference in dispersion can immediately be seen. Higher filler content is seen throughout the film (Figure 5.13 (a)) and agglomerated clusters are significantly larger, in the range of 1 µm to 5 µm (Figure 5.13 (b)). Not all of the surfaces of the larger clusters are covered by PLA; some are exposed to the surface.

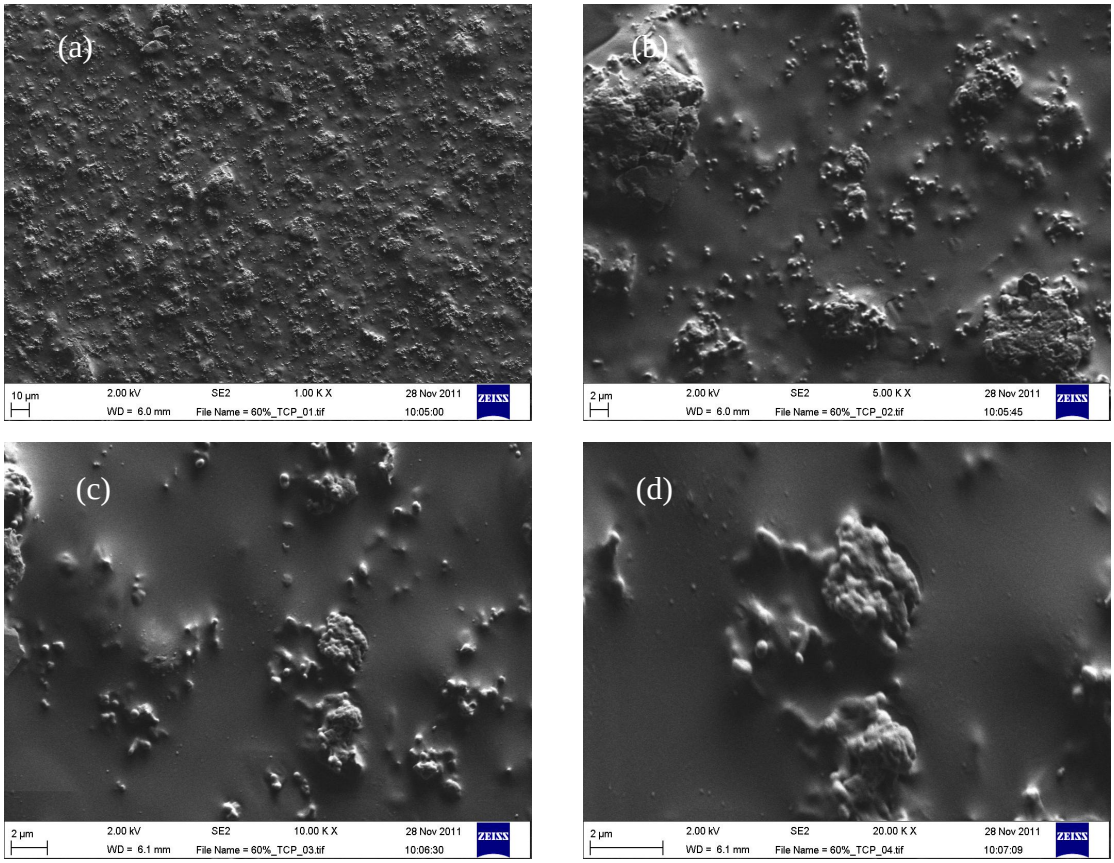

Figure 5.13 SEM images of 60 wt% PLA-βTCP film at (a) 1 k, (b) 5 k, (c) 10 k and (d) 20 k magnification (scale bars (a) 10 µm and (b-d) 2 µm, respectively)

60 wt% PLA-MgTCPcomposite film

Figure 5.14 shows the surface morphology of the 60 wt% composite film containing MgTCP. It can be observed that, although the filler particles are distributed throughout the sample, in this case more than any other there are large clusters of filler intermittently spaced, whilst all other particles appear significantly smaller. These clusters are typically ~3.5 µm across. As seen for previous samples, the tips of these clusters remain uncovered by PLA.

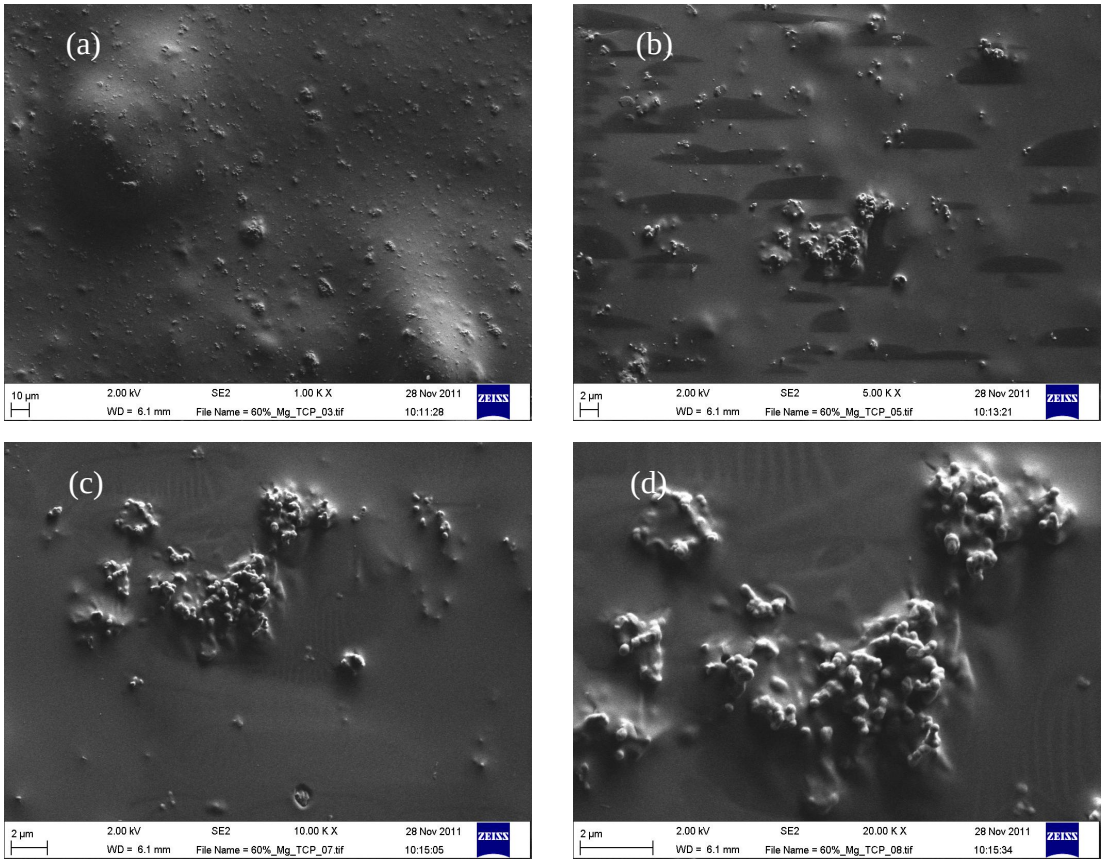

Figure 5.14 SEM images of 60 wt% PLA-MgTCP film at (a) 1 k, (b) 5 k, (c) 10 k and (d) 20 k magnification (scale bars (a) 10 µm and (b-d) 2 µm, respectively)

60 wt% PLA-casein composite film

Incorporating the casein nanoclusters at a higher wt% has had a substantial effect on the surface morphology of the film. Pores are visible on the surface (Figure 5.15 (b)), whilst craters have appeared on the surface to give the film a rough, textured appearance (Figure 5.15 (c)). It is difficult to distinguish the filler material from the polymer matrix.

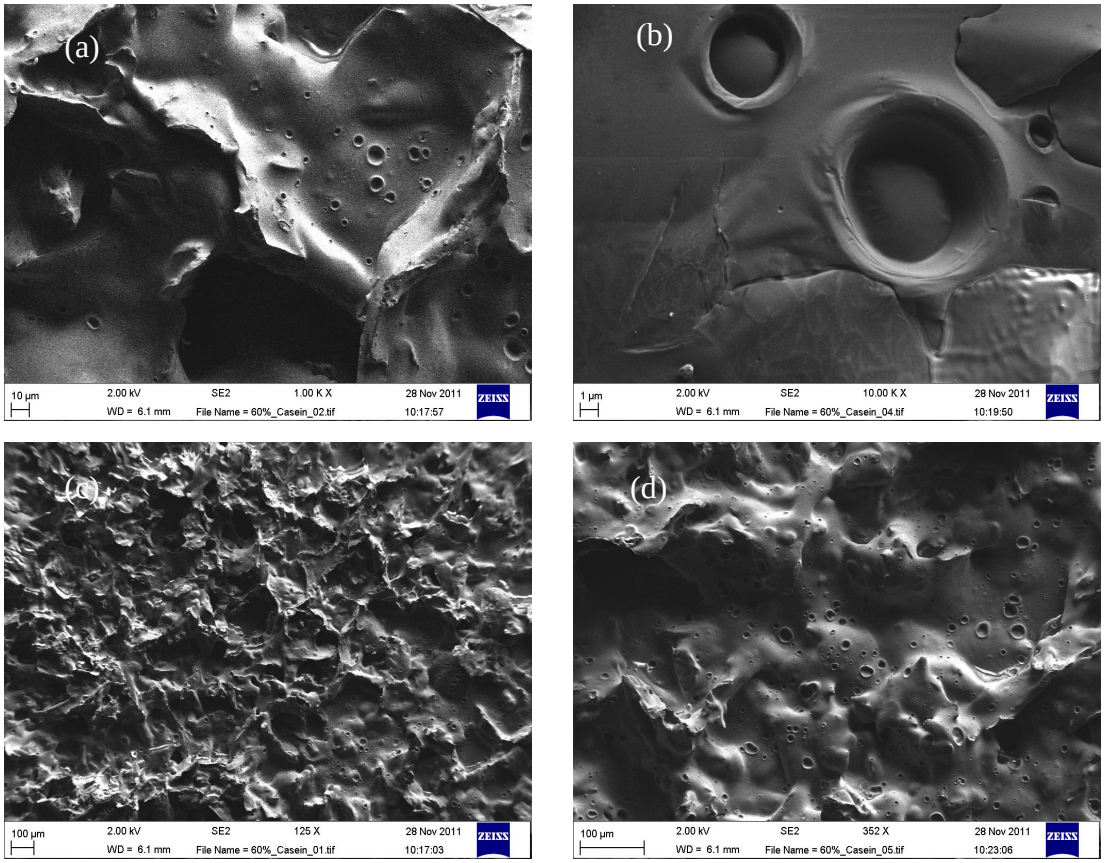

Figure 5.15 SEM images of 60 wt% PLA-casein film at (a) 1 k, (b) 10 k, (c) x125 and (d) x 325 (scale bars (a) 10 µm, (b) 1 µm and (c-d) 100 µm, respectively)

5.3.3 Raman Spectroscopy

PLA film

The Raman spectrum of the PLA film is shown in Figure 5.16. Its structure is confirmed through the presence of specific peaks, including one at 877 cm^{-1}, attributable to carbon-carbonyl bond stretching (C-COO). Peaks at 1040 and 1452 cm^{-1} correspond to C-CH_3 stretches and CH_3 bending, respectively, whilst the C=O carbonyl stretch is identified at 1766 cm^{-1}. [11]

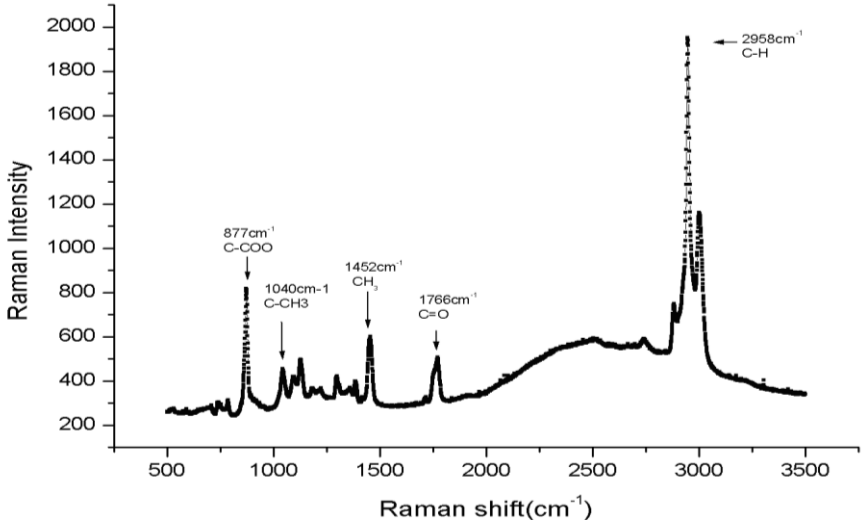

Figure 5.16 Raman spectrum of PLA film

PLA-βTCP composite film

Figure 5.17 shows the Raman spectrum for the 40 wt% PLA-βTCP composite film. Characteristic peaks of both the filler and matrix material can be observed; 876cm^{-1} corresponds to the carbon-carbonyl stretch in PLA, whilst the distinct stretch at 960 cm^{-1} is attributable to the *v*1 PO_4 stretch in the β-TCP crystal structure, in correlation with the stretch visible in the Raman spectrum of β-TCP in Figure 4.15. The broad peak visible between ~500-800 cm^{-1} comprises of peaks related to PO_4^{3-} bending (585cm^{-1}) and asymmetric stretching (774 cm^{-1}).[30]

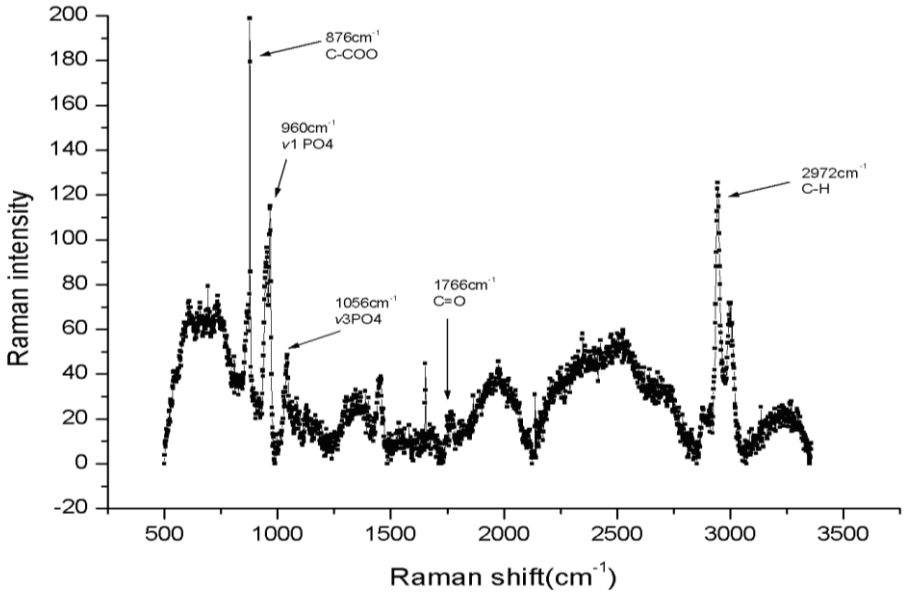

Figure 5.17 Raman spectrum of PLA-βTCP composite film

PLA-MgTCP composite film

The Raman spectrum of PLA-MgTCP also shows peaks corresponding to both PLA and β-TCP. The carbon-carbonyl stretch of the C-COO bond in PLA and the *v*1 PO_4 stretch in β-TCP are observed in Figure 5.18. The broad peak visible between ~500-800 cm^{-1}comprises again of peaks related to PO_4^{3-} bending (585cm^{-1}) and asymmetric stretching (774 cm^{-1}).

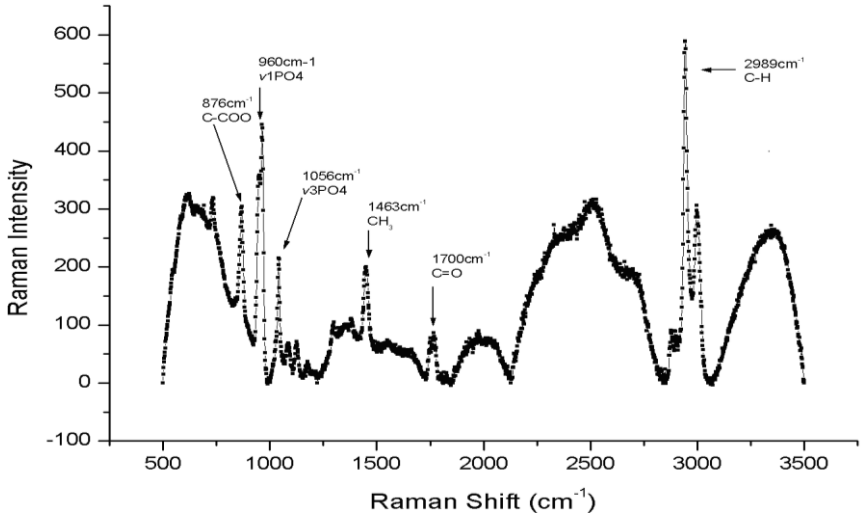

Figure 5.18 Raman spectrum of PLA-MgTCP composite film

PLA/casein composite film

Without specific information regarding the final structure and composition of the casein material, it is difficult to assign accurately specific peaks in Figure 5.19. PLA peaks are still observed, yet the intensity of the *v*1 PO_4 peak has been reduced significantly, indicating that the calcium phosphate component of the material is not β-TCP.

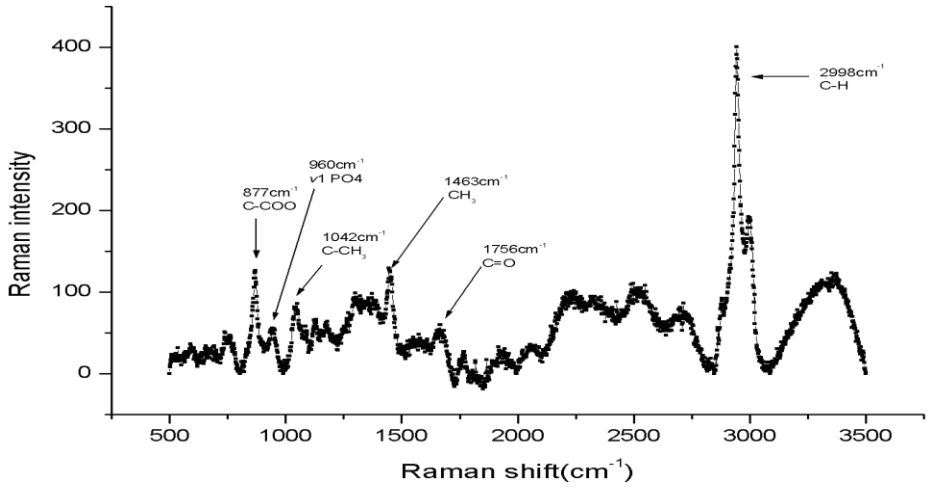

Figure 5.19 Raman spectrum of PLA-casein composite film

5.3.4 Degradation

Degradation studies aimed to investigate the effect that filler content and filler volume had on the rate of degradation of PLA and PLA composite films. All films were subjected to the same experimental conditions: incubation in deionised water at 37 °C for up to 8 weeks.

PLA film

Figure 5.20 shows the absorption behaviour of PLA films, and the percentage wet weight gain throughout the experiment. PLA initially absorbed water in its 1st and 2nd weeks, reaching a maximum of 0.11%, before the weight began to decrease. A continual decrease in weight was thereafter observed until the end of testing, wherein a maximum loss of 1.05% was recorded.

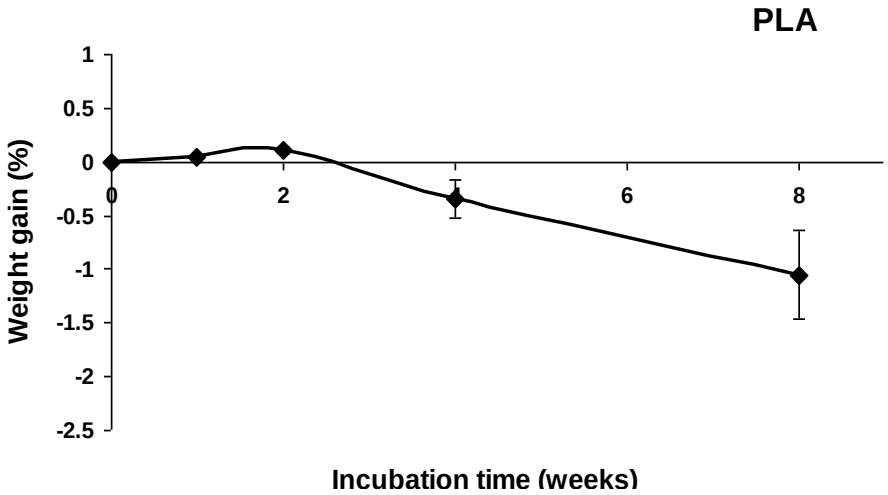

Figure 5.20 Percentage wet weight gain by PLA films after incubation in deionised water at 37 °C, for a maximum of 8 weeks. Mean ± SD, n = 5 at each time point.

Figure 5.21 shows the percentage dry weight loss recorded for PLA films. PLA progressively loses weight at each time point, until a maximum weight loss of 2.22% is observed after 8 weeks.

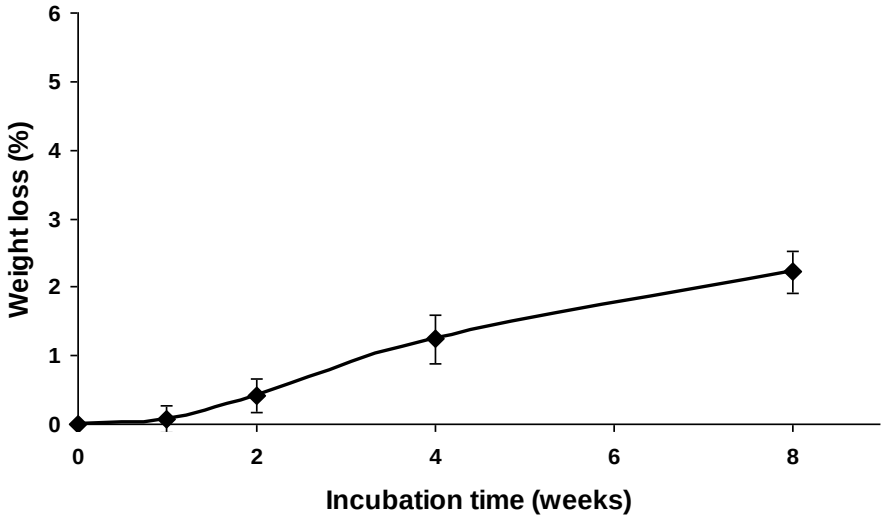

Figure 5.21 Percentage dry weight loss of PLA films after incubation in deionised water at 37 °C, for a maximum of 8 weeks. Mean ± SD, n = 5 at each time point.

PLA-β TCP composite film

Figure 5.22 illustrates the difference in percentage wet weight gain between 40 and 60 wt% PLA-βTCP composite films, and non-filled PLA film. No initial absorption of water is witnessed for the 40 wt% PLA-βTCP composites, in comparison to that observed for the PLA film. The 40 wt% PLA-βTCP film continually decreases in mass at every stage of the measurement, until reaching a maximum wet weight loss of 0.85% at 8 weeks. An initial absorption of water is observed for the 60 wt% PLA-βTCP in the 1st week, with a wet weight gain of 0.53%. From weeks 2-8, however, the overall wet weight mass is seen to decrease, with a final loss of 0.88%. PLA, in comparison, loses more overall wet weight mass with 1.05%

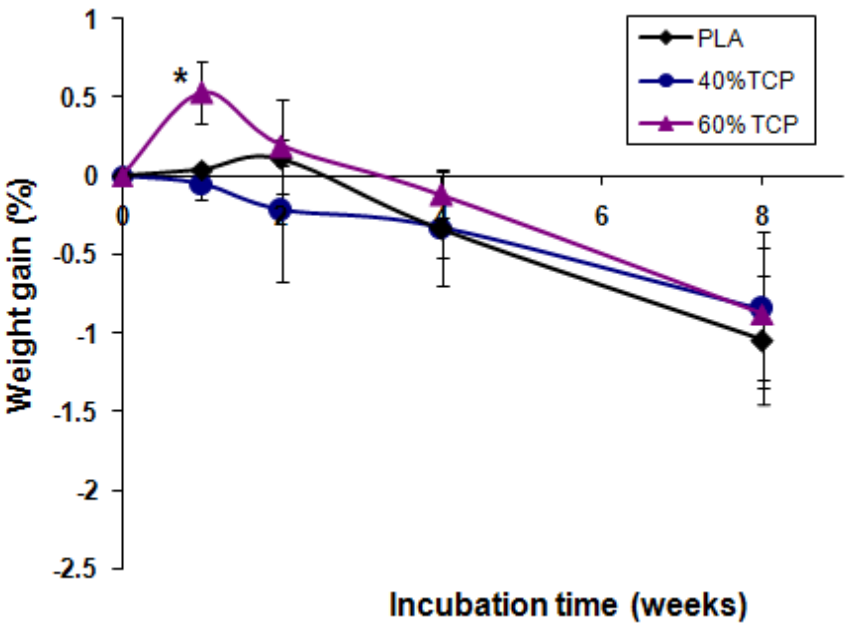

Figure 5.22 Percentage wet weight gain by 40 and 60 wt% PLA-βTCP films after incubation in deionised water at 37 °C, for a maximum of 8 weeks.Mean ± SD, n = 5 at each time point. * = p < 0.05 compared to non filled PLA, paired t-test.

Comparing the dry weight losses of 40 and 60 wt% PLA-βTCP and PLA films (Figure 5.23), the 40 and 60 wt % PLA-βTCP films degrade faster, and lose more overall mass, than the PLA film. A maximum weight loss of 2.54% for the 40 wt% PLA-βTCP film, compared to 2.22% for the PLA equivalent, provides early indications that filler content may influence degradation rate. Degradation rates are significantly accelerated with regards to the 60 wt% PLA-βTCP. By the 4th week the filled composite has already lost 3.37% of its overall mass, whilst the unfilled PLA has only lost 1.24%. The highest overall mass loss is seen in this sample out of any other composite film tested; with a 4.83% loss, it loses over twice the mass of the comparative PLA film.

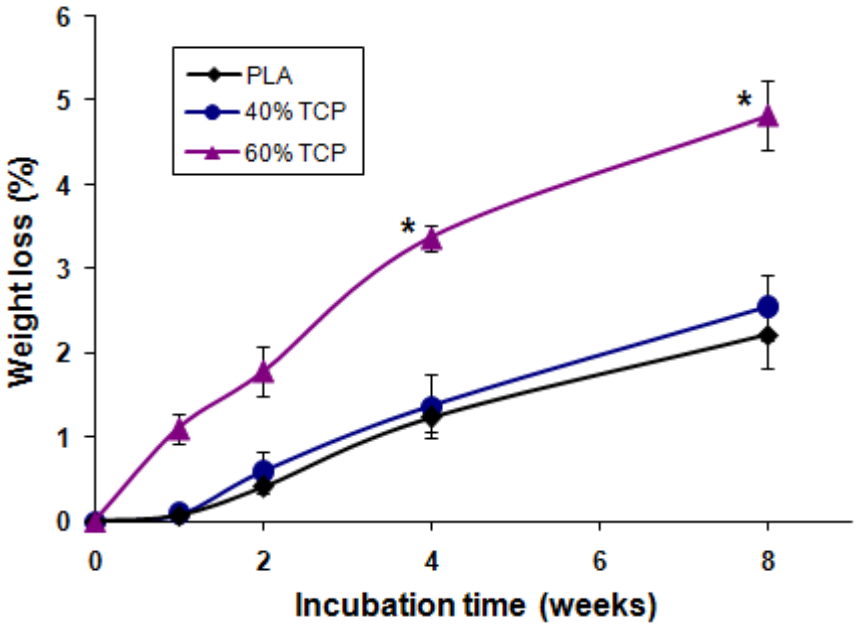

Figure 5.23 Percentage dry weight loss of 40 and 60 wt% PLA-βTCP films after incubation in deionised water at 37 °C, for a maximum of 8 weeks.Mean ± SD, n = 5 at each time point.
*** = p < 0.05 compared to non filled PLA, paired t-test.**

PLA- MgTCP composite film

Figure 5.24 shows the percentage wet weight gain of 40 and 60 wt% PLA-MgTCP composite films, versus the control PLA film.The 40 wt% PLA-MgTCP film shows no initial absorption of water and continually decreases in mass at every measurement, until an overall wet weight loss of 1.03% is reached. This is almost identical to the wet weight loss noted for the PLA film (1.05%). A higher initial absorption of water is shown for the 60 wt% PLA-MgTCP film than the PLA film, with respective values of 0.33% and 0.04%. A higher overall wet weight loss of 1.14% is shown for the 60 wt% PLA-MgTCP film.

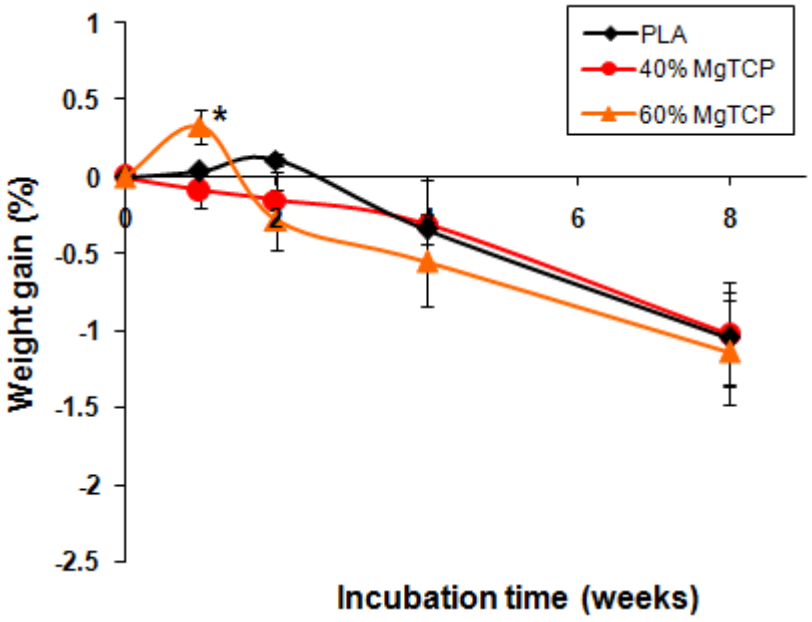

Figure 5.24 Percentage wet weight gain by 40 and 60 wt% PLA-MgTCP films after incubation in deionised water at 37 °C, for a maximum of 8 weeks.Mean ± SD, n = 5 at each time point. * = p < 0.05 compared to non filled PLA, paired t-test.

Figure 5.25 compares the percentage dry weight loss of 40 and 60 wt% PLA-MgTCPfilms to PLA film. Similarly to that observed for the non substituted β-TCP composite film (Figure 5.23), an increase in the overall rate of degradation and mass loss is observed. The 40 wt% PLA-MgTCP films decrease in mass slightly more so than the PLA films, with overall mass losses of 2.28% and 2.22% noted for the 40 wt% PLA-MgTCP and PLA films, respectively.

The effect of filler content and volume is further shown with regards to the 60 wt% MgTCP film, with an illustration that increasing the filler volume increases both the rate of degradation, and overall mass loss (Figure 5.25). The 60 wt% PLA-MgTCP film provides an overall mass loss of 3.98%, which is nearly double that of PLA. Degradation rates are also much quicker; by the 2nd week the mass loss of the 60 wt% PLA-MgTCP film is 1.43%, whilst for PLA the mass loss is only 0.41%.

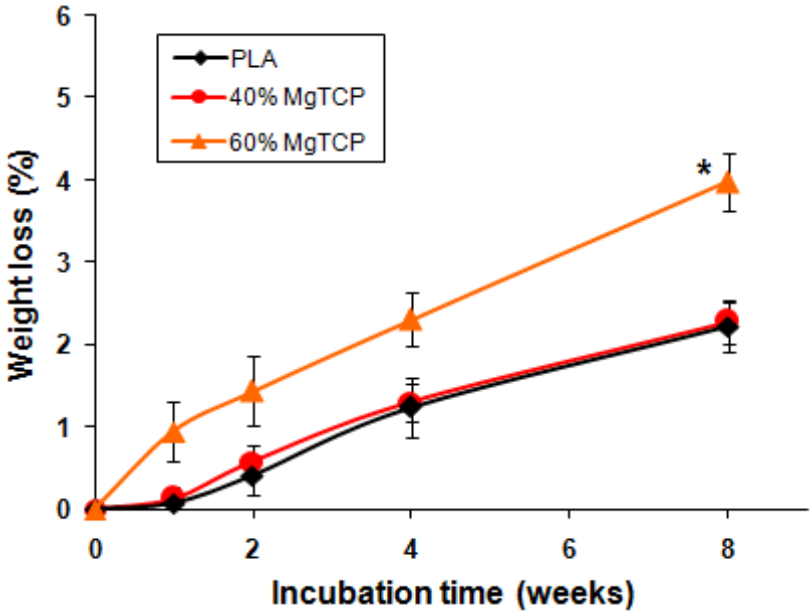

Figure 5.25 Percentage dry weight loss of 40 and 60 wt% PLA-MgTCP films after incubation in deionised water at 37 °C, for a maximum of 8 weeks.Mean ± SD, n = 5 at each time point. * = p < 0.05 compared to non filled PLA, paired t-test.

PLA- casein composite film

Figure 5.26 shows the percentage wet weight gain by 40 and 60 wt% PLA-casein film versus PLA film. A substantial weight loss of 1.2% is observed for the 40 wt% PLA-casein films in the 1st week; the rate of weight loss thereafter decreases, and after 8 weeks an overall wet weight loss of 2.33% is recorded.The 60 wt% PLA-casein film shows substantial weight loss in the experiment, with an overall mass loss of 3.42% noted at the 8th week, compared to 1.05% for the PLA film at the same time point. This is substantially greater than any other wet weight loss noted thus far.

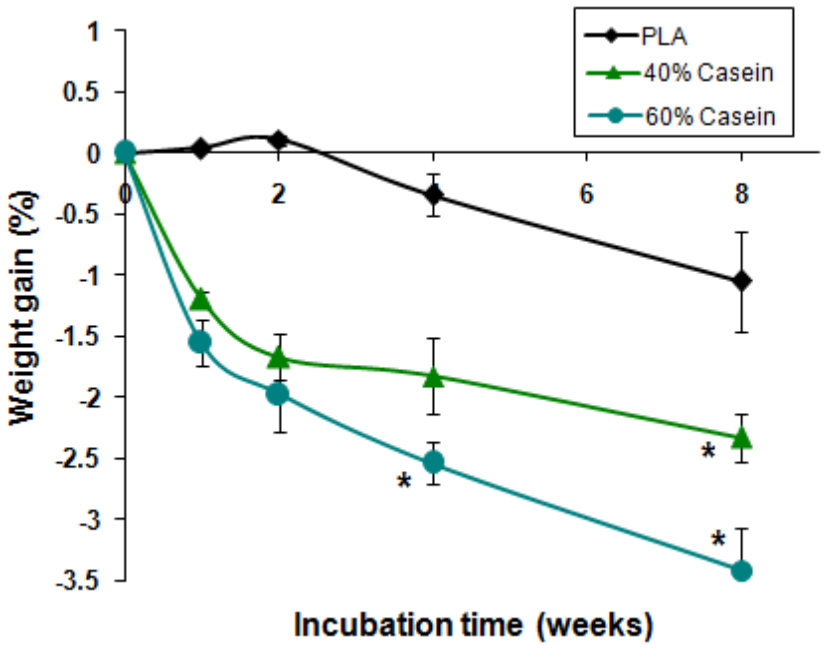

Figure 5.26 Percentage wet weight gain by 40 and 60 wt% PLA-casein films after incubation in deionised water at 37 °C, for a maximum of 8 weeks.Mean ± SD, n = 5 at each time point. * = p < 0.05 compared to non filled PLA, paired t-test.

The dry weight loss of 40 and 60 wt% PLA-casein films is compared to PLA film in Figure 5.27. It is obvious that the 40 wt% PLA-casein film degrades faster than the PLA film; in the 1st week the 40 wt% PLA-casein film loses 1.4% of its overall mass, whilst PLA only loses 0.07% of its overall mass at the same time point. The rate of weight loss slows down thereafter for the 40 wt% PLA-caseinfilm, with a total mass loss of 2.72%, compared to 2.22% for PLA, seen at 8 weeks.At each stage of measurement for the 60 wt% casein film, whether it was the 1st, 2nd, 4th or 8th week, the 60 wt% PLA-Casein film showed increased levels of degradation when compared to the unfilled PLA film. An overall mass loss of 3.95% for the 60 wt% PLA-casein film was noted; substantially higher than the 2.22% overall mass loss of PLA.

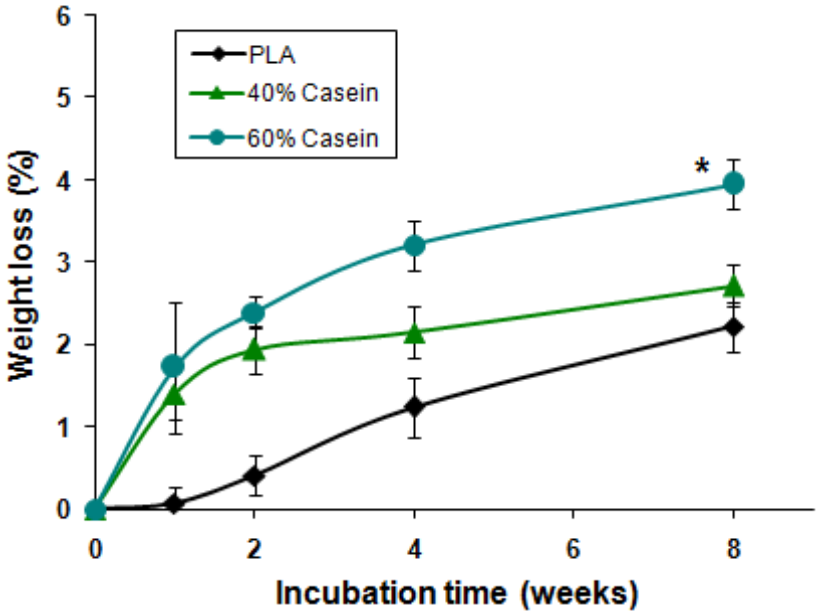

Figure 5.27 Percentage dry weight loss of 40 and 60 wt% PLA-casein films after incubation in deionised water at 37 °C, for a maximum of 8 weeks. Mean ± SD, n = 5 at each time point. * = p < 0.05 compared to non filled PLA, paired t-test.

5.3.5 Mechanical properties

Figure 5.28 shows typical stress/strain curves for the PLA and composite films. The PLA film is ductile, with the highest tensile strength. All composite films demonstrate lower strain to failure than the non-filled PLA. The PLA-βTCP and PLA-MgTCP show strengths one fifth or less than the non-filled PLA, which is further reduced as the filler content increases from 40 to 60 wt%. However the strength is increased from the 40 wt % casein filled film, but at 60 wt% casein the strength is drastically reduced to a lower level similar to the 60 wt% β-TCP and Mg-TCP films. Casein composites are more ductile than the other composite films. Increasing each of the filler volumes from 40 to 60 wt% reduces the strength of the films and decreases strain.

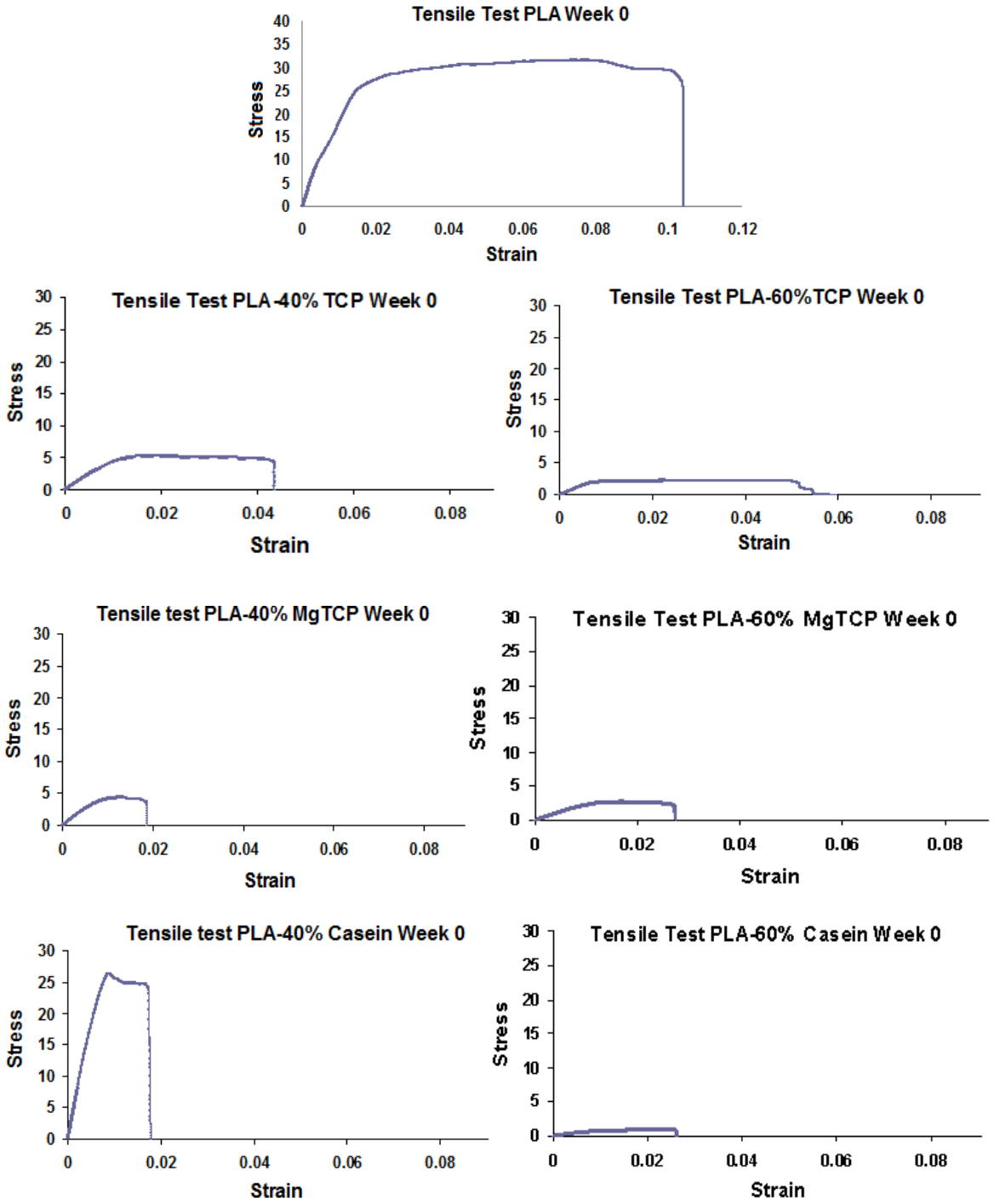

Figure 5.28 Typical stress and strain curves for each of the PLA and composite films

Figure 5.29 shows the tensile strengths of each composite film on day zero of the degradation experiment i.e. before incubation in deionised water. This provides a good basis of comparison of the relative starting strengths for each of the composite films.

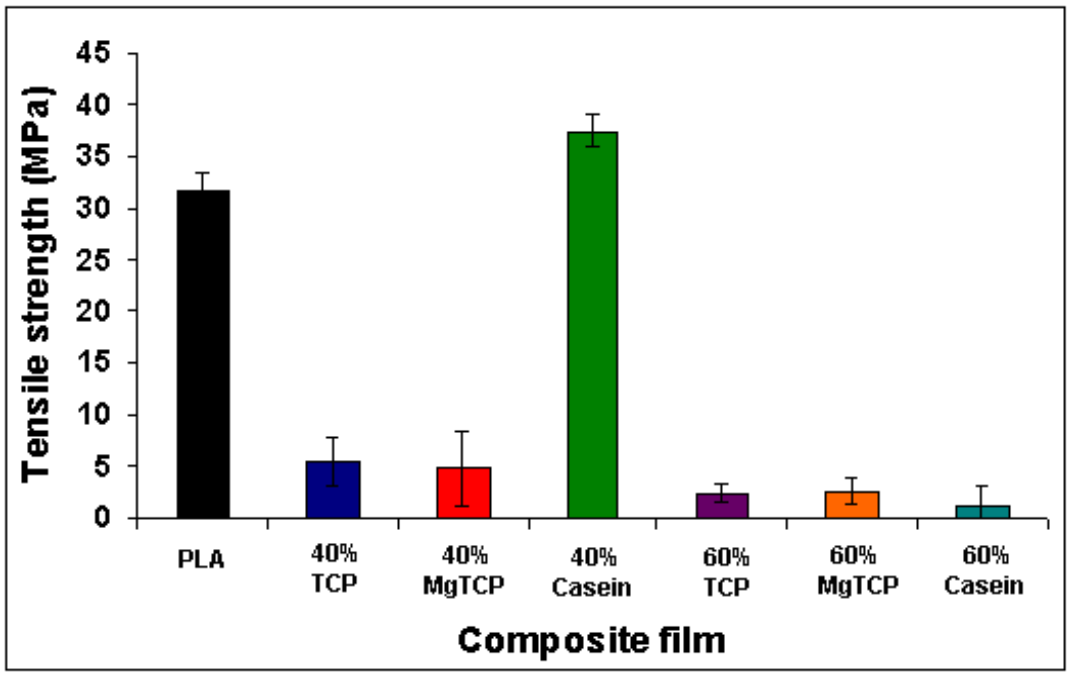

Figure 5.29 Tensile strengths of composite films before incubation. Mean = ± SD, n=5.

The highest initial tensile strength is seen for the 40 wt% PLA-casein film, at 37.4 MPa. The unfilled PLA film is the second strongest at 31.6 MPa, after which the tensile strengths drop considerably for the 40 wt % PLA-βTCP (5.48 MPa) and 40 wt% PLA-MgTCP (4.78 MPa) composite films. Each of the 60 wt% composite films is weaker than the corresponding 40 wt% films, for example the 60 wt% PLA-βTCP films yielded a max strength of 2.45 MPa, compared to 5.48 MPa observed for the 40 wt% PLA-βTCP film.

The tensile strengths of each composite material were measured over the degradation period, to analyse how the incubation affected the mechanical integrity of each film. Figure 5.30 illustrates the effect that incubation duration has on tensile strength in the unfilled PLA films. As time progresses, the tensile strength decreases gradually, to eventually provide an overall reduction in strength of 40% after 8 weeks incubation in SBF. The sharpest drop in strength is between weeks 1 and 2, where the ability of the composite to withstand stress reduces from a tensile strength of 30.04 MPa to 25.58 MPa.

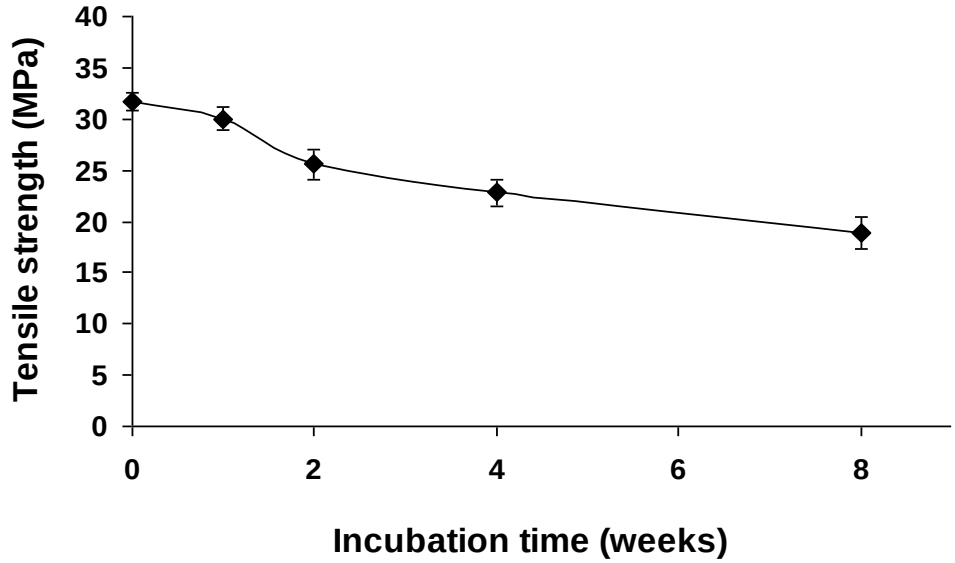

Figure 5.30 Tensile strength of PLA films after incubation in deionised water at 37 °C, for a maximum of 8 weeks. Mean ± SD, n = 5 at each time point.

To investigate whether any of the fillers employed in this research could improve upon PLAs ability to withstand load during the degradative process, changes in tensile strength of the filled films were compared to that of the non-filled PLA material. Figure 5.31 charts the correlation between tensile strength and incubation period in the 40 and 60 wt% PLA-βTCP films. Whilst a decrease of 40% was noted for the PLA films, it is clear that the inclusion of the calcium phosphate ceramic allowed the composite to withstand mechanical testing during incubation, without as drastic a reduction in strength. Over the 8 week period, a reduction in strength of 15% was observed in the 40 wt% PLA-βTCPfilm; greatly improved on the larger reduction seen for PLA, although the two films initial strengths were very different. Similarly to the PLA films, the sharpest reduction in strength was witnessed between weeks 1 and 2, wherein there is a drop from 5.27 MPa to 4.84 MPa. Whilst the 40 wt% composites generally demonstrated a gradual drop in strength, results for the 60 wt% samples show a more staggered drop in mechanical integrity. A pronounced drop from 2.45 MPa to 1.52 MPa occurs between week 0 and 1, whilst very little change occurs between weeks 1 and 2. A similar pattern is seen for the second period of the degradation process, with a decrease of 1.44 MPa to 0.72 MPa between weeks 2 and 4, then very little change for the rest of the experiment. Compared to the 40 wt% films, a substantial loss of 76% of the materials tensile strength is seen. This is higher than the 40% lost by the unfilled PLA films, and is much higher again that the 40 wt% PLA-βTCP films, which only suffered an overall loss of 15% tensile strength.

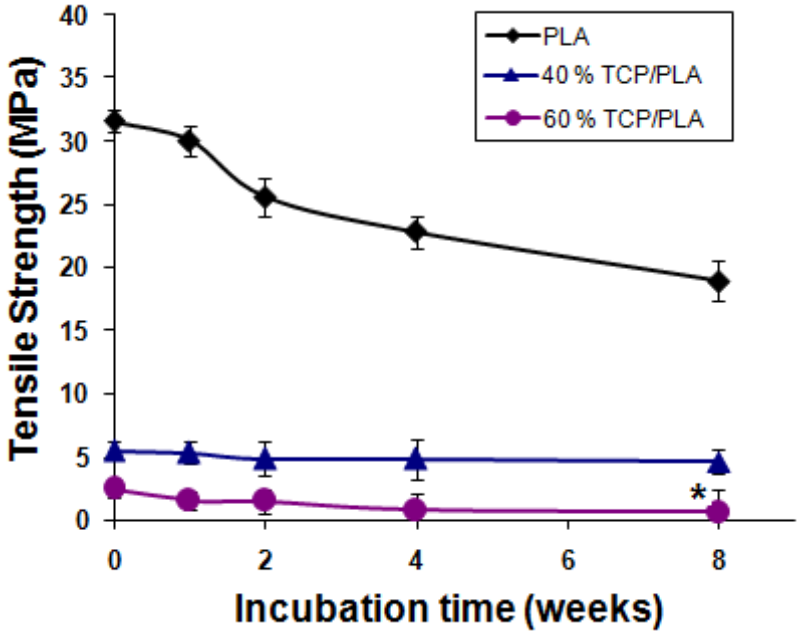

Figure 5.31 Tensile strength of 40 and 60 wt% PLA-βTCP films after incubation in deionised water at 37 °C, for a maximum of 8 weeks.Mean ± SD, n = 5 at each time point.* = p < 0.05 compared to non filled PLA, paired t-test.

Figure 5.32 illustrates changes in tensile strength as a direct result of increasing incubation duration for the 40 and 60 wt% PLA-MgTCP films. Similarly to that seen for the corresponding 40 wt % PLA-βTCP films, there is not as drastic a reduction in strength for these films, when compared to the unfilled PLA composites: only 14%, compared to 40% for PLA. The most significant weakening for these samples occurred in the first week of incubation, where tensile strength dropped from 4.78 MPa to 4.51 MPa.In contrast, the higher filled 60 wt% filmsshow an overall decrease in tensile strength of 70%, obtained after 8 weeks incubation. This is in keeping with the large reduction in tensile strength witnessed for the 60 wt% PLA-βTCP films, wherein a 76% reduction was observed.There is a gradual decrease in mechanical strength of the higher loaded films over the 8 week incubation period, with the highest loss of strength observed in the early weeks of the experiment. Between weeks 0 and 1, the strength drops from 2.59 MPa to 1.74 MPa.

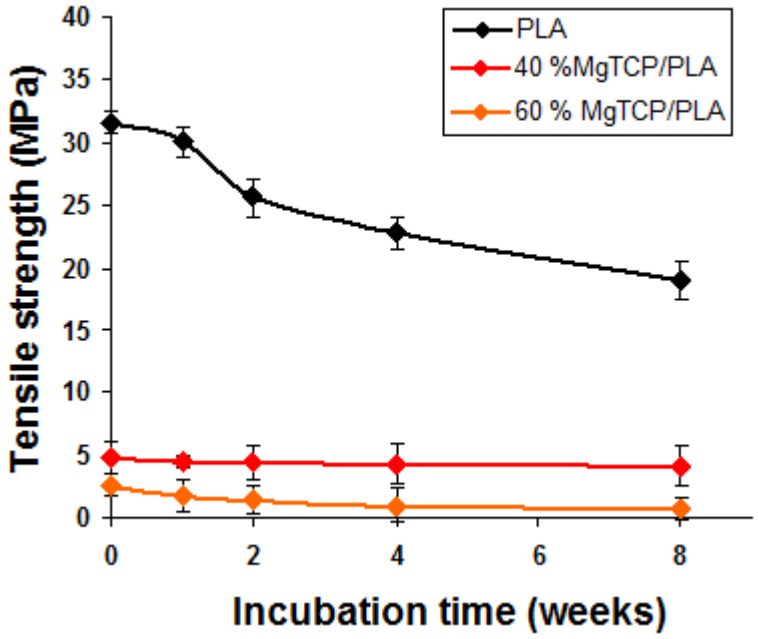

Figure 5.32 Tensile strength of 40 and 60 wt% PLA-MgTCP films after incubation in deionised water at 37 °C, for a maximum of 8 weeks.Mean ± SD, n = 5 at each time point.

The 40 wt% PLA-casein samples yielded the highest initial tensile strength out of all of the composite films, and changes in strength of these, and the 60 wt% films, are plotted against incubation time in Figure 5.33. A gradual decrease is seen across the 8 weeks, with no particular time point losing significantly more strength than another. The overall reduction in strength is 29% after 8 weeks; the largest decrease of all the 40 wt% films thus far. With regards to the higher loaded composite films, very little change in the tensile strength is seen between weeks 0 and 1, and a gradual reduction is seen for the following weeks until the experiments end at week 8. An overall reduction in tensile strength of 56% is noted for this composite; these samples have maintained their mechanical strength best out of the three 60 wt% films.

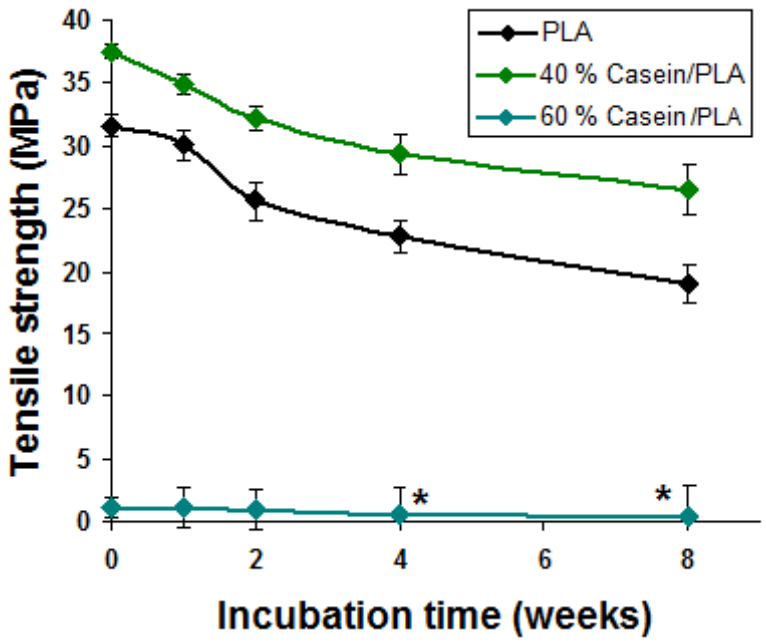

Figure 5.33 Tensile strength of 40 and 60 wt% PLA-Casein Ca P films after incubation in deionised water at 37 °C, for a maximum of 8 weeks.Mean ± SD, n = 5 at each time point.* = p < 0.05 compared to non filled PLA, paired t-test.

5.3.6 Bioactivity

Figure 5.34 (a) displays the SEM images of the PLA control film and all of the composite films after 28 days immersion in SBF. No apatite formation is observed on the surface of the PLA control film; only surface impurities are visible, similar to those seen in Figure 5.9. Distinct from the corresponding image of the PLA control, the SEM image of the 40% PLA-βTCP (Figure 5.34 (b)) surface shows the formation of a layer of apatite on the surface of the film. Covering most of the sample surface, the apatite is dense, thick, and consists of several layers. SEM imaging of 60 wt% PLA-βTCP composites showed heightened levels of apatite on the surface of the films (Figure 5.34 (c)). Apatite covered large areas of the surface, and the layer appeared to be growing outwards of the films surface 3-dimensionally, indicating that substantial amounts of apatite had been formed during the 28 day immersion in SBF.

Very little apatite formation is observed on the surface of the 40 wt% PLA-MgTCP composites, seen in Figure 5.34 (d). It should be noted that this particular sample was charging very strongly, and thus it was very difficult to attain a high quality SEM image of the surface morphology of the film. The surface is largely unaffected by the 28 days

immersion in SBF. In contrast to results observed for 60 wt% PLA-βTCP samples, 60 wt% PLA-MgTCP composites again show no apatite formation on the surface of the film after immersion in SBF solution for 28 days, as shown in Figure 5.34 (e). It is therefore apparent that the MgTCP samples do not facilitate the growth of an apatite layer onto the film surface. Composite films of 40 wt% PLA-casein were imaged under SEM, and can be seen in Figure 5.34 (f). After 28 days immersion in SBF, no dense apatite layer has been formed on the surface of the film. Several larger clumps of material appear visible on the film, but these could be the result of sodium chloride salt deposition, or surface impurities. Figure 5.34 (g) shows the SEM image of the 60 wt% PLA-casein sample, which again shows no difference in surface morphology, despite immersion in SBF after 28 days

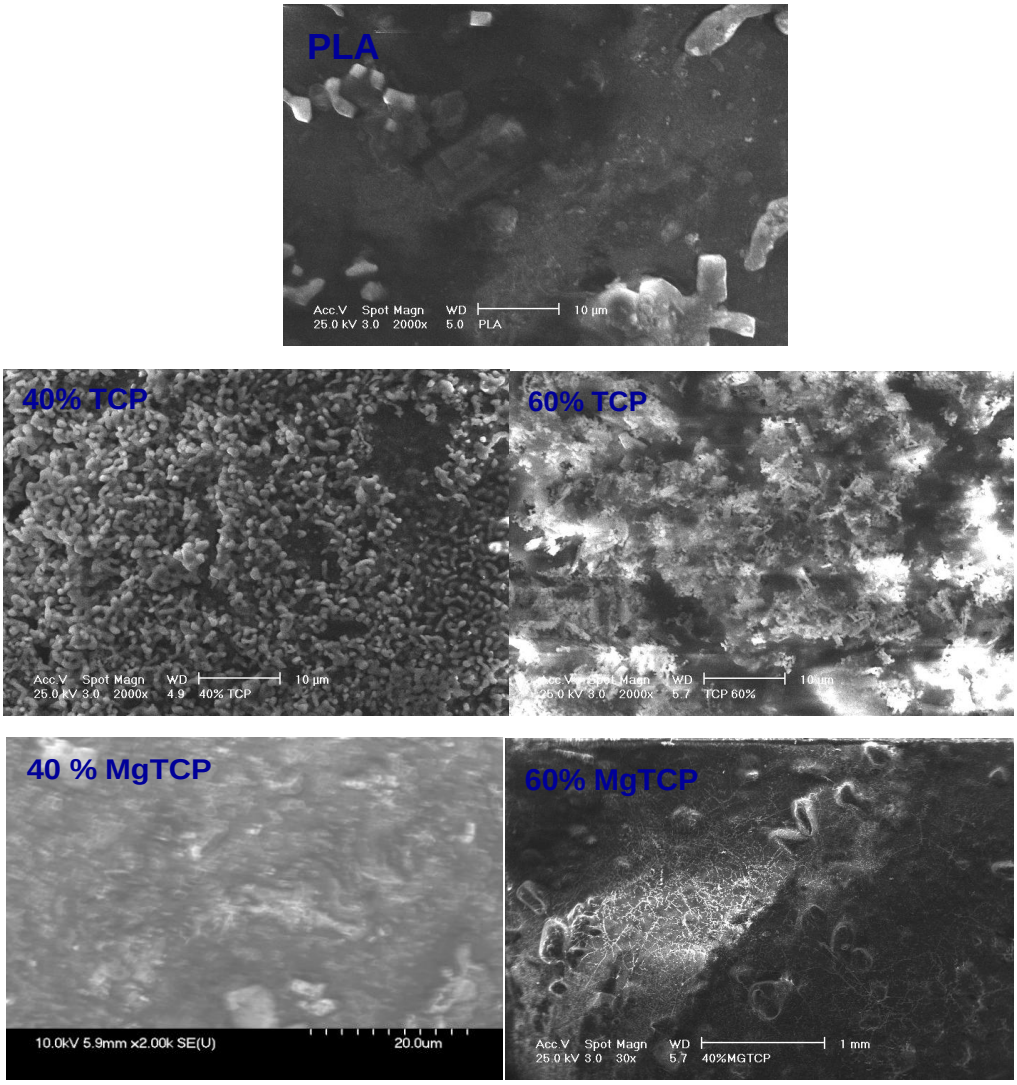

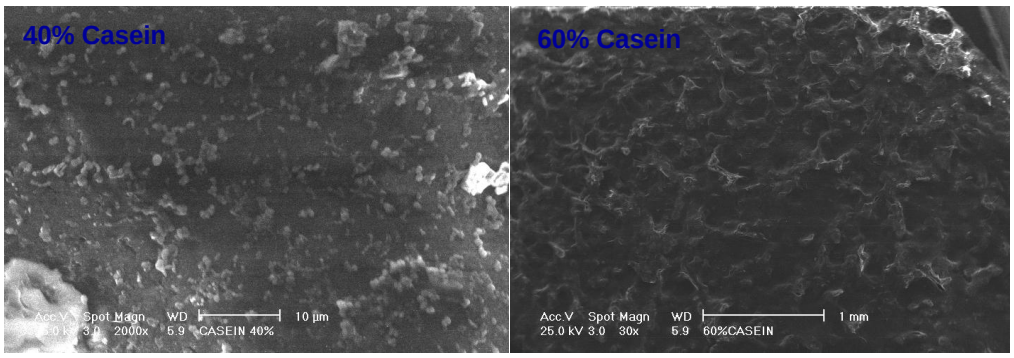

Figure 5.34 (a-g) SEM images of (a) PLA, (b) 40 wt% TCP, (c) 60 wt% TCP, (d) 40 wt% MgTCP (e) 60 wt% MgTCP, (f) 40 wt% Casein and (g) 60 wt% Casein at 28 days after immersion in SBF

The EDX spectrum of the PLA film is shown in Figure 5.35 (a). It can be seen that the spectrum shows no Ca or P peaks, which would be indicative of an apatite layer forming on the film surface. The only peaks visible are those of C and O, corresponding to carbon and oxygen present in the polymer, and those of Na and Cl. The latter two peaks most likely arise from deposition of NaCl from the SBF solution onto the film surface. Figure 5.35 (b) shows the corresponding spectrum for the 40 wt% PLA-βTCP composite, which does indicate the presence of an apatite layer on the surface of the film. Whilst peaks for C and O again correspond to the polymer film, peaks belonging to Ca and P confirm apatite formation.EDX of the 60 wt% PLA-βTCP confirms significant growth of an apatite layer on the film, with stronger, higher intensity peaks for P and Ca in this spectrum, compared to that of the 40 wt % sample.

Figure 5.35 (d) displays the EDX analysis for the 40 wt% PLA-MgTCP film. In accordance with the lack of apatite seen on the SEM image, there is no phosphorus peak on the sample, and peaks corresponding to calcium are weak, both of which indicate that no surface apatite has been formed. High intensity peaks for Na and Cl allude that large amounts of sodium chloride has been deposited from the SBF solution, and C and O peaks again are due to the carbon and oxygen in the polymer film. Similar results are observed for the 60 wt% PLA-MgTCP film, in that no evidence of apatite formation is presented (Figure 5.35 (e)).

EDX analysis of the 40 wt% PLA-casein film, after 28 days immersion in SBF, does not show the presence of apatite on the film surface (Figure 5.35 (f)). Only peaks attributable

to PLA and NaCl are visible. This result is also maintained in the 60 wt% version of the composite film.

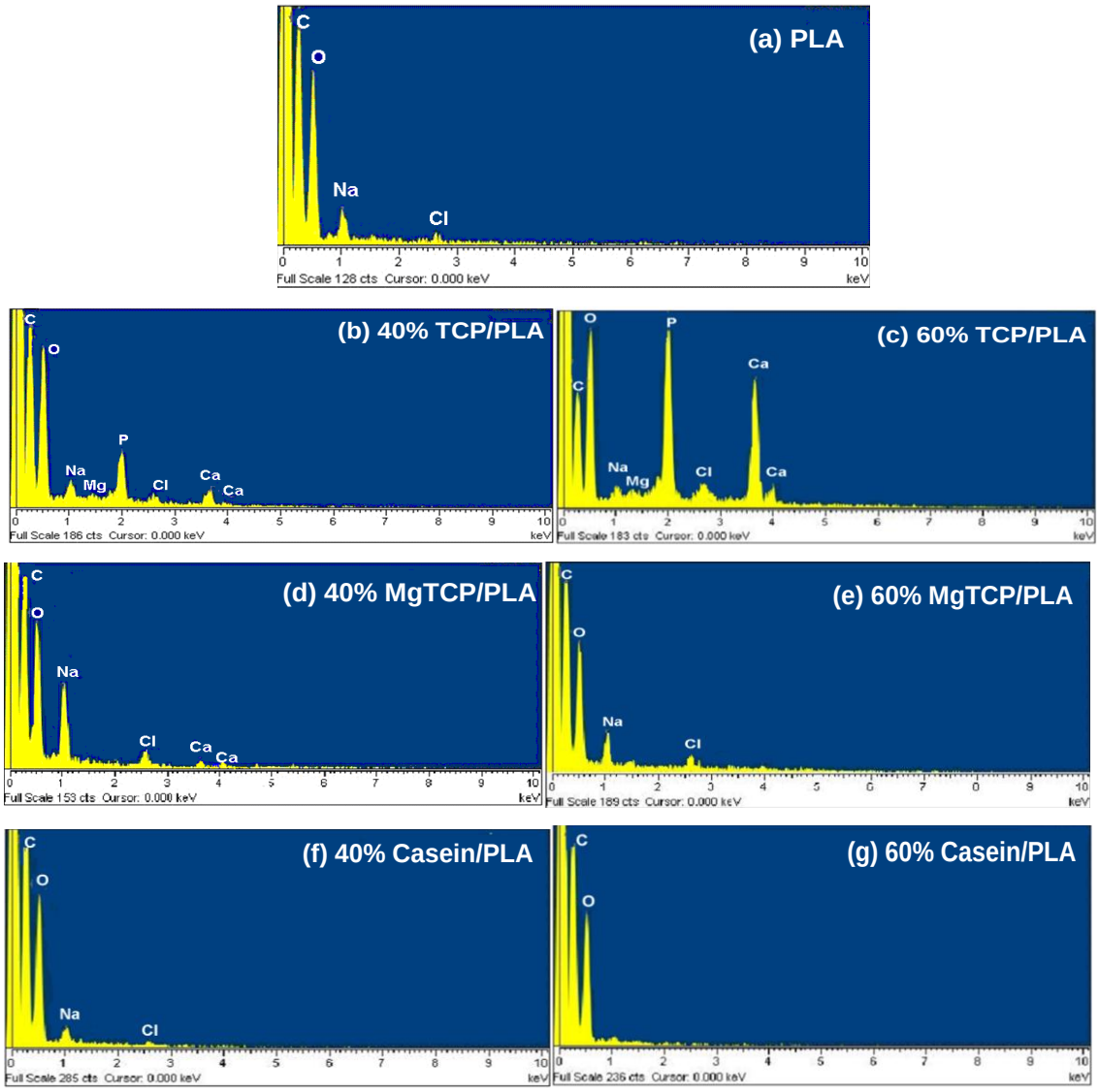

Figure 5.35 (a-g) EDX spectra of (a) PLA, (b) 40 wt% TCP, (c) 60 wt% TCP, (d) 40 wt% MgTCP (e) 60 wt% MgTCP, (f) 40 wt% Casein and (g) 60 wt% Casein at 28 days after immersion in SBF.

5.4 Discussion

Composites were chosen for use in this research because, currently, no single material exists which encompasses both adequate levels of bioactivity and mechanical properties similar to those of natural bone. Introducing filler materials into polymer films allows for greater control over the materials properties, including degradation rates and mechanical strength. In particular, the rate of degradation is studied through the addition of different

Ca P compounds; with primary focus on the influence β-TCP has on PLAs degradation rate. β-TCP is known and used in biomaterials for its resorbability and it is the aim of this work to produce materials with potential applications as scaffolds in areas of the body where high levels of bone regeneration are needed. This would require materials with controlled degradation rates, in order for the newly formed bone to replace the scaffold at the same rate as the scaffold degrades. Casein composites were synthesised primarily to evaluate their influence on cellular activity, but their degradation and mechanical properties have also been considered.

SEM imaging allowed the surfaces of the films to be studied, and also showed how the filler materials dispersed throughout the polymer matrix. Images of the unfilled PLA film indicated that the surface of the films was smooth. Each of the filled composite films, however, showed rougher surfaces. All β-TCP filler materials, both substituted and unsubstituted, were agglomerated fused spheres with smooth surfaces (Chapter 4). Casein nanoparticles, on the other hand, showed much less particle agglomeration. The morphology and extent of agglomeration in the filler particles appears to influence the degree of dispersion in the film. Those films which contained either form of β-TCP showed clusters of material forming throughout the film, as opposed to dispersing evenly. Casein nanoparticles were able to disperse to a greater and more even extent, although slight areas of clusters were still observed. In the 40 wt% films, the majority of the filler material was covered by a thin layer of PLA, with only the peaks of clusters uncovered and exposed to the surface. An increase in wt% of filler resulted in an increased amount of filler material exposed to the surface. Exposing filler particles at the surface, and thereby creating materials with a rougher surface, could be advantageous to the bioactivity of the composites, because research has shown rough surfaces to increase cell adhesion and differentiation.[31]

Raman spectra of the materials allowed for the identification of both matrix and filler components of the composite, and proved that the mixing stage of the synthesis was only physical and that no chemical reactions had occurred between the two components. Characteristic peaks for PLA were identified at 877cm^{-1}(C-COO stretching), 1040cm^{-1}(C-CH_3 stretching) and 1766cm^{-1}(C=O stretching). The presence of β-TCP was confirmed by the strong peak at 960 cm^{-1}, which is attributed to the $\nu 1$ PO_4 stretch.

Degradation studies investigate the rate at which materials degrade when placed in an aqueous medium. The first stage in the degradation process is the absorption of water into the composite; this initiates hydrolytic decomposition of the polymer chain.[32] Upon decomposition, oligomers are produced, which can be formed either on the surface or inside the matrix. Those formed on the matrix surface are able to easily escape into the surrounding solution, whilst those formed in the inside are forced to diffuse out slowly to the surface. In many instances the oligomers do not reach the surface, and instead cause an autocatalytic effect, increasing the rate of degradation inside the material.[33] However, in the case of the composites produced in these researches, which are very thin, this process seems unlikely to occur.

Although this degradation study focuses on the breakdown of PLA, it should be noted that dissolution of the filler particles into the surrounding solution will also influence mass loss. Amongst the PLA and both PLA-βTCP films, the least wet weight gain was observed by PLA. This is expected, as PLA is hydrophobic, and the unfilled film has no interfaces between filler particles and matrix through which water can diffuse. Those composite films with a higher wt% absorbed the maximum amount of liquid after the 1st week, confirming a relationship between the level of filler present, and the volume of liquid absorbed. This correlation has been confirmed in previous studies, wherein larger wt% of filler materials leads to more liquid absorption.[34] As it is believed that water tends to concentrate at the particle-matrix interface, it is probable that more filler results in more interface area for water to be adsorbed. After the initial 1st week the absorption levels decreased across all composites, indicating that polymer degradation and/or particle dissolution was contributing to mass loss.

The highest overall mass loss was seen in the 60 wt% PLA-βTCP film, with 4.98% of its original mass lost after 8 weeks. Each of the higher wt% filler composites showed significantly higher mass losses than their equivalents at 40 wt%. This could be due to increased dissolution of the particles. The PLA film lost, in comparison, 2.2% in 8 weeks. Each of the four TCP composite films, whether at 40 wt% or 60 wt%, all increased the rate of degradation of the PLA in the composite. This is in agreement with other studies, which argue that the increased resorbability and dissolution of β-TCP aids degradation.[35]

The degradation results discussed above have not taken into account those of the casein composites: these will be discussed separately. It is difficult to assess the rationale behind

degradation results without a thorough knowledge of the filler material. In both composite films, the lowest wet gain is observed, with losses of 2.3% and 3.4% for the 40 wt% and 60 wt% composite films, respectively. This indicates that the material is unable to absorb any liquid into the composite film, suggesting that the casein protein may be hydrophobic. Mass losses of 2.7% and 3.9% were noted for the 40 wt% and 60 wt% at 8 weeks, respectively.

In addition to degradative and bioactive properties, materials used in a scaffoldingcapacity must also be able to withstand the mechanical pressures exerted on them at the site of implantation. It is essential that they maintain adequate mechanical strength throughout the early degradation process, despite the ongoing decreases in molecular mass.Figure 5.29 displayed the initial tensile strengths of the composite films. The unfilled PLA film, with strength of 31.6 MPa, is below the typical range quoted for this polymer.[36] Casein nanopowders have reinforced the PLA matrix and increased its tensile strength.

It is evident from Figure 5.29 that the inclusion of the β-TCP particles synthesised in Chapters 3 and 4, both non-substituted and substituted, have a detrimental effect on the mechanical properties of the composite films. Loboa *et al* also found that the addition of β-TCP caused significant weakening in the tensile strength of PLA films, causing a decrease from 847 ± 89.43 kPa for neat PLA, to 336 ± 31.87 kPa for a PLA film with 5 wt % of β-TCP added.[37] Research shows that when particle to particle contact occurs within a polymer composite material, in that polymer does not completely surround each of the filler particles, the strength of the composite is compromised.[38] Further works would therefore concentrate on ensuring that thicker samples have better coverage of the filler with PLA. SEM images of all β-TCP samples show samples with severe agglomeration (Figure 5.36):

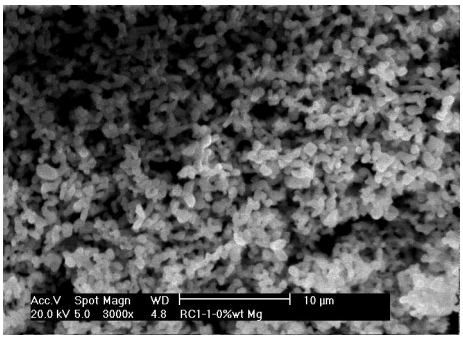

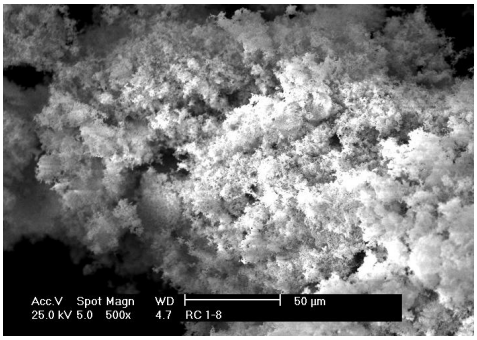

Figure 5.36 SEM micrographs showing the presence of highly porous agglomerated samples of a) β-TCP and b) MgTCP at 3000x

It could therefore be conceived that, whilst using these compounds as filler materials, the PLA polymer would never be able to infiltrate the agglomerated clusters and completely surround each particle separately. This means that there are high levels of β-TCP to β-TCP particle contact within the composite films, which leads to the low strength values observed in these films. In the case of the 60 wt% films, the situation is only worsened with the increase in filler content, as is seen in Figures 5.13 and 5.14. Even more particle to particle contact occurs, which accounts for the decrease in strength for these higher loaded films, in comparison to their 40 wt% counterparts.

One issue encountered in the mechanical testing of these composite films was the measurement of the sample thicknesses. As they were typically between 1.4-1.5 x 10^{-4} m, it proved difficult to attain accurate measurements. As discussed in section 5.2.2.5, laser displacement measurements were taken of the films; however several points in the film were averaged, and thereafter used as the sample thickness. The low strength observed in several of the composite films will result from the thinnest point in the films, yet the sample thicknesses used are averages which include some of the thickest points of the film. Therefore, an inaccurate representation exists between the mechanical properties and the sample thicknesses.

Individual studies of tensile strength variation with incubation in deionised water were conducted for each composite film. For both the β-TCP and MgTCP 40 wt% films, there was the minimum change in tensile strength, indicating that these two composites retained tensile strength effectively. The calcium phosphate materials have reinforced the PLA composites, and enabled them to withstand stresses throughout the incubation period with minimal loss. This is reinforced by reference to degradative results: PLA, β-TCP and MgTCP lost 2.22%, 2.54% and 2.28% of their dry mass loss over 8 weeks, respectively. With very little difference in overall mass loss, it can be assumed that such retention of strength is due to the presence of the filler. For the corresponding 60 wt% β-TCP and β-MgTCP films, the opposite is true; losses of 76% and 70% of tensile strength, respectively demonstrate that the filler materials have hindered the retention of mechanical strength. Again, it must be reminded that the higher loaded films degraded substantially throughout the same time period, which will naturally detrimentally affect the ability of the composite

films to withstand mechanical stress. There are two processes occurring simultaneously in solution, the first of which is the degradation of PLA to lactic acid, which is therefore chemically buffered by the β-TCP, keeping the pH neutral. Secondly, the absorption of liquid to the filler particle-polymer interface increases degradation at the interface. It appears that at 40 wt% the chemical buffering process is predominating, while at 60 wt% interface failure is the major problem.

Apatite layers are formed on the surface of bioactive materials upon implantation.[39] This layer consists of carbonate-containing hydroxyapatite, which is similar in composition and structure to bone apatite. As a result, osteoblasts are able to proliferate and differentiate preferentially on this apatite layer, producing apatite and collagen. It was proposed by Kokubo *et al* that the formation of an apatite layer on an artificial material was an essential requirement to bond to living bone.[25] To assess the potential bioactivity of materials in this capacity, but without the multiple complications of in vivo experiments, Kokubo synthesised a solution, Simulated Body Fluid (SBF), which mimicks ion concentrations nearly equal to those of human blood plasma. The evaluation was made that if an apatitic layer was formed in SBF, then that same material would induce the same formation of the bioactive layer in vivo. The apatite layer is formed from the initial formation of apatite nuclei which subsequently grow, consuming calcium and phosphate ions from the SBF solution.

After immersing all composite films in SBF solution for 28 days, the formation of an apatitic layer was highest on the 60 wt% PLA-βTCP samples, followed thereafter by the 40 wt% βTCP composite. The unfilled PLA film, in contrast, showed no apatite formation on its surface. Whilst a lack of apatite on the PLA film was expected, its absence was surprising with respect to the 40 wt% PLA-MgTCP and 60 wt% PLA-MgTCP films. The only difference in chemical composition between these, and the two β-TCP films which gave positive bioactivity results, was the substitution of Mg into the crystal structure. As this compositional change is so small, it is safe to assume that the difference in results must be a consequence of changes in surface area and dispersion of the filler material throughout the polymer film. Apatite layers preferentially form directly on top of bioactive calcium phosphate materials, and so if the filler material is severely agglomerated and poorly dispersed throughout the film; it can be assumed that the formation of apatite would be inhibited, as the apatite needs a nucleation point in the form of a filler particle to initiate deposition on the surface. SEM images of both the 40 wt% PLA-MgTCP and 60 wt%

PLA-MgTCP samples (Figures 5.11and 5.14) show the filler material to be agglomerated into large clusters, instead of being finely dispersed throughout the film. Although the equivalent β-TCP films also show agglomeration, it is not to the same extent. Both casein composite films, at both 40 and 60 wt%, show no apatite formation, despite the filler being dispersed finely throughout the surface of the film. It can therefore be concluded that the casein nanoclusters are not bioactive.

5.5 Conclusions

Non-filled PLA and PLA composite films were analysed using Raman spectroscopy, and surface features studied by SEM. Films with higher wt% of filler material exhibited surfaces with a roughened morphology and clusters of materials exposed at the surface, uncovered by PLA.

Degradation studies focused on the water absorption and weight loss of each film. Water absorption increased with filler content in the composite materials. Dry weight loss takes into account two processes contributing to overall mass loss; PLA breakdown and dissolution of filler particles. The highest overall mass loss was seen in the 60 wt% PLA-βTCP film, and each of the higher wt% composites showed substantially higher mass losses than their equivalents at 40 wt%. Dissolution of particles into surrounding solution is believed to be largely responsible for the increased mass loss. The degradation rate of PLA composite films can thus be adjusted by varying the concentration of calcium phosphate filler materials.

This study showed that the tensile strength of PLA composite materials depends on both the filler material and its concentration within the film. In all cases, as wt% of filler increased, the tensile strength of the films decreased. The 40 wt% PLA-Casein film was the only material to exhibit a stronger tensile strength than neat PLA, but this also decreased with an increase to 60 wt%. Interface failure is believed to be the major problem with the 60 wt% films, whilst particle-particle contact could explain the generally low strength results attained for the 40 wt%.

Bioactivity testing on all films, using SBF, showed formation of an apatite layer on both of the 40 and 60 wt% PLA-βTCP composite materials. Apatite layers were absent from all other samples.

In order for a biomaterial to be employed successfully in a scaffolding capacity, it must possess mechanical properties similar to bone, and have a degradation rate which can be adjusted to suit a range of clinical applications. However, it is not enough for a material to fulfil the mechanical and physical requirements of a scaffolding material; it must also illicit a biological response to encourage osteogenesis. The composite films tested in this chapter will be assessed for their biological activity in the next chapter.

5.6 References

[1.] Springer Handbook of Mechanical Engineering,K. H. Grote, E. K. Autosson, *Springer*, New York, 2009, 110

[2.]Engineering Materials, 3rd Edition, M. A. Ashby and D. R. H Jones, *Butterworth Heinemann*, Oxford UK, 2005, 121

[3.]College Physics, 9th Edition, R. A. Serway, J. S. Aughn, C. Vuille, *Brooks/Cole*, 2009, 437

[4.] General Chemistry, 3rd Edition, D.D. Ebbing, S. D. Gammon, *Houghton Mufflin Company*,Boston USA, 2002, 1185

[5.]D.K. Gilding, A. M. Reed, *Polymer*, 1979, **20**, 1459

[6.] Advances in Biochemical Engineering/ Biotechnology 102,K. Lee, D. Kaplan, C. Chan, *Springer*, 2006, 63

[7.] Biomaterials Science, 1st Edition, B. D. Ratner, A. S. Hoffman, F. J. Shoen, J. E. Lemons, *Academic Press*, 1996, 50

[8.] A Manual for Biomaterials/Scaffold Fabrication Technology, G. Khang, M.S. Kim, H.B. Lee, *World Scientific Publishing Company*, 2007, ISBN: 9812705953

[9.]Organic Chemistry,11th Edition, H. Hart, L. E. Craine, D. J. Hart, *Houghton Mifflin Company*, 2003, 481

[10.] L. S. Nair, C. T. Laurencin, *Prog. Pol. Sci.*, 2007, **32**, 762

[11.] A. Talal, *PhD Thesis*, University of Glasgow 2010

[12.] P. U. Rokkanen, O. Bostman, E. Hurrensale, E. A Makela, E. K. Portio, H. Paticula, S. Vainiopaa, K. Vihtonen, P. Tormaila, *Biomater.*, 2000, **21**, 2607

[13.] V. Lassalle, M. L. Ferreira, *Macromol. Biosci.*, 2007, **17**, 767

[14.] D. Garlotta, *J. Polym. Environ*., 2001, **9**, 63

[15.] K. Boua-In, N. Chaiyut, B. Ksapabutr, *Optoelectron. Ad. Mat.*, 2010, **4**, 1404

[16.] B. Gupta, N. Revagade, J. Hilborn, *Prog. Pol. Sci.*, 2007, **32**, 455

[17.] J. Huang, M. S. Lisowki, J. Runt, E. S. Hall, R. T. Kean, N. Buchter, *Macromolecules*, 1998, **31**, 2593

[18.] J. A. Cicero, J. R. Dorgan, *J. Polym. Environ*., 2001, **9**, 1

[19.] R. A. Miller, J. M. Brady, D. E. Cutright, *J Biomed. Mater. Res.*, 1977, **11**, 711

[20.] T. Nakamura, S. Hitomi, S. Watanabe, *J Biomed. Mater. Res.*, 1989, **23**, 1115

[21.] S. Li, *J Biomed. Mater. Res.*, 1999, **48**, 342

[22.] B. C. Benicewicz, P. K. Hopper, *J. Bioact. Compat. Pol*., 1990, **5**, 453

[23.] S. Vainionpaa, P. Rokkanen, P. Tormala, *Prog. Pol. Sci*.,, 1989, **14**, 616

[24.] R. K. Kulkarni, E. G. Moore, A. F. Hegyeli, F. Leonard, *J Biomed. Mater. Res.*, 1971, **5**, 169

[25.] T. Kokubo, H. Takadama, *Biomater.*, 2006, **27**, 2907

[26.] T. Kokubo, *Biomater.*, 1991, **12**, 155

[27.] T. Kokubo, M. Kushiyani, Y. Ebisawa, T. Kitsugi, S. Kotani, K. Oura. H. Aaki, K. Sawai, *Bioceramics*., 1988, **1**, 157

[28.] M. Neo, S. Kotani, T. Nakamura, C. Ohtsuki, T. Kokubo, *J Biomed. Mater. Res.*, 1992, **26**, 1419

[29.] R. Z. Legeros, S. Lin, R. Rohanizadeh, D. Mijares, J. P. Legeros, *J Mater. Sci.-Mat. Med.*, 2003, **14**, 201

[30.] I. Rehman, R. Smith, L. L. Hench, W. Bonfield, *J. Biomed. Mater. Res.*, 1995, **29**, 1287

[31.] M. Ball, D. M. Grant, W. J. Lo, C. A. Scotchford, *J Biomed. Mat. Res. Part A*, 2008, **86A**, 637

[32.] Poly (lactic acid): Synthesis, Structures, Properties, Processing and Applications, R. A. Auras, L-T. Lim, S. E. M. Selke, H. Tsuji., *Wiley*, 2010, 343

[33.] I. Grizzi, H. Garrew, S. Li, M.Vert, *Biomater.*, 1995, **16**, 305

[34.] J. Suwanprateeb, K. E. Tanner, S. Turner, W. Bonfield, *J Mater. Sci.*, 1997, **8**, 469

[35.] P. Ducheyne, S. Radin, L. King, *J Biomed. Mat. Res.*, 1993, **27**, 25

[36.] Handbook of Engineering Biopolymers: Homopolymers, Blends & Composites, S. Fakirov, D. Bhattachoryya, *Hanser*, 2007, 132

[37.] S. D. McCullen, Y. Zhu, S. H. Bernacki, R.J Narayan, B. Pourdeyhimi, R. E. Corga, E. G. Loboa, *Biomed. Mater.*, 2009, **4**, 9

[38.] W. Bonfield, *J Biomed. Eng.*, 1988, **10**, 522

[39.] O. P. Filho, G. P. LaTorre, L. L. Hench, *J Biomed. Mater. Res*., 1996, **30**, 509

6. Bioactivity of Composites

6.1 Introduction

6.1.1 Osteogenic Differentiation

Human mesenchymal stem cells (hMSC) are multipotent stem cells of the bone marrow which are able to differentiate along the osteogenic lineage.[1] The expression of genes and proteins during osteogenic differentiation from stem cells has been extensively studied to further understand the relationship between bone growth and differentiation. An appreciation of the time points of different genes and proteins allows for the establishment of differentiation activity occurring on the surfaces of materials.

In 1993 early work by Stein *et al* stated that osteogenic differentiation is coupled with a decrease in cell proliferation. This decrease causes an increase in extracellular matrix proteins such as type I collagen (COL) and fibronectin (FN). Osteopontin (OPN) and osteocalcin (OCN) proteins are observed in the last stage of osteogenic differentiation, mineralisation (Figure 6.1). In addition, OPN is also expressed during the period of active proliferation.

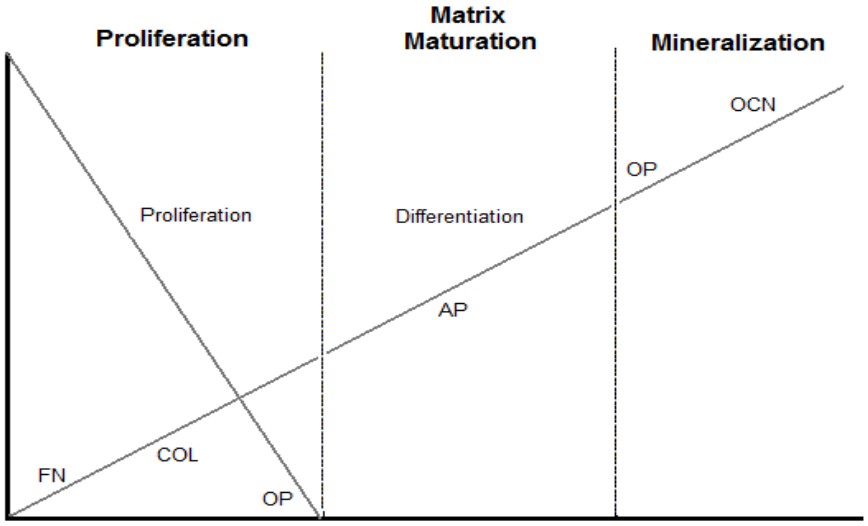

Figure 6.1 Osteogenic differentiation. Differentiation occurs in three stages, the first stage being proliferation. A decrease in proliferation coincides with an increase in markers associated with the extracellular matrix. The last stage, mineralization of the extracellular matrix (ECM), sees an increase in osteogenic markers osteopontin and osteocalcin. (Image adapted from(Stein and Lian 1993))[2]

More recently, Runx2, a key transcriptional factor (sometimes called the osteogenic master gene) is involved in the signalling and control of osteoblast differentiation through regulation of bone-related genes. It has been shown to induce osteoblast differentiation at the early stage of the differentiation process, and inhibit it at the late stage.[3]

6.1.2 Focal adhesions and cell cytoskeletons

Stimulating bone tissue formation e.g. osteogenesis starts at the adhesion level.Osteogenic activity of biomaterials requires an increase in the attachment and spreading of osteoblasts to the material surface. Links between the cells and surfaces of biomaterials are initially formed by attachments called focal adhesions, which are critical to cellular responses to biomaterials.[4] Focal adhesions are found around the periphery of a cell, and are commonly between 2-5 μm in length.[5]

The second stage after focal adhesion formation is the development and organisation of the cell cytoskeleton. This refers to the internal framework of a cell, composed largely of actin (microfilaments) and tubulin (microtubules) and also including intermediate filaments (vimentin for mesenchymal-origin cells).[6] Actin is a 43 kDa protein, the most abundant protein to be found in typical eukaryotic cells. Microfilaments simply refer to linear assemblages of this structural protein. Microtubules are assemblages of the 110 kDa tubulin dimer protein. In addition to providing structural stability, the cytoskeleton is responsible for cell movements, which includes the internal transport of organelles through the cytoplasm, as well as overall movement of the cell.[7] If cells react favourably to a biomaterial's surface, focal adhesions are formed which support polymerisation and contractionof mature actin stress fibres and tubulin networks for vesicle movement. The cells spread rapidly across the material surface and become metabolically active.

All three features (focal adhesions, tubulin and actin formation) are of great importance for cellular activity because integrin proteins (transmembrane proteins capable of binding proteins of the ECM) located within both the actin cytoskeleton and adhesion plaques are involved in signal transduction and other key stem cell functions, which can affect cell differentiation.[8] For this reason, it is important in this research to study the extent of focal adhesions and cytoskeletal activity (cell spreading) on the surfaces of the film samples.

Cytoskeletal networks are thought to maintain a constant, basal level of tension, mainly through actin/myosin interactions causing contraction. Any disruptions in the surrounding environment of the cytoskeleton will consequently affect the overall cytoskeletal tension, initiating cellular deformation. [9] The manipulation of cytoskeletal tension has been proven to influence stem cell differentiation, with higher levels of cytoskeletal tension inducing osteogenic differentiation and osteogenesis, whilst lower tensions favoured adipogenic differentiation.[10]

Research conducted by Biggs *et al* studied the differences in focal adhesions and cellular spreading in human osteoblast cells (HOBs) in relation to materials with different surface features (the subject of altering surface properties to influence bioactivity will be discussed further in section 6.1.3).[11] Significant differences were noted for cells seeded onto planar substrates, and substrates which possessed a nanopit surface array. HOB's on planar control substrates were observed to spread rapidly and formed numerous adhesions to the substrate surface. Nanopit arrays, conversely, disrupted cellular spreading and adhesion formation in HOB's (Figure 6.2).

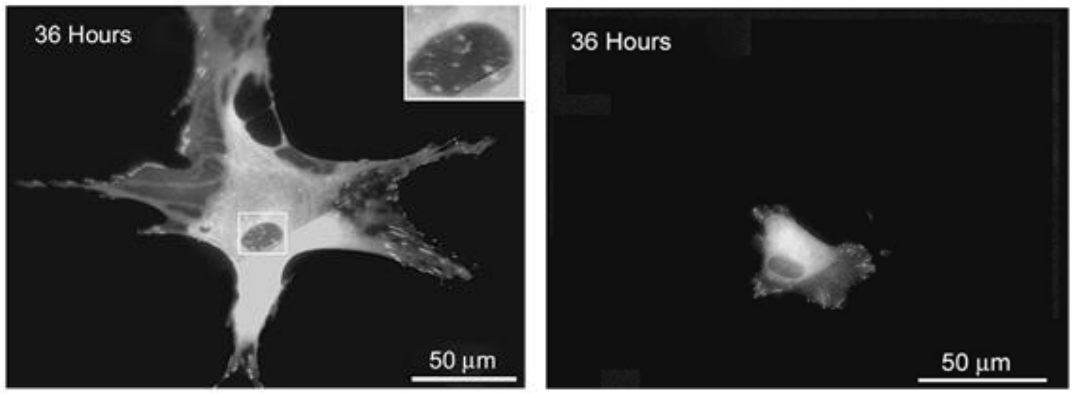

Figure 6.2 YFP-vinculin analysis of the dynamics of adhesion formation in HOB's on (a) planar and (b) nanopit arrayed substrates. Focal Adhesions are observed on the planar substrate, and the mechanism of cellular spreading is also observed. The onset of cell spreading was reduced in the nanopit arrayed substrates, with focal complexes formed at the periphery.

As cells establish dynamic contacts with the underlying substrates through focal adhesions, integrin proteins found within both these adhesions and the cytoskeleton of the cell are responsible for activating signalling pathways that direct cell growth and differentiation, it is conceivable that the more 'links' a material can form with the cell population, the higher

level of ‘biological activity’ it will possess. This increases the potential of the biomaterials to attain clinical success as an implant material.

6.1.3 Topography

Altering the surface topography of a material is known to be important in the cell-material interaction, allowing cell adhesion and migration, amongst other cellular functions.[12,13] Cell-substrate interactions define a biomaterials performance, and determine the long-term viability of the device. The manipulation of integrin protein binding through topography holds great interest due to the regulatory role the proteins play in key stem cell functions. Nano scale topography (nanotopography) is increasingly used to infer bioactivity because the features it creates are relative to the size of integrins (approximately 10 nm).[5] The number of focal adhesions between a cell-material interface, and the maturity of the cytoskeleton, are thereby thought to be affected by nanotopography. It was proven that disordered (controlled levels of disorder) surfaces promoted the formation of larger focal adhesions and osteogenic differentiation of mesenchymal stem cells (MSCs), whilst ordered (or totally random) surfaces did not.[14]

For HA composites, the influence of topography has been investigated for both focal adhesion and cytoskeletal behaviour.[15] Two different HAPEX® surfaces were used for the study; one of which was attained through polishing (to expose HA) and roughening (sonication with alumina to give a topography), whilst the other surface was simply as-machined. The treated surface shows a good dispersion of HA on the surface, whilst the as-machined sample shows very little HA on the surface. Results indicate that the optimised surface establishes contacts and cytoskeletal maturity before the machined sample, again indicating that the bioactivity of a sample can be improved through the manipulation of a material surface using topography. Further study into osteogenesis indeed confirmed increased bone formation on the optimised surface. [16]

These studies demonstrate something of greatpotential importance to this thesis: the polymer can form a thin film over the bioactive mineral that can be detrimental to cell performance. Thus, whilst study of topography *per se* is out of remit, the surface was considered. To this effect, each film was plasma etched after production, and before seeding any cell populations on the sample surfaces. Plasma etching is a constituent of plasma processing, which is a technology aimed at altering the physical and chemical

properties of a surface through plasma-based material processing. Etching involves removing material from the surface by bombarding it with a high energy source of atoms, a percentage of which can be in the form of either ions or radicals.[17] These volatile particles can form chemical reactions with the material surface being etched, thereby removing unwanted layers, or simply sputter material off the surface.[18] Plasma etching, and its subsequent alteration of surface properties, has been proven to affect the cell growth and morphology of human fibroblast cells.[19]The aim of plasma etching in this research is to remove the surface layer of PLA from the composite films, thereby exposing the filler materials at the surface, wherein easier contact with osteoblast cells can be established. This is, in turn, hoped to increase the biological viability of the samples, if the cells are able to attach and spread across the material surfaces to a greater extent.

6.2 Experimental

6.2.1 Plasma etching

Plasma etching of the composite films was achieved using a Harrick Plasma Cleaner, model PDC-001/002(115/230V), as shown in Figure 6.3. 1cm^2 samples of all films were secured inside the cleaner, and the chamber was closed and secured. Once a sufficient vacuum had been reached, the radiofrequency was switched on for 5 seconds after activation, and the samples thereafter removed.

Figure 6.3 Harrick plasma cleaner

6.2.2 Cell culture

Human bone marrow osteoprogenitors were obtained from haematologically normal patients undergoing routine surgery, using only tissue which would have been discarded afterwards. Cells were grafted by Carol-Anne Smith after initial ficol gradient and plating of the cells in tissue culture flasks.

Passage 1 osteoprogenitor cells were grown in 75 cm^2 tissue culture flasks, at 37°C with 5% CO_2, in 20ml of DMEM media (Dulbecco's modified eagles medium with 10 % foetal bovine serum (FBS)). Fresh media was added every 3 days, until 80-90% confluency was obtained. Flasks were rinsed with HEPES saline before trypsinization by adding 5 ml of trypsin/versene solution (20ml versene in 0.5 ml trypsin) and incubating at 37°C for 5 minutes to let cells detach. DMEM media was thereafter added (5ml) to deactivate the trypsin, and centrifugation at 1,400 rpm for 5 minutes collected the cell suspensions. The suspensions were resuspended in 1 ml of media solution and counted using a cell haemocytometer, before seeding cells onto the surfaces of the composite films.

6.2.3 Immunofluorescence

Similar procedures were employed to view cells on materials for fluorescent microscopy studies, differing only in the various antibodies used. Cells were seeded onto the film surfaces at 1×10^4 cells / ml and cultured for 7, 10, 21 and 28 days in DMEM media at 37 °C with 5% CO_2, with the media changed twice weekly. At each time point the cells were fixed in 4 % formaldehyde for 15 minutes, and thereafter permeabilised in permeabilising buffer for 5 minutes. To make a solution of permeabilising buffer, the following chemicals were required into 100 ml of phosphate-buffered saline:

- 10.3 g sucrose
- 0.292 g NaCl
- 0.06 g $MgCl_2$
- 0.476 g HEPES

The pH of the solution was thereafter adjusted to 7 and 0.5 ml of Triton X added to complete the solution. The buffer was removed and the cells blocked for non-specific antibody using a 1 % BSA/PBS solution for 5 minutes, and samples were then stained for

osteogenic markers using mouse-monoclonal OPN antibody (1:50) (Santa Cruz Biotechnology), mouse-monoclonal β3-tubulin (1:50) (Santa Cruz Biotechnology)and rhodamine-phalloidin (to stain actin) (1:50) (Sigma) for 1 hour at 37 °C. The stain was removed and the cells washed gently in PBS/0.5% Tween (detergent) 3 times. An anti-mouse secondary biotinylated (1:50) antibody (Sigma) was then added and incubated for 1 hour at 37 °C. Samples were again washed three times to remove the secondary antibody with the Tween solution. A tertiary FITC-labelled streptavidin probe (1:50) (Sigma) was added and incubated at 4 °C for 30 minutes. The tertiary probe was washed away using the Tween solution again, and mounted in a fluorescent mountant that contains the fluorescent DNA stain DAPI (to stain cell nuclei). This process was repeated at 10 and 21 day time points.

6.2.4 RNA isolation

After cells were seeded and cultured to the appropriate time points, they were lysed and RNA extracted using a Qiagen RNeasy Micro Kit, in accordance with the manufacturers' protocols (Qiagen, West Sussex, UK).

Initially, the cell suspension was homogenised by vortexing and passing the lysate solution through a 20-gauge syringe needle. 70 % ethanol was added to the homogenised lysate, mixed, and centrifuged at 8,000 g for 15 seconds. To denature proteins, buffer RW1 (containing guanidine thiocyanate) was added to the spin column (350ml). The spin column was centrifuged again at 8,000 g for 15 seconds. A solution of DNase I and the spin column was centrifuged for 15 seconds at 8,000 g. After washing, all filtrate was discarded and washings with buffer RPE and ethanol, consecutively, were conducted to precipitate the RNA. To remove any remaining ethanol, the filter was centrifuged at full speed for 2 minutes. The filter was redispersed in a 1 ml Eppendorf tube with 14 µl of RNase-free water. Both the tube and filter were centrifuged at full speed for 1 minute and the yields of RNA extracted were measured with a NanoDrop® ND-1000 UV-Vid Spectrophotometer at ratios of 230/260 nm and 260/280 nm.

6.2.5 cDNA synthesis

To convert the obtained RNA into the corresponding DNA, the RNA was reverse transcribed using the Qiagen QuantiTect® Reverse Transcription Kit (Qiagen, West Sussex, UK).

Initially, a 10 µl solution of RNA was prepared, containing equal concentrations of RNA, and the volume made up with RNase-free water. The solutions were incubated at 42 °C for 2 minutes, and then placed immediately on ice. A reverse transcription factor master mix was prepared, in order to synthesise first strand cDNA, to a volume of 20 µl:

Quantiscript Reverse Transcriptase	1 µl
Quantiscript RT Buffer, 5×	4 µl
RT Primer Mix	1 µl
Template RNA	14 µl

The master Mix and RNA samples were added together and chilled on ice whilst the thermal cycler programme was set. The following programme was used to run the thermal cycler:

25 ^{o}C	10 min
37 ^{o}C	120 min
85 ^{o}C	5 min
4 ^{o}C	hold

6.2.6 Quantitative real time PCR

Osteoprogenitor cells were cultured on the composite films for 7 and 10 day time points (3 replicas for each material). As described in section 6.2.4, the cells where thereafter lysed and RNA extracted using a Qiagen RNeasy micro kit (Qiagen, UK). Following this, RNA samples were reverse transcribed using Qiagen QuantiTect® Reverse Transcription Kit (Qiagen, UK).

To conduct real-time qPCR analysis, the 7500 Real Time PCR system from Applied Biosystems was used. The housekeeping gene used was β-actin, with expression of genes

normalised to β-actin expression. Using the SYBR green method of analysis, 18 µl of mastermix was added to each well, together with 2 µl of each cDNA sample:

Quantifast SYBR Green PCR Kit	10 µl
Forward primer (100 µM)	0.3 µl
Reverse primer (100 µM)	0.3 µl
RNase free water	7.4 µl

The comparative cycle-threshold method[20] was used for quantification of OPN gene expression, and the relative transcript levels expressed as ± s.d. for plotting as graphs. Significance was calculated using paired t-test.

6.3 Results

6.3.1 Plasma etching

As discussed in section 6.1.3, evidence has proven that altering the topography of surfaces influences cellular activities including cell attachment and proliferation. To this effect, each composite film was plasma etched for two reasons; firstly, to remove any surface impurities or particles from the materials, and secondly, to remove the top cover layer of polymer film from the surface, exposing the filler materials to the cells directly. It is hypothesised that allowing the cells more direct access (i.e. not relying on biodegradation) to the filler materials could increase bioactivity levels.

Preliminary experiments on the duration of plasma treatment of the samples had to be performed. Three experiments were conducted, with treatment times of 0, 5 and 25 seconds and the resultant surfaces were examined using atomic force microscopy (AFM). The results shown are from experiments using the casein/PLA nanocluster materials. These were used as a model material while the nanoscale β-TCP composites were being developed. Using a protein also confers advantage as antibodies could be used to probe exposure.

6.3.1.1 Zero seconds

Figure 6.4 shows the AFM results attained from the control sample with no plasma treatment. The surface looks very polymeric, suggesting the smear which is to be expected from a sample with no etching i.e. there are no nanoclusters present on the surface. Results from roughness analysis confirm that there are no casein nanoclusters on the surface; the control is smooth with a mean roughness (Ra) of 12.5 nm over the 40 µm scan.

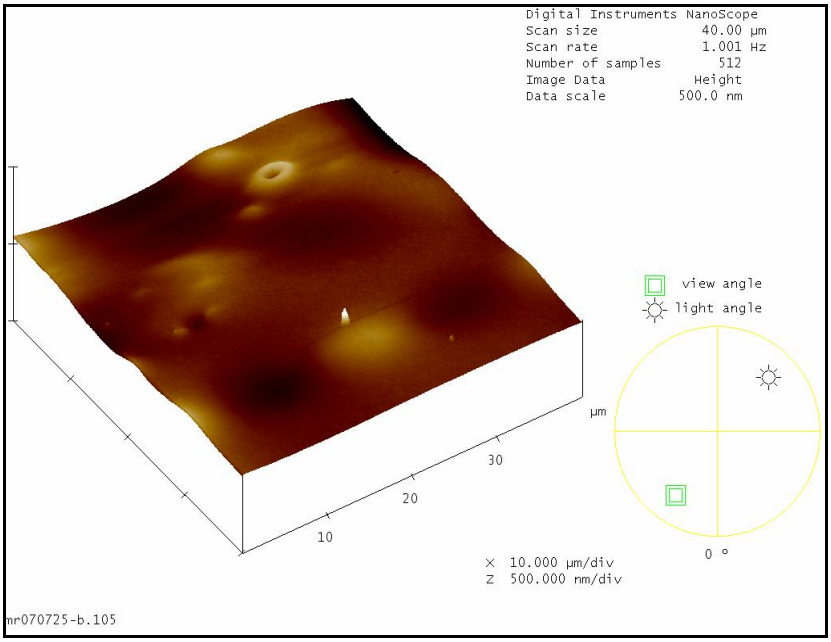

Figure 6.4 AFM image of casein/PLA composite surface with no etching (40 µm scan)

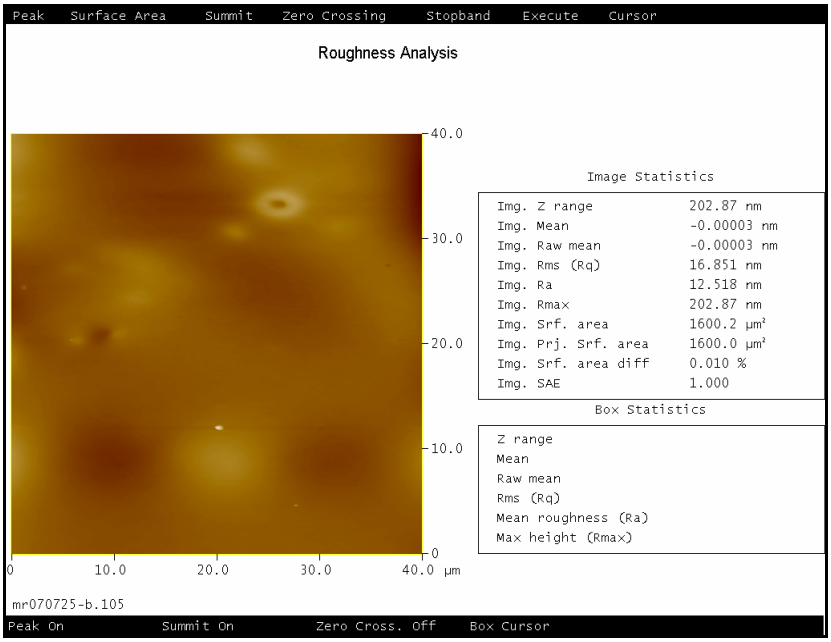

Figure 6.5 AFM roughness analysis of casein/PLA composite films after no etching

6.3.1.2 Five seconds

The landscape of samples etched for 5 seconds is very different from the control. It would appear that the large ‘cliffs’ (shown as the whiter regions in Figure 6.6) are clusters of clusters of the casein material and that the AFM etch has preferentially removed the softer polymer. Whilst the control samples possessed a mean roughness of 12.5 nm, a rougher terrain with larger peaks on the surface is noted for the five second samples, which have, in direct contrast, a mean roughness of 118.6 nm (Figure 6.7). Just below the bottom cliff in Figure 6.6 are some speckles, which were zoomed in on Figure 6.8. These potentially show individual clusters at around the expected 40 μm in size.

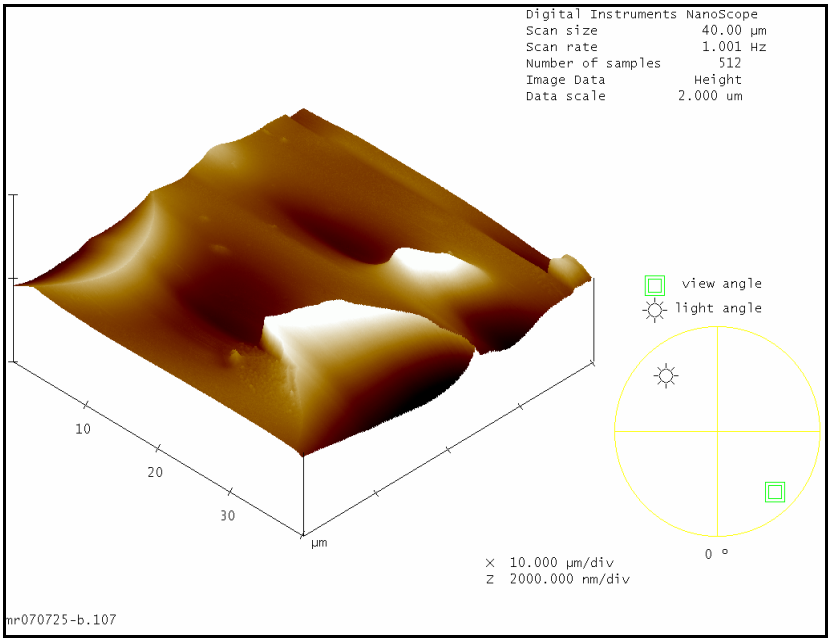

Figure 6.6 AFM image of casein/PLA composite surface after 5 seconds etching (40 μm scan)

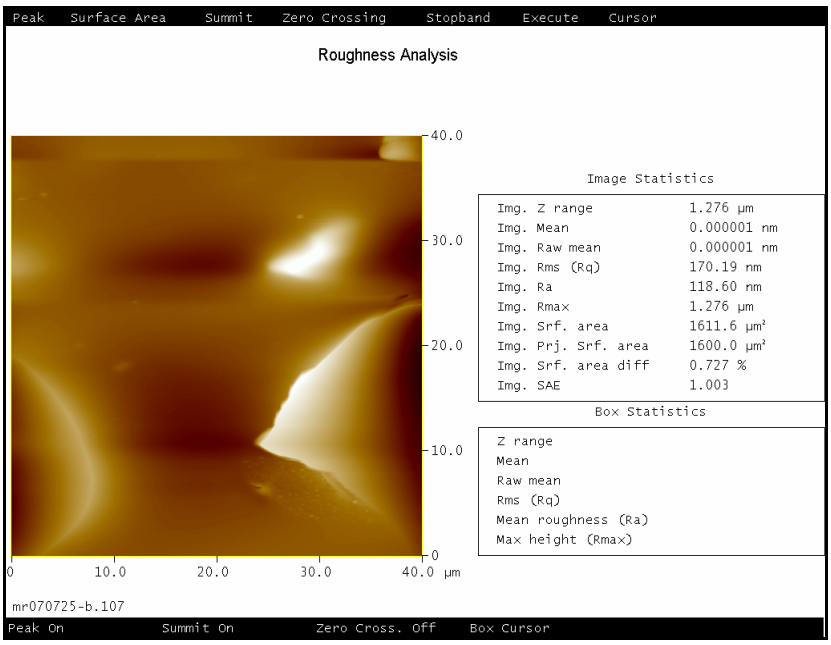

Figure 6.7 AFM roughness analysis of casein/PLA composite films after 5 seconds etching

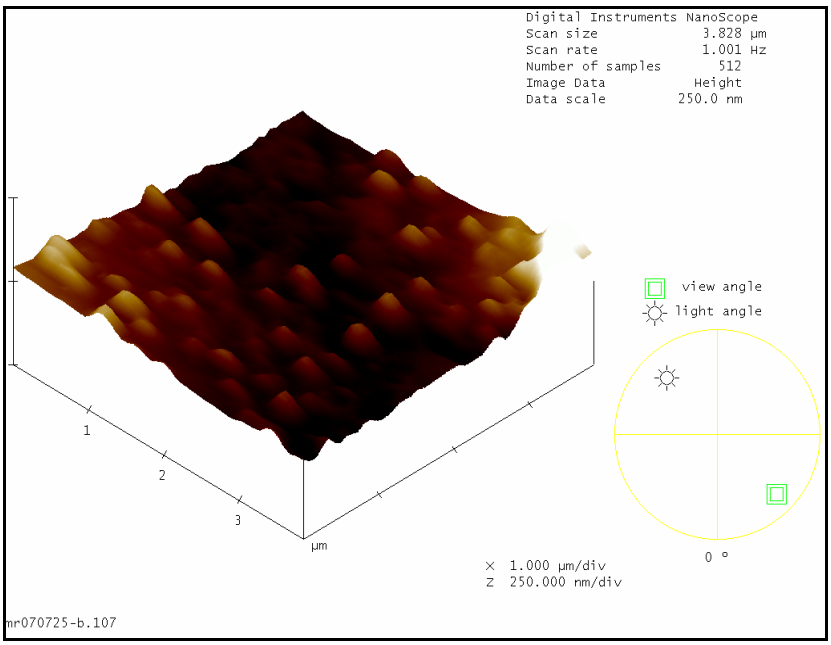

Figure 6.8 AFM image of cas/PLA composite surface after 5 seconds etching (3.8 µm scan)

6.3.1.3 Thirty seconds

The AFM image from the casein/PLA film etched for thirty seconds is shown in Figure 6.9. The sample is very flat and smeared in appearance; this could be the result of too long an exposure to the plasma and subsequent melting of the polymer. Roughness analysis of the same sample (Figure 6.10) also indicates a flattened surface, with no clusters present on the surface and a mean roughness of just 7.3 nm.

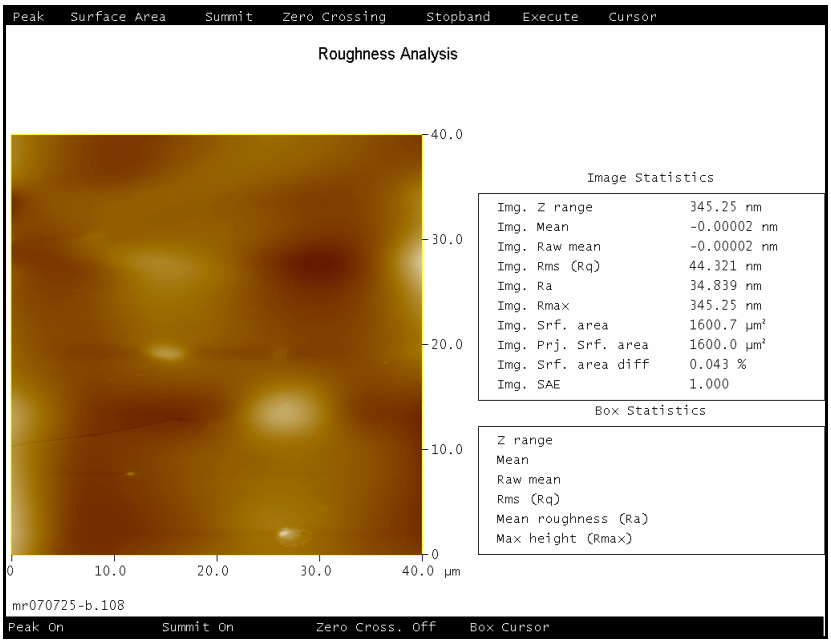

Figure 6.9 AFM image of casein/PLA composite surface after 30 seconds etching (40 µm scan)

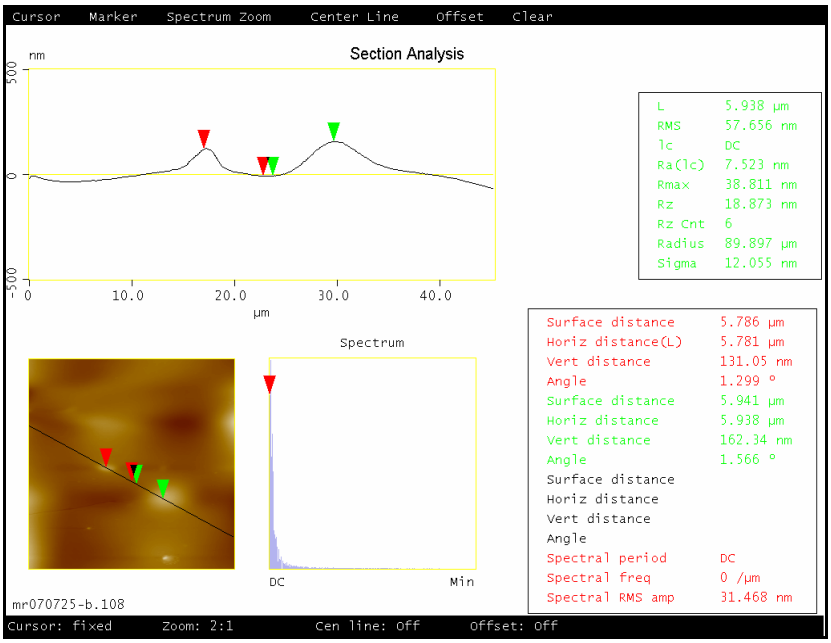

Figure 6.10 AFM roughness analysis of casein/PLA composite films after 30 seconds etching

6.3.2 Fluorescent Microscopy

Antibody labelling and fluorescent microscopy studies were conducted to confirm AFM results and to ascertain whether the protein could survive the film fabrication and etching without major structural damage or denaturation. Figure 6.11 (a-b) indicate fluorescence

results of the casein films with no etching; it is clear that the sample is largely void of any fluorescence, indicating that no casein is present on the surface. Samples etched for five seconds, conversely, show a high level of fluorescence when viewed under microscope (Figure 6.11 (c-d)). Increasing etching duration to 30 seconds (Figure 6.11 (e-f)) generates images similar to those seen for the control sample, as again very little active fluorescence is noted.

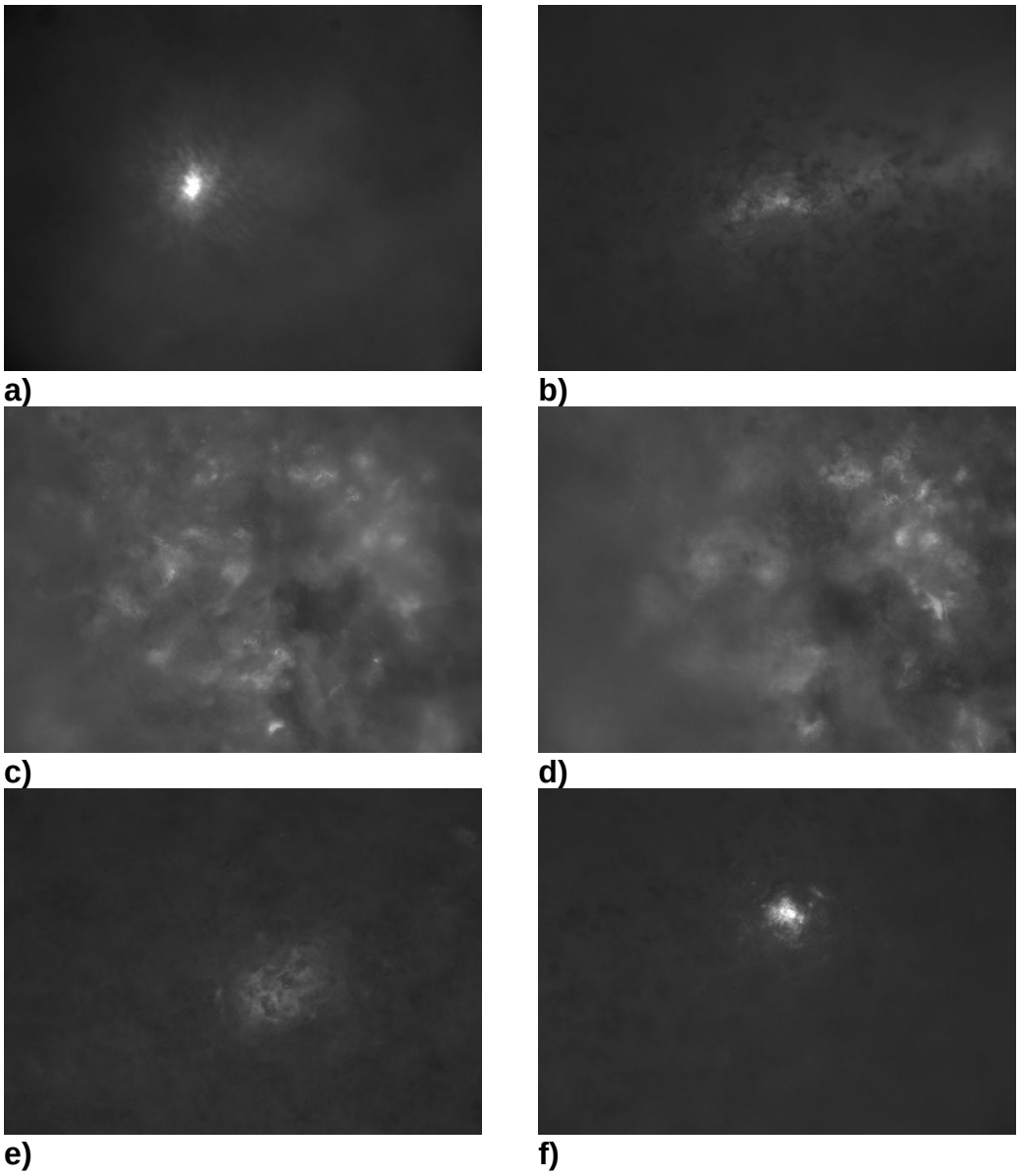

Figure 6.11 Fluorescent microscopy images for casein/PLA composite films etched for (a-b) zero seconds, (c-d) five seconds, and (e-f) thirty seconds

6.3.3 Immunofluorescence studies

Due to results obtained from section 6.3.2, all further samples tested were etched for five seconds before cell culture. Figure 6.12 shows actin/vinculin staining for focal adhesions in the film samples after 10 days. Whilst the PLA film (6.12 (a)) showed several adhesions, greater attachment is observed in the β-TCP and MgTCP images (6.12 (b) and (c), respectively). Focal adhesions, highlighted as white dots, are visible around the periphery of the cells and at the end of actin bundles. Casein composites (6.12 (d)) show weak anchoring to the material surface, with no mature focal adhesions visible. Stress fibres from actin organisation are prominently observed in the β-TCP and MgTCP images (6.12 (b) and (c), respectively). Although actin organisation is also present in the PLA sample cells, it appears to be at a lesser extent, whilst the casein sample shows weaker actin organisation again (6.12 (a) and (d), respectively).

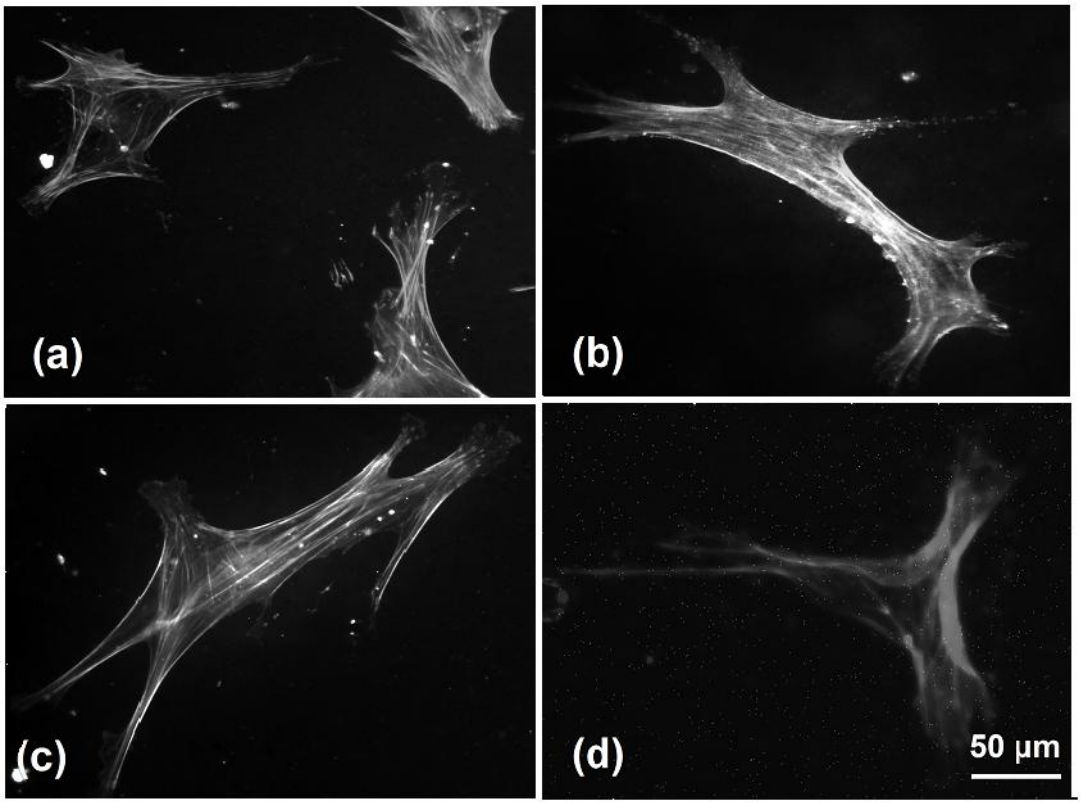

Figure 6.12 Vinculin and actin staining for focal adhesions and cytoskeleton on (a) PLA, (b) TCP, (c) Mg-TCP and (d) casein composite samples. Adhesions are observed as white dots around the periphery of the cells. Weaker attachment is noted for both the PLA (a) and casein (d) films, whilst mature focal adhesions are shown for both the TCP (b) and Mg-TCP (d) samples. Scale = 50 µm. Similarly, higher levels of actin organisation and stress fibres are observed on the surfaces of theTCP (b) and Mg-TCP (c) samples.

Actin and tubulin staining provide information on the structure and organisation of the cell cytoskeleton. An increased level of organisation of the microtubule network is seen for both the TCP and Mg-TCP composite film samples (Figure 6.13 (b) and (c), respectively), whilst only weak staining of tubulin is noted for both the PLA and Casein samples (Figure 6.13 (a) and (d), respectively). Similarly, actin shows good organisation in both TCP samples, and is least organised in the PLA and casein films.

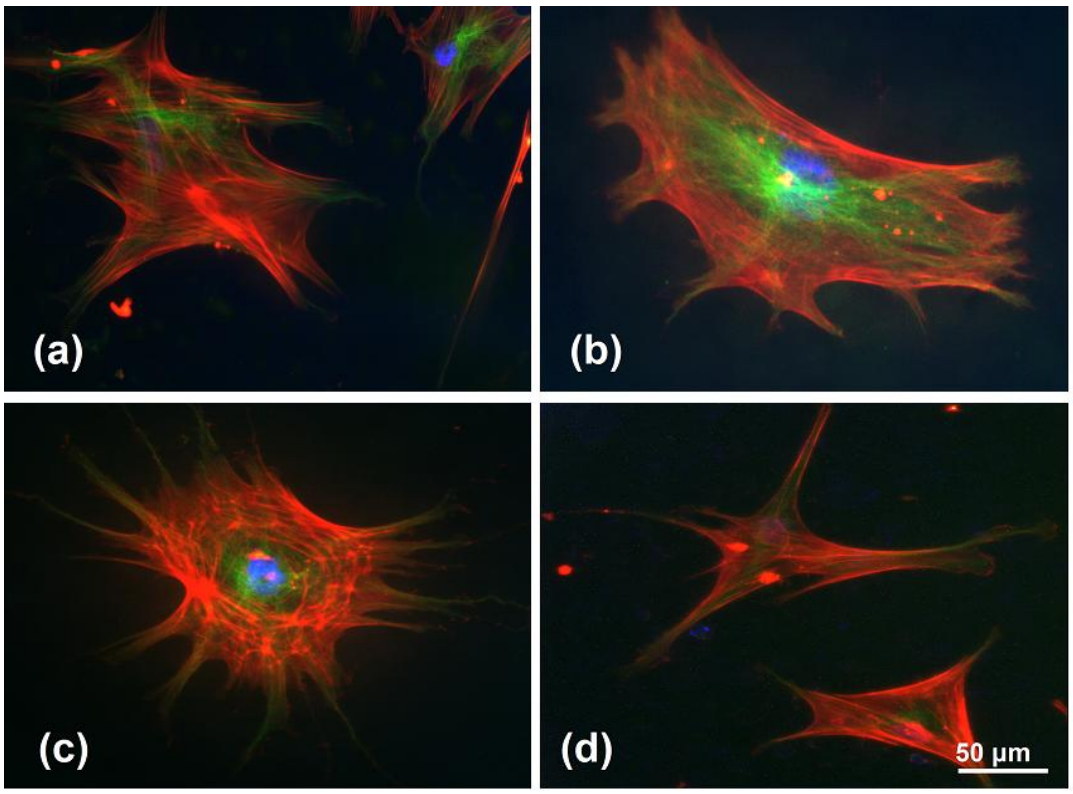

Figure 6.13 Tubulin and actin staining for cytoskeleton on (a) PLA, (b) TCP, (c) Mg-TCP and (d) casein composite samples. Tubulin = green, actin = red, nuclei = blue. Well organised and substantial microtubule networks (green) are observed for both the TCP (b) and MgTCP (b) samples. Good organisation of actin is also noted for the two TCP samples (red). Microtubule networks are limited in both the control PLA sample (a) and the casein composite (d), with lower levels of actin organisation also presented. Scale = 50µm.

Both the β-TCP and MgTCP composite film samples, which each showed high levels of actin and tubulin organisation within the cell cytoskeleton, also stained positively for OPN expression (Figure 6.14 (b) and (c), respectively), indicating the production of the glycoprotein, which is required for bone formation. PLA and casein samples, conversely, showed no staining for OPN on the material surface. (Figure 6.14 (a) and (d), respectively)

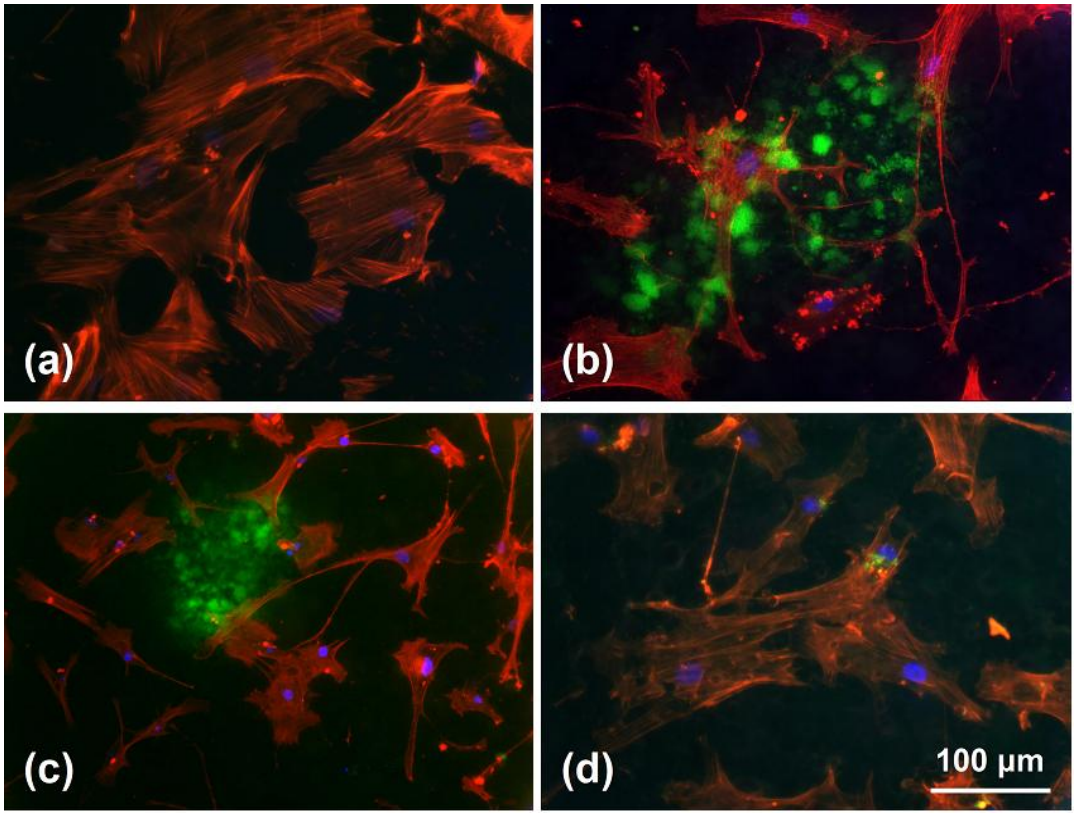

Figure 6.14 Osteopontin staining on (a) PLA, (b) TCP, (c) Mg-TCP and (d) casein composite samples. Green = OPN, red = actin, blue = nuclei. Both the TCP (c) and MgTCP (d) samples stain positively for osteopontin, showing distinct areas of high expression on the sample surfaces. PLA (a) and casein (d) samples indicate negligible expression for OPN. Scale = 100 µm.

6.3.4 real-time Polymerase Chain Reaction (PCR)

Verification of previous immunofluorescence results, which indicate that both β-TCP composite films facilitate the highest levels of cellular activity, was carried out at a transcriptional level through PCR studies. Runx 2 expression levels were studied for each of the four films at 7 and 10 day time points, and Figure 6.15 displays results. An up-regulation in Runx-2 expression is observed for the Mg-TCP film sample at 7 days, with an expression level of 1.24, compared to the PLA control expression of 1. No distinct changes in expression levels are noted for the β-TCP or casein films at 7 days.

Across all three composite films at the 10 day time-point, nothing has changed significantly from the control.

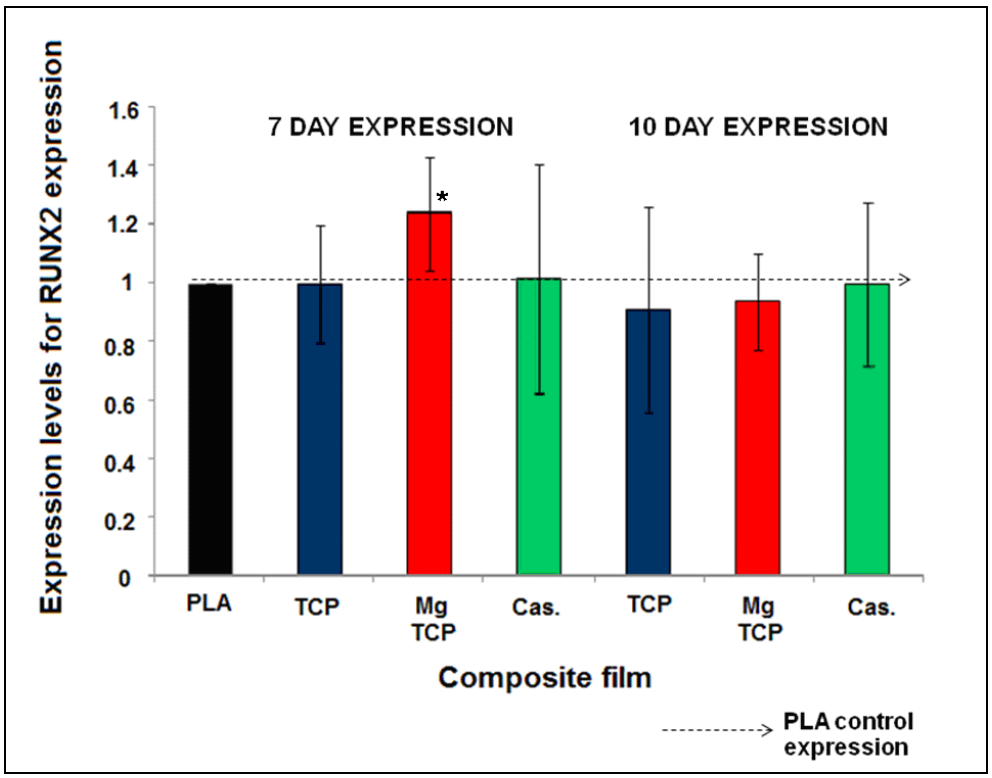

Figure 6.15 Expression levels for the Runx-2 gene at 7 and 10 day time points, for the polymer and three composite films. Expression levels are highest overall for the MgTCP composite material at 7 days; after which a down-regulation is observed for each composite at the 10 day time point. Results = mean ± s. d. * = p<0.05, paired samples t-test.

6.4 Discussion

Biomaterials are believed to change and influence cellular responses initially at the cell-biomaterial interface, wherein protein interactions and focal adhesions are affected.[21] Studies have indicated that surface treatments can have strong influences on cellular activity and differentiation, as discussed in section 6.1.3. Results in this chapter were studied both qualitatively and quantitatively, through immunofluorescence studies and q-PCR analysis, respectively.

A novel etching process was developed to remove the top layer of the polymer film and expose the filler materials to the surface, creating a nanoscale texture. Samples without etching (zero seconds) showed no clusters present at the surface, which was expected. At the opposite end of the spectrum, samples etched for thirty seconds also showed a flat and polymeric surface; it is believed that the film was exposed to the plasma for too long and the polymer has melted. Results indicate that five second etching provided enough time to

remove the top layer of polymer without melting or damaging the surface topography. After this stage, all film samples were thereafter plasma treated before any bioactivity testing, as previous research demonstrates that cellular activity is higher on surfaces with a rough, rather than smooth, topography.[11]

Fluorescent microscopy studies were conducted on the casein composite films to determine whether the nanoclusters would be available to the cellsafter compositing and etching. Drawing on the ability of an antibody to bind only to a specific antigen through a highly selective 'lock and key mechanism', a casein antibody was used to determine whether it would recognise the casein binding site in the composite. If an attachment was made through the antibody-antigen bonding mechanism, the fluorescent molecule attached to the antibody would be visible under microscope, indicating that using the casein nanoclusters were presented on the material surface. Fluorescence results mimicked those attained from AFM analysis of the films: without etching (zero seconds), the casein antigen molecules were not exposed to the antibodies at the material surface, and melting of the polymer at thirty seconds meant that the casein molecules were again shielded from interacting with the antibody molecules. Only samples etched for five seconds showed high levels of fluorescence, which indicates that the casein antigens were not only present at the material surface, but had not undergone denaturation during the synthesis and etching processes. This indicates that proteacious nanoparticles could be considered for use in the future.

Immunofluorescence studies focused on the focal adhesions, microtubules and actin filaments formed during the cell cultures. Although the casein molecules appeared to survive the compositing process, images showed poor cellular growth and activity on the material surface, with few mature focal adhesions and poor actin and microtubule growth. This too was the case for the PLA control film; limited organisation of actin and microtubules were noted. Both the unsubstituted and Mg-substituted β-TCP samples, however, initially showed good attachment to the material surface through numerous focal adhesions around the periphery of the cells. Well organised actin and microtubule networks were observed for both β-TCP composite films. As actin is involved in cell movement and contraction, and is linked to cell signalling, the high levels present in the two films suggest that the cell is actively signalling to trigger differentiation. With microtubules responsible for protein processing, the highly organised construction of the microtubule networks in cells seeded onto these two composites is indicative of high levels of proteins being pumped into and out of the cell i.e. they are metabolically active. The

combination of high levels of actin and tubulin, from cells on the β-TCP films, provides a well organised cell cytoskeleton, and subsequently an active cell.

An active cell with a good cytoskeleton leads to cytoskeletal tension. The rational next step in cellular activity, upon reaching cytoskeletal tension, should be osteogenesis.[22] OPN staining provided another indication that the β-TCP composite films may induce the highest levels of cellular activity; only in these two images can positive staining for the osteogenic protein be observed. Immunofluorescence studies therefore show that the highest levels of cellular activity are observed from cells seeded onto the surfaces of the β-TCP composite films.

To quantify results at a transcriptional level, q-PCR analysis was performed on cells cultured on the films at 7 and 10 day time points. Of all four films, Mg-TCP composites showed the highest levels of Runx2 expression, noted at the 7 day time point. This result correlated with those previously seen from cellular imaging on the material surface. It is curious that the unsubstituted β-TCP sample did not also demonstrate an up-regulation of gene expression, when considered that the immunofluorescence results were similar. At this early stage of research, it is our theory that the capricious nature of the osteoblast cells, alongside the rapidly changing Runx2 expression levels during the differentiation process, have attributed to this unexpected result. Although further testing must be carried out to verify these initial results, it is believed that the substituted Mg-TCP composite film induced the highest levels of biological activity.

6.6 Conclusions

Promising bioactivity results indicate that the plasma etching process and synthesised calcium phosphate materials, combined in the polymer composite, may constitute the early stages in the development of a novel bioscaffold material. Further studies at the transcriptional level would allow for confirmation of osteogenesis, after which research could focus on comparing bioactivity results against a range of composites with different filler materials, including those with multiple substitutions of different cations and anions, and those fillers with different morphologies.

6.6 References

[1.] A. W. Lund, J. A. Bush, G. E. Plopper, J. P. Stegemann, *J. Biomed Mater Res B Appl Biomater.*, 2000, **87**, 213

[2.] G. S. Stein, J. B. Lian, *Endocr. Rev.*, 1993, **14**, 424

[3.] T. Fujita, Y. Azuma, R. Fukuyama, Y. Hattori, C. Yoshida, m. Koida, K. Ogita, T. Komari, *J. Cell. Biol.*, 2004, **166**, 85

[4.] B. G. Keselowsky, A. J. Garcia, *Biomater.*, 2005, **26**, 413

[5.] Rebecca McMurray, *PhD thesis*, University of Glasgow, 2011

[6.] Molecular Biology of the Cell, 4th Edition, B. Alberts, A. Johnson, J. Lewis, M. Raff, K. Roberts, P. Walter, *Garland Science*, 2002, 908

[7.] The Cell: A Molecular Approach, 2nd Edition,G. M. Cooper, *Sinauer Associates Inc.*,2000, 486

[8.] B. J. Keselowsky, D. M. Collard, A. J. Garcia, *Proc. Natl. Acad. Sci. USA.*, 2005, **102**, 5953

[9.] Fahsai Kantawong, *PhD thesis*, University of Glasgow, 2009

[10.] K. A. Kilaan, B. Bugarija, B. T. Lahn, *Proc. Natl. Acad. Sci. USA.*, 2010, **107**, 4872

[11.] M. J. Biggs, R. G. Richards, N. Gadgaard, C. D. W. Wilkinson, R. O. C. Oreffo, M. J. Dalby, *Biomater.*, 2000, **30**, 5094

[12.] A. S. Curtis, C. D. Wilkinson, *J. Biomat. Sci. Polym. Ed.*, 1998, **9**, 1313

[13.] A. S. Curtis, C. D. Wilkinson, *Biochem. Soc. Symp.*, 1999, **65**, 15

[14.] M. J. P. Biggs, R. G. Richards, N. Gadegaard, C. D. W. Wilkinson, M. J. Dalby, *J. Orth. Res.*, 2007, **25**, 273

[15.] M. J. Dalby, M. V. Kayser, W. Bonfield, L. Di Silvio, *Biomater.*, 2002, **23**, 681

[16.] M. J. Dalby, L. DiSilvio, N. Gurov, B. Annaz, M. V. Kayser, W. Bonfield, *Tissue Eng.*, 2002, **8**, 453

[17.] http://www.harrickplasma.com/plasma-physics.php. Accessed 21/07/12

[18.] Plasma Processes for Semiconductor Fabrication, W. N. G. Hitchen, *Cambridge University Press*, 1999, 12

[19.] C. P. Pennsii, V. Zachor, L. Gureuich, A. Patriciu, J. J. Struijk, 32nd Annual International Conference of the IEEE EMBS, Buenos Aires Argentina, 2010

[20.] R. D. McGurdy, J.J. McGrath, A. Mackay-Sim, *Gene Ther. Mol. Biol.*, 2008, **12**, 15

[21.] M. J. P. Biggs, R. G. Richards, S. McFarlane, C. D. W Wilkinson, R. O. C. Oreffo, M. J. Dalby, *J. R. Soc. Interface*, 2008, doi:10.1098/rsif.2008.0035

[22.] M. J. Dalby, M. J. P. Biggs, N. Gadegaard, G. Kalma, C. D. W. Wilkinson, A. S. G. Curtis, *J. Cell Biochem.*, 2007, **100**, 326

7. Conclusions and Future work

7.1 Conclusions

This thesis documents the synthesis, characterisation and analysis of calcium phosphate polymer composite biomaterials. Both conventional and novel methods were employed to synthesise β-TCP and magnesium substituted β-TCP (Mg-TCP). XRD and SEM studies were primarily employed for the structural and morphological characterisation of the calcium phosphate filler materials, respectively. Degradation studies and tensile testing constituted the main aspects of mechanical testing. Immunofluorescence studies and real-time PCR testing assessed the *in vitro* biological activity of the composites.

A primary focus of the research presented in this thesis was the synthesis and characterisation of β-TCP. Conventional wet-chemical and novel methods using microwaves were employed to synthesise the material. The microwave and two aqueous precipitation methods were studied in depth to optimise the syntheses and attempt to obtain single phase β-TCP. However, PXD data showed that only one of the three methods, an aqueous precipitation reaction using $Ca(NO_3)_2$ and $NH_4H_2PO_4$ starting materials, could produce β-TCP as the final sole product. PXD yielded lattice parameters of a = 10.4469 (2) and c = 37.4047 (7), which is in good agreement with the literature.[1] When the microwave and second aqueous precipitation method was employed, it was evident from results that deviating from a Ca: P ratio of 1.5 resulted in the formation of unwanted by-products. Each method required a high temperature calcination stage (minimum 700 °C) to convert intermediate phases to β-TCP. A degree of morphological control was obtained over the samples through the incorporation of the cationic organic surfactant cetyltrimethyl ammonium bromide (CTAB, $(C_{16}H_{33})N(CH_3)_3Br$)). Increasing or decreasing CTAB concentration influenced surface area and pore size. The substitution of CTAB for other organic surfactants with different end groups and carbon chain lengths also changed the morphological features of the samples. Although two of the synthetic methods produced an end product containing unwanted additional phases, the analysis and optimisation of each experimental procedure has provided information on the importance of specific experimental parameters. It is believed that a more stringent, careful control over the pH of the reaction solutions could allow the two techniques to be advanced into producing single phase β-TCP in the future.

Cationic substitution of the β-TCP structure with magnesium produced a range of Mg-substituted β-TCP samples (Mg-TCP). Magnesium was specifically chosen as the primary cationic substitute because it has been proven to stimulate osteoblast differentiation, which could therefore assist in the overall bioactivity of the composite materials. [2]Initial PXD patterns of the substituted samples showed peak shifts in relation to the unsubstituted β-TCP material.This provided an early indication that Mg had substituted into the crystal structure. Reductions in lattice parameters (due to the smaller ionic radii of Mg) also confirmed that substitution had occurred, and a further investigation into the level and method of substitution was carried out using Rietveld refinements. A range of refined dopant levels between 5.45 and 8.81 mol% were confirmed. Increasing the Mg ion concentration to 36.3 mol% produced a material which could not be refined due to the presence of too many by-products. $Ca_3(PO_4)_2$ and $Mg_3(PO_4)_2$ have completely different crystal structures, so it is conceivable that the addition of high levels of Mg into the reaction system could not simply be incorporated into the previous crystal structure to produce 100% cationic substitution within the same unit cell. Mg preferentially substituted onto one of five of the Ca sites in the crystal structure: Ca (5). High levels of substitution observed at this site are attributed to its low coordination number. Evidence for substitution at the Ca (5) site is attained from the Ca (5)-O bond lengths, which shorten as the % of Mg added is increased. At high mol% levels of substitution, evidence from bond lengths suggests that the Ca (4) site could additionally be occupied by low levels of Mg present on the site. This is in agreement with the literature. [3]

Both unsubstituted and Mg-substituted β-TCP samples were processed into polymer composite films, alongside casein composites and PLA-only control films. A higher wt% of filler materials (60 wt%) yielded a rougher surface morphology than those films with only 40 wt% of filler. Degradative studies showed that each of the higher wt % composites showed substantially higher mass losses than their equivalents at 40 wt%. This is largely attributable to the dissolution of more filler particles into the surrounding solution. The morphology of the β-TCP samples, i.e. agglomerated, fused spheres, hindered the mechanical properties of the composite films. Tensile strengths for the β-TCP composite films were greatly reduced in relation to the PLA control. The cause of this is believed to centre on the fact that the PLA could not distribute throughout the entire filler material when the composite was being produced. Incomplete distribution of the polymer around the filler molecules means that particle to particle contact occurs, and research shows that the strength of the composite is compromised under this condition. [4] Increasing filler wt%

only served to heighten the degree of particle to particle contact and caused interface failure, thereby worsening the mechanical properties.An assessment of the bioactivity of the composite films was carried out using simulated body fluid (SBF).Formation of an apatite layer on both of the 40 and 60 wt% PLA-βTCP composite materials was observed. Apatite layers were absent from all other sample surfaces.

Research has shown cells to adhere and spread better on surfaces with a rough surface, as opposed to those with smoother surfaces. [5] To enhance the biological activity of the composite films *in vitro*, a novel etching process was developed to give the films a 'roughened' surface morphology, with filler materials available to the cells at the surface of the films. Fluorescent microscopy studies using antibodies indicated that the casein protein present in the equivalent composite film was able to survive the compositing process without suffering denaturation. However, subsequent immunofluorescence studies showed poor adhesion and cytoskeletal organisation on the casein film surfaces. q-PCR analysis likewise showed no up-regulation for Runx2 expression. These results imply that the casein composites are not bioactive. The β-TCP and Mg-TCP composite films, conversely, showed strong indicators of bioactivity. Cells present on the surfaces of these films showed strong adherence and cellular spreading, with good organisation of actin and tubule fibres. Osteopontin expression was observed on both surfaces, and q-PCR analysis showed a significant up-regulation of Runx2. A combination of immunofluorescent results and Runx2 expression demonstrate that the Mg-TCP composite films show the highest levels of bioactivity of all the composite films.

7.2 Future work

An expansion of the optimisation results attained from each of the three synthetic methods is required to further assess the influence of experimental parameters on product formation. Introducing surfactants with more distinct structural features into the reaction system could potentially result in materials with a range of different morphological features, for example the incorporation of branched chain organic surfactants, as opposed to the previously used straight chain molecules. It has been hypothesised in this thesis that CTAB distributes within the reaction system *via* a process of molecular recognition, as a result of its cationic end group. [6] However, to test this theory, anionic and neutral surfactants could be used to ascertain whether they exhibit the same levels of dispersal as their cationic equivalent.

Morphological control has only been achieved in this research through the use of synthetic organic surfactant molecules, but the idea of using natural products which also act in a templating capacity is thought to have significant potential and clinical relevance in the synthesis of a biomaterial. An example of such an avenue of exploration could focus on the use of amino acids to control crystal growth of the material.

Synchrotron XRD data could potentially provide higher quality diffraction data for substituted samples, allowing for a more thorough investigation of substitution at both low levels and higher % doping. Substitution of different cations into the structure would be an obvious next step, to investigate whether the same mechanism of substitution applies as is the case of Mg, or whether different cations incorporate into the crystal structure *via* a different mechanism to different sites. Research has shown ions with a larger ionic radius than Ca^{2+} (e.g. Si^{4+}) substitute preferentially onto different cation sites than those observed in this research for Mg^{2+}, and show expansion of the unit cell parameters and cell volume. [7] Effects on the biological activity and mechanical properties of composite films containing these samples could also be investigated. Once different substituted materials are developed, the next stage would be the substitution of multiple cations within the crystal structure, to create a material with the analogous element composition of bone.

To improve on the mechanical properties of the composite films, a method of producing β-TCP materials with no agglomeration must be developed. This is well documented in literature to be a difficult task, as a result of the high temperature calcination stage required. If a nano powder material was developed, it is logical to presume that the PLA would be able to surround each filler particle during the composite film production process, thereby eliminating the problem of particle to particle contact. This should, in turn, greatly enhance the tensile strength of the composite films. It is also plausible that the degradative properties of the films could be controlled more closely with a smaller mean particle size.

Further investigation into the biological activity of the composites must be conducted to confirm initial results. Immunofluorescence and q-PCR studies must be repeated to ensure the validity of the results, with a greater range of time points examined. Research in this chapter only focused on assessing the biological activity of the 40 wt% films; however it would be interesting to also test the 60 wt% films. Testing composite films with a more

finely dispersed filler material would be useful to determine if more uniform results would be obtained.

Research in this thesis has produced initial results which could eventually contribute to a novel range of composite films used in clinical applications. Promising bioactivity results must be maintained in future work with an improvement in the mechanical properties of the composite films. The success of this, it is believed, relies firmly on developing a novel method for synthesising nanoscale, non agglomerated β-TCP samples and subsequent nano-composites with PLA.

7.3 References

[1] M. Yashima, A. Sakai, T. Kamiyamana, A. Hoshikawa, *J. Solid State Chem.*, 2003, **175**, 272

[2] Y. Wang, S. Zhang, K. Wei, N. Zhao, J. Chen, X. Wang, *Mater. Lett.*, 2006, **60**, 1484

[3] E. Bertoni, A. Bigi, G. Cojazzi, M. Gandolfi, S. Panzavolta, N. Roveri, *J. Inorg. Biochem.*, 1998, **72**, 29

[4] N. Matsumoto, K. Yoshida, K. Hashimoto, Y. Toda, *Mater. Res. Bull.*, 2009, **44**, 1889

[5] M. K. Mekki-Berrada, C. Damia, E. Champion, *Key Eng. Mater.*, 2009, **396-398**, 165

[6] W. Bonfield, *J Biomed. Eng.*, 1988, **10**, 522

[7] M. J. Biggs, R. G. Richards, N. Gadgaard, C. D. W. Wilkinson, R. O. C. Oreffo, M. J. Dalby, *Biomater.*, 2000, **30**, 5094